The effect of the catalyst on the formation of RF xerogels

By Lynsey Anderson

A thesis submitted to the Department of Process and Chemical Engineering, the University of Strathclyde, in part fulfilment of the regulations for the Degree of Doctor of Philosophy.

Copyright declaration

Signed:

Dated:

Acknowledgements

Firstly, I would like to extend my sincere gratitude to my supervisor, Ashleigh Fletcher. Throughout my PhD, and beyond, she has supported and guided me with my studying, allowing me to develop and achieve my goals. Over the last year she has continued to assist me with my thesis writing and has always been available to provide support and encouragement. We have become good friends and without her continued guidance and friendship my end goals would have been considerably harder to achieve.

I would like to acknowledge Alison Nordon for her technical support and along with my other colleagues, within the Analytical Chemistry Department, for rehoming us when we were evacuated from Chemical Engineering by the 'fire'.

Great thanks also go to the Chemical Engineering lab technicians, with a special mention to Iain Airdrie for all his help and guidance with the BET equipment and to Jim Murphy and John Wilkie for all their help and support over the years (especially the gossip sessions, which kept me going in the lab).

I would also like to extend appreciation to my colleagues and friends, within the Chemical Engineering Department, with a special mention to Stewart Taylor, for all his help in my final months and to his continued help in the last year, and to Jaclyn Dunn for always being a great friend, even when going through a difficult time herself. University wouldn't have been the same without you Jaclyn.

I would like to thank, my future husband, Mark, mainly for putting up with me throughout the thesis writing stage, where I am sure I have been hard to live with at times.

And finally I would like to take this opportunity to sincerely thank my parents, John and Agnes Anderson, who have guided and encouraged me throughout my university career. Without their financial support, and friendship throughout my life I wouldn't be the person I am today and I certainly wouldn't have completed a PhD, thank you for always being there.

Abstract

The ability to alter the nanostructure of resorcinol formaldehyde (RF) gels by varying the synthesis conditions, along with the obtainable properties, makes them valuable for a number of applications. Consequently, optimising the synthesis process is important to produce high quality gels that possess desired properties for the desired application.

In order to control the formation of RF gels, it is vital to understand the specific role of the catalyst (C), with previous studies suggesting that its function is to alter the initial sol pH [1, 2], enabling gel formation to take place. It has been reported that controlling sol pH, allows the nanostructure of the final gel to be controlled [3], with lower initial pHs resulting in gels with higher surface areas, pore volumes and wider pore size distributions, where the inverse is true for higher pHs. This theory, however, does not explain why gels prepared from sols with equivalent initial pH possess significantly different characteristics, for example average pore diameters and pore volumes. Furthermore, studies into the effect of initial sol pH alter the alkalinity of the sol by modifying the molar ratio of R to C, subsequently, making it difficult to differentiate between the effects of catalyst and sol pH.

In this study organic xerogels were prepared using the pre described poly-condensation method, however, a wide range of base catalysts (Na_2CO_3, K_2CO_3, $NaHCO_3$, $KHCO_3$, NaOH, KOH, $CaCO_3$, $SrCO_3$, $BaCO_3$ and $(NH_4)_2CO_3$) were employed, at varying concentrations, with all other experimental variables kept constant. Through the use of HPLC, titration and DLS the RF polymerisation reaction was monitored allowing effects of R/C ratio, initial sol pH, cation size, charge and presence, as well as base type and deprotonating ability to be identified, differentiated and comprehensively studied.

It was found that, in general, for each individual catalyst, increasing R/C ratio caused an increase in average pore diameter and total pore volume, and a decrease in specific surface area. When all catalysts were considered together it became apparent that, rather than initial sol pH influencing the final properties, the xerogel nanostructure was dependent on the potential deprotonation ability (DPA) of the catalyst. Comparing RF gels prepared with Group I and Group II metal catalysts confirmed that cation size and charge affects the polymer stability and aggregation, subsequently, influencing overall structure. Monitoring the reaction of gels catalysed with no catalyst or $(NH_4)_2CO_3$ demonstrated that the presence of a metal cation is vital for base catalysed sol-gel polymerisation of R and F.

Identifying and distinguishing the specific role of the basic catalyst, will allow RF polymerisation to be studied in full, using Design of Experiments (DoE). This approach will not only determine the effects of individual variables, but will also establish the combined influence of experimental conditions. Understanding the polymerisation fully will offer complete control of RF structure, permitting gels to be prepared with precise desired properties.

Contents

1 List of abbreviations

ANOVA	Analysis of Variance
ATR	Attenuated Total Reflectance
AUFS	Absorbance Units Full Scale
BET	Brunauer Emmett and Teller
BJH	Barrett Joyner Halenda
DLS	Dynamic Light Scattering
DPA	Deprotonation Ability
$Dp_{average}$	Average pore diameter
DVLO	Derjaguin, Verwey, Landau and Overbeek
EDLC	Electrochemical Double Layer Capacitor
F	Formaldehyde
HETP	Height Equivalent of Theoretical Plates
HM	Hydroxy-methyl
HOMO	Highest Occupied Molecular Orbital
HPLC	High Performance Liquid Chromatography
IR	Infra-Red
LC	Liquid Chromatography
LCMS	Liquid Chromatography Mass Spectrometry
LSC	Liquid Solid Chromatography
LUMO	Lowest Unoccupied Molecular Orbital
MIR	Mid Infra-red
MP	Mobile Phase
NIR	Near Infra-red
NP	Normal Phase
ODS	Octadecylsilane
PEM	Polymer Electrolyte Membrane
PMT	Photomultiplier Tube
PSD	Pore Size Distribution
R	Resorcinol
R/C	Resorcinol/Catalyst molar ratio
R/F	Resorcinol/Formaldehyde ratio
RSD	Relative Standard Deviation
R/W	Resorcinol/Water molar ratio

SAXS	Small Angle X-Ray Scattering
S_{BET}	BET Specific surface area
S_{MIC}	Micropore volume
SEM	Scanning Electron Microscopy
TGA	Thermo Gravimetric Analysis
TEM	Transmission Electron Microscopy
SP	Solid Phase
UV	Ultra violet
V_{MIC}	Micropore Volume
V_{MES}	Mesopore Volume
V_{TOT}	Total pore volume

2 Introduction

2.1 History of aerogels/xerogels

The first inorganic silica gels were manufactured by Ebelman in 1846 [4]. The ease of preparation of these inorganic gels was then utilised in 1932 by Kistler [5] to prepare the first aerogels. Kistler's synthesis first involved the acidic condensation of sodium silicate producing a silica hydrogel and sodium chloride. The reaction is illustrated in Equation 1.

$$Na_2SiO_3 + 2HCl + (x-1)H_2O \rightarrow SiO_2xH_2O + 2NaCl$$

Equation 1

Kistler noted that, independent of the liquid within the pores, most gels demonstrated a resistance to recompression, this lead him to believe that the liquid in the gel could be replaced with a gas, creating an aerogel, which would hold the same shape and volume as the original wet gel [4].

Kistler discussed [4] that drying by evaporative means resulted in surface tension and subsequent collapse of the gel, thus a supercritical method of drying was developed. This process allowed gradual transfer of the liquid to a gas, transitioning the critical temperature, without the presence of two phases at any one time (i.e. no vapour-liquid interface, thus no surface tension and compressive forces). Kistler also established that due to the high critical temperature and pressure of H_2O (647 K and 218 atm [6]), and its poor solubility in supercritical solvents [7], water within the system had to first be exchanged with a solvent that was completely miscible with the supercritical solvent, which meant that the method was time consuming.

It was this lengthy step that lead Stanislas Teichner's group at the University of Lyons to develop a sol-gel synthesis procedure using tetramethoxysilane [8], the overall reaction is shown in Equation 2.

$$Si(OCH_3)_4 + 2H_2O \rightarrow SiO_2 + 4CH_3OH$$

Equation 2

The process produced a '*sol*' with a methanol liquid phase, thus removing the need for the water exchange step.

2.2 History of resorcinol formaldehyde aerogels

2.2.1 Invention of resorcinol formaldehyde (RF) aerogels

In the 1980s, the Lawrence Berkeley Laboratory [8] discovered that supercritical CO_2 could be used as a replacement to supercritical methanol for the drying of silica aerogels [8], this presented a much safer alternative due to its significantly reduced critical temperature (CO_2 critical point = 304.18 K, 73.8 atm [9], methanol critical point = 513.5 K and 78.5 atm [10]). In 1989, Pekala *et al*. [11, 12] used this discovery, along with previous knowledge on resorcinol formaldehyde (RF) resins to prepare organic aerogels from the polycondensation of resorcinol (R) and formaldehyde (F).

Pekala's method was similar to that used for silica gel formation and involved a sol-gel processing technique (discussed further in Section 2.4) involving the reaction of resorcinol with formaldehyde, at stoichiometric ratios, in aqueous solution using an alkaline catalyst.

2.2.2 RF carbon gels

R and F are now the most common precursors for carbon aerogels, which are generally formed by pyrolysis of dried gels, at elevated temperatures, in inert atmospheres. During these procedures micropores are often formed, converting the organic aerogels into highly porous and electrically conductive carbon systems [4].

2.3 The reaction

2.3.1 Reactants

R is a 1,3-dihydroxy phenol activated in the 2, 4 and 6 positions, due to the combined ortho-para directing nature of the two hydroxyl groups. This is demonstrated by the resonance forms of R shown in Figure 2-1.

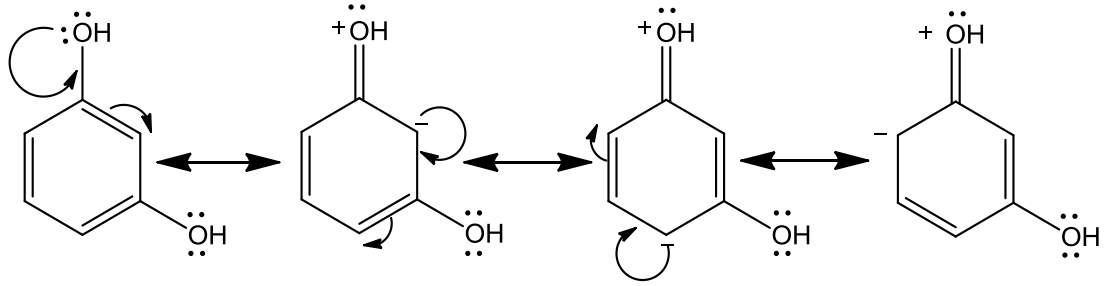

Figure 2-1: Ortho, para directing nature of R hydroxyl groups.

Due to the 1, 3 substitution the reactive positions on the ring are all double activated compared to the singly activated positions in phenol. Consequently, R is much more reactive than phenol.

F contains a carbonyl group and, thus, has an electrophilic carbon centre that can react with the activated carbon centres of R [13].

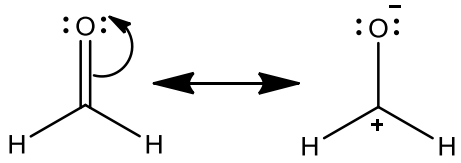

Figure 2-2: Resonance forms of F showing nucleophilic carbon centre.

2.3.2 Proposed reaction mechanism

(a) Uncatalysed

Due to the enhanced reactivity of R (see section 2.3.1), the condensation of R and F can occur with no catalyst, whereas the majority of studies involving the reaction of phenol and formaldehyde report the use of a catalyst. Raff *et al*. [14] studied the kinetics of the uncatalysed R F reaction and found that the reaction was first order in respect to the R/F molar ratio, i.e. decreasing the molar ratio (increasing the F concentration) increased the rate of reaction. Raff *et al*. [14] compared the rate constant for the uncatalysed RF reaction, at 90 ˚C, to the rate for a catalysed phenol F reaction, at 98 ˚C, and reported that the rate constant for uncatalysed RF reaction was 2.54 times that of the phenol F reaction. Given that this comparison compared uncatalysed RF with catalysed phenol F it demonstrates the increased reactivity of R towards condensation with F.

(b) Base Catalysed

The general reaction occurs in two main stages: first a hydroxy-methyl derivative is generated from an addition reaction between R anion and two F molecules, which can add at the 2, 4 and 6 positions. Condensation of the hydroxy-methyl products follows, resulting in methylene and methyl-ether bridged clusters. Subsequent aggregation of these clusters leads to the formation of a highly cross-linked sol gel. The reaction is illustrated in Figure 2-3 [15].

At the start of the reaction, the RF sol is colourless, however, as the reaction proceeds the sol changes colour to yellow, then orange and finally to a deep red [12, 16, 17]. The colour change from colourless to yellow is due to the formation of hydroxyl-methyl compounds,

which are known to be colourless crystals individually [18], however in the sol they are present in large quantities, resulting in a yellow colour. As the sol-gel transformation proceeds these compounds increase in concentration and cross link together forming a dense conjugated polymer that appears red in colour [19].

The initial formation of hydroxy-methyl derivatives occurs rapidly [20], subsequent reaction with F forms form hydroxy-methyl compounds, which condense forming bridged compounds. The condensation reaction occurs slower than the initial reaction with the base; therefore this is the rate determining step. However, the formation products of the condensation reaction, bridged compounds, are more reactive than R anions and therefore react rapidly to form many small clusters [11].

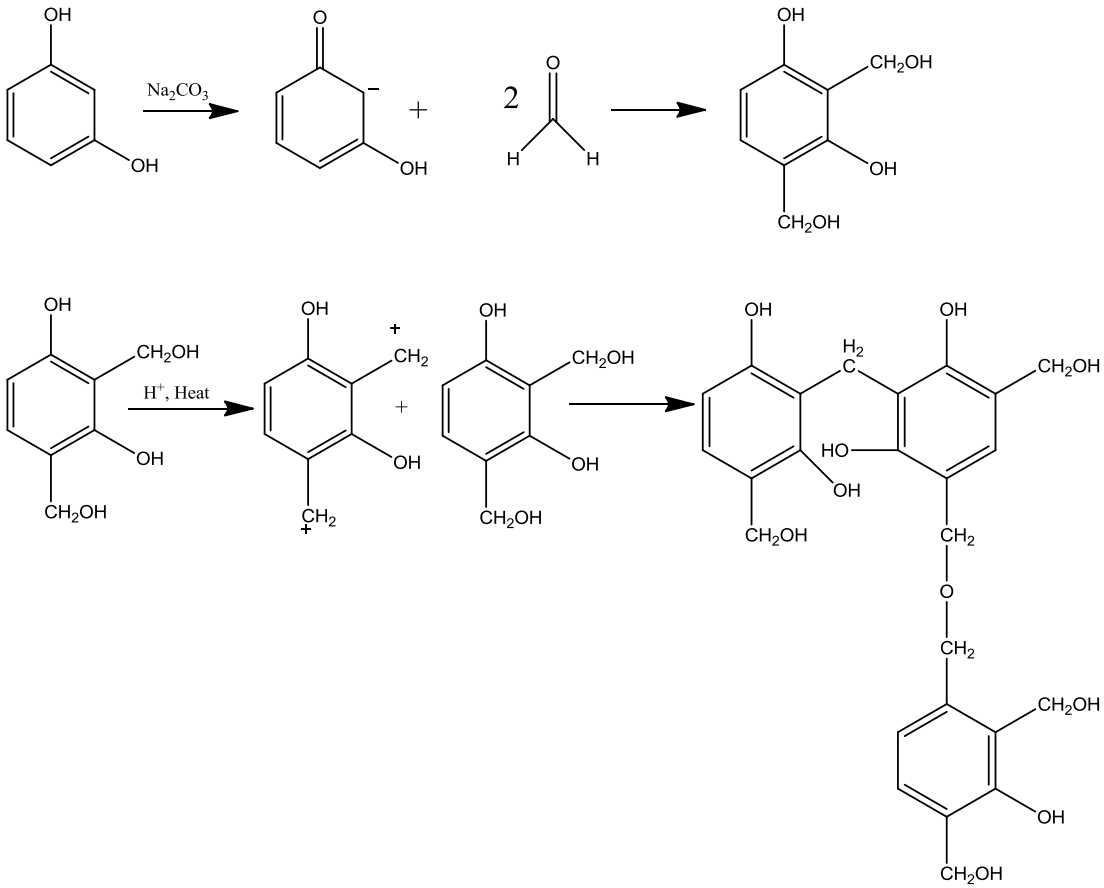

Figure 2-3: Proposed reaction mechanism for the formation of RF gels [15].

(c) Acid catalysed

Although base catalysed RF polycondensation is the most common method in forming RF gels, the process can also be acid catalysed. In this type of catalysis the acid protonates both the R ring and F, as illustrated in Figure 2-4 and Figure 2-5 respectively. Protonation of the

aromatic R ring makes the structures less active as a nucleophile; however F becomes a more effective electrophile, compensating for the less reactive R [20].

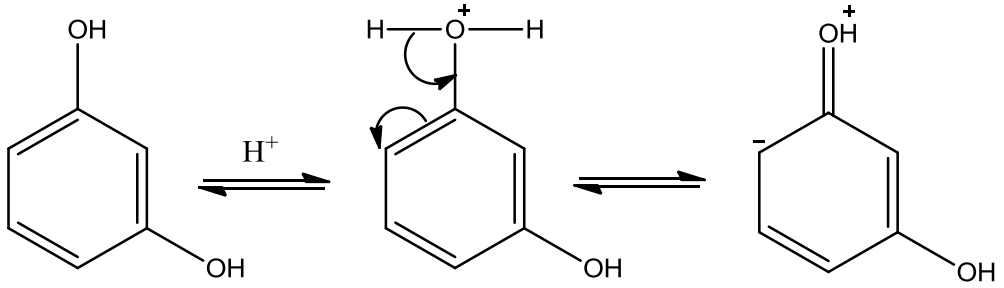

Figure 2-4: Protonation of R during acidic catalysis, derived from the protonation of phenol shown in [20].

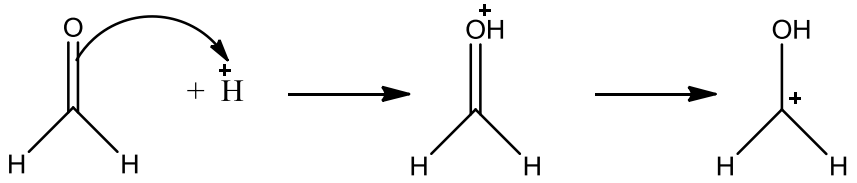

Figure 2-5: Protonation of F during acidic catalysis [20].

Consequently, condensation proceeds via electrophilic substitution on the R, to form hydroxy-methyl derivatives, subsequent loss of H_2O results in the formation of carbonium ions, which react together forming methylene bridged structures. Due to the slow formation of phenolic alcohols, the initial electrophilic substitution to form hydroxy-methyl occurs slowly and therefore determines the rate of the overall reaction. This is in contrast to base catalysed polycondensation, during which, the formation of hydroxy-methyl groups occurs rapidly, followed by slower polycondensation.

Reuß *et al*. [21] demonstrated hydrochloric acid catalysis as a means of preparing RF aerogels. They demonstrated that using this method, RF aerogels could be prepared with very short gelation times (seconds to minutes) compared to the long gelation times observed for basic catalysis. However, it should be noted that this method produced gels with significantly diminished surface areas (4.76 m^2/g – 14.19 m^2/g), when compared to gels prepared via basic catalysis which typically have surface areas in the region of 400 – 1200 m^2/g [15].

This reduced gelation time was also demonstrated by Barberi *et al*. [7] who reported reduced gelation time for gels catalysed by perchloric acid. This acid catalysed method produced RF gels with fractal structures, compared to the uniform '*string of pearls*' appearance normally observed for base catalysed gels. Barberi *et al*. proposed that, this structural difference

resulted due to differences in the aggregation of particles. Given that, in acidic medium the initial reaction between R and F is slow, compared to the rapid reaction observed in basic medium, it is likely to be this initial stage that causes the observed structural differences.

Under basic catalysis the initial reaction occurs rapidly forming many hydroxyl-methyl derivatives, which react together forming many small clusters, whereas under acid catalysis the formation of the hydroxyl-methyl derivatives is much slower, resulting in the formation of fewer clusters and as a result a reduced number of active reaction sites. Subsequently, in acid catalysed systems it is likely that the reaction will proceed in chains rather than clusters, which would explain the fractal appearance.

2.4 Sol-gel synthesis

2.4.1 Introduction to sols and gels

The gels formed in this study will be synthesised through the use of sol-gel synthesis, which involves starting with a sol, which reacts to form a gel as illustrated in Figure 2-7.

A sol is a discontinuous dispersion of particles in a continuous liquid phase [23]. Whereas, gels are colloidal systems in which a continuous solid phase is extended throughout a discontinuous dispersion medium. In terms of both weight and volume, gels are mostly made up of their extender fluid; however, due to the formation of a continuous three dimensional cross-linked network, they exhibit solid-like behaviour [24]. It is this solid-like framework that gives rise to the unique properties of gels, allowing them to be employed in a wide variety of applications [12], for example electrophoresis of protein mixtures, chromatographic packaging and in the manufacture of soft contact lenses.

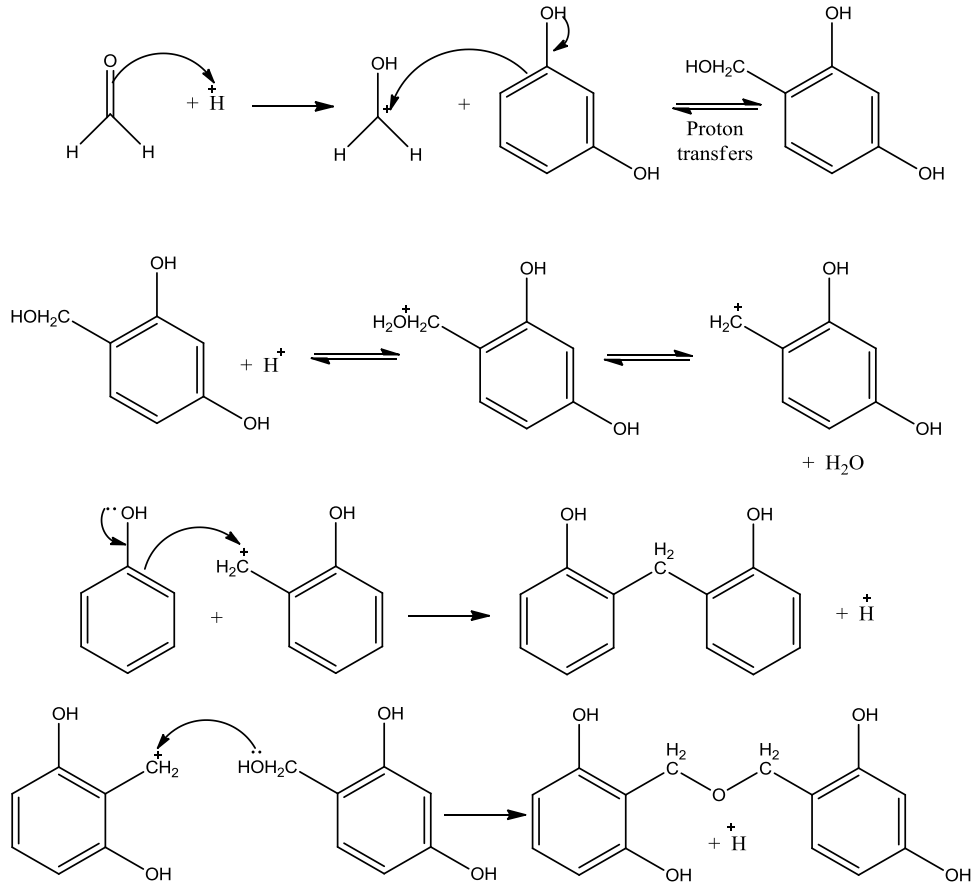

Figure 2-6: Acid catalysed polycondensation of R and F. Derived from the condensation of phenol and F illustrated in [20, 22].

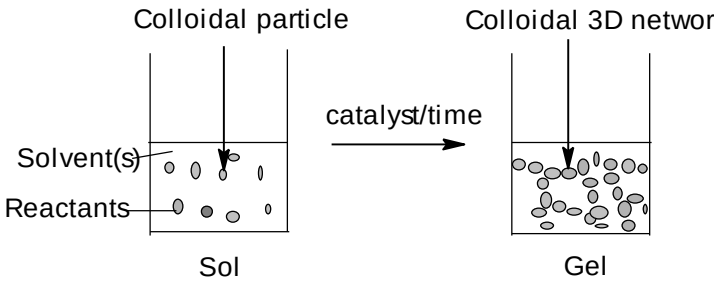

Figure 2-7: Sol-gel synthesis procedure.

2.4.2 Sol-gel transformation

The sol-gel transformation is usually defined as the gelation time and is observed as a rapid increase in viscosity of the sol [24, 25]. This rapid viscosity change prevents the sol from flowing when tipped at a 45 °C angle [26], and it is then referred to as a gel. The sol-gel transition is of significant importance, as it is during this stage that the porous properties of the final gel structure are defined [27-30].

(a) Microphase separation or colloidal aggregation

As discussed in Section 2.2, RF xerogels are formed through the poly-condensation of R and F, which react in water forming suspended particles that grow and aggregate through the solution, with eventual gelation. However, the processes resulting in the sol – gel transition have long been debated, with some researchers favouring colloidal aggregation [27, 31] and others proposing microphase separation [30, 32].

The process of colloidal aggregation involves the aggregation of gel colloids until the polymer mass spans the entire volume of solution [33], whereas microphase separation is thought to result from incompatibility between the colloidal gel and the solution, which causes a significant decrease in the entropy of the polymer, initiating de-mixing [32].

Early work by Keefer *et al.* [34], investigating the growth of fractal colloids in aqueous solutions of TEOS demonstrated the growth of mass fractals to form a solid with fractal surfaces (where a mass fractal is defined as a colloid demonstrating mass that scales with radius and a fractal surface displays similar mass scaling with radius but also demonstrates a more rapid scaling of surface area with radius).

This study showed that with increasing water concentration (i.e. increasing reactant concentration) colloidal suspensions changed from mass fractals to surface fractals, suggesting that as the reaction proceeds colloids grow and aggregate. The crossover from mass to surface fractals with increasing reactant concentration suggests that particle growth is dependent on the rate of reaction, consequently pointing towards a colloidal aggregation mechanism, which results from growth of the colloidal suspension until it fills the reaction space.

Similar results, for RF systems, were reported by Tamon *et al*. [27] who demonstrated that during the initial stages of the reaction small mass fractal clusters existed. Subsequent aggregation of these clusters then formed particles displaying surface fractal characteristics, which formed RF xerogels with smooth surface morphology and a *'string of pearls'* appearance.

These results are in contrast to the microphase separation process theorised by Pekala *et al*. [32], who unlike Tamon *et al*. [27] reported no indication of fractal clusters in the final gel structure but concluded that the most likely explanation for this is that structural development is dependent on processes occurring near equilibrium and the most reasonable process is microphase separation [32]. This phase separation occurs due to decreased

entropy of the branched polymer network resulting in demixing between the suspension and the solution. With small molecules this change in entropy would result in macrophase separation, however, with the large RF clusters phase separation causes the polymer network to fold up, creating pores filled with solvent [35] and, due to this distortion of polymer configuration, macrophase separation is resisted. As a result microphase separation occurs, during which small domains within the solution demix and as the reaction proceeds a transition from traditional nucleation and growth to spinodal decomposition occurs [32], explaining the '*string of pearls*' appearance.

The two processes discussed above, therefore, present two opposing theories on the sol-gel transition of RF xerogels, however, both result in the same structure with a '*string of pearls*' appearance. Gommes *et al*. [35] investigated RF polymerisation, throughout the sol-gel transition, using Small Angle X-Ray Scattering (SAXS) analysis and modelled both processes for comparison. They proposed two main hypotheses; (i) RF xerogels are biphasic consisting of two defined phases – solvent and polymer (ii) RF structure has two different length scales, where they proposed two different structure models; (a) the RF gel is made up of a solid polymer skeleton which is surrounded by a liquid polymer suspension (small-scale), which also fills the pores of the polymer backbone and (b) the RF gel skeleton is surrounded by pure solvent, which also fills the small pores of the polymer [35]. These models are represented by Figure 2-8.

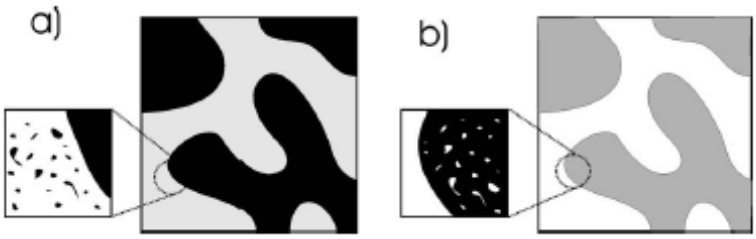

Figure 2-8: Schematic representation of model (a) and model (b) proposed by Gommes *et al*. [35].

The study also demonstrated how SAXS data could be interpreted to fit either model. In model a (colloidal aggregation), as the reaction proceeds the polymer skeleton reacts with the surrounding liquid suspension, resulting in an increase in the volume of the RF skeleton and a decrease in the volume fraction of the polymer suspensions, however, simultaneously some suspensions within the pores aggregate resulting in an increase in the volume of the colloidal suspensions within the pores. In model b (microphase separation), it is theorised that the polymer skeleton is initially of a high volume with many pores. As the reaction proceeds, and the polymer and solvent become incompatible, solvent is extracted/expulsed

from the pores and the volume of the RF skeleton decreases, along with the volume fraction of pores within the skeleton. This model proposes that the smallest pores will disappear first, resulting in an overall increase in the volume of micropores [35].

The results, therefore, demonstrate that SAXS data, from RF polymerisations, can be fitted to both colloidal aggregation and microphase separation and the two processes should not be considered as mutually exclusive, with Gommes *et al*. [35] proposing that these processes are two idealisations of the same complex physical process.

2.4.3 Gelation and curing

Horikawa *et al.* [25] demonstrated, through the use of SAXS, that the initial gelation period and immediate aftermath are fundamental to primary particle formation. They illustrated that the primary particles formed during the initial synthesis stages are responsible for the final porous properties of dried gels, more specifically that the pore size distributions were dependent on this initial particle formation.

The study showed that particle formation was dependent on the initial sol conditions, namely the catalyst used, and the results obtained show that the use of different catalysts resulted in differing gelation times, where gelation time was defined as the time when a rapid increase in viscosity of the sol was observed [24, 25]. Consequently these results suggest that the gelation time may be dependent on particle formation and subsequent reactions of the particulate matter.

2.4.4 Stability of sol (stability of colloidal suspensions)

The stability of the RF sol, before transition to gel, is based upon the solubility of the RF colloidal suspension. This stability is affected by the aggregation and flocculation of colloidal particles.

(a) Interparticle attraction forces

Due to their surrounding electrons every particle has a fluctuating dipole, which results in attraction forces between particles. This attraction is caused by van der Waals forces, which result due to three main interactions, permanent dipole-permanent dipole, permanent dipole-induced dipole and transitory dipole-transitory dipole. The latter interaction is known as London forces and these lead to long range attraction in colloidal suspensions. As particles approach each other London forces are caused by reorganisation of electrons, resulting in attraction between the surface charge of one particle with the electrons of another. As the

separation distance increases the electrons do not reorganise and the attractive forces are reduced [24].

The attractive force was quantified by Haymaker [36], who assumed that pairs of molecules were attracted to one another and the total interaction energy could be calculated by summation of these pair-wise additive attractive forces. This approach led to the following equations for calculating the van der Waals attraction energy (V_A), for colloidal aggregation:

(a) For parallel plates

$$V_A = \frac{-A}{12\pi h^2}$$

Equation 3

(b) For equal spheres

$$V_A = \frac{-Ar}{12h}$$

Equation 4

Where *h = particle separation (any measurement of length i.e. m, nm etc.)*

a = sphere radius (any measurement of length i.e. m, nm etc.)

r = centre-centre separation (any measurement of length i.e. m, nm etc.)

A = Haymaker's constant (~10^{-19} to 10^{-20} J)

Haymaker determined that the intermolecular potential was proportional to $-1/h^6$, consequently comparing this interaction with the above equations it is evident that the attractive forces between particles extend over a long range [36], thus, to prevent aggregation, a repulsive force must be added.

(b) DVLO theory

Derjaguin, Verwey, Landau and Overbeek (DVLO) theorised that the net force between colloidal particles could be calculated as the sum of the van der Waals attractive energy and the repulsive energy (V_R) according to Equation 5:

$$V = V_A + V_R$$

Equation 5

The total potential energy (V) can be presented graphically as shown in Figure 2-9.

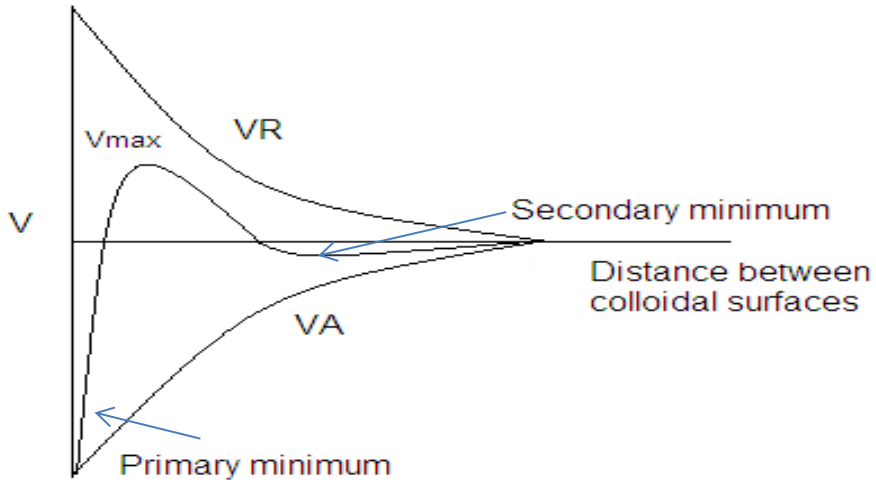

Figure 2-9: DVLO potential energy showing both the repulsive and attractive forces [37].

Repulsive forces can be introduced by adding charged species that can absorb on to the surface of colloidal particles. In the synthesis of RF gels this electrostatic repulsion is caused by addition of metal salts, which introduce metal cations to the sol. The cations pack around the surface charge as illustrated in Figure 2-10.

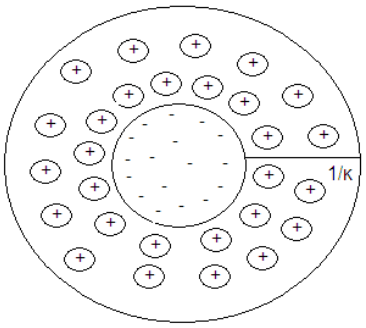

Figure 2-10: Illustration showing the packing of cations around an anionic surface charge [24].

In aqueous solutions the cations become hydrated, large cations and less highly charged ions hold water molecules less tightly, resulting in smaller hydrated radii. Small cations have a high charge density and therefore more water molecules surround the cation, resulting in a large hydrated radius. Consequently, for larger cations and highly charged ions with smaller hydrated radii, the denser the hydrated cations can pack (i.e. larger ionic radii, smaller hydrated radii), resulting in more effective screening of the surface charge.

(c) Debye Huckel theory

The ability of an ion to screen the surface charge was defined by Debye and Huckel [24] as the screening length ($1/\kappa$), see Figure 2-10, where κ is determined using Equation 6. As the ability of ions to screen the surface charge increases, as the screening length decreases (i.e. cations pack more densely around the particle), which allows colloidal particles to come closer together and promotes aggregation/flocculation; as a result the repulsive force between particles decreases, as shown in Equation 7.

$$\kappa = \sqrt{\frac{F^2 \sum_i c_i z_i^2}{\varepsilon_0 \varepsilon R_g T}}$$

Equation 6

Where *F = Faraday's constant (C mol^{-1})*

c = concentration of ion (mol m^{-3})

z = charge of the ion

ε = dielectric constant of the solvent

ε_0 = permittivity of the vacuum (F m^{-1} = C^2/J)

T = Temperature (K)

R_g = Gas constant (J mol^{-1} K^{-1})

$$V_R \propto e^{-\kappa(h-H)} \qquad (h \geq H)$$

Equation 7

From Equation 6, it is evident that as the ionic charge or concentration increases, κ increases, resulting in a decrease in screening length. This reduction in the Debye Huckel length reduces the energy barrier for coagulation [24].

Hsu *et al*. [38] demonstrated that the particle size also has an effect on the repulsive energy barrier, concluding that, as the particle size decreased, the repulsive force between particles decreased. In the synthesis of RF gels this suggests that smaller particles are more likely to react together than larger particles (clusters).

Within RF sols, as the reaction proceeds, the concentration of colloidal particles and clusters will increase, resulting in reduced separation distance and lower repulsion. With decreased repulsion a secondary minimum can appear in the total potential energy diagram (see Figure 2-9), this minimum results in partial flocculation/aggregation, but not enough to cause destabilisation. Brinker reported that for a colloid to be stable within a sol the repulsive potential should be $\geq$ 30-50 mV [24]. As the repulsive potential decreases below this level, the overall energy becomes attractive and the critical flocculation concentration is reached,

resulting in coagulation and resultant gelation. Russel *et al*. [36] reported that the transition from stability to flocculation occurs over a narrow range of ionic strengths (where ionic strength is proportional to c_i and z_i^2), thus it can be concluded that small changes in the repulsive barrier (e.g. from changes in ion charge, size and concentration) can result in destabilisation of the sol, forcing gelation.

(d) Hofmeister series

The initial Hofmeister series was based on the ability of anions to precipitate egg white proteins (second paper written in a series of 7) [39]. Hofmeister found that Li_2SO_4 was the most effective salt for salting out the egg white proteins, requiring 8.6 g/100ml. The following series was developed from Hofmeister's work, with the anions and cations on the left demonstrating the most effective salting out ability, with the overall salting out ability depending on both the anion and cation present:

$$Anions: SO_4^{2-} > HPO_4^{2-} > Cl^- > NO_3^-$$

$$Cations: Li^+ > Na^+ = K^+ > NH_4^+ > Mg^{2+}$$

As expected the concentration of polymer within the solution has an effect on the salting out, and Hofmeister reported that for higher polymer concentrations less salt was required for precipitation. In Hofmeister's initial publication he proposed that these salting out effects were most likely to be caused by the ability of the salts to attract water.

In his next report Hofmeister examined the possibility that precipitation was caused by interactions with the salt and the macromolecule and/or interactions between the salt and the water molecules. Hofmeister established that after precipitation there was little change in the properties, of most of the macromolecules tested, and it was therefore concluded that interactions between the salt and macromolecule were not causing precipitation. Hofmeister then studied the ability of the ions to bind with water molecules, absorbing them from the polymer substance resulting in a greater concentration of protein remaining in the bulk water, causing precipitation. Hofmeister concluded that the most likely explanation for the salting out effects was due to ion binding with water, however his work did present some instances where the properties of the macromolecules were altered after precipitation; consequently the effects were not fully understood [39].

A full understanding of the effects of ions on polymer precipitation is still not fully understood however research in this area has suggested that ions can cause either stabilisation effects (kosmotropic ions) or destabilising effects (chaotropic ions), caused by water interactions, macromolecule-water interactions and direct interactions between the ion

and the macromolecule. The stabilising effects of a number of ions are illustrated in the Hofmeister series shown in Figure 2-11.

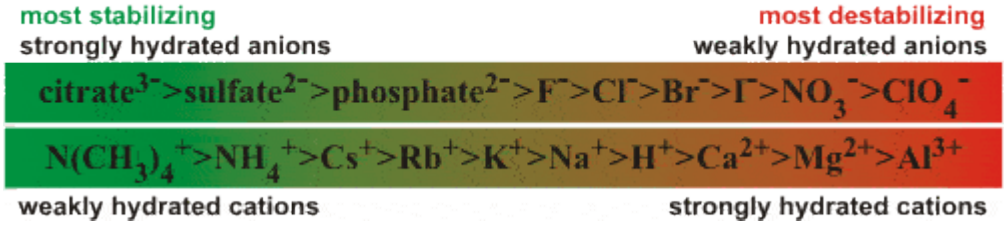

Figure 2-11: Schematic showing Hofmeister series with respect to water stabilisation [40].

Ion effects on bulk water

Expanding on Hofmeister's work, many reports in the literature state that ions are capable of destroying hydrogen bonding, consequently, affecting the structure of bulk water. Some ions exhibit strong interactions with water, breaking down the tetrahedral network (kosmotropes – structure makers). Kosmotropes will strengthen the hydrogen bonding in inner shell water molecules, which results in a decrease in hydrogen bonding in the bulk water structure. These ions remain hydrated near the surface, consequently increasing the surface tension, which was thought to reduce the solubility of hydrocarbons and proteins, as it is more difficult to make a cavity within the water structure to fit the non-polar molecule [40].

Strongly hydrated ions (chaotropes) fit within the cavity of water clathrate structures, causing puckering and rotation of the water network, resulting in a disordering of the neighbouring water molecules i.e. it destabilises the hydrogen bonding network, which decreases the hydrophobic effect, resulting in reduced aggregation of hydrophobic macromolecules and as a consequence reduce stability (salting in). Kosmotropes (high charge density) on the other hand interact strongly with the water molecules, through hydrogen bonding, which results in decreased mobility of the water structure, resulting in a more ordered structure. As the water structure is more ordered the hydrophobic effect is increased, i.e. unipolar macromolecules have a tendency to aggregate to exclude the surrounding polar solvent molecules [40, 41].

However, more recent work by Bakker *et al*. [42], which involved monitoring the O-H stretching vibration, of H_2O, using mid-IR, indicated that the ions had little effect on the bulk water solution and affected only the bonding of H_2O in the direct vicinity. Further thermodynamic studies by Pielak *et al*. [43] substantiated Bakker results. Pielak *et al*. [43] considered bulk water as a density equilibrium, and assumed that differences between hydration water and bulk water was caused by a shift in this equilibrium.

$$Less\ dense\ (more\ stuctured) \leftrightarrow More\ Dense(less\ structured)$$

It was theorised that structure makers (kosmotropes) would result in a shift to the left and structure breakers (chaotropes) would result in a shift to the right. To test this theory the heat transfer, from a pressure change above the solution, was measured, where the change in partial molar heat capacity with change in pressure, should be negative for structure makers and positive for structure breakers [43].

$$\left(\frac{\Delta\overline{C_p}}{\Delta P}\right)_T$$

Equation 8

However the results of this test showed no correlation between the sign of equation and stability effects, substantiating the findings of Bakker *et al*. [42].

Hofmeister's hypothesis was further challenged by Cremer *et al*. [44], who used vibrational sum frequency spectroscopy to show that anions caused order within a octadecylamine monolayer in the same sequence that was reported by Hofmeister, i.e. SO_4^{2-} caused more order than Cl^- etc. ($Cl^- > NO_3^- > Br^- > I^- > ClO_4^- > SCN^-$). However when they tested, the water structure using the same method, the Hofmeister trend was not followed with ClO_4^- showing a high degree of water ordering but SCN^- resulting in very little.

The results presented by Bakker, Pielak and Cremer [42-44] suggest that the ions have negligible effect on the structure of water and direct ion interactions with the polymer must also be taken into account [45]. Zhang *et al*. [45] reported that the effect of the ions could be explained by, the following three ion/macromolecule interactions:

i) Kosmotropes are able to polarise water molecules that are directly bonded to the macromolecule, resulting in salting out.

ii) The surface tension at the polymer/water interface is increased in the presence of kosmotropes and chaotropes, again resulting in salting out.

iii) Chaotropes are able to bind directly to macromolecule side chains, stabilizing the polymer backbone, resulting in salting in.

These ion/macromolecule interactions follow the same trends originally reported by Hofmeister.

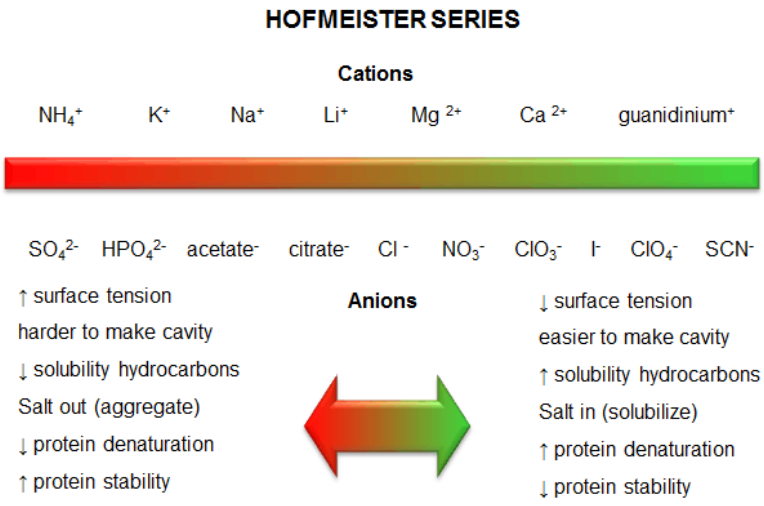

Figure 2-12: Hofmeister series [45].

2.4.5 Multi-step sol-gel process

Sol-gel processing involves solid synthesis within a liquid medium and is generally performed at temperatures of less than 100 °C [4]. In Pekala's original method, and in this study, the solids consist of R, F and catalyst, which are dispersed in water to form a sol, the sol is then heated to 85 ± 5 °C to accelerate the reaction. The system becomes a gel when both liquid and solid phases exist, during the RF reaction this point is marked with a colour change from very pale yellow to orange. Further reaction of the gelation products during a curing stage results in a further colour change to dark red/orange, indicating the formation of a highly cross-linked gel [16]. Pekala's synthesis involved a simple multi-stage sol-gel process, which is shown in Figure 2-13.

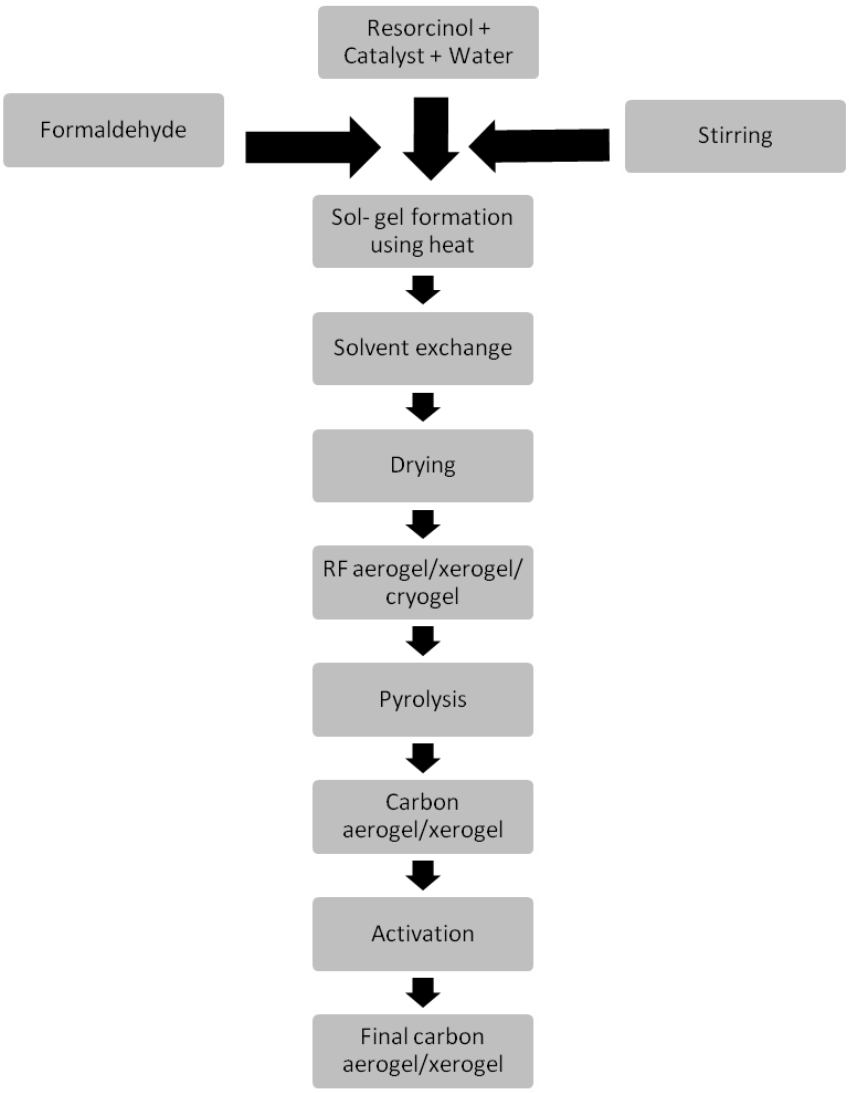

Figure 2-13: Multi-step sol-gel process.

Subsequent to gel formation the RF hydrogel undergoes solvent exchange before supercritical drying to form an aerogel. However, further studies into RF gels have discovered that other drying methods can be used, for example conventional evaporative drying to form xerogels (xero meaning dry in Latin) [1] and freeze drying to form cryogels [31, 46-48].

The dried gel can then be pyrolysed and activated to form a continuous carbon network with large surface area, high porosity and a large pore volume, which lends them to a variety of applications (see section 2.8). The complete process from sol to carbon is depicted by Figure 2-14.

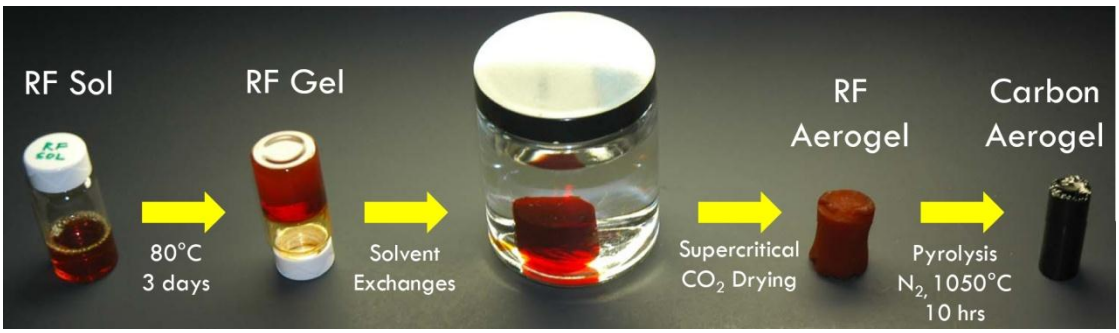

Figure 2-14: Images showing sol-gel synthesis steps in the production of RF carbon aerogels [49].

2.4.6 Flexibility of the sol-gel process

The simplicity of the sol-gel process allows many experimental variables and factors (discussed in detail in section 2.6) to be altered or changed during synthesis, thus the process can be optimised to produce gels with a variety of properties, demonstrating that both the synthesis and characteristics of RF gels can be controlled and tuned as desired.

2.5 Carbonisation

Pyrolysis, otherwise known as carbonisation, is defined as thermolysis of ceramic precursors into pure ceramics [50]. In other words carbonisation involves conversion of organic materials into carbonaceous solid. As the definition suggests this process is carried out at elevated temperatures and, in order to minimise oxidation, is generally performed under an inert atmosphere.

As the materials are heated they thermally decompose to produce water, gas and solid char by products, with the extent of decomposition dependant on the applied pyrolysis temperature. The observed decomposition reactions include condensation, dehydrogenation and bond cleavage, with concurrent isomerisations, aggregations and transformations.

2.5.1 Allotropes & properties of carbon

Carbon has an atomic number of 6 and therefore has electronic configuration of $1s^2\ 2s^2\ 2p^2$, however, due to the stability of involving all four outer electron orbitals, this ground state is very rarely observed and the small energy barrier for promotion of an electron into the 3^{rd} p orbital is overcome, as illustrated in Figure 2-15 [51].

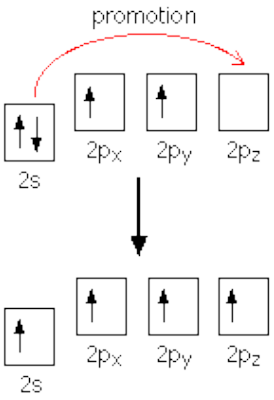

Figure 2-15: Electron promotion in carbon [52].

These electrons are then capable of rearranging themselves to form the following hybrid orbitals:

(a) Four sp^3 orbitals

(b) Three sp^2orbitals and one p orbital

(c) Two sp orbitals and two p orbitals

Consequently, carbon is capable of forming both σ and π bonds with other atoms, with the π bonds allowing carbon to form stable and complex structures [51]. These bonding combinations result in two principle bonding systems for carbon compounds; (i) σ bonds and (ii) a combination of σ and π bonds [51]. In the former system, carbon atoms form tetrahedral structures, which link together to form aliphatic carbon chains. This structure is known as diamond (Figure 2-16) and is rigid and stable with consistent physical properties that are independent of direction (i.e. the structure is isotropic) [51]. In the latter system, carbon atoms form σ bonds with three other neighbouring carbon atoms, resulting in hexagonal two-dimensional networks (as represented in Figure 2-17). The fourth available electron, from each carbon, is then delocalised over the carbon network, allowing the layers to conduct electricity. Due to the delocalisation, dipole moments form in the carbon networks, which induce dipoles in neighbouring sheets, allowing layers of networks to be held together by dispersion forces. This structure is known as graphite, as illustrated in Figure 2-17. The individual sheets, within graphite, are held together by strong covalent bonds and, due to the delocalised electrons, the networks are stronger than those observed in diamond, however, due to the distance between the individual layers the overall strength is reduced compared to diamond and graphite is softer to the touch. As discussed above electricity can be conducted within the individual graphite layers, however, it cannot be conducted between the sheets, and consequently, graphite is described as anisotropic [51].

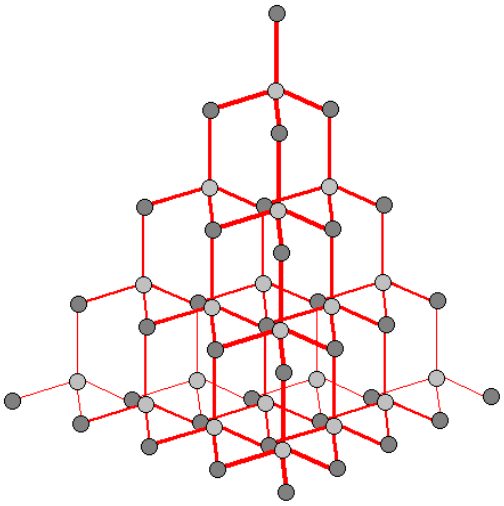

Figure 2-16: Schematic illustrating the structure of diamond [53].

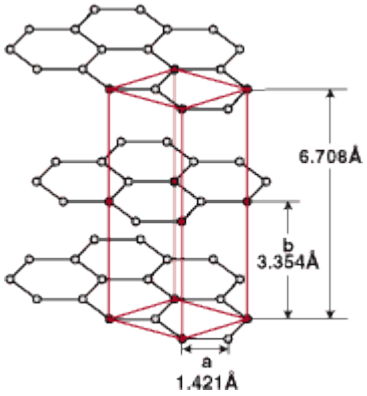

Figure 2-17: Structure of graphite showing ABA lattice [54].

2.5.2 Carbonisation of RF xerogels

Organic RF gels are composed of carbon, hydrogen and oxygen, at 45 %, 38 % and 17 % respectively [55]. From the expected carbonisation reactions mentioned in Section 2.5, it is expected that during pyrolysis of RF xerogels the following reactions will occur:

(a) Loss of residual acetone from the solvent exchange process
(b) Loss of absorbed water
(c) Loss of hydroxyl O-H
(d) Breakage of C-H bonds (loss of H)
(e) Breakage of C-O bonds (loss of O)
(f) Structural aggregations and transformations

This results in the loss of most of the O and H within the gel structure [55] leaving a pure carbon with only negligible amounts of O and H [56].

As anticipated, the reactions occurring are dependent on the pyrolysis temperature and Mirzaeian *et al*. [57] have shown that the carbonisation reactions occur in order of

increasing boiling points and bond strengths with the following observations; desorption of residual acetone, desorption of adsorbed H_2O, breakage of C-O bonds and breakage of C-H bonds.

A comprehensive study of the reactions and transformations occurring during RF carbonisation was carried out by Kuhn *et al*. [58] who utilised in situ infra-red (IR) spectrometry to monitor the pyrolysis process. This study demonstrated that, up to 250 °C, adsorbed H_2O was desorbed from the RF gel structure, and increasing the temperature further to 600 °C resulted in the full disappearance of the broad O-H absorption band, which was attributed to breakage of C-O bonds and subsequent loss of bound hydroxyl groups.

Absorption due to C-O stretching, of CH_2-O-CH_2 linkages (1000 cm^{-1}), disappears between 250 °C and 600 °C. During the same temperature range absorption bands relating to CH absorption also undergo a change during the pyrolysis process (slightly < 3000 cm^{-1}, slightly > 3000 cm^{-1} and approx. 1500 cm^{-1}), with the ratio between aliphatic and aromatic CH bands shifting during carbonisation, demonstrating a change, with increasing temperature, from mainly aliphatic (CH_2) to principally aromatic (CH) species. This change is attributed to the breakage of CH bonds, resulting in the cleavage of CH_2 crosslinks between aromatic rings within the RF structure. These two processes result in unbonded aromatic structures, which recombine to form larger networks, with partially graphitised structures, demonstrated by C-C vibrations at ~ 900 cm^{-1}. Given that temperatures of up to 2000 °C are required for full graphitisation it was concluded that the RF gel structures are only partially graphitised [58].

2.6 Experimental factors/variables

2.6.1 Initial pH and R/C molar ratio

The initial pH of the sol is thought to be a very important factor in RF gel synthesis, with previous studies suggesting that variances in RF gel properties result mainly due to differences in the initial sol pH, with Job *et al*. [1] and Sharma *et al*. [2] describing the catalyst as a pH adjuster only, concluding that it does not undertake a typical catalytic role. As basic catalysis is the most common form, this discussion will focus on alkaline synthesis.

During basic catalysis, the pH dependence is thought to be caused by the fact that the initial stage of the reaction, i.e. addition of F to R^-, is favoured at alkaline pH, whereas condensation of hydroxy-methyl derivatives is enhanced at acidic pH, consequently only a small range of initial pH values allow a gel to be formed [1].

During normal synthesis the pH is altered by changing the R/C molar ratio, and it has been reported that, in general, increasing the basic catalyst concentration (decreasing R/C and increasing pH) decreases particle size, reduces pore size and increases surface area. However, above a certain pH, the pore volume and surface area diminish; this can be explained by increased shrinkage, during drying and pyrolysis, caused by a lack of cross-linking [1].

Pekala *et al*. [11] described the reaction as an '*auto-catalytic growth mechanism'* during which the catalyst abstracts hydrogen from R forming R^-, which react with F to form hydroxy-methyl compounds. The hydroxy-methyl derivatives then rapidly react, forming bridged compounds, which are more reactive than R^- and thus react with each other to form many small clusters.

Consequently, if there is more catalyst present, more anions are formed initially and as a result, more clusters are formed, these clusters then cross-link tightly, forming a material with small pores, whereas if there is only a small amount of catalyst present only a small amount of anions are generated and '*preferential growth of polymer clusters'* [11] follows, resulting in larger particles and larger pores. This phenomenon was also described by Poljansek *et al*. [59] who reported that monomer consumption was lower at lower pHs, owing to a lack of R^-, which would reduce the rate of reaction between R and F.

Consequently, it is expected that, due to higher catalyst concentration (higher pH) the gelation time will be quicker than when less catalyst is present. This anticipated trend was demonstrated by Hwang *et al*. [60] who showed that the gel time decreased almost linearly with increasing catalyst and pH, as illustrated by Figure 2-18.

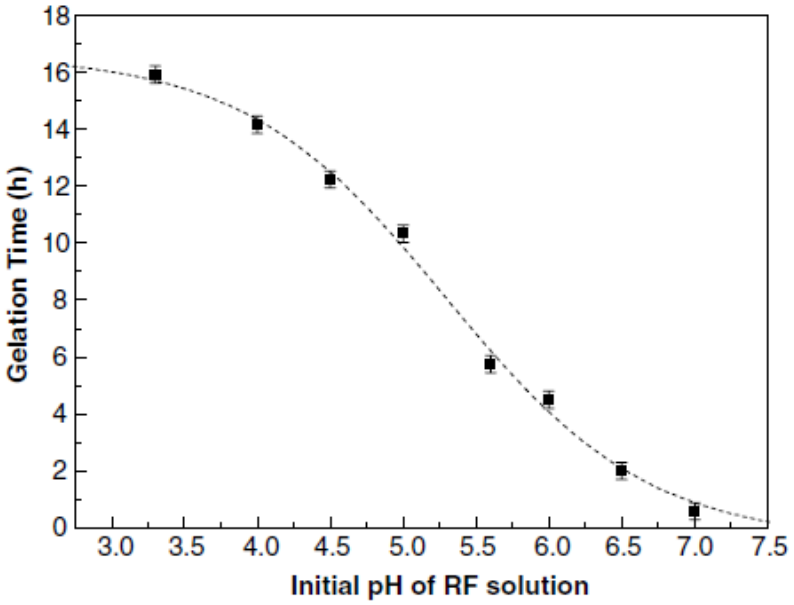

Figure 2-18: Gelation time as a function of initial pH [60].

In order to determine if the catalyst has a specific effect or whether pH is responsible for the resulting properties, some studies have used nitric acid to alter the initial pH, thus keeping the R/C ratio fixed, however, other than altering the sol pH, it is unknown if the addition of acid has any effect on the reaction as this has not been studied. Lin *et al*. [3] reported that there appears to be only a small pH window in which the reaction will proceed, they found that a lower initial pH (5.5 - 6.0) resulted in xerogels with higher pore volumes and pore size distributions. At a pH of greater than 6.5 the surface area was found to decrease to almost zero. A similar working pH range was demonstrated by Job *et al*. [1], who established that for gels prepared with a dilution ratio of 5.7 (~57 % solids), below a pH of 5.5 the RF xerogel was micro/macroporous, resulting in limited mechanical strength. Whereas when the pH was greater than 6.25, as a result of gelation occurring too quickly before the structure could cross-link, the prepared gel became non porous.

By altering the drying method, Hwang *et al*. [60] demonstrated that even at low pHs when the gel structure is weak, xerogels with porous properties could still be obtained. Their study involved ambient drying as opposed to vacuum drying [1] or tube drying under N_2 [3], which would be less harsh on the weaker gel structures (low pH) resulting in the preparation of porous gels within a pH range of 3.0 – 6.5.

Pizzi *et al*. [20] illustrated the accepted rate of polymerisation as a function of pH for phenolic resins (Figure 2-19). Given the increased activation of R compared with phenol (R

activated in the 2, 4 and 6 position, whereas phenol activated in the 2 and 6 position), the polymerisation rate for R is expected to follow similar trends but occur more rapidly. Consequently, it was expected that below a pH of approximately 3 (acid catalysis) and above a pH of 7 (base catalysis) rapid polymerisation between R and F would occur. This expected trend with pH was demonstrated by Aero Research Ltd in Duxford [61] (Figure 2-20), indicating that RF gels can be formed in an acidic medium (pH less than 3.0) and in a basic medium (pH greater than 3.0). Comparison of the polymerisation time for R resins compared to phenol resins indicates slower reaction times for the R counterparts, however it should be noted that the reaction conditions for these figures are unknown, therefore they are not directly comparable.

The results proposed by Hwang *et al*. [60], Lin *et al*. [3] and Job *et al*. [1], demonstrate that basic catalysed RF xerogels can be formed from sols with an initial pH from 3.0 to 6.5, which is as expected given the results illustrated by Figure 2-20. However, the results presented suggest that the working pH range is also dependent on the synthesis conditions employed.

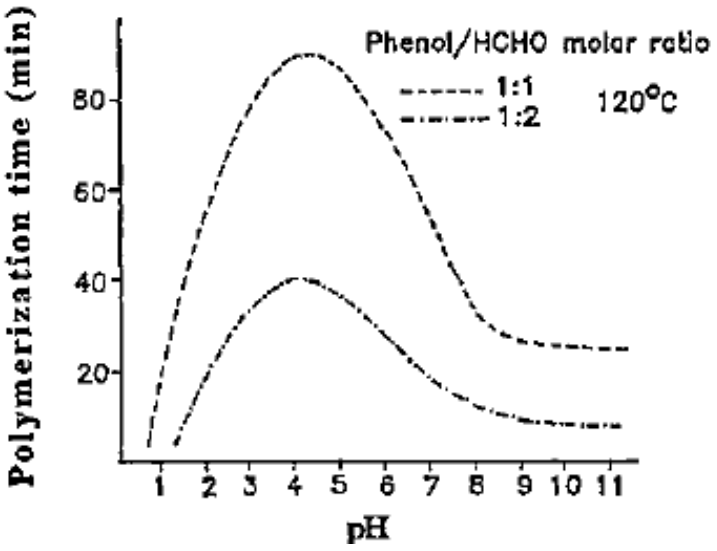

Figure 2-19: Rate of polymerization as a function of pH for phenolic resols of different molar ratios at 120 ˚C [20].

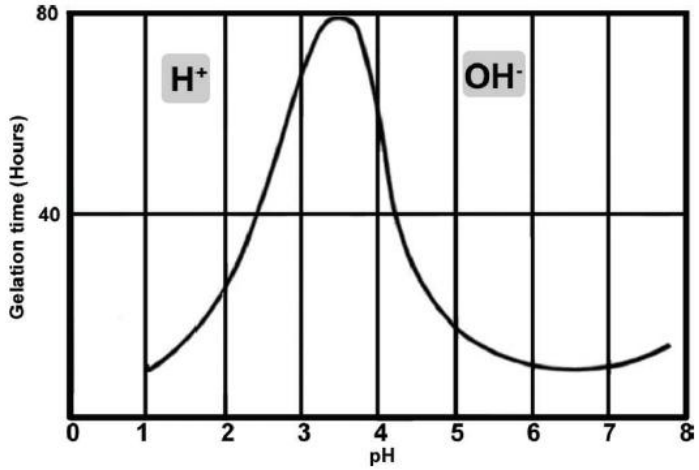

Figure 2-20: Rate of polymerization as a function of pH for R and F [61].

Horikawa *et al*. [25], studied the effect of different catalysts; namely K_2CO_3, $KHCO_3$ and Na_2CO_3 and $NaHCO_3$ on the properties of RF gels. They explained that differences between carbonate and bicarbonate prepared sols were based solely on the alkalinity effects of the catalysts present. As expected, they theorised that the stronger carbonate bases would result in a higher sol pH, resulting in K_2CO_3 and Na_2CO_3 prepared sols having smaller pores than their $KHCO_3$ and $NaHCO_3$ counterparts, and subsequently smaller pore volumes and larger surface areas [25].

2.6.2 Effect of the catalyst

(a) Cationic radius

Torres *et al*. [62] employed five different Group I carbonate catalysts to study the effect on the properties of RF gels. They reported that, as Group I was descended (i.e. going from Li to Cs carbonate) the RF gelation time increased with increasing cation size. They theorised that this increased gelation time allowed increased aggregation, resulting in gels with larger particles and in turn increased pore volume and decreased surface area.

This is in contrast to the results presented by Job *et al*. [63] who utilised Li, Na and K hydroxide catalysts and found that the porous properties were independent of the cation size.

(b) Cation charge

Job *et al*. reported that gels prepared from Group II metal catalysts, where the metal has a 2^+ charge produced gels with significantly larger pores than their Group I counterparts. They hypothesised that this increased pore size was caused by destabilisation of the RF sol, due to a reduction in the Debye Huckel Screening Length, as a result of increased cation charge. It

was proposed that, in the presence of Group II cations, dispersive forces would increase resulting in demixing and overall faster gelation times. Unlike Torres *et al*., who stated that increased gel times would result in larger pores, Job *et al*. reported that decreased gelation time would result in larger pores. Similar results were reported by Cohaut *et al*. [64], who demonstrated increasing porous volume fractions and decreased total surface areas for RF gels carbonised by $Ca(OH)_2$ when compared to their NaOH counterparts.

2.6.3 Addition of HNO_3

Many studies involve the addition of nitric acid (HNO_3) to the RF sol, which has the effect of fixing the sol pH. This procedure has been used on a number of occasions to test the effect of the pH on the gel properties, by removing the effect of R/C ratio [60, 65, 66]. For carbonate catalysts, the addition of HNO_3 to the RF sol results in the following reactions occurring between the catalyst and the added acid:

$$2HNO_3 + Na_2CO_3 \rightarrow 2NaNO_3 + H_2CO_3$$

Equation 9

$$HNO_3 + NaHCO_3 \rightarrow NaNO_3 + H_2CO_3$$

Equation 10

As illustrated in Equation 9 and Equation 10, the acid added reacts with the basic catalyst present in the solution, thereby reducing the concentration of C in the sol (increasing R/C). Therefore, the addition of HNO_3 to the RF sol will not remove the effect of C unless enough acid is added to react fully with the catalyst.

Awadallah-F *et al*. [65] utilised HNO_3 to set the initial sol pH of sols prepared with R/C ratios of 50 and 500. Using Design of Experiments (DoE) they then studied the effect of both initial sol pH and R/C ratio on the final gel properties. Given that addition of HNO_3 will affect the [C] (see Equation 9 and Equation 10 above), concurrent investigation of the effects of both parameters is difficult. The results presented by Awadallah-F *et al*. [65], reflect this difficulty; with increasing R/C ratio (decreasing catalyst concentration) resulting in an unexpected increase in pore volume and surface area. This is against the accepted convention of increasing catalyst concentration (increasing pH) resulting in increased surface area and pore volume.

The R/C 50 sols will have a significantly higher initial pH than the R/C 500 sols; consequently, they will require an increased concentration of acid to set the pHs to equivalent values. The unanticipated results presented by Awadallah-F *et al*. may have

arisen due to too much acid being added to the R/C 50 sol, resulting in continued reaction with C after measurement of the initial sol pH. Overall this would result in decreased pH and reduced [C] compared to the equivalent prepared R/C 500 sol.

The study carried out by Awadallah-F *et al.* [65] demonstrates the complexity of investigating and separating the effects of both R/C ratio and initial sol pH.

When considering different catalysts of different strengths, i.e. carbonates, bicarbonates and hydroxides, setting the initial sol pH sets the H^+ concentration within the sol. However, this will not necessarily set the base concentration. Consequently, varying concentrations of base can remain within the sols, which will result in differing reactions with F, e.g. when a higher concentration of catalyst remains, a larger quantity of R will be activated towards reaction with F, resulting in increased cross-linking and as a result smaller pores and pore volumes.

This is illustrated by the BATE pH calculations for Na_2CO_3_100, $NaHCO_3$_100 and NaOH_100 displayed in Chapter 17 (Appendix F). These calculations demonstrate that at equal concentrations (equal R/C ratios) the pH varies, consequently different concentrations of acid would be required to set the pH, resulting in varying remaining base concentrations.

Separating the effect of pH and R/C ratio and the effect of acid addition will be considered further during this study.

2.6.4 Solid content

Changing the solid content alters the concentration of reactants present in the sol, thus increasing the solid content essentially increases the reactants. As a consequence more R^- are formed and more hydroxy-methyl compounds are generated, which, in turn, results in a greater amount of small clusters, smaller particles, smaller pore sizes and larger densities [67]. As a result, gels prepared with a low solid content have a weaker structure caused by a lack of cross-linking, this is illustrated by the orange colour (red/yellow [68]) and softness of the hydrogel (sol-gel containing water). On the other hand, gels prepared with a high solid content are harder and are deep red in colour.

Unlike Bock *et al*. [67], Tamon *et al*. [68] found the surface area and average pore diameter to be independent of solid content [68]. However, it should be noted that, the solid contents used in this study were considerably higher than those employed by Bock *et al*. (typical solid content of 20 % = R/W of 0.022 mols, Tamon *et al*. utilised R/W ratios of between 0.1 and 0.3 molar). At high solid content, the reactant concentration is high, and the reaction rate

between R and F will have reached a maximum, which is dependent on the amount of catalyst present. When the catalyst concentration is constant no change in reaction rate with increasing solid content will be observed and the particle size constituting the RF network will remain constant, as will the related surface area [67].

2.6.5 R/F molar ratio

A stoichiometric ratio of R/F is normal (i.e.1/2 = 0.5), and too high a quantity of F has been reported to cause collapse of the mesoporous structure of the gel, this is known as the '*dilution effect*' which causes an increase in particle size, however a lack of F limits the formation of hydroxy-methyl derivatives and restricts the development of the gel [15].

2.6.6 Solvent exchange & drying method

In order to convert the RF hydrogel to xerogel, aerogel or cryogel the water is first exchanged with a suitable solvent (xerogel = acetone, aerogel = acetone, cryogel = t-butanol), which is then removed to produce a gel containing air rather than water. Due to surface tension, within the pores of the gel, the solvent exerts pressure; consequently the chosen solvent and resultant drying method can significantly influence the properties of the final gel and are therefore important parameters in RF gel synthesis [47].

(a) Surface tension

Molecules in a solution experience cohesive forces from surrounding molecules. These forces occur in all directions and cause the liquid to contract into a minimised volume. The molecules on the surface experience only inward cohesive forces and as result they cohere more strongly to the molecules in their immediate vicinity. The cohesive forces involved result in surface tension (see Equation 11), which is the force required to break an area of the liquid.

$$\sigma_r = \frac{2\gamma cos\theta}{r}$$

Equation 11 [69]

Where: σ_r = *pressure exerted on pore radius r(N)*

γ = *liquid surface tension (N m^{-1})*

θ = *wetting angle (°)*

r_{pore} = *pore radius (m)*

Within the pores of a gel, the liquid will rise up the sides of the pores, wetting the walls, this capillary action continues until a balance is reached between the adhesive forces (between liquid and pore wall) and cohesive forces within the liquid. During the drying process liquid is withdrawn from the pores and, due to capillary stress, the adhesive forces, between the liquid and the pore, results in the liquid pulling the walls inward, causing collapse [69].

The surface tensions for various common solvents are given in Table 2-1, demonstrating that t-Butanol has a significantly lower surface tension than water. Consequently, given Equation 11 it is expected that the pressure exerted on pores will be significantly reduced when t-Butanol is used compared to water. This affect was demonstrated by Kraiwattanawong *et al*. [70] who established that solvent exchanging with t-Butanol significantly reduced gel shrinkage during drying, resulting in RF gels with greater porosity than their acetone exchanged counter parts.

Table 2-1: Properties of different solvents utilised for solvent exchange [70].

Solvent	Surface tension at 25 °C (mN/m)	Boiling point (°C)
Water	71.99	100
Ethanol	21.79	78.5
Acetone	23.46	56.5
Toluene	27.93	110.6
t-Butanol	19.96	82.4

Jabeen *et al*. [17] demonstrated that surface tension of the solvent is not the only factor that affects shrinkage of RF gels. By comparing amyl acetate and n-butanol, which have very similar surface tensions; they observed that n-butanol resulted in enhanced shrinkage. Jabeen *et al*. [17] theorised that this was due to the increased ability of n-butanol to form hydrogen bonds, which causes increased attractive forces and as a result increased shrinkage.

(b) Drying method

Czakkel *et al*. [47] compared the effects of three different drying methods; drying in an inert atmosphere, freeze drying and supercritical drying, on the porous properties of RF gels and carbons. They reported that, due to the improved solvent quality of t-butanol compared to CO_2, the highest pore volumes and surface areas were observed in the organic and carbon RF cryogels. They also demonstrated that the lowest yield of carbon was obtained in carbonisation of RF xerogels, yielding only 40.7 % compared to 46.6 % and 50.5 % for the aerogel and cryogel respectively. This can be explained due to the weakened gel structure,

obtained during drying in an inert atmosphere, which arises due to the formation of a liquid-vapour interface and resultant surface tension [15].

A novel drying method was proposed by Zubizarreta *et al*. [16] who demonstrated that drying using a multimode microwave technique produced RF gels that, upon activation, had significantly increased pore volumes and surface areas compared to their vacuum dried counterparts, even although the microporous nature of carbons, prior to activation, prepared via both methods were similar. A full explanation for the enhanced properties was not presented; however, Zubizarreta *et al*. [16] concluded that the drying method must affect the structural properties of the dried RF gels. The evaporatively dried gels must have a weakened pore structure which collapses further upon activation. Microwave drying presents an exciting alternative, as it is quicker than conventional drying methods (vacuum drying and supercritical drying) and typically uses less energy.

Another alternative drying method was reported by Jabeen *et al*. [17], who compared conventional air drying, followed with overnight oven drying at 100 ˚C, with an azeotropic distillation technique. During the distillation water within the pores was exchanged with n-butanol or amyl acetate. The remaining solvent was then replaced with acetone and dried overnight in an oven at 100 ˚C. Jabeen *et al*. [17] demonstrated that exchanging the original water with a lower surface tension solvent resulted in reduced shrinkage and as a result increased pore volumes. This indicates that, even after a long acetone solvent exchange, residual water remains within the pores of the RF gel, resulting in increased surface tension during the formation of liquid-vapour interface.

2.6.7 Gelation/curing time and temperature

As discussed in Section 2.4.3 the gelation stage is a significantly important phase in the formation of RF gels, as it is this process that defines the final RF gel structure [25, 27-30]. Consequently, controlling the gelation time is of vital importance in the synthesis of RF gels.

The gelation step consists of the formation of hydroxy-methyl groups and initial cluster formation and can occur in anything from one hour up to two days, dependent on the synthesis conditions [15]. The curing step involves the cross-linking of clusters, which hardens the gel. This step occurs slowly, however curing rate can be increased by addition of an acid after gelation, causing an increase in the degree of condensation reactions [15]. The gelation and curing step are shown in Figure 2-21.

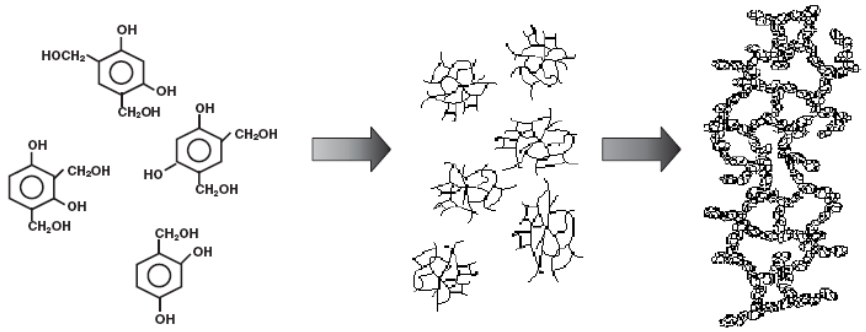

Figure 2-21: Schematic showing gelation and curing processes during RF gel formation [15].

As reviewed previously the experimental variables, namely; pH (R/C ratio) [60], decreased Debye Huckel screening length [24] with increasing cation size and charge [62, 63], and catalyst type (i.e. acid or base) [7, 21] can affect the gelation process. In general, these experimental conditions control gelation time, subsequently affecting the formation of hydroxy-methyl groups and initial cluster formation. If this step occurs too quickly crosslinking within the structure is hindered and the RF gel becomes non porous [63].

The gelation temperature can also influence the final RF gel properties; however will have a less significant effect. R and F will react at room temperature; however, carrying out the reaction at elevated temperatures increases the reaction rate, consequently, increasing the cross-linked nature of the gel and therefore improving the final gel properties, however small increases in the gelation temperature have been reported to have little effect on the porous properties of RF gels [71].

Gelation and curing are usually carried out at a temperature of 85 ± 3 °C for between three and seven days [15].

2.6.8 Pyrolysis conditions

As discussed in Section 2.5.2 pyrolysis alters the structure of RF xerogels, with the extent of pyrolysis being dependent on the applied temperature. As the carbonisation progresses, linkages between aromatic carbon rings are broken allowing the structure to reorganise and re-aggregate. This variation in structure causes increased crosslinking, resulting in increased micropore volume and enhanced surface areas. The restructuring of the aromatic carbon network results in partial graphitisation, which affects the conductivity of the RF structures [58].

To minimise oxidation, creating a pure carbon gel, pyrolysis is generally carried out in an inert atmosphere, utilising a moderate flow of inert gas (i.e. Ar flowing at 200 ml/min). The

pyrolysis temperature can be determined using Thermo Gravimetric Analysis (TGA), which outputs a plot of weight loss versus temperature, thus, showing the temperatures at which the main carbonisation reactions occur [15], and demonstrating the maximum temperature required.

Mirzaeian *et al*. [57] confirmed that, increasing carbonisation temperature to 800 °C caused an increase in the surface area, total pore volume and micropore volume. However, they found that, any further temperature increase resulted in a decrease of the afore mentioned properties.

The same effect was described by Hulsey *et al*. [72] and Lin *et al*. [73], however, they found that, at temperatures above 900˚C and 600 ˚C respectively, the surface areas and pore volumes were found to decrease. These studies demonstrate that pyrolysis temperature is significantly important for the determination of RF carbon properties, and the required temperature is dependent on the individual gel structures. If the selected temperature is too high the gel structure collapses, resulting in decreased pore volumes and surface areas [57].

Although pyrolysis temperatures of between 600 and 900 °C are typical for RF xerogel carbonisation, Wiener *et al*. [74] demonstrated that thermal conductivity increases with pyrolysis temperatures between 800 and 2500 °C, however Lu *et el*. [75] reported that graphitisation at temperatures of 850 ˚C could be enhanced with the addition of Co^{2+}. These studies therefore provide further evidence that the optimal carbonisation temperature is dependent on the properties of the RF gel being carbonised.

2.6.9 Activation conditions

Activation further increases the pore volume and surface areas of carbon gels [57], resulting in extra porous materials that are valuable for a large number of applications.

Activation involves oxidisation of a carbonaceous material and can be carried out in two different ways:

(a) Physical activation

Following pyrolysis the carbon is placed in a furnace and heated to a high temperature (900 ˚C to 1200 ˚C), under the flow of oxygenated gas, i.e. CO_2. This process has been shown to cause an increase in pores within the gel structure, and resultant increase in pore volume and surface area [57]. In general increasing the activation time or activation temperature increases the percentage burn off (% weight loss) and increases the pore volume.

Mirzaeian *et al*. [57] found that a rise in percentage burn off caused an increase in small mesopores, resulting in an increase in total pore volume and surface area but having little effect on the average pore diameter. Lin and Ritter [73] reported similar results, however, they found that increasing the activation time, up to two hours, caused an increase in the number of micropores, in the 0.6 and 1.3 nm regions, and the number of mesopores, of approximately 20 nm in size. They also found activation to have little effect on average pore diameter.

Consequently, depending on the gels' original structure, physical activation causes an increase in pores of different sizes resulting in an increase in the total pore volume and surface area but having a small effect on the average pore size.

(b) Chemical activation

Chemical activation involves submerging the gel in a material capable of oxidising (generally a base or an acid is used). The benefit of this type of activation is that pyrolysis can be performed simultaneously and in general a lower temperature is required. During this combined process the gel is immersed in a bath containing a mixture of oxidiser and H_2O, the bath is agitated or stirred at room temperature, which removes any residual H_2O from the gel structure. The bath is then heated to elevated temperatures (~ 750 ˚C) under a flow of pyrolysis gas (i.e. Ar of N_2).

Zubizarreta *et al*. [55] compared the effects of chemical activation, with KOH, on the properties and structure of organic and carbon RF xerogels. They demonstrated that simultaneous pyrolysis and activation resulted in highly microporous structures, with the final properties dependent on both the initial R/C ratio and the concentration of KOH. These activated structures maintained little of the structure developed during the polycondensation of R and F. Whereas, when RF chemical activation was carried out subsequent to pyrolysis, the carbon maintained the meso/macro pore structure developed during synthesis, with the quantity of KOH used during activation altering only the quantity of micropores (higher KOH concentration resulting in increased microporosity), with the overall structure remaining either micro-meso porous or micro-macro porous.

Similar to the effects of pyrolysis discussed in Section 2.6.8, Zubizaretta theorised that these differences were attributed to the structure of the precursor. With concurrent pyrolysis and activation the organic xerogel is a mixture of C, H and O, consequently the organic backbone is significantly more reactive towards KOH, than the carbonised derivative. This results in an aggressive reaction, which causes disruption of the interconnected RF network, possibly

before carbonisation has occurred. Consequently, the meso/macroporosity is destroyed and micropores form as a result of chemical erosion [55].

In the carbonised structure strong carbon-carbon bonds already exist and the low concentration of H and O limits KOH activation. In these structures the meso/macro structure remains and microporosity results from the creation of new micropores and the erosion of existing micropores [55].

The disruption of the RF gel network with simultaneous carbonisation/activation was also demonstrated by Conceicao *et al*. [76] who illustrated that increasing concentrations of phosphoric acid, during carbonisation/activation, resulted in increasing microporosity within the final carbon structure. Partial collapse of the mesoporous RF gel structure and erosion of new pores produced carbon gels with inter-particle micro/mesoporosity and intra-particle microporosity, respectively [76].

2.7 Gel properties

2.7.1 Control of particle size

The particle size of RF gels is mainly controlled by the catalyst concentration and the molar ratio of R to catalyst (R/C). When a high catalyst concentration (or low R/C) is present many small clusters are initially formed resulting in a material with small particles and pores, whereas when a low catalyst concentration (high R/C) is used preferential growth of polymer clusters occurs, resulting in gels with larger particles and pores [11, 30, 67, 77] . Bock *et al*. [78] reported that by altering the R/C ratio, particle size could be controlled to span sizes in the region of a few nm to a few μm, thus by altering only one synthesis parameter, properties of RF gels can be significantly changed.

The catalyst is not the only factor that affects the particle size of RF gels and many other variables have been shown to have an effect. The stirring of the sol has been shown to be important, as agitation rate [79] and length of stir time [2] can influence particle aggregation, with longer stirring times and reduced agitation resulting in larger particles. Another variable that can be used to control particle size is the solid content, i.e. the percentage of reactants to sol volume, which affects the rate of reaction, in turn, inducing particle size effects. High solid contents cause the reaction between R and F to occur rapidly, resulting in small mass fragments and small pores, where low solid contents result in particle growth, giving rise to structures with large mass fragments and large pores. The effects of low solid contents were demonstrated by Scherdel *et al*. [80], who utilised very low percentage

reactants to form RF gels with particles as large as a few micrometres (> 1000 nm). Zubizarreta *et al*. [16] employed a novel microwave oven drying technique and reported that gels consisting of uniform microspheres could be prepared.

From this discussion it is clear that particle size can be varied widely and, comparing the micro particulate gels prepared by Zubizarreta *et al*. [16] with the large RF macro particles reported by Scherdel *et al*. [80], demonstrates that, an extremely high level of particle size control is achievable.

2.7.2 Pore size

RF gels can be prepared with pores ranging from microporous (< 2 nm) to macroporous (> 50 nm), thus their properties can vary extensively. Essentially, the porosity of these materials can be manipulated by controlling the aggregation of RF particles throughout the reaction [25], therefore the pore size is fundamentally dependent on the RF particle size.

2.7.3 Resultant porous properties

The particle size and resultant pore sizes affect the surface area and total pore volumes of the RF gels. With small particles and pore sizes giving rise to smaller pore volumes and large surface areas and larger particles/pores resulting in lower surface areas but higher pore volumes. Consequently, it follows that higher R/C ratios/pH will result in increased surface areas and reduced pore volumes, whereas lower R/C ratio/pH sols will form gels with lower surface areas and higher pore volumes. Al-Muhtaseb *et al*. [15] has reported typical surface areas of between 400 and 1200 m^2/g.

2.8 Applications

The ability to alter the nanostructure of the gels by varying the synthesis conditions, together with the fact that they can be obtained in many different forms, for example monoliths, beads, powders or thin films, makes them valuable for a variety of applications.

2.8.1 Electrochemical applications

Possible monolithic structures, high surface areas, small pores and high electrical conductivity of RF carbon aerogels make them suitable for many electrochemical applications, for example as electrodes in Electrochemical Double Layer Capacitors (EDLCs) and LiO_2 batteries [8]. EDLCs are energy storage devices in which the charge is separated using two plates of activated carbon acting as opposing electrodes, separated by a porous membrane. When a voltage is applied electrons migrate from the electrolyte solution,

stored in the pores of the activated carbon, to the oppositely charged electrode and charge is stored at the electrode/electrolyte interface [81]. The process is illustrated in Figure 2-22.

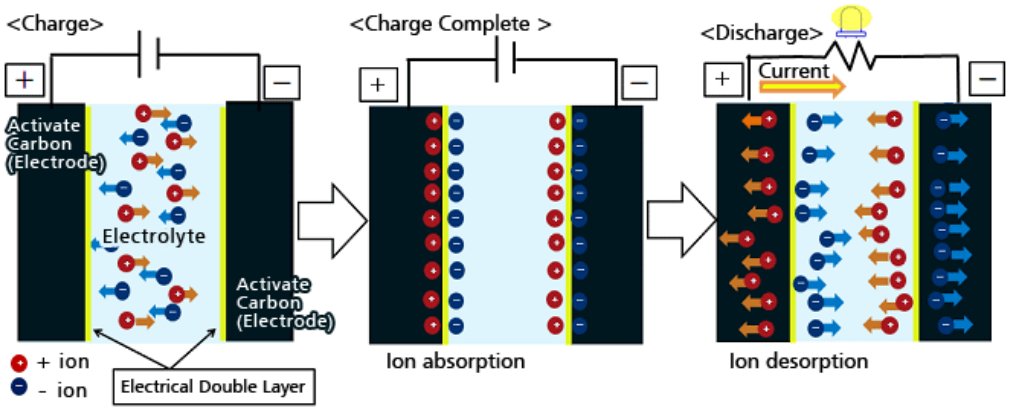

Figure 2-22: Schematic diagram of EDLC, where the activated carbon would be RF carbon gel [82].

It is widely known that supercapacitor performance is enhanced when the pores of the electrode match the size of the ions [83], following on from this Frackowiak *et al*. [84], reported that activated RF carbons with pores in the region 0.7 - 0.9 nm are the most useful for charging the EDL. Similar results were reported by Lin *et al*. [85] who found that pores less than 0.8 nm had little effect on the double layer capacitance.

In a similar manner to EDLCs, carbon gels can also be used in capacitive deionisation (CDI) systems to remove ions from aqueous streams. A voltage is applied to a stack of aerogel electrodes and the aqueous electrolyte is passed over them; ions within the electrolyte migrate to the opposing electrode and are stored at the electrode double layers at the electrolyte interface [8].

In LiO_2 batteries, carbon aerogels can be used as a gas transport medium, which transports oxygen to the carbon-electrolyte interface. In this type of system Li acts as the anode and oxygen as the cathode material, however, by using a carbon aerogel as the transport medium oxygen is not stored in the battery, consequently allowing a much higher specific energy than conventional LiO_2 batteries, which typically have a $LiCoO_2$ cathode with limited energy storage capacities [57].

Carbon gels can also be used as a replacement for carbon blacks as Pt catalyst supports in Polymer Electrolyte Membrane Fuel Cell (PEMFC) cathodes. PEMFC's operate by feeding an easily oxidised fuel (generally hydrogen) to the anode, while the cathode is fed by oxygen/air. Once H_2 reaches the anode it is oxidised producing protons and electrons.

Separating the anode and cathode is a hydrated membrane, which allows protons to pass through from the anode to the cathode, while the electrons travel along an external circuit. Once the protons and electrons reach the cathode, oxygen is reduced allowing it to react with the protons to form H_2O and heat. To enable oxidation to occur the anode and cathode each have a layer of catalyst, typically Pt, which is supported on the anode and cathode [86]. The small pore volumes of RF carbons presents them as suitable catalyst supports, where the small pore volumes minimise diffusion of reactants and, therefore, increase cell efficiency [87]. Marie *et al*. [88] reported the use of carbon aerogels as suitable supports, demonstrating efficiency similar to those obtained with commercial electrodes. Following on from this work Job *et al*. [87] established that RF xerogels could also be used as potential catalyst supports and demonstrated that when the pore sizes were large enough the fuel cell performance was close to that exhibited by RF aerogels.

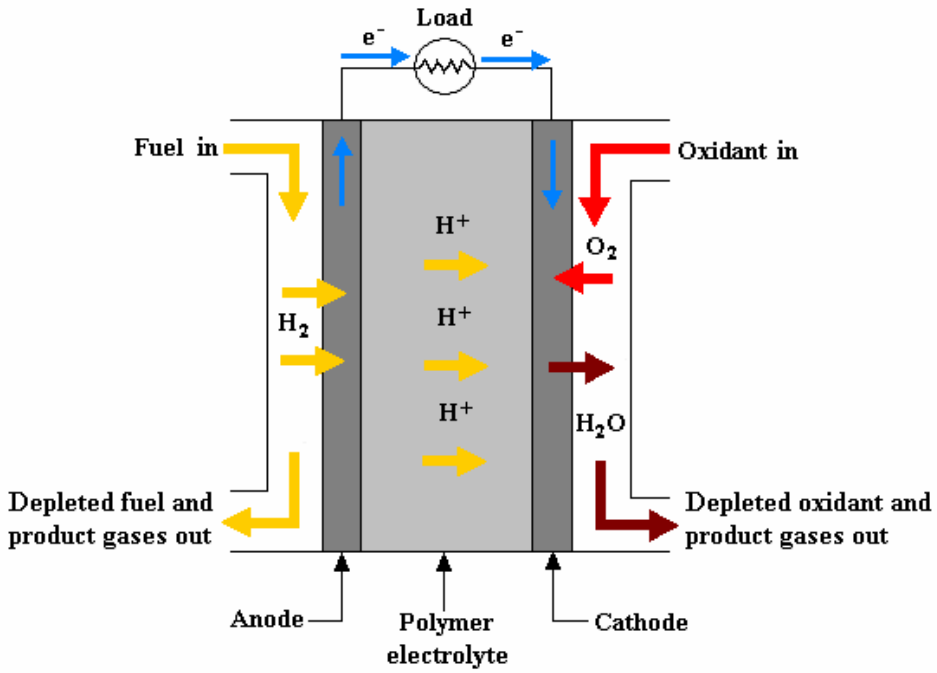

Figure 2-23: Schematic of PEMFC [86].

2.8.2 Catalysis applications

The ability to prepare different forms of carbon aerogels and their tuneable properties also make them attractive materials for applications in adsorption and catalysis. Metal-doped carbon aerogels can be easily prepared in three ways; by adding a metal salt directly to the sol, by replacing R with a derivative, which has enhanced ion exchange capabilities and by directly depositing the metal onto the carbon structure [89]. The prepared metal-doped structures contain a homogenous dispersion of metal ions. The dispersed metal nano-

particles, not only increase the electrical conductivity of the gel but also, provide the gel with some of the catalytic properties of the dispersed metal ion. To date these metal-doped RF structures have shown promise as catalysts in the isomerisation of 1-butene, toluene combustion, the synthesis of methyl-tert-butyl ether, and the formation of nanofilaments from CO decomposition [89].

2.8.3 Chromatographic packing material

Yamamoto *et al*. [90] demonstrated that by utilising an inverse emulsion technique carbon cryogels could be prepared as microspheres. This method involved dispersing the RF sol, which was removed from the oven just before loss of fluidity occurred, in a mixture of cyclohexane and surfactant. The emulsion was then agitated at a set temperature until the RF particles had gelled. Cryogels were then prepared following previously described methods [46]. Yamamoto *et al*. [90] established that the properties of the RF microspheres could be controlled by altering the emulsion and pyrolysis temperature, with increasing emulsion temperature increasing the microporosity of the microsphere surface, and increasing pyrolysis temperature increasing the hydrophobicity. Due to their small size the RF microspheres are suitable for chromatographic packing materials and Yamamoto *et al*. [90] demonstrated the potential of the mesoporous microspheres for use as HPLC column packing materials.

2.8.4 Other applications

Their highly porous nature makes these materials useable for gas separation techniques. Yamamoto *et al*. [91] reported that air separation could be achieved on both carbon cryogels and carbon xerogels of certain pore size distribution, due to the different adsorption rates of nitrogen and oxygen within the micropores of the carbon.

Additionally, the mesoporous nature, controllable surface area, mass density, and continuous porosity, make them effective physisorbents, hence suitable candidates for gas storage including hydrogen storage [92].

2.9 Objectives

Absolute understanding of the processes involved during the polymerisation of RF gels would allow the final gel properties to be controlled and pre-determined, thus allowing specific nanostructures to be prepared for particular applications. From the preceding discussion, surrounding the effects of experimental variables/conditions, it is apparent that

the final gel properties are some-what dependent on the catalyst, however, it is clear from current literature that the catalyst's specific role is not fully understood.

The aim of this work is to comprehensively study the polymerisation reaction, allowing determination and differentiation between the effects of the following variables:

1) Initial sol pH
2) Base type
3) Base concentration
4) Cation size
5) Cation charge
6) Cation presence

3 Techniques – Theory

This chapter introduces the techniques that will be employed during this study, providing an introduction into the processes involved. Section 3.1 discusses techniques used only for RF xerogels, whereas, section 3.2 examines methods common to both RF xerogels and RF carbons.

3.1 Techniques used on RF xerogels only

3.1.1 Dynamic Light Scattering (DLS)

Dynamic Light Scattering (DLS) is a spectroscopic technique that can be used to determine particle size of a solid suspension [93] or polymer size in solution [94]. DLS works by passing a light source through the solution, when photons meet solid particles they interact in one of two ways, by either passing on energy or gaining energy. When photons strike the solid particles they scatter in different directions and then interact with other surrounding particles within the liquid medium, consequently, the frequency of scattered radiation varies from the frequency of incident light. The size, shape and molecular interactions within the solid particles affects the frequency shifts, scattering angle, polarisation and frequency of the scattered light, consequently the scattered light can be used to determine the size and shape of the suspended particles [93]. A schematic of a typical DLS set up is shown in Figure 3-1.

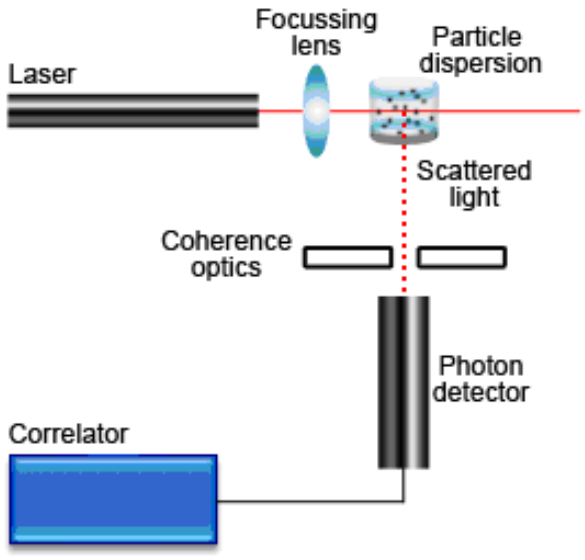

Figure 3-1: Schematic representation of 90 ° DLS set-up [95].

Through the use of monochromatic light, i.e. a laser, both very small and low energy shifts in frequency can be measured, providing information on the translational and rotational degrees of freedom, of the suspended particles. These degrees of freedom result from a phenomenon known as Rayleigh scattering.

In order to obtain information about the system, the changes in the incident light upon interaction with sample matter need to be explained. Due to the fact that incident light is weak, it is assumed that the response by the system is linear, and due to the weak coupling between scattering of light and the properties of the interaction material a time correlation function can be used to describe photon interaction [93].

The scattering intensity is measured at various time intervals, $t + \tau$, where t is equal to the time the incident light strikes the sample and τ is the delay time, as shown in Figure 3-2. As the delay time increases the correlation between the measured intensities decreases, i.e. the difference between them increases. This correlation continues to decrease with increasing τ, until there is no correlation between two measurements. As a result a plot of the correlation coefficient as a function of time forms an exponential decay, which is known as the auto correlation function (see Figure 3-3) [93, 96].

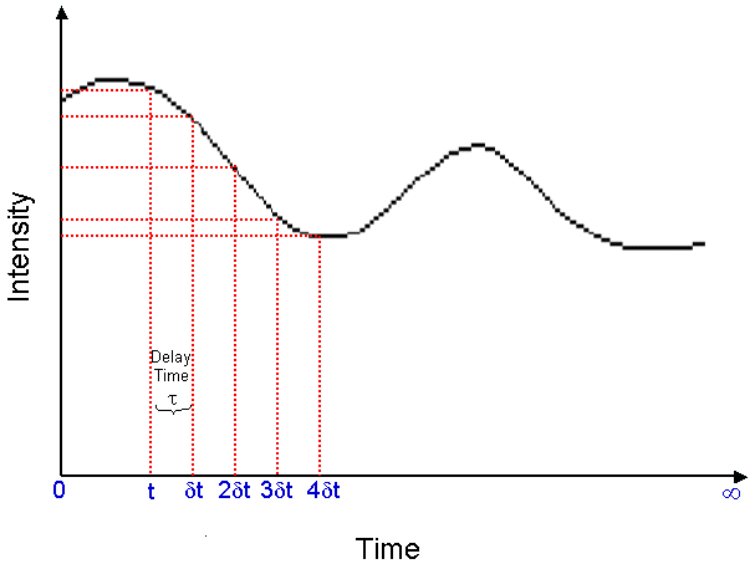

Figure 3-2: Schematic showing fluctuation in intensity of scattered light as a function of time [96].

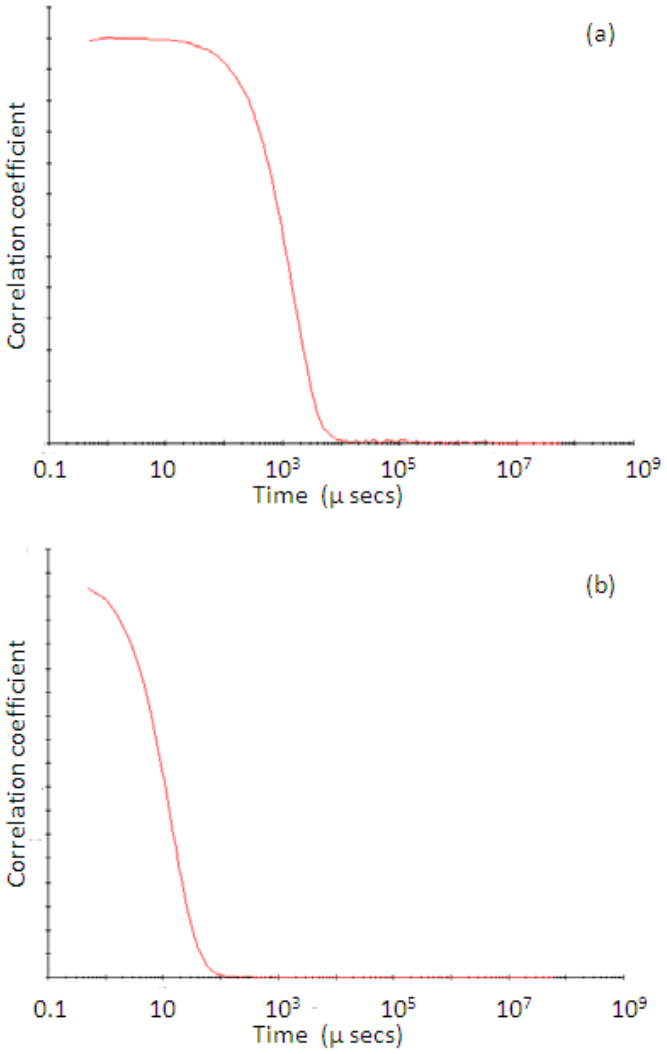

Figure 3-3: Auto-correlation functions for (a) large and (b) small particles. Redrawn from [96].

As particle size increases Brownian motion slows, resulting in slower fluctuation in the scattered light, whereas smaller particles move more rapidly and are moved further by the solution causing a more rapid fluctuation of the scattering intensity. As a result of the scattering effects large particles display longer correlation than smaller particles. The effects of particle size on the intensity of scattered light and on the auto correlation function are shown in Figure 3-3 and Figure 3-4, respectively [96].

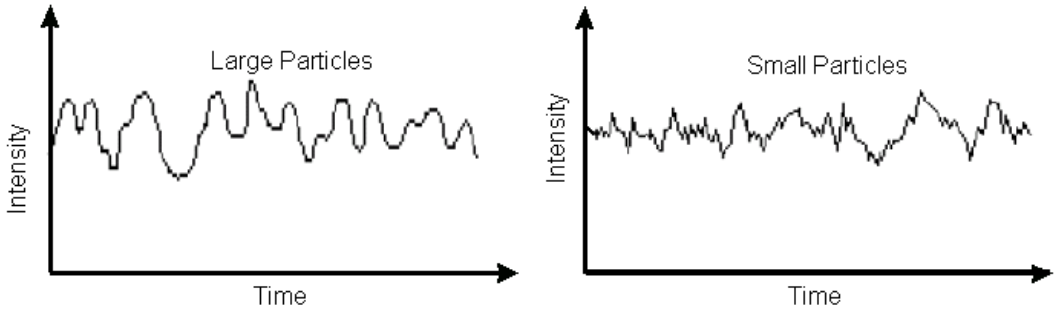

Figure 3-4: Typical intensity fluctuations for large and small particles [96].

The point in the auto correlation function where the coefficient significantly decays provides information on the average particle size within the solution, where a steep decay is indicative of a monodisperse solution, with monodispersity decreasing with an increase in the slope of decay (i.e. when the slope becomes less negative) [96].

The velocity of Brownian motion is characterised using a parameter known as the translational diffusion coefficient, D, which is related to hydrodynamic particle diameter using the Stokes-Einstein equation (Equation 12) [96].

$$d(H) = \frac{kT}{3\pi nD}$$

Equation 12

Where *d(H) = hydrodynamic diameter (m)*

D = translational diffusion coefficient ($m^2\ s^{-1}$)

k = Boltzmann's coefficient ($m^2\ kg\ s^{-2}\ K^{-1}$)

T = absolute temperature (K)

η = viscosity (Pa s)

The correlation function of a single particle is calculated using the Equation 13; for a large number of similar sized particles this function is an exponential decay, as described by Equation 14.

$$g(\tau) = \langle \tau(t).\tau(t+1) \rangle$$

Equation 13

$$g(\tau) = A[1 + B\ \exp(-2\Gamma\tau)]$$

Equation 14

Where *A = baseline of correlation function*

B = intercept of correlation function

Γ = decay rate of correlation function ($time^{-1}$)

The decay rate, Γ, is determined by fitting an exponential to the auto correlation function. This fitting is known as Cumulant analysis and forms a polynomial curve displaying scattered light intensities as a function of particle size. A scattering vector, q, is then calculated using Equation 15 [96].

$$q = \left(\frac{4\pi n}{\lambda_0}\right) sin\frac{\theta}{2}$$

Equation 15

Where *n = refractive index of the solvent*

λ_0 = wavelength of laser light (m)

θ = scattering angle (radians)

The scattering vector is then substituted into Equation 16 allowing a value of for the translational diffusion coefficient, D (m^2 s^{-1}), to be determined [96]. Equation 12 can then be used to determine the hydrodynamic diameter.

$$\Gamma = Dq^2$$

Equation 16

3.1.2 High performance liquid chromatography (HPLC)

IUPAC definition of chromatography – *"Chromatography is a physical method of separation in which the components to be separated are distributed between two phases, one of which is stationary while the other moves in a definite direction [97]".*

(a) An introduction to LC

Liquid chromatography (LC) involves passing a sample matrix through a column packed with an adsorbent, typically a silica based compound. The sample matrix is passed through the column using an eluant and separation of analytes is based upon their affinity for both the adsorbent, within the column, and the eluant [98]. Consequently, the interaction of the analytes with both the adsorbent and eluant must be considered, making the choice of both phases important [99].

In this study a solid chromatographic packing, which will now be referred to as the stationary phase (SP), is used. In this type of LC, separation is based on the affinity of analytes for the SP and the method is known as liquid solid chromatography (LSC), where the liquid refers to the eluant, which will now be referred to as the mobile phase (MP). Other types of LC exist, namely, LLC, which involves the use of a liquid SP where

separation is based on the partition coefficients of the analytes of interest. As only LSC will be applied in this study future discussions will be based only on this method.

Early LC methods involved packing a long column (approximately 1 m) with the SP of choice and passing the MP, containing the sample matrix, through the column. Separation was then achieved by dividing the column and removing bonded analytes through evaporation. Due to the length of these columns and the methods required to remove analytes, separation was time consuming and, as the columns had to be destroyed for analyte removal, the columns could only be used once [98].

In the 1960s it was observed that to increase the efficiency of current LC methods, to make them comparable to gas chromatography, the size of packing material had to be significantly decreased to values in the region of 2 – 20 μm [97, 98]. Achieving this particle size allowed the SP to be densely packed, resulting in a pressure drop across the column, leading to issues with passing the sample over the SP. This lead to the inclusion of high pressure pumps, allowing the MP to be pumped through the column rather than relying on gravity to carry it through, this type of LC is now commonly referred to as High Performance or High Pressure Liquid Chromatography (HPLC) [97, 98].

(b) HPLC

An HPLC instrument consists of the following components, a solvent reservoir containing the MP, which is pumped through a filter using a high pressure pump, an injection valve allowing the correct sample volume to be injected into the continuous flow of MP and into the column. The eluted analytes are then detected at the detector and data is recorded [98]. A schematic of a typical HPLC instrument is shown in Figure 3-5.

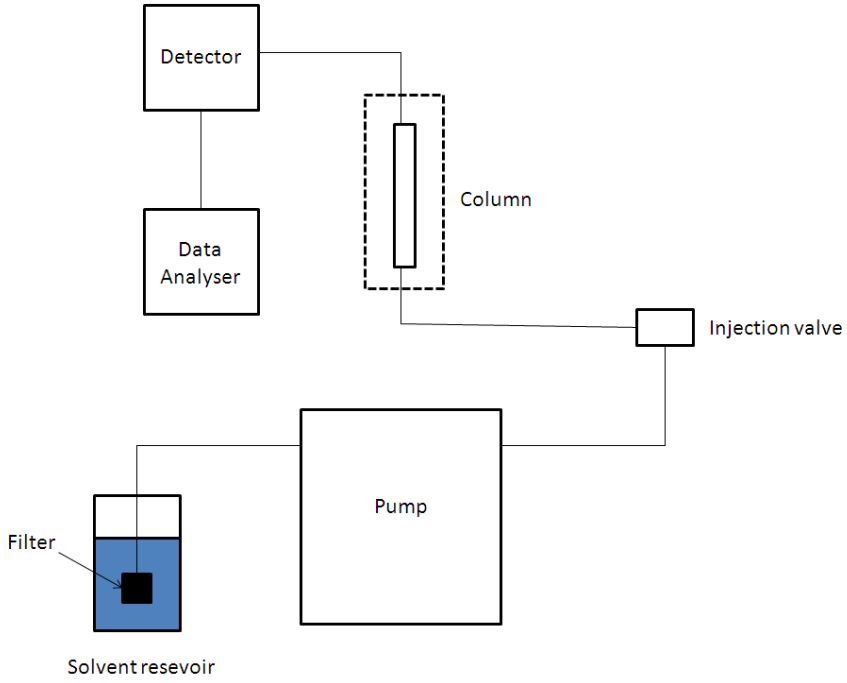

Figure 3-5: Schematic of HPLC instrument.

The most important part of the HPLC is the column, as this is where the analytes are separated; the discussion herein will, therefore, focus on the chemistry that occurs within the HPLC column. Separation of analytes in the column can be carried out via a number of sorption processes as shown in Table 3-1.

Table 3-1: Sorption processes for analyte separation [97].

Sorption mode	Mechanism of retention
Liquid-solid adsorption	Surface adsorption based on affinity (polarity)
Liquid-liquid adsorption	Partitioning of analytes into the liquid MP
Ion Exchange	Charge interaction between analytes and SP
Ion pair	Partitioning of neutral ion pairs between phases
Size exclusive	Filtering effect on the basis of hydrodynamic volume
Chiral	Diastereoisomeric interactions between solute enantiomers and chiral sites on SP
Affinity	Bio-specific binding of solute to immobilized ligand

As mentioned in section (a) this study will involve the use of liquid solid adsorption. In this type of system, separation is based on the polarity of the solid packing material and the polarity of the analytes. Two main types of LSC exist; the first is normal phase (NP) which involves the use of a SP, that is more polar than the MP [97, 98]. Typically a polar, silica based phase is used, which is prepared using high purity silica gel [100]. Polar analytes are, therefore, attracted to the surface silanol groups of the silica packing (see Figure 3-6) and are retained in the column longer, consequently elution is in the order of increasing polarity.

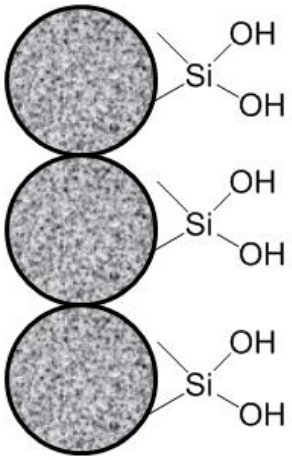

Figure 3-6: Schematic illustrating the surface polar groups of silica packing materials.

The second type of LSC is known as reverse phase (RP), which, as the name suggests, is the reverse of NP- HPLC and utilises a SP less polar than the MP. The most common SP utilised is octadecylsilane (ODS), which is shown in Figure 3-7. The long hydrocarbon chain makes this phase non polar and attracts non polar analytes, resulting in elution being in the order of decreasing polarity, with the most polar analytes eluting first.

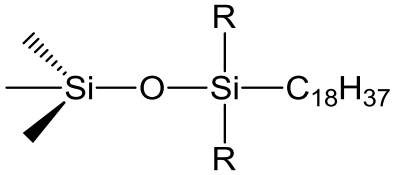

Figure 3-7: ODS SP for reverse phase HPLC [97].

Although the SP must be carefully selected for each sample, the MP is also very important to ensure correct and efficient elution of analytes from the column. For NP-HPLC the MP is generally a non polar solute, and for reverse phase a polar solute, often water is used, however, if these solvents are too non-polar or too polar, respectively, strongly retained analytes will be difficult to remove from the column. For this reason a modifier is added to the MP, in NP this is an analyte that is more polar than the main MP liquid and in RP this is a less polar analyte. These modifiers displace analytes from the column moving them further down and eventually eluting them [98]. Table 3-2 gives the polarity index for a range commonly used of solvents, illustrating hexane as the most non-polar and water as the most polar.

Table 3-2: Polarity index (P^I) for a range of solvents [98]

Solvent	P^I
Hexane	0.1
Methylbenzene	2.4

Tetrahydrofuran	4.0
Trichloromethane	4.1
Butanone	4.7
Ethyl ethanoate	4.4
Dichloromethane	3.1
1,2-dichloromethane	3.5
Propanone	5.1
1,4-dioxane	4.8
2-methoxyethanol	5.5
Acetonitrile	5.8
Ethanol	4.3
Methanol	5.1
Water	10.2

For a sample containing both polar and non-polar analytes either mode could be used with the elution order reversing when changing between the two types, however, RP has become the method of choice for a number of reasons. Firstly, there are a range of RPs available, which allow a wide range of polarities to be separated, secondly a part aqueous MP can be used, meaning that it is an inexpensive option and the solute can be easily prepared, finally RP is said to be faster, easier and often more reproducible. Nevertheless RP chromatography also has its disadvantages; unreacted silanol groups within the column can attract polar groups. Attraction of polar analytes can lead to peak tailing and retention of polar analytes/polar MP can alter the chemistry of the column packing and can result in reproducibility problems, making comparison between different columns a problem. Another issue concerning RP LC is that the reaction mechanism between analytes and the solid phase is not properly understood [98].

(c) Analyte retention

As mentioned previously the separation of analytes is based on their distribution between the SP and MP. As the analytes travel through the column they reach a distribution equilibrium between the two phases as shown in Equation 17.

$$[A_s] \leftrightarrow [A_M]$$

Equation 17

Where $[A_S]$ = *concentration of analyte in the SP*

$[A_M]$ = *concentration of analyte in MP*

The distribution ratio of the analyte, K_A, is [97]:

$$K_A = \frac{[A_S]}{[A_M]}$$

Equation 18

The distribution ratio will be different for different analytes; as they travel through the column the distribution will be established at all interaction sites along the column. This process is shown in Figure 3-8, which illustrates that all analytes are injected into the column together and separation between the two phases occurs continuously as they travel through the LC column. Essentially, each analyte travels through the column interacting at sequential sites, thus analytes with a high distribution ratio move more slowly through the column (analyte C in Figure 3-8) than analytes with a low affinity (analyte A in Figure 3-8) [97].

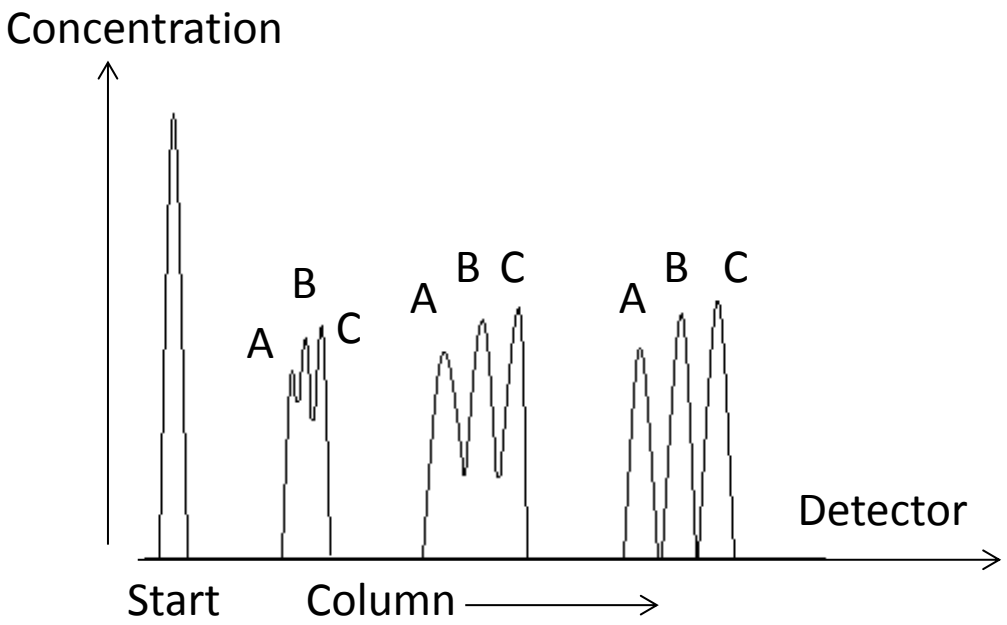

Figure 3-8: Schematic illustrating the separation of a three component system (A, B and C). Redrawn from [97].

Assuming that there is no tailing, i.e. the peak is Gaussian, the number of interaction sites within a column is defined as the number of theoretical plates, N, which is calculated from:

$$N = 5.54\left(\frac{t_R}{\omega_{1/2}}\right)^2$$

Equation 19

Where t_R = *rentention time (mins)*

$\omega_{1/2}$ = *width at half peak height (mins)*

To ensure the peak is Gaussian an asymmetry factor, A_s, is calculated:

$$A_s = \frac{b}{a}$$

Equation 20

Where *a = width of the first half of the peak at 10 % peak height*

b = width of the second half of the peak at 10 % height

The efficiency (HETP) of a well packed column should be in the region of 95 000 m^{-1} ± 5 % and can be calculated from Equation 21.

$$HETP = \frac{L}{N}$$

Equation 21

Where *HETP = Height Equivalent of Theoretical Plate (m^{-1})*

L = total column length (m)

N = number of theoretical plates

Columns of different lengths can be compared by calculating an efficiency based on the column length, as shown in Equation 22.

$$Efficiency = 100\left(\frac{N}{L}\right)$$

Equation 22

(d) Analyte detection

Once eluted from the column, analytes pass to the detector, a number of different types exist for use with LC apparatus. These include; spectroscopic detection techniques, UV-VIS, fluorescence, IR, atomic absorption, inductively coupled plasma and mass spectrometry (this will be discussed further in section 3.1.3) [98] other detectors include refractive index measurement [101], electrochemical detectors and conductivity detectors [97].

The most widely used detector is the UV-VIS spectrometer, this technique involves the use of a combined deuterium/tungsten light source and involves measuring the difference in light absorbed from the incident beam by the sample analytes compared with that of the MP. The absorbance is related to concentration by the Beer Lambert Law as shown in Equation 23 [97]:

$$A = \log\frac{I_0}{I_t} = \varepsilon cl$$

Equation 23

Where A = *absorbance*

I_0 = *intensity of incident light*

I_t = *intensity of transmitted light*

ε = *molar absorptivity (L mol^{-1} cm^{-1})*

c = *concentration (mole L^{-1})*

l = *path length (cm)*

As the spectrometer measures the difference in absorbance between the analytes and the MP it is important to choose a MP that is weakly absorbing in the UV-VIS region, e.g. water. Analytes that absorb in the region of interest are alkenes, aromatics and compounds with multiple bonds between C and O/N/S (the absorption regions for specific functional groups are given in section 3.1.4) [98].

UV-VIS detectors can either be fixed or variable wavelength; as the name suggests, fixed wavelength detectors only allow absorbance to be measured at one specific wavelength (typically set to 254 and 280 nm), whereas variable wavelength detectors allow the wavelength to be set by the analyst, consequently allowing increased sensitivity [98, 101]. To determine the most sensitive wavelength for absorbance, the UV-VIS spectra for the sample to be analysed is measured prior to HPLC analysis.

The main components of a UV-VIS detector are shown in Figure 3-9. The light source passes through a monochromater and then through a sample cell, containing the sample flow and is detected by a photomultiplier, before being analysed to form the chromatogram [101].

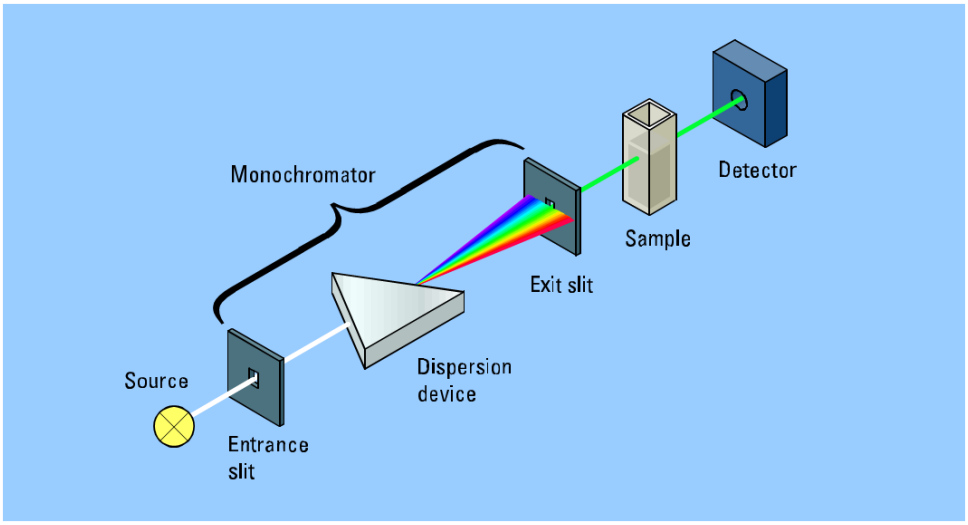

Figure 3-9: Schematic of UV-VIS detector [102].

3.1.3 LCMS

(a) Interpretation of mass spectra

Singly charged ions are easily identifiable in mass spectra and the mass of the molecule can be determined by either adding or subtracting 1 on to the mass calculated from Equation 24, for negative and positive ion spectra, respectively.

$$Observed\ peak\ value = m/z$$

Equation 24

Where *m = mass of the molecule plus/minus any protons*

z = charge

Peaks resulting from double, triple and quadruple charged ions require slightly more interpretation. Firstly the parent peak (tallest peak) should be identified; secondly the spectra should be inspected for peaks with half and double the m/z ratio. It is then assumed that these peaks are related and that they differ by 1 unit of charge. Consequently, Equation 24 can then be rewritten to add or subtract the protons [103]. As an example, consider the spectra shown in Figure 3-10. The parent peak can be identified as the peak at 265.3 m/z and it can be observed that the peak at 531.2 is approximately double this mass.

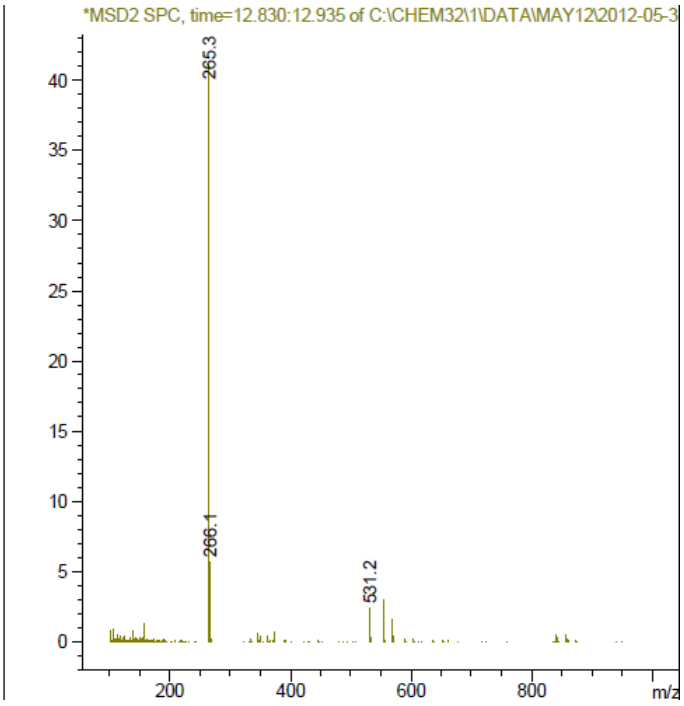

Figure 3-10: Mass spectra LC peak with retention time of 12.886 min for $CaCO_3$ at T_{40}.

As this is a negative ion spectra, Equation 24 can be rewritten for both of the observed peaks as shown below:

$$265.3\ (z+1) = m - 1$$
$$531.2\ (z) = m$$

If these peaks are related then the mass, m, will be equal and thus can be solved as follows:

$$[(265.3\ (z+1)] + \ 1 = \ 531.2\ z$$
$$265.3\ z + 265.3 + 1 = \ 531.2\ z$$
$$265.9\ z = 266.3$$
$$z = 1$$

This indicates that the two peaks are related and the charge state of the observed peak at 265.3 m/z is 2+ and the peak at 531.2 m/z can is a result of a +1 charged species. Given that the spectra used resulted from negative ions the mass of the compound can be calculated by determining the average mass of the two calculated masses.

$$(531.2 + 1) \times 1 = 532.2$$
$$(265.3 + 1) \times 2 = 532.6$$

When positive ion spectra are used it is interpreted in a similar manner, with the only exception being in the rewriting of Equation 24, where 1 unit is added to m rather than being subtracted.

3.1.4 UV-Visible Spectroscopy

Visible light is considered as a wave function, which is characterised by a wavelength, λ, or frequency, υ, which are related as shown in Equation 25 [104].

$$\upsilon = \frac{c}{\lambda}$$

Equation 25

Where *c = velocity of light (3 x 10^{10} cm s^{-1})*

Consequently, the wavelength and frequency of light are inversely related. The wavelength of light is defined as the distance between adjacent wave peaks, as illustrated in Figure 3-11, and is typically designated in nm.

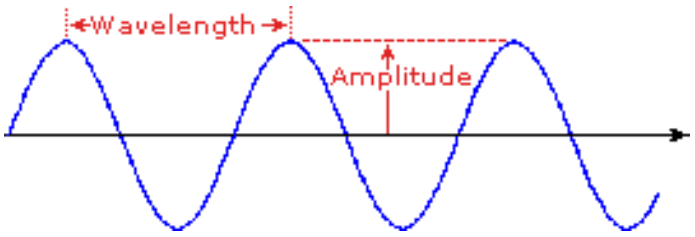

Figure 3-11: Schematic of light as a wave function.

The frequency of the wave is the number of waves passing a fixed point in a fixed period of time and is typically measured in Hertz (Hz). The UV region is from 200 nm to 400 nm, where the visible region begins and covers the range up to 800 nm as shown in Figure 3-12 (a).

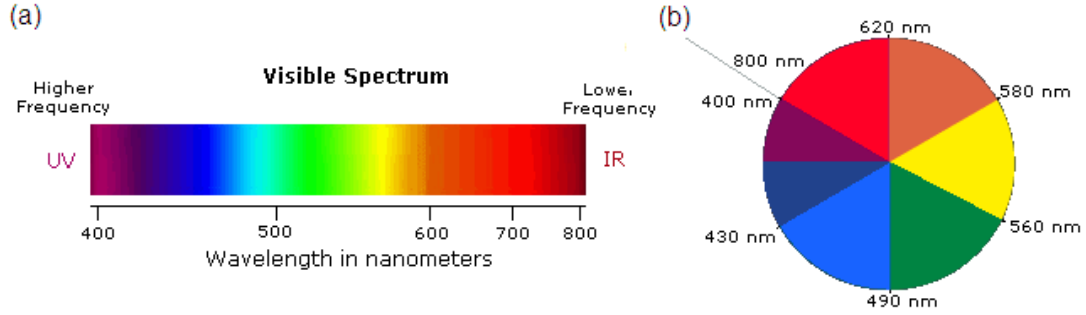

Figure 3-12: (a) Electromagnetic spectrum of light between 400 and 800 nm and (b) wheel of light illustrating the corresponding colour diagonally opposite the region of absorption (b) [105].

Sunlight is observed by the human eye as white light, however in reality is made up of a number of different coloured light covering the UV, visible and Near infra-red (NIR) region of the spectrum. When this light meets a medium it interacts and some is absorbed. The unabsorbed incident light adopts the complementary colour of the adsorbed wavelength and it is this colour that is observed as the colour of the medium. This phenomenon is demonstrated in Figure 3-12 (b), which shows the observed colour diagonally opposite the colour of the absorbed light, for example, the RF gels appear red in colour, indicating that they absorb light in the region of 490 nm to 560 nm [104].

(a) UV-Vis absorption – an introduction

Absorption of light results from molecular transitions from the Highest Occupied Molecular Orbital (HOMO) to the Lowest Unoccupied Molecular Orbital (LUMO), and the energy of these transitions are related to the frequency of the wave by Equation 26 [104]. Essentially, for a transition to occur, a molecule must absorb enough energy, E, to promote an electron from the HOMO to the LUMO.

$$E = h\upsilon$$

Equation 26

Where h = *Planck's constant* (6.6×10^{-34} *J s*)

v = *frequency* (s^{-1})

Different types of transitions are shown in Figure 3-13, which also compares the energy required for each transition class. UV-Vis light has energy in the region of 151 to 598 kcal/mole and energy is this region allows transitions from non-bonding orbitals to π anti-bonding orbitals and from π-bonding orbitals to π anti-bonding orbitals, as a result absorbing molecules must contain π or non-bonded electrons. For the higher energy transitions shown in Figure 3-13 lower wavelengths (higher frequencies) of light are required.

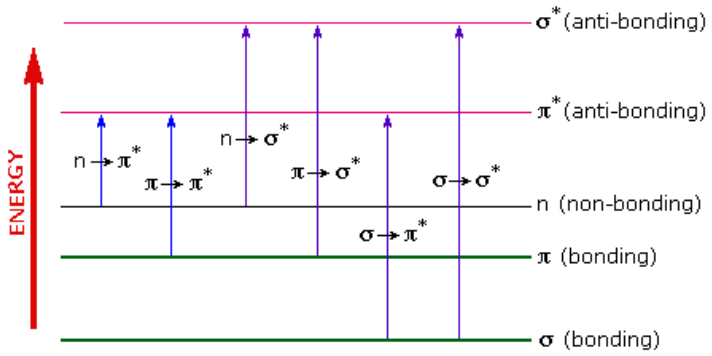

Figure 3-13: Electronic orbital transitions.

(b) Molecular transitions resulting in absorbance

The absorbing functionalities within a molecule are known as chromophores and due to the transitions involved, these are typically multiple bonds and lone pairs [106]. Conjugation within a molecule intensifies and shifts absorbance to higher wavelengths, which can be explained by a decrease in the energy gap between the HOMO and LUMO, and decreased energy results in lower frequencies and higher wavelengths [107].

In the RF systems, absorption will be caused by electron promotion from the π-orbital of a double bonded carbon to the π anti-bonding orbital or from the non-bonded orbital of the oxygen lone pair to the π anti-bonding orbital of carbon. In order to understand these transitions it is important to understand the bonding in benzene and phenol.

The electronic configuration of carbon is $1s^2 2s^2 2p^2$, in order to satisfy the three bonds (two to carbon and one to hydrogen) one electron is promoted from the *2s* to the $2p_z$ orbital, resulting in four unpaired electrons. As only three are required for bonding hybridisation occurs between the *2s* orbital and two of the p orbitals resulting in three sp^2 hybrid orbitals, which form sigma bonds between hydrogen and two carbons. Consequently one p electron remains unbounded on each carbon and these orbitals are orientated above the benzene plane, where

they overlap resulting in a delocalised spread of π electrons, where electrons are no longer shared between two carbons but are spread over the ring structure [108]. Given there are six electrons this spread occurs over three orbitals [108]. A schematic showing the corresponding bonding and anti-bonding orbitals for one of the three orbitals, is shown in Figure 3-14.

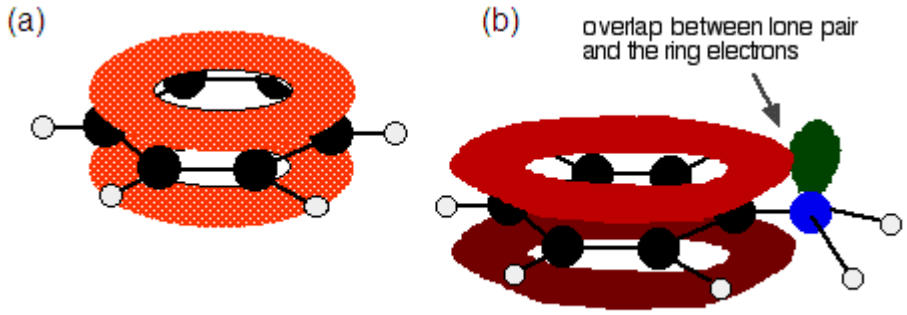

Figure 3-14: Schematic showing (a) one molecular orbital (bonding and anti-bonding) with electron delocalisation and (b) electron delocalisation in phenol illustrating the lone pair of electrons [109].

Upon interaction with UV-Vis light, RF systems are able to absorb enough light to promote electrons from π-bonding orbitals to π anti-bonding orbitals (orbitals shown in Figure 3-15), of carbons in the phenol ring. The OH groups of phenols have lone pairs of electrons, and consequently have non-bonding orbitals, which are orientated as shown in Figure 3-14. These non-bonding orbitals are higher in energy than bonding orbitals, therefore, lowering the energy gap between the HOMO and the LUMO meaning that higher wavelengths (lower frequencies and lower energies) of light result in promotion of electrons from the non-bonding orbital to the π anti-bonding orbital [108].

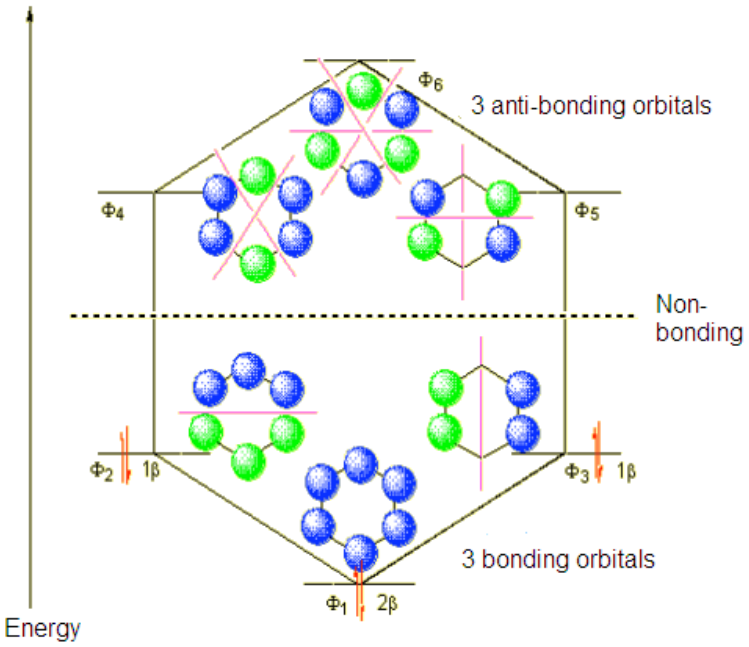

Figure 3-15: Bonding, anti-bonding and non-bonding orbitals of phenol. Edited from [110].

(c) UV-Vis spectrometer

Two main types of UV-Vis spectrometer exist, a double beam spectrometer, which measures the absorbance of the sample and a reference simultaneously, or a single beam spectrometer, which measures the absorbance of a reference prior to analysing the sample absorbance. This study involves the use of a single beam spectrometer, consequently further discussions will focus on this type of set up.

A schematic of a single beam instrument is shown in Figure 3-16. In order to cover the whole UV-Vis/NIR region a combined deuterium/halogen lamp is used, which covers the regions of 185 to 350 nm and 350 to 3300 nm, respectively. The light from both lamps is focused through a lens and, for single wavelength instruments is then passed through a monochromator. To allow a region of wavelengths to pass through, a rotating diffraction grating is utilised. This has the effect of splitting the light like a prism and passing the chosen range of wavelengths into the instrument gradually. The light then passes through the sample, which is typically held in a cuvette, and the difference between the incident light and transmitted light is measured as the sample absorbance, as per the Beer Lambert equation (Equation 23) [104].

The most common detectors are Photo-Multiplier Tubes (PMTs) for the lower wavelengths (180 – 800 nm) and solid state detectors for higher wavelengths (800 – 3330 nm). PMTs are high vacuum systems; incident light enters and hits a photocathode, producing multiple electrons, which are then directed into the tube, where they interact with dynodes producing

secondary electrons; as this process continues a cascade of electrons forms, which eventually reaches the anode and is detected as a sharp current [104].

Another detector type is the lead sulfide (PbS) detector. Due to the semiconducting properties of PbS it acts as a direct photon detector and either measures the change in current or the change in electrical resistance when light photons hit the surface. At room temperature this type of detector is usually only sensitive at very low wavelengths and requires significant cooling to increase the sensitivity to higher wavelengths. It is this type of detector that is utilised in the spectrometer used in this study, however, Varian have adapted smart technology to allow its use over the range 175 to 3330 nm [111].

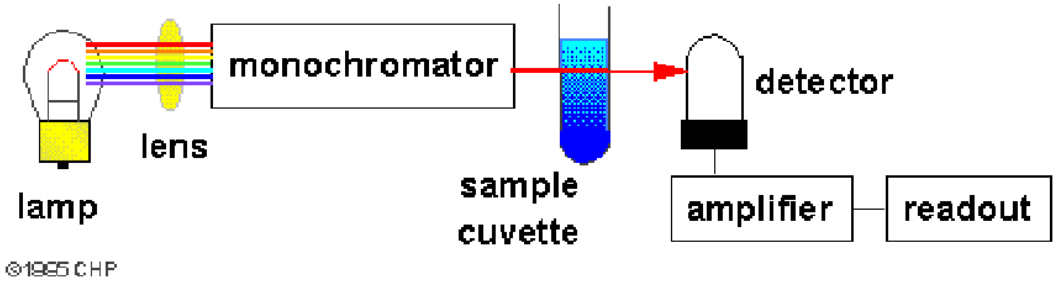

Figure 3-16: Schematic representation of UV-Vis NIR spectrometer [112].

3.1.5 Thermo Gravimetric Analysis (TGA)

TGA is a thermo-analytical technique in which a sample is heated on a high precision balance, within a furnace. The balance records changes in mass as a function of temperature and a curve of percentage weight against temperature can be plotted. The first derivative of this curve can be used to identify the temperatures at which main mass losses occur. Nitrogen or argon atmospheres are often employed to avoid unwanted oxidation of the sample [113-115]. Consequently, TGA can be used to determine the optimum pyrolysis temperature, as it gives an indication of the point where no further mass loss occurs. Example TGA curves are shown in Figure 3-17 for $(NH_4)_2CO_3$_25. The 1st derivative plot shows three clear weight losses at approximately 100, 400 and 600 °C. It can be deduced that the peak at 100 °C is due to desorption of residual water and, given that the RF xerogels consist of mainly C-O and C-H bonds, and that the bond enthalpies of these bonds are 358 kJ mol^{-1} and 413 kJ mol^{-1} [116], it can be concluded that these areas of weight loss are due to the breakage of C-O and C-H bonds, respectively [57].

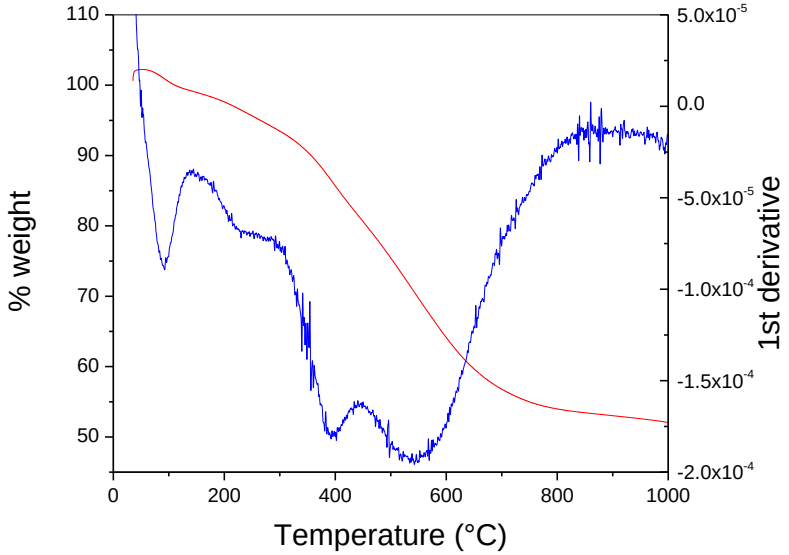

Figure 3-17: % weight and 1st derivative TGA plots for $(NH_4)_2CO_3$_25.

3.1.6 Scanning Electron Microscopy (SEM)

SEM involves irradiating a sample with a focused beam of electrons, which interacts with the material producing signals. These signals result from different volumes within the sample and can include back scattered electrons, secondary electrons and X-rays, allowing different characteristics (e.g. surface topography, morphology and composition) of the material to be observed and characterised [117].

A schematic of an SEM instrument in shown in Figure 3-18, illustrating the main components; the electron column, consisting of the electron gun, electron lenses, scanning system, objective aperture, specimen chamber, electron detector, a vacuum system and an electronics console, allowing image viewing and optimisation [118].

The electron gun fires a broad beam of electrons, with an accelerating voltage in the region of 1-40 keV, down an evacuated column, allowing the electrons to travel much further than they would in air. There are numerous types of electron guns available, namely thermionic electron emission, triode, tungsten hairpin, lanthanum hexaboride and field emission guns. In this study a field emission gun was used, in comparison to other guns this type produces a very small beam, subsequently allowing simple lenses to be used for reduction and focusing of the beam, whereas, in other systems complex optics are required to reduce and focus the broad electron beam. Typically the beam reaching the specimen will have a spot size of a few nm and the beam will penetrate the sample to a depth of approximately 1 μm. Interaction of the beam with the sample surface and beam penetration will produce signals,

collection of these signals from a scan of the surface allows an image to be produced [117, 118].

The quality of the SEM micrograph is highly dependent upon the electron beam. There are three beam parameters that must be optimised in order to obtain the highest possible image quality, beam spot size, beam convergence angle and beam current. The beam spot size (or diameter, d_p) is altered through the use of condenser lenses and higher resolution images are possible with smaller spot sizes. The smaller the spot size the smaller the convergence angle, α, as illustrated in Figure 3-19.

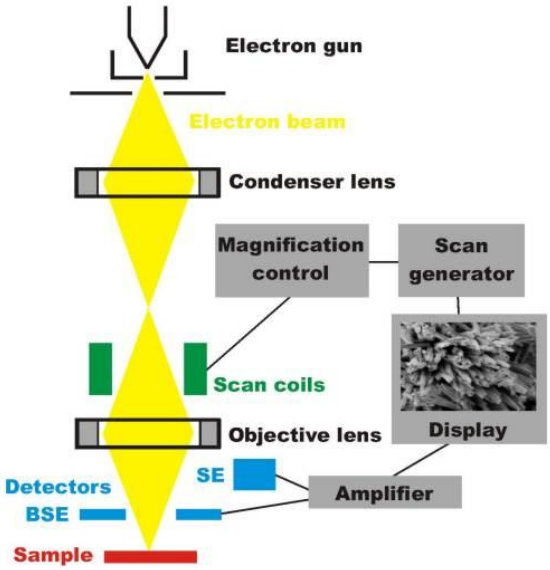

Figure 3-18: Schematic diagram of SEM instrument [119].

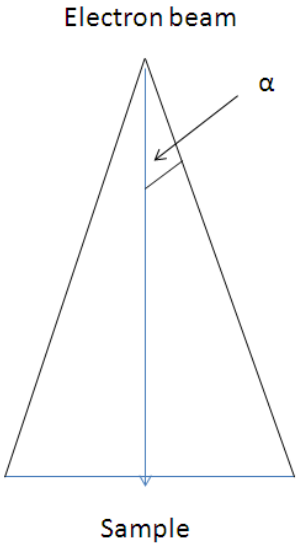

Figure 3-19: Beam convergence angle. Redrawn from [118].

The electron beam affects the depth of field, D, achieved within the sample under investigation, where a large depth of field allows samples with varied surfaces (i.e. rough samples) to be imaged in the best quality [118]. As illustrated by Equation 27, depth of field is affected by the aperture (width) of the final lens (A), the magnification of the beam (M) and the distance between the sample and the lens (W) [120].

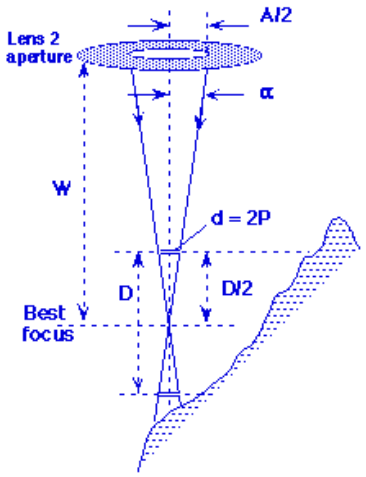

Figure 3-20: Beam convergence angle [120].

$$D = \frac{4 \times 10^5 W}{A\,M}\ \mu m$$

Equation 27

Where W = *distance between beam and specimen (μm)*

A = *lens aperture (μm)*

M = *magnification*

Within the depth of field, images appear focused and sharp, whereas outwith the field signals from adjacent pixels overlap resulting in blurred images.

The beam current, i_p, is also important, and higher beam currents result in increased interaction with the sample, consequently resulting in better quality micrographs, hence, as the beam diameter and convergence angle decreases the probe current decreases, consequently a balance between the three parameters is required to obtain the best possible SEM images.

The electron beam interacts with the sample in two ways; elastic scattering, which alters the course of beam electrons without changing the energy, and inelastic scattering, which involves a transfer of energy from the beam to the atoms within the specimen, forming

secondary electrons [117]. To allow the electron beam to pass through the sample and reach an electrical ground, and to prevent a build-up of electrons on the surface, the sample must be conductive. If the sample is not conductive electrons build up on the surface, resulting in a net negative charge which causes poor image quality [118].

Elastic scattering results in a change in direction of the electron beam, however, the speed of the electrons through the sample remains unchanged, thus the energy, E, remains constant (Equation 28).

$$E = \frac{m_e v^2}{2}$$

Equation 28

Where m_e = *electron mass (Kg)*

v = *electron velocity (m* s^{-1}*)*

The electron beam interacts with the nucleus of the sample, transferring a very small amount of energy (< 1 eV) and causing the electron to be scattered with an angle of, φ_e (Figure 3-21 a). In contrast, during inelastic scattering energy is transferred to electrons within the sample, which can result in electron promotion and the formation of secondary electrons. The transfer of energy significantly reduces the energy of the incident electron, resulting in a very small (< 0.1 °) scattering angle of the exciting electron (Figure 3-21 b) [117].

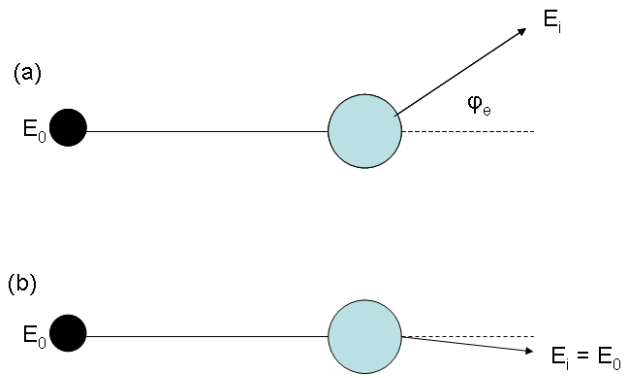

Figure 3-21: Schematic of (a) elastic and (b) inelastic scattering. Redrawn from [117].

As discussed above, backscattered electrons are beam electrons, consequently they have high energies, typically in the region of 0.8 – 0.9 times the incident beam radiation (i.e. 1-40 keV), whereas secondary electrons arise from the transfer of energy from the electron beam to the specimen and have energies in the region of 3-5 eV. Thus, backscattered electrons

have much higher energies than secondary electrons making simultaneous detection of both electron types difficult.

The most commonly applied detector is the Everhart -Thornley detector (Figure 3-22), which is able to detect both types of electrons. The detector is positioned near the specimen, and consists of the following main components, Faraday cup (cage), scintillator, light guide and photomultiplier tube. High energy backscattered electrons collide with the scintillator forming photons. For the lower energy secondary electrons a positive potential is applied to the scintillator, which accelerates the low energy electrons producing light in the scintillator.

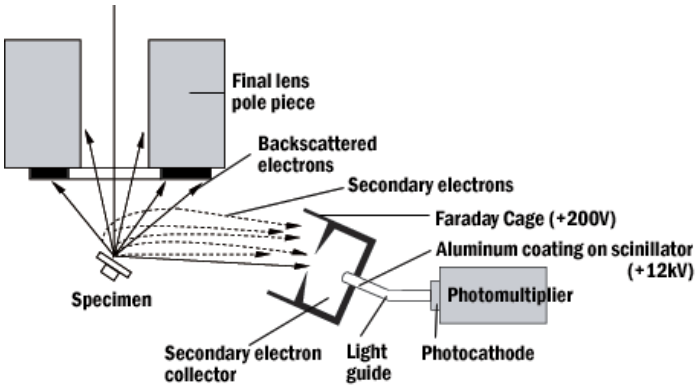

Figure 3-22: Schematic of Everhaut-Thornley detector [121].

The generated photons of light are then conducted within the light guide to the photomultiplier. At the photomultiplier, the light interacts with a cathode, that's converts them back to electrons, which accelerate through consecutive electrodes forming further electrons. This electron detection technique occurs rapidly and allows specimen properties, i.e. topography and composition to be determined. To enable an image to be constructed, the electron detection technique is carried out at various locations over the sample and the results are collated [117, 118].

3.2 Techniques used for RF xerogels and carbons

3.2.1 Nitrogen adsorption/desorption analysis

(a) An introduction to porosity

A porous solid is defined as a solid with pores, i.e. cavities, channels or interstices, which are deeper than they are wide [122]. In this study, pores are formed as a result of the aggregation of small clusters and subsequent cross-linking, thus, as discussed previously, the porous structure depends on the initial reaction. For materials with high specific surface

areas it is useful to split the material into total external and internal surfaces. The external surface area includes the surface that from the outer shell of the material including the surface area of any cracks, i.e. rough edges that cannot be defined as pores as they are wider than they are deep; whereas the internal surface area is the area of all pores accessible to the adsorbate molecules.

Pores can be classified into four categories (a) open pores, (b) closed pores, (c) transport pores and (d) blind pores as shown in Figure 3-23.

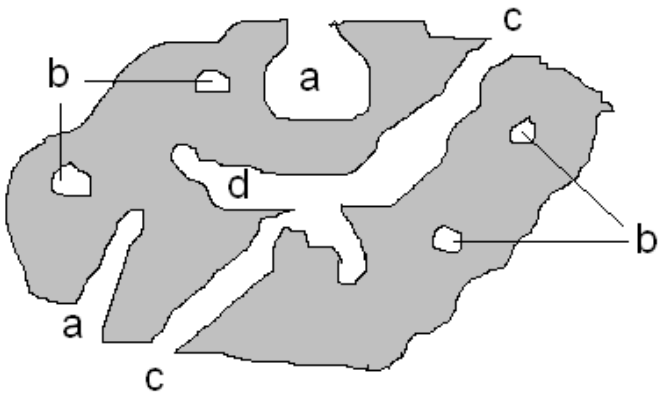

Figure 3-23: Schematic showing different types of porosity.

Open pores are connected to the external surface of the material, whereas closed pores are voids and, thus, are not accessible. Transport pores connect internal areas to the external surface and are also known as through pores, blind pores are connected to transport pores but not to the external surface [122].

To determine the internal pore size by gas adsorption the pores must be accessible to the gas molecules being used for analysis, thus, it is essential to classify pores by size. The IUPAC classification of pore size is shown in Table 3-3 [123].

Table 3-3: IUPAC classification of pores [123].

IUPAC classification	Width of pore (nm)
Micropores	< 2
Mesopores	2-50
Macropores	> 50

(b) Introduction to adsorption

Adsorption is defined as *'the enrichment of one or more components in the interfacial layer* [124]' and it can be split into two categories, chemisorption and physisorption.

Chemisorption involves the formation of chemical bonds between the adsorbent, *'a substance on the surface of which a substance is adsorbed'* [125] and the adsorbate, *'a substance that is adsorbed on a surface'* [125], whereas physisorption involves the formation of weak van der Waal's forces. It is the physisorption process that occurs during gas adsorption onto a porous solid.

Physisorption

Gas molecules are attracted to the reactive surfaces resulting in charge distributions between the gas molecules and the surface, which causes weak van der Waal's forces to form. This phenomenon is only witnessed at low temperatures due to the weakness of the forces involved. At low pressures gas molecules begin to adsorb onto the surface; as the pressure increases a monolayer is formed, and further increase in the pressure causes the formation of a multilayer, which is not in direct contact with the porous material. Multilayers continue to form as pressure is increased [123].

The physisorption mechanism involved varies for pores of different size, in micropores where the diameter of the pore is small, all of the adsorbed gas molecules are attracted to the surface of the porous solid and the number of interactions between gas molecules is negligible, however, in larger mesopores when the adsorbed layer reaches a critical thickness there is an increase in the intermolecular forces, resulting in surface tension. This causes the outer layer to condense, below the saturated vapour pressure, in a phenomenon known as capillary condensation. For porous solids containing mesopores, capillary condensation leads to differences in the adsorption and desorption isotherms and, consequently, hystereses are formed (see Section (c)) [126]. Monolayer and multilayer formation is illustrated in Figure 3-24.

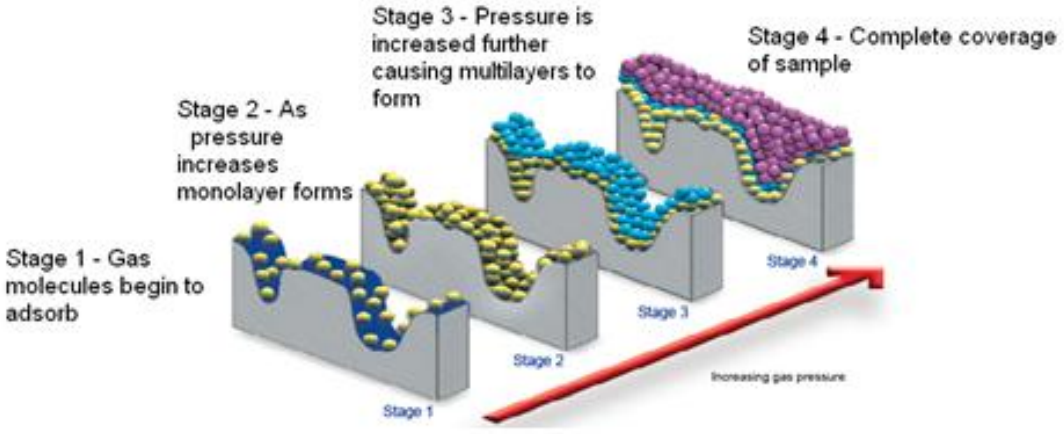

Figure 3-24: Monolayer and multilayer formation during gas adsorption [127].

(c) Adsorption isotherms

The relationship between the amount of gas adsorbed and relative pressure, at fixed temperature, is known as an adsorption isotherm [123]. Isotherms will have different shapes depending on the gas used for analysis, structure of the porous solid, and types of interactions occurring. The first classification of isotherms was established in 1940 by Brunauer, Deming, Deming and Teller [124], who identified five different Types of isotherm (I – V), another isotherm was later proposed by Sing (VI) and it is these six isotherms that are now classified by IUPAC. These are illustrated below in Figure 3-25 [123].

Type I isotherms are characteristic of microporous materials and show that micropore filling occurs at low relative pressures. Type II and Type III isotherms are indicative of non-porous or macroporous solids with strong and weak gas-gas interactions respectively, however, materials with both micro- and meso-pores produce Type II isotherms. Type IV show hysteresis, caused by capillary condensation within a mesoporous material. The early part of the isotherm (up to point B), shows monolayer adsorption, which is followed by multilayer formation. As the pressure increases to high P/P_0 values uptake becomes limited.

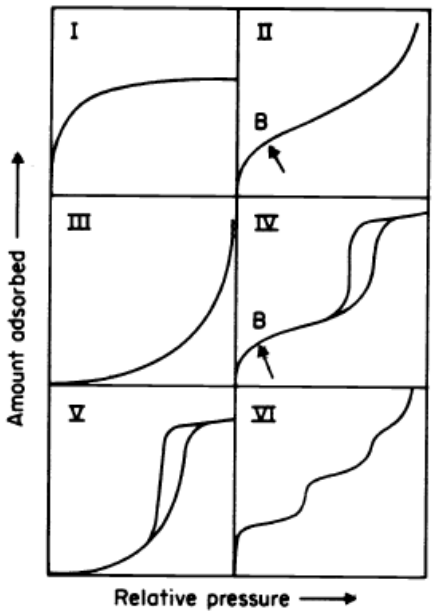

Figure 3-25: IUPAC classification of adsorption isotherms [123].

Like Type III isotherms, Type V isotherms are related to weak gas-gas interactions in materials with either micro or mesopores. Type VI isotherms show steps, which correspond to stepwise multilayer formation on non-porous solids [123].

Hystereses have also been classified by IUPAC as illustrated in Figure 3-26.

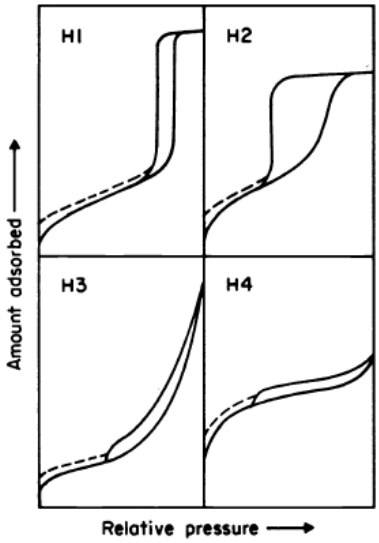

Figure 3-26: IUPAC classification of hysteresis loops [123].

H1 and H2 loops occur when the porous material consists of uniform spheres, where H1 result from narrow pore size distribution and H2 form as a result of wide pore size distribution. Slit shaped pores give rise to H3 and H4 loops, the difference being that H4 loops are as a result of wide slits [123].

(d) Determination of surface area – Langmuir and BET models

The first model for surface area determination was reported by Langmuir [128] and was based on the following assumptions:

(i) The surface of a solid consists of a collection of adsorption sites
(ii) Each adsorption site can adsorb only one molecule
(iii) There are no adsorbate-adsorbate interactions, i.e. only monolayer formation

A linear form of data was obtained by plotting relative pressure (P/P_0) against (P/P_0n), where n is the molar uptake in mmol g^{-1}; using the assumptions above and the linear plot, the Langmuir equation can be used to calculate the surface area for microporous solids demonstrating Type I isotherms.

$$\theta = \frac{KP}{1 + KP}$$

Equation 29

Where θ = *fraction of sites covered with adsorbed particles*

P = *partial pressure* (P/P_0)

K = equilibrium constant of adsorption

If V_m is the amount of gas adsorbed by the material forming the monolayer (i.e. when θ = 1) then the fraction of sites covered at equilibrium, θ, is equal to V/V_m, where V = volume of adsorbate adsorbed at equilibrium. Thus Equation 29 can be expressed linearly as shown in Equation 30 to Equation 34.

$$\theta = \frac{KP}{1+KP} = \frac{V}{V_m}$$

Equation 30

$$V_m KP = V + VKP$$

Equation 31

$$P = \frac{VKP}{KV_m} + \frac{V}{KV_m}$$

Equation 32

$$P = V\left(\frac{1}{V_m K} + \frac{P}{V_m}\right)$$

Equation 33

$$\frac{P}{V} = \frac{1}{KV_m} + \frac{P}{V_m}$$

Equation 34

Hence, a plot of P/V against P will have a gradient of $1/V_m$ and the specific surface area can be calculated using Equation 35.

$$S = \frac{V_m A_m L}{m}$$

Equation 35

Where *S = specific surface area ($m^2 g^{-1}$)*

A_m = average area occupied by one molecule during monolayer coverage (m^2)

L = Avogadro's constant = 6.022 x 10^{23} mol^{-1}

m = mass (g)

V_m= Amount absorbed at monolayer formation (mol)

The theory proposed by Langmuir was then extended in 1938 by Brunauer, Emmett and Teller (BET), to include the formation of multilayers. The BET method extends on the assumptions made by Langmuir, but it also assumes that multilayer formation is limitless and that the Langmuir theory can be applied to each layer.

This method has now become the most widely used for the determination of specific surface area. The BET equation is given in Equation 36:

$$\frac{P}{V\ (P_0 - \ P)} = \frac{1}{V_m C} + \frac{(C-1)P}{P_0 V_m C}$$

Equation 36

Where *P = equilibrium pressure (mmHg)*

V = amount adsorbed at P (mol)

V_m = amount absorbed at monolayer formation (mol)

C = constant related to adsorption system

P_0 = saturation vapour pressure (mmHg)

Thus, a plot of $P/V(P_0-P)$ against P/P_0 yields a linear form. The slope ($C-1/V_mC$) and the intercept ($1/V_mC$) are then used to determine V_m and C and, using Equation 35, the specific surface area can be calculated [129].

(e) Adsorption in mesoporous materials

Mesopore analysis – Barrett Joyner Halenda (BJH) model

In the BJH model both the adsorption and desorption branch of the isotherm can be used to determine pore volume and area distributions. However, all calculations are centred round a desorption model, thus the adsorption branch must be arranged in reverse order. This then allows a relationship between the amount of nitrogen lost, at each pressure step, and the average pore size emptied at this pressure to be established.

The condensed liquid N_2 in the pores is known as the core and different sized pores will have varied core sizes. There is a critical pressure, which is dependent on core radius and, when this pressure is reached, the entirety of the core desorbs. After desorption of the core, a layer of N_2 remains in the pore, and as P/P_0 decreases the layer becomes thinner. Thus at each pressure step the quantity desorbed is equal to the quantity due to desorbed cores plus the quantity desorbed from pore walls when the cores have already been desorbed.

The first relative pressure, Pr_1, is assumed to be very close to 1, at which all the pores are filled. The core radius, Rc_1, at this pressure, can then be determined from the Kelvin Equation:

$$Rc_I = \frac{-A}{(1+F)[ln(Pr_1)]}$$

Equation 37

Where *A = adsorbate property*

F = fraction of pores open at both ends

The thickness, T_{w1}, of the remaining nitrogen layer at a relative pressure close to unity is calculated using Equation 38:

$$Tw_1 = HP_1 \left[\frac{HP_2}{ln(Pr_1)}\right]^{HP_3}$$

Equation 38

Where HP_1, HP_2 and HP_3 = Halsey parameters 1, 2 & 3 respectively (which, in this study, are given in the analysis report from the Micromeritics ASAP 2420).

The BJH model focuses on carrying out a number of calculations at each pressure interval (where I refers to each pressure step i.e., I = 1, I+1 = 2, I+2 = 3 I+3 = 4…., J refers to each previous interval during which new pores were opened and K refers to the total number of intervals in which new pores were opened). These calculations include determining the following:

- Thickness of adsorbed layer at the end of the interval
- Change in thickness of the adsorbed layer due to desorption from pores, which have previously lost their core
- Annular cross sectional area of the desorbed wall layer
- Total volume of gas desorbed (Vd_I) from open pores, which is related to the length of previously opened pores, LP_J

If the volume desorbed from previously opened pores is greater than the current incremental value (V_I-V_{I+1}), desorption occurs from walls only, which allows calculation of the surface of exposed walls. If the volume desorbed from previously opened pores is less than V_I-V_{I+1} the difference is caused by core evaporation (number of intervals, K, with new pores open increases by 1) and the volume desorbed from cores can be calculated using Equation 39:

$$Vc_I = [V_I - V_{I+1}] - V_d$$

Equation 39

Where Vc_I = *volume desorbed from newly open pores*

This allows determination of a radius, Rc_{K+1}, for the last pores to be opened in this interval and all the pores opened can be expressed by an average pore diameter, D_{avK}, and length, LP_K, which accounts for the amount of N_2 required to fill the pore, at the relative pressure, P_{avgK}. Using the relative pressure allows the thickness of the adsorbed layer, Tw_{avgK}, to be calculated, which, in turn, allows the decrease in thickness, ΔT_d, during the second portion of

desorption, the cross-sectional area, $CSAc_K$, and the length, LP_K, of the newly opened pores, to be determined.

As mentioned previously, during each interval the quantity desorbed is equal to the quantity due to desorbed cores plus the quantity desorbed from pore walls, thus, the pore diameters and radii have to be adjusted for the change in wall thickness.

For new pores that have been opened within this interval the core will be lost at the beginning thus the diameter has to be corrected for the change in thickness of the adsorbed layer during the second part of desorption:

$$Davg_{Knew} = Davg_{Kold} + 2(\Delta T_d)$$

Equation 40

Where $Davg_{Knew}$ = *corrected diameter for pores opened within the interval (nm)*

$Davg_{Kold}$ = *old diameter (nm)*

ΔT_d = *change in thickness of adsorbed layer (nm)*

Pores that were opened during the previous interval, $Davg_{Inew}$, will continue losing N_2 from their walls, thus, the diameter, $Davg_{Iold}$, is corrected by adding the total change in thickness, ΔT_W:

$$Davg_{Inew} = Davg_{Iold} + 2(\Delta T_w)$$

Equation 41

A similar calculation is carried out to determine the corrected radius, Rc_{Jnew}, of the last pores opened within an interval (where Rc_{Jold} is the uncorrected radius), which allows the diameter of the last pores in the range, DP_J, to be determined:

$$Rc_{Jnew} = Rc_{Jold} + \Delta T_w$$

Equation 42

$$DP_J = 2Rc_{Jnew}$$

Equation 43

If no new pores are opened during a pressure step, no radii or average diameters are calculated, thus the tabulated intervals do not always equal the relative pressure intervals, and the calculations begin, for the next pressure step, at the thickness of the adsorbed layer. When new pores are opened all calculations are carried out. This process is repeated for each interval.

Using the calculated average pore diameters, D_{avg}, and the pore lengths, LP, incremental pore volumes, Vp_I, and surface areas, SA_I, are calculated for values within the BJH diameter range.

$$Vp_I(cm^3g^{-1}) = \pi(LP_I)\left[\frac{Davg_I}{2}\right]^2 10^{16}cm^2nm^{-2}$$

Equation 44

$$SA_I(m^2g^{-1}) = \pi(LP_I)(10^{-2}m\,cm^{-1})(Davg_I)10^{-10}m\,nm^{-1}$$

Equation 45

Summation of these incremental values stepwise then allows determination of cumulative pore volumes, VP_{CUM}, and surface areas, SA_{CUM}.

Determination of the change in volume and area with the change in diameter, dV/dD, and dSA/dD, or the logarithmic versions, dV/dlog(V), and dA/dlog(A) plotted against diameter, allows differential plots to be constructed, which illustrates a visual representation of average pore diameter.

The BJH diameter range covers pores within 1.7 nm to 300 nm thus the BJH model gives poor estimations for microporous materials, however, is very useful for mesoporous materials.

(f) Adsorption in microporous materials

Micropore analysis – t-plot method

The t-plot method was introduced by Lippens and Deboer [129, 130] who made the following assumptions:

- The adsorbed layer, of thickness t, behaves as normal liquid N_2, with its proper density at given T
- N_2 molecules pack densely and hexagonally

Using the above assumptions and given that a monolayer has a thickness of 0.35 nm, the quantity adsorbed is converted to a number of layers, n, before converting to layer thickness, t, as follows:

$$n = \frac{V_a}{V_m}$$

Equation 46

$$total\ thickness = n \times 0.35\ nm$$

Equation 47

Where V_m = *monolayer volume*

V_a = volume of nitrogen adsorbed at equilibrium

A BET master curve of P/P_0 against layer thickness is plotted and compared with experimental data by plotting layer thickness ($[13.99/(0.34-\log P/P_0)]^{1/2}$) against quantity adsorbed at different pressures, in the form of a t-plot (example shown in Figure 3-27). The linear range (0.35 - 0.5 nm) lies between monolayer and capillary condensation, thus it does not include micropores as these are filled during monolayer formation and do not contribute to multilayer formation.

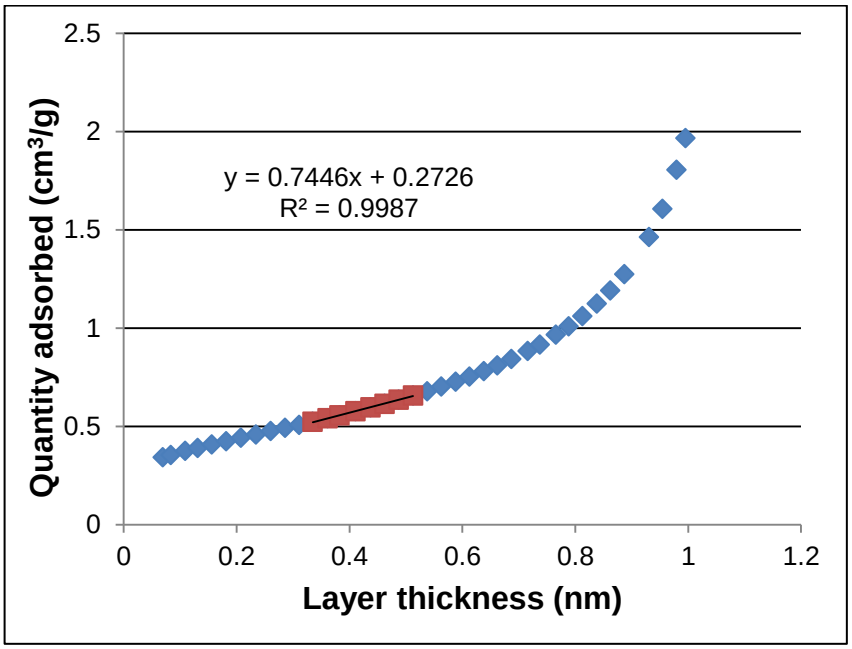

Figure 3-27: Example t-plot.

The linear region is described by Equation 48, and the slope of the t-plot, kS_{ex}, can be approximated as being equal to V_a/t (i.e. the y intercept value, V_{micro}, is negligible). Consequently, the external surface area (meso and macro pores and external surface area), S_{ex}, can be calculated using Equation 49:

$$\boldsymbol{V_a\left(\frac{P}{P_0}\right) = V_{micro} + kS_{ext}t\left(\frac{P}{P_0}\right)}$$

Equation 48

$$S_{ex} = 1.5468 \times \frac{V_a}{t}$$

Equation 49

Where *0.0015468 = density conversion factor (i.e. conversion of gaseous quantity adsorbed to liquid quantity = density of gaseous nitrogen/density of liquid nitrogen = 0.00125 g cm^{-3}/0.8081 g cm^{-3} = 0.0015468). Therefore, V_a converted from cm^3 to m^3 and t converted from nm to m (i.e. 1 cm^3 = 1 x 10^{-}*

^{6} m^3 and 1 nm = 1 x 10^{-9} m) = 0.0015468 x 1 x 10^{-6} m^3/1 x 10^{-9} m = 1.5468 m^2

The micropore surface area, S_{mic}, can then be calculated from Equation 50 and the micropore volume, V_{mic}, can be determined by multiplying the y intercept by the density conversion factor.

$$S_{mic} = S_{TOT} - S_{ex}$$

Equation 50

Where $S_{TOT} = S_{BET}$

The model is only valid within a small pressure range for adsorption after monolayer formation, typically pressures between 0.2 - 0.5 P/P_0, or thicknesses between 0.35 to 0.5 nm, thus it is not suitable for highly microporous materials [131].

Micropore analysis – α_s plot

This model was proposed by Sing [132, 133] and involves comparing an experimental adsorption isotherm with a standard isotherm for a non-porous solid. The amount adsorbed on the reference material, a_{ref}, at each pressure is expressed as a reduced standard adsorption value, α_s (Equation 51). The experimental adsorption isotherm, α_x, is then expressed in terms of α_s, using the corresponding αs value for each given relative pressure and the adsorption of the reference at a relative pressure of 0.4 (Equation 52).

$$\alpha_s = \frac{a_{ref}}{a_{ref}(0.4)}$$

Equation 51

$$\alpha_x = \frac{a_{ref}}{a_{ref}(0.4)}$$

Equation 52

Where s and x refer to relative pressure values and a_{ref} and $a_{ref}(0.4)$ are the amounts adsorbed at equilibrium and at a relative pressure of 0.4, respectively.

Linear regions of the α-plot relate to pressure regions where adsorption is similar for both the sample and the reference material. The slope of these lines can be used to determine a surface area for either the external area or for pores of a certain size, whereas the intercept describes the amount adsorbed in certain pores [133]. The α-plot is considered a more useful method for characterisation of microporous materials as monolayer capacity is not required [131].

Kaneko *et al.* [134] improved on the model of Sing *et al*. by introducing a high resolution α-plot. This model allows calculation of α values for the low pressure region and allows features to be assigned to pore structure [135].

In the region of low relative pressure, linear portions can be defined by setting upper and lower alpha limits, where the lower limit correlates to the relative pressure at which micropores are completely filled and the upper limit is the relative pressure at which capillary condensation begins. The linear region can then be described by Equation 53 [136]:

$$\alpha_x = k_{std}.S_{ex.}\alpha_s + a_{micro}$$

Equation 53

Where S_{ex} = *surface area of meso, macro and external areas*

a_{micro} = *adsorption in saturated micropores*

S_{ref} = *specific surface area of reference material*

$$k_{std} = \frac{a_{ref}(0.4)}{S_{ref}}$$

Equation 54

Thus, from the slope and the y intercept, of the linear region, the external surface area and the volume of micropores, Vmic, can be calculated using Equation 55 and Equation 56, respectively. Equation 50 can then be used to calculate the micropore area. An example alpha plot is illustrated in Figure 3-28.

$$S_{ex} = slope\left[\frac{S_{ref}}{a_{ref}(0.4)}\right]$$

Equation 55

$$V_{mic} = a_{mic} \times 0.0015468$$

Equation 56

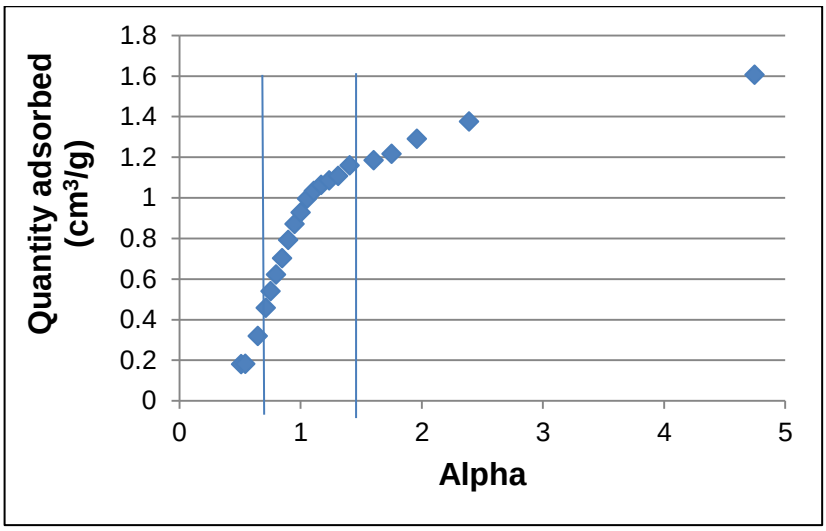

Figure 3-28: Example alpha plot.

Micropore analysis – Horvath Kawazoe model

The original Horvath Kawazoe model is based on a slit pore geometry and involves setting a lower relative pressure limit so that the calculated pore width, L, minus the average diameter of the adsorbate and adsorbent, d_0, never equals zero (i.e. pore is always open)[137], see Figure 3-29. Equation 57 is solved for each equilibrium pressure and a value of L (pore width) is calculated when the equilibrium pressure is within 0.1 % of the collected absolute pressure.

$$ln\frac{P}{P_0} = \frac{K}{RT} \times \frac{IP \times 10^{32} \times \frac{JA^4}{Jcm^4}}{\sigma^4 \times (L - 2 \times d_0)} \times \left[\frac{\sigma^4}{3 \times (L-d_0)^3} - \frac{\sigma^{10}}{9-(L-d_0)^9} - \frac{\sigma^4}{3 \times d_0^3} + \frac{\sigma^{10}}{9 \times d_0^9}\right]$$

Equation 57

Where *K = Avogadro's number*

R = Gas Constant (8.314 x 10^7 ergs/mole K)

T = absolute temperature (K)

σ = gas solid separation at zero interaction energy = Z_s+Z_a/2

Z_s = sample equilibrium diameter at zero interaction energy

Z_a = adsorbate (i.e. N_2) equilibrium diameter at zero interaction energy

d_0 = average diameter of the adsorbate (N_2) and adsorbent (sample) = D_A+D_S/2

D_S = diameter of sample atom ≈ 0.34 nm

D_A = molecular diameter of adsorbate (N_2) = 0.30 nm

*L = distance between molecular centre of 2 opposite pore walls (*Figure 3-29*)*

P = *equilibrium pressure*

P_0 = *saturation pressure*

I_P = *interaction parameter* (10^{-43} *ergs* cm^4)

This allows plots of P/P_0 against pore width, and pore width against pore volume to be constructed and the volume of micropores, V_{mic}, can be calculated from Equation 58.

$$V_{mic} = Quantity\ adsorbed\ at\ highest\ \frac{P}{P_0} \times 0.0015468$$

Equation 58

Calculating the change of pore volume with pore width, dV/dL, allows the data to be presented as a differential pore volume plot, which allows the average pore diameter to be determined.

The Horvath Kawazoe method results in poor pore size estimations for materials with larger micropores (0.8 – 2 nm) [138].

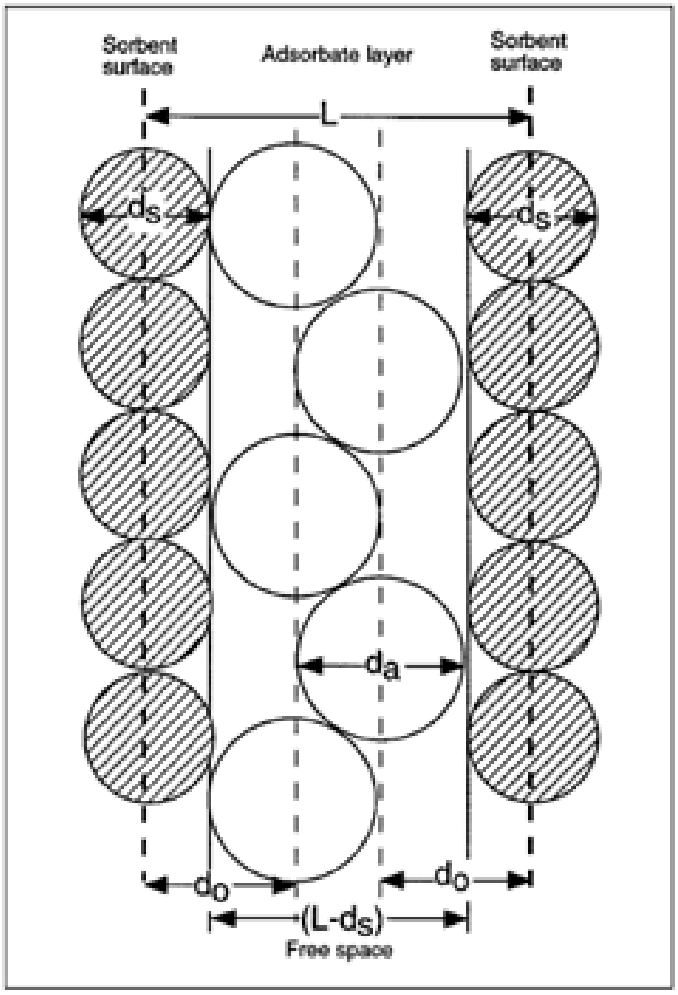

Figure 3-29: Single layer of adsorbate molecules in a slit-shaped pore of width L [138].

(g) Nitrogen adsorption instrumentation

Nitrogen adsorption analysis is carried out in a sealed chamber, which is held under vacuum. The sealed chamber is encased in a Dewar of liquid nitrogen, which allows the temperature to be held at -196K. The chamber is then flushed with a mixture of N_2/He gas and the relative pressure is increased from 0 to 1.0, and subsequently decreased from 1.0 back to 0. At each incremental pressure the amount of gas adsorbed is recorded, allowing an isotherm to be constructed.

3.2.2 Infra-Red (IR) spectroscopy

Almost all organic substances will absorb radiation in the mid infra-red (MIR) region, which covers approximately 4000 cm^{-1} to 400 cm^{-1}. For molecules to absorb IR radiation they must possess a dipole, and the dipole must change during the vibration [139]. The absorption of IR radiation causes the promotion of electrons between vibrational energy levels [140]. When the transition involves promotion from the ground state to vibrational level one (i.e. $\Delta v = 1$) or any other transition where $\Delta v = 1$ the transition is allowed and is known as a fundamental vibration [141]. The resultant spectra contain peaks arising from vibrations of specific functional groups within the molecule, and thus the spectra obtained will give a good indication of the chemical structure of the molecule. The main absorption regions for different chemical groups are shown in Figure 3-30.

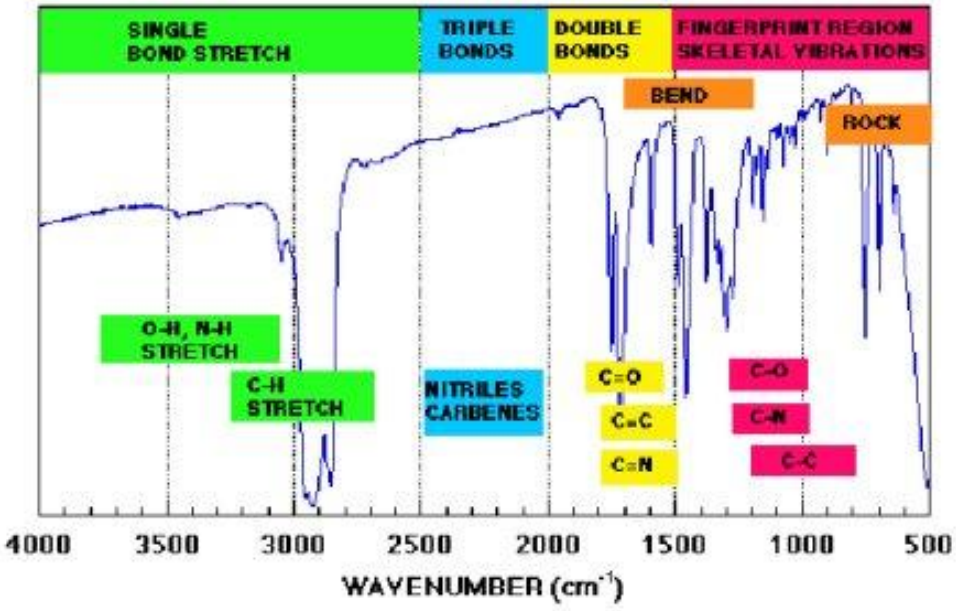

Figure 3-30: MIR absorption regions for different chemical groups [142].

(a) IR instrumentation

In general, structural information is obtained by passing IR radiation through the sample and measuring the amount of incident light transmitted. However, this method requires solid samples to be prepared as a Nujol or ground with a purified salt to create a disc. These sample preparation methods can be difficult and time consuming, consequently, to negate the need for sample preparation an Attenuated Total Reflectance (ATR) crystal will be utilised [113]. This method involves monitoring the changes that occur in a totally internally reflected IR beam. The IR beam is directed towards the ATR crystal, which is in contact with the sample, and the occurring internal reflectance generates an evanescent wave. The evanescence extends into the sample and is attenuated in the regions of the spectrum at which the sample absorbs. The attenuated light passes back to the IR beam and onto to the detector, thus, a spectrum representative of the sample can be obtained [143].

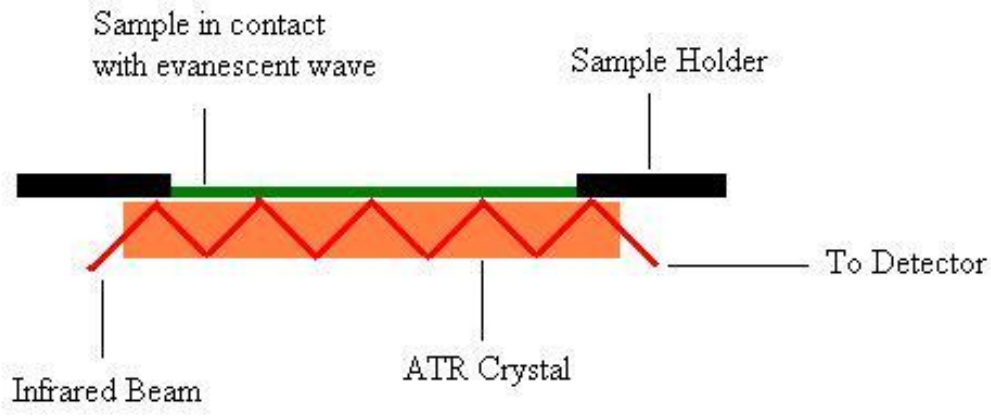

Figure 3-31: ATR IR spectrometer [143].

Detectors utilised in IR spectrometry are generally one of two types, thermal or photon. Thermal detectors measure the heating effect of IR radiation, whereas, photon detectors generate a current/voltage between IR radiation and a semiconducting material.

4 Data analysis

"Far better an approximate answer to the right question, which is often vague, than an exact answer to the wrong question, which can always be made precise".

- *John Tukey*

4.1 Introduction

This chapter introduces the methods and techniques used to analyse experimental data.

4.2 Univariate - linear regression analysis

Regression analysis allows the determination of relationships between '*variables*'. In this study it will mainly be used to determine the relationship between [R] and liquid chromatography peak area. The analysis involves obtaining the peak area for a set of R/W standards and plotting this against R molar concentration. Equation 59, is then used to produce a line of best-fit, allowing the relationship between the two factors to be determined [144].

$$y = mx + c$$

Equation 59

Where y = *LC peak area*

x = *[R]/M*

c = *intercept*

The [R] of an unknown sample can then be determined using the equation of the best-fit line and the associated errors can be determined using the linear regression analysis tool in Excel.

Linear regression analysis will also be used to determine the line of best-fit for F consumption as a function of time in the oven, allowing interpolation of the data [144].

4.3 Repeat measurement statistics

4.3.1 Normal probability distributions

Normal probability distributions can be used to assess whether a data set is normally distributed (i.e. follows a Gaussian distribution). To produce a normal probability distribution the response values (x data) are ordered smallest to largest and each value is

assigned an index variable, i. This index variable is essentially a data point number, i.e. the first response value is labelled i = 1 and the next i = 2, until all responses, where n = number of response values, have been assigned an index variable. Employing Equation 60, the index values and total number of values are used to determine a normal percentile for each response.

$$Normal\ percentile = \frac{\left(i - \frac{3}{8}\right)}{\left(n + \frac{1}{4}\right)}$$

Equation 60

A plot of the response values against the normal percentiles will be a straight line if the data fits a normal distribution (i.e. if approximately 68 % of repeats fall within the mean value ± standard deviation), as illustrated in Figure 4-1.

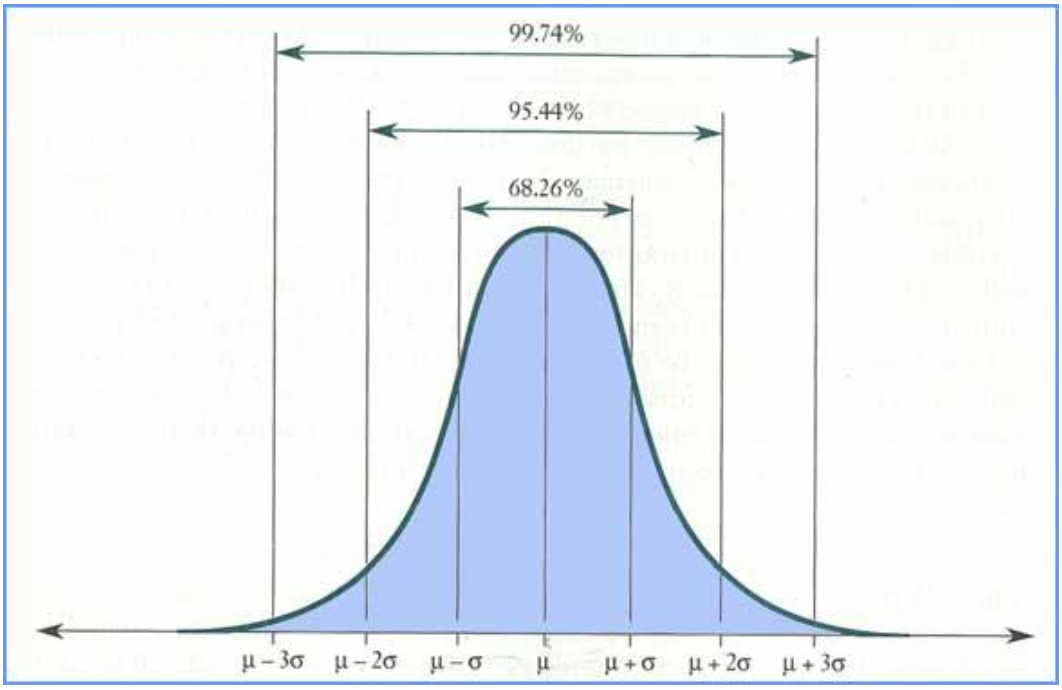

Figure 4-1: Schematic of normal Gaussian distribution.

Where the straight line represents the inverse of the cumulative distribution, which is determined by plotting the response values against a cumulative frequency (i.e. the percentage of values in the original data set that are equal to or less than the response value). Consequently, the closer the data points lie to the line the more normalised the data set is, indicating that results are repeatable [144].

4.4 Analysis of variance (ANOVA)

This technique involves analysing the means of more than two sets of data to determine whether there is significant variance both within and between the data sets. In doing so, the difference between random error and the error due to altering a fixed factor can be separated. Essentially ANOVA determines whether the error between data sets can be attributed to only random error or whether other sources of error exist.

In order to carry out ANOVA the following assumptions are made:

1. *The sample populations are approximately normally distributed.*
2. *The samples must be independent.*
3. *The variances of the populations must be equal.*

ANOVA adopts the null hypothesis that there is no significant difference between the sample means, consequently all samples with have a mean, $\bar{X}_{SET}$, and standard deviation, σ_0^2 [145].

4.4.1 ANOVA calculations

To test the null hypothesis a sum of squares approach is utilised to calculate both the within sample and between sample variance. The calculated values are then and compared and the difference determined statistically. The variation within each data set (i.e. within sample variation), SS_W, is calculated using Equation 61. This value is then divided by the number of degrees of freedom, as shown in Equation 62, to give the mean square value, MS_W, which can be used as an estimate of within sample variance [144].

$$SS_W = \sum (x_i - \bar{x})^2$$

Equation 61

$$MS_W = \frac{SS_W}{dof_w}$$

Equation 62

Where x_i = *measurment*

$\bar{x}$ = *sample mean*

dof_w = *N - K (sum of the dof associated with each dataset)*

N = total number of samples

K = number of datasets

The variation between the samples (i.e. between the groups) can be determined by calculating the between sum of squares, SS_B, (Equation 63), which utilises the overall mean for all measurements, $\overline{X}_{SET}$, which is determined using Equation 64.

$$SS_B = \sum n(\bar{x} - \overline{X}_{SET})^2$$

Equation 63

$$\bar{X}_{SET} = \frac{\sum x}{N}$$

Equation 64

The between sample variance, MS_B, is then calculated in a similar manner to MS_W (Equation 62), however in this case the degrees of freedom are equal to the number of datasets minus 1 (k-1).

In order to test the null hypothesis the two calculations of variance (MS_W and MSB) are then compared in an F test. This involves determining a calculated F value, F_{calc}, as shown in Equation 65.

$$F_{calc} = \frac{MS_B}{MS_W}$$

Equation 65

If the hypothesis is correct the F_{calc} value will be less than a critical F value, F_{crit}, which is determined from statistical F tables (see Chapter 13 Appendix A). In this instance variation can be attributed to random error. However, if $F_{calc} > F_{crit}$ the between sample variance is greater than the within sample variance and the null hypothesis is rejected, and differences in the sample means cannot be attributed to random error.

Table 4-1 summarises the calculations required for one-way ANOVA. In order to check the values obtained for the between and within sample sum of squares the total sum of squares (total variation) can be calculated using the equation given in the table, the calculated value should be equal to the sum of SS_B and SS_W [144].

Table 4-1: ANOVA summary table

Source of variance	SS	dof	MS	F_{calc}
Between sample	$SS_B = \sum n(\bar{x} - \bar{X}_{SET})^2$	*k-1*	$MS_B = \frac{SS_B}{dof_B}$	$F_{calc} = \frac{MS_B}{MS_W}$
Within sample	$SS_W = \sum (x_i - \overline{x})^2$	*N-k*		
Total	$SS_{TOTAL} = \sum (x - \bar{X}_{SET})^2$ Or $SS_{TOTAL} = SS_B + SS_W$	*N-1*		

4.5 pH

In the reaction of R with F, initial sol pH of the starting sol is a very important parameter that is believed to govern the final properties of the gel and carbonised derivatives. The sol pH is affected by the dissociation of H_2O, acid (R) and base (catalyst), therefore to understand the concept fully the dissociation of each needs to be understood [145].

4.5.1 Dissociation of water

In solution water will dissociate slightly, forming protons and hydroxide ions, as illustrated by Equation 66, where the reaction constant for the equilibrium is calculated using Equation 67.

$$H_2O \leftrightarrow H^+ + OH^-$$

Equation 66

$$K_w = \frac{[H^+][OH^-]}{[H_2O]}$$

Equation 67

In dilute solutions it can be assumed that $[H_2O]$ is constant and Equation 67 can be rewritten as Equation 68:

$$K_w = [H^+][OH^-] = 10^{-14}$$

Equation 68

Given that the density of water is 1g/ml there is approximately 1000g of H_2O per litre, and therefore 55.6 mols per litre, allowing the dissociation constant to be calculated using Equation 69:

$$K_w = \frac{10^{-14}}{55.6} = 1.8 \times 10^{-16}$$

Equation 69

Taking the log of both side results in Equation 70, which gives a pK_w value of 15.74 (Equation 71).

$$pk_w = -log_{10}(1.8 \times 10^{-16})$$

Equation 70

$$pk_w = 15.74$$

Equation 71

Where, the pk_w is equal to the sum of the –log of the concentration of H^+ and OH^- ions, as demonstrated by Equation 72 to Equation 74.

$$pk_w = pH + pOH$$

Equation 72

$$pH = -log_{10}[H^+]$$

Equation 73

$$pOH = -log_{10}[OH^-]$$

Equation 74

By calculating either the $[H^+]$ of $[OH^-]$ the pH can then be determined by substituting into Equation 72 [145].

4.5.2 Dissociation of an acid

In the RF system R acts as an acid and dissociates according to Equation 75, forming its conjugate base, R^-, and a proton:

$$HA \leftrightarrow H^+ + A^-$$

Equation 75

The acid dissociation constant, K_a, can then be determined using Equation 76. This constant is often reffered to on a logarithmic scale (Equation 77), where the lower the pK_a value (higher K_a value) the stronger the acid and the greater the extent of dissociation [145].

$$K_a = \frac{[A^-][H^+]}{[HA]}$$

Equation 76

$$pK_a = -log_{10}(K_a)$$

Equation 77

4.5.3 Dissociation of a base

Similar to R, the basic catalyst present in the RF sol will also dissociate, however, this reation forms the comjugate acid (B^+) and a hydroxide anion (Equation 78), for example when Na_2CO_3 is used it dissociates forming $NaHCO_3$ (B+) and Na^+OH^-.

$$BOH \leftrightarrow OH^- + B^+$$

Equation 78

Again, the dissociation constant, K_b, can be calculated by dividing the product of the concentration of compounds formed, by the concentration of reactant (Equation 79). The strength of the base is represented by its pK_b value (Equation 80), where a lower pk_b (higher K_b) value is indicative of a stronger base [145].

$$K_b = \frac{[B^+][OH^-]}{[BOH]}$$

Equation 79

$$pK_b = -log_{10}(K_b)$$

Equation 80

4.5.4 Polyprotic constants

From the acid and base dissociations given in Sections 4.5.2 and 4.5.3 respectively, it follows that, polyprotic acids/bases (e.g. Na_2CO_3) will have dissociation constants for each dissociation step (K_{b1}, K_{b2}) and an overall dissociation constant ($K_{b1,2}$), which is the product of the individual dissociation constants:

$$K_{b1,2} = K_{b1}K_{b2}$$

Equation 81

With polyprotic substances the idea of conjugate acids/bases becomes more difficult to comprehend. For example if polyprotic base, Na_2CO_3, is considered, this will dissociate as follows:

$$Na_2CO_3 + H_2O \overset{K_{b1}}{\longleftrightarrow} NaHCO_3 + NaOH^-$$

Equation 82

$$K_{b1} = \frac{[NaHCO_3][NaOH^-]}{[Na_2CO_3]}$$

Equation 83

$$NaHCO_3 + H_2O \overset{K_{b2}}{\longleftrightarrow} H_2CO_3 + NaOH^-$$

Equation 84

$$K_{b2} = \frac{[H_2CO_3][NaOH^-]}{[NaHCO_3]}$$

Equation 85

With polyprotic substances the conjugate products can act as either acid or a base. For example consider the $NaHCO_3$ formed in Equation 82, this can either receive a proton, acting as an acid (Equation 84), or lose a proton, acting like a base (Equation 86).

$$NaHCO_3 + H_2O \overset{K_{a1}}{\longleftrightarrow} Na_2CO_3 + H_3O^+$$

Equation 86

Consequently, the first base dissociation step, k_{b1}, creates the conjugate acid ($NaHCO_3$) for the second acid dissociation (K_{a2}), as illustrated by Equation 87.

$$H^{-}CO_3 + H_2O \overset{K_{a2}}{\leftrightarrow} {CO_3}^{2-} + H^{+}$$

Equation 87

Thus, for a substance with 2 protons the Ka and Kb values are related according to Equation 88 Equation 89 [145].

$$pk_{a1} + pk_{b2} = pk_w$$

Equation 88

$$pk_{a2} + pk_{b1} = pk_w$$

Equation 89

4.5.5 Bronsted & Lowry

RF polymerisation occurs in an aqueous medium, therefore the effect of water dissociation on the acid (R) and base (C) must be considered.

As discussed in Section 4.5.3, a base dissociates forming B^+ and OH^-, however, in aqueous solutions OH^- are already present from water dissociation (Section 4.5.1) and will react with B^+, forming BOH, and lowering the OH^- concentration. This reduction in $[OH^-]$ causes H_2O to dissociate further, resulting in a final solution containing some BOH and an excess of H^+. The excess H^+ results in the overall solution being acidic in nature, which is surprising given that the solution contains only a base and water.

To explain this phenomenon Bronsted and Lowry proposed the following definitions:

1) *An acid is a substance that can donate a proton*
2) *A base is a substance that can accept a proton*

Consequently, in the base/water solution discussed above, upon dissociation, the base becomes a Bronsted and Lowry acid (i.e. a proton acceptor), which, is often referred to as conjugate acid of the base.

The conjugate acid, B^+, reacts with water according to Equation 90:

$$B^+ + H_2O \rightarrow H^+ + BOH^-$$

Equation 90

Where the dissociation constant can be determined using Equation 91 (where the $[H_2O]$ is assumed to be constant).

$$K_a = \frac{[H^+][BOH^-]}{[B^+]}$$

Equation 91

Multiplying the base dissociation constant (Equation 79), with the dissociation constant of the conjugate acid (Equation 91) results in Equation 92:

$$K_b K_a = \frac{[B^+][OH^-]}{[BOH]} \frac{[H^+][BOH^-]}{[B^+]} = [H^+][OH^-] = K_w$$

Equation 92

The theory proposed by Bronsted and Lowry therefore demonstrates that either acid or base dissociation constants can be used to describe acid/base properties of substances in water [145].

4.5.6 Calculating pH of acid or base solution

To determine the pH of an acidic solution the dissociation of both the acid and water needs to be combined. Considering the dissociation of H_2O, Equation 68 demonstrates that, at equilibrium, the products of the concentrations of hydroygen and hydroxide ions were equal to 10^{-14}. In a neutral aqueous solution the charges must balance and the system can be described using Equation 93:

$$[H^+] = [OH^-] + [A^-]$$

Equation 93

The concentration of acid added, C_a, to the solution will be known, and due to mass balance the concentration of all acid forms present will equal the initial concentration.

$$[A^-] + [HA] = C_a$$

Equation 94

Combining Equation 68 and Equation 93 results in Equation 95:

$$[H^+] - \frac{K_w}{[H^+]} - [A^-] = 0$$

Equation 95

Rearranging Equation 94, results in $[HA] = C_a - [A^-]$, which can be substituted into Equation 76:

$$K_a = \frac{[A^-][H^+]}{C_a - [A^-]}$$

Equation 96

This can then be solved for $[A^-]$, according to Equation 97 to Equation 100:

$$K_a C_a - K_a[A^-] = [H^+][A^-]$$

Equation 97

$$[H^+][A^-] + K_a[A^-] = K_a C_a$$

Equation 98

$$[A^-]([H^+] + K_a) = K_a C_a$$

Equation 99

$$[A^-] = \frac{K_a C_a}{([H^+] + K_a)}$$

Equation 100

[A^-] can then be substituted into Equation 95 and expanded to give Equation 102.

$$[H^+] - \frac{K_w}{[H^+]} - \frac{K_a C_a}{([H^+] + K_a)} = 0$$

Equation 101

$$[H^+]^3 + K_a[H^+]^2 - (C_a K_a + K_w)[H^+] - K_a K_w = 0$$

Equation 102

Using both the concentration of acid (C_a) and the acid dissociation constant (K_a) Equation 102 can be used to determine [H+], which can then be substituted into Equation 73, allowing determination of the solution pH.

A similar method can be used to determine the pH of basic solutions, where Equation 103, can be used to determine the [OH^-], which is substituted into Equation 74 determining the pH.

$$[OH^-]^3 + K_b[OH^-]^2 - (C_b K_b + K_w)[OH^-] - K_b K_w = 0$$

Equation 103

Equation 102 and Equation 103 are third degree equations and therefore are very difficult to solve by hand, consequently they can either be solved using Newton's numerical method or the determination can be simplified [145].

(a) Strong acids and bases

For strong acids and bases, 100 % dissociation is assumed to occur; consequently, for acid dissociation, the concentration of acid added is equal to the concentration of the conjugate base formed (Equation 104):

$$[A^-] = C_a$$

Equation 104

Equation 104 can then be substituted into the charge balance equation (Equation 105):

$$[H^+] = [OH^-] + [A^-] = [OH^-] + C_a$$

Equation 105

This equation can be rearranged further by replacing $[OH^-]$ with $K_w/[H^+]$:

$$[H^+] - \frac{K_w}{[H^+]} - C_a = 0$$

$$[H^+]^2 - C_a[H^+] - K_w = 0$$

Equation 106

This second order equation can also be formed for strong bases by replacing, $[H^+]$ and C_a with $[OH^-]$ and C_b, respectively, and is much easier to solve, allowing pH to be easily determined [145].

(b) Weak acid and bases

If the acid/base is not very dilute and not too weak the dissociation of water is negligible and can be ignored, consequently Equation 93 can be rewritten as Equation 107:

$$[H^+] = [A^-]$$

Equation 107

This can then be used to redetermine Equation 76 (Equation 108), which can be rearranged further by substituting for [HA], using Equation 94, to give Equation 109 and the rearranged Equation 110 [145].

$$K_a = \frac{[H^+]^2}{[HA]}$$

Equation 108

$$K_a = \frac{[H^+]^2}{C_a - [H^+]}$$

Equation 109

$$[H^+]^2 + K_a[H^+] - K_aC_a = 0$$

Equation 110

4.5.7 Acid base reaction

4.5.8 Bate pH equation [145]

In order to calculate the pH of an aqueous RF sol the following equations have to be considered:

- R dissociation
- R mass balance (acid mass balance)
- C dissociation (base dissociation)
- C mass balance (base mass balance)
- Electroneutrality
- Water ionisation constant

The above equations are combined to give what is known as the BATE pH equation (Equation 111), which can be used to estimate the pH of an aqueous solution containing R and various different catalysts. It should be noted that this will only give an estimate of the initial sol pH as it does not take into account the F present.

$$\frac{C_a \sum_{i=1}^{n} i\, K_{ai}[H]^{n-i}}{[H]^n + \sum_{i=1}^{n} K_{ai}\,[H]^{n-i}} + \frac{K_w}{[H]} = \frac{C_b \sum_{i=1}^{m} i\, K_{bi}[H]^i K_w^{m-i}}{K_w^m \sum_{i=1}^{m} [H]^i K_{bi} K_w^{m-i}} + [H]$$

Equation 111

Where *m = number of base dissociation steps*
n = number of acid dissociation steps
K_a = acid dissociation constant
K_b = base dissociation constant
K_w = water dissociation constant
C_a = concentration of acid added
C_b = concentration of base added

(a) Derivation

In both aqueous and basic solutions R will initially dissociate following the reaction shown in Equation 112. The deionised product will then further dissociate as illustrated in Equation 113. The reaction constants for these reactions are described by Equation 114 and Equation 115 respectively.

$$C_6H_6O_2 + H_2O \xrightarrow{pk_{a1}} C_6H_5O_2^{-} + 2H^+ + OH^-$$

Equation 112

$$C_6H_5O_2^{-} + H_2O \xrightarrow{pk_{a2}} C_6H_4O_2^{2-} + 2H^+ + OH^-$$

Equation 113

$$K_{a1} = \frac{[C_6H_5O_2^{-}][H^+]}{[C_6H_6O_2]}$$

$$[C_6H_5O_2^{-}] = \frac{[C_6H_6O_2]K_{a1}}{[H^+]}$$

Equation 114

$$K_{a2} = \frac{[C_6H_4O_2^{2-}][H^+]}{[C_6H_5O_2^{-}]}$$

$$\left[{C_6H_4O_2}^{2-}\right] = \frac{[C_6H_5O_2{}^-]\,K_{a2}}{[H^+]}$$

Equation 115

Equation 115 can then be rewritten by substituting for $[C_6H_5O_2^-]$, as shown in Equation 116:

$$\left[{C_6H_4O_2}^{2-}\right] = \frac{[C_6H_6O_2]K_{a1}K_{a2}}{[H^+]^2}$$

Equation 116

Considering the dissociation reactions discussed the total concentration of acid, C_a, must be equal to the sum of R concentration and its dissociated forms. This relationship is shown in Equation 117.

$$C_a = [C_6H_6O_2] + [C_6H_5O_2{}^-] + \left[{C_6H_4O_2}^{2-}\right]$$

Equation 117

Using the dissociation constants the mass balance can then be re-established as shown in Equation 118.

$$C_a = [C_6H_6O_2] + \frac{[C_6H_6O_2]K_{a1}}{[H^+]} + \frac{[C_6H_6O_2]K_{a1}K_{a2}}{[H^+]^2}$$

$$C_a = \frac{[C_6H_6O_2]}{[H^+]^2}[H^+]^2 + K_{a1}[H^+] + K_{a1}K_{a2}$$

$$\frac{[C_6H_60_2]}{[H^+]^2} = \frac{C_a}{[H^+]^2 + K_{a1}[H^+] + K_{a1}K_{a2}}$$

Equation 118

Like R, Na_2CO_3 is capable of dissociating twice, as shown in Equation 119 and Equation 120:

$$Na_2CO_3 + H_2O \xrightarrow{pk_{b1}} NaHCO_3 + NaOH$$

Equation 119

$$NaHCO_3 + H_2O \xrightarrow{pk_{b2}} H_2CO_3 + NaOH$$

Equation 120

The reaction constants for the first and second dissociation steps, for Na_2CO_3, are described by Equation 121 and Equation 122 respectively.

$$K_{b1} = \frac{[NaHCO_3][OH^-]}{[Na_2CO_3]}$$

$$[NaHCO_3] = \frac{[Na_2CO_3]K_{b1}}{[OH^-]}$$

Equation 121

$$K_{b2} = \frac{[H_2CO_3][OH^-]}{[NaHCO_3{}^-]}$$

$$[H_2CO_3] = \frac{[NaHCO_3]\,K_{b2}}{[OH^-]}$$

Equation 122

Equation 122 can then be rewritten by substituting for [$NaHCO_3$], as shown in Equation 123:

$$[H_2CO_3] = \frac{[Na_2CO_3]K_{b1}K_{b2}}{[OH^-]^2}$$

Equation 123

In order to ensure that the only unknown, for the overall pH calculation, is [H^+] the [OH^-] term is replaced using the ionisation constant (Equation 124).

$$K_w = [H^+][OH^-]$$

$$[OH^-] = \frac{K_w}{[H^+]}$$

Equation 124

Consequently, Equation 121 and Equation 123 can be rewritten as Equation 125 and Equation 126 respectively.

$$[NaHCO_3] = \frac{[Na_2CO_3]K_{b1}[H^+]}{[K_w]}$$

Equation 125

$$[H_2CO_3] = \frac{[Na_2CO_3]K_{b1}K_{b2}[H^+]^2}{[K_w]^2}$$

Equation 126

The total concentration of catalyst, C_b, will be equal to the sum of the remaining Na_2CO_3 concentration and the concentrations of its dissociated forms. This relationship and its subsequent reorganisation (substitution for [$NaHCO_3$] and [H_2CO_3]) are shown in Equation 127:

$$C_b = [Na_2CO_3] + [NaHCO_3] + [H_2CO_3]$$

$$C_b = [Na_2CO_3] + \frac{[Na_2CO_3]K_{b1}[H^+]}{[K_w]} + \frac{[Na_2CO_3]K_{b1}K_{b2}[H^+]^2}{[K_w]^2}$$

$$\frac{[Na_2CO_3]}{[K_w]^2} = \frac{C_b}{K_{b1}[H^+]K_w + K_{b1}K_{b2}[H^+]^2}$$

Equation 127

The individual dissociations and their associated charge balances, for the reaction between R and Na_2CO_3, are given in Equation 128 and Equation 129:

$$C_6H_6O_2 + Na_2CO_3 \rightarrow C_6H_5O_2{}^- + Na^+ + NaHCO_3$$
$$[Na^+]_1 = [C_6H_5O_2{}^-]$$

Equation 128

$$C_6H_5O_2{}^- + NaHCO_3 \rightarrow C_6H_4O_2{}^{2-} + Na^+ + H_2CO_3$$
$$[Na^+]_2 = [C_6H_4O_2{}^{2-}]$$

Equation 129

The overall charge balance, including the dissociation of H_2O, can then be written as Equation 130.

$$[C_6H_5O_2{}^-] + 2[C_6H_4O_2{}^{2-}] + [OH^-] = [Na^+]_1 + [Na^+]_2 + [H^+]$$
$$[C_6H_5O_2{}^-] + 2[C_6H_4O_2{}^{2-}] + [OH^-] = [NaHCO_3] + [H_2CO_3] + [H^+]$$

Equation 130

Subsequent substitution for $[C_6H_5O_2^-]$ (Equation 114), $[C_6H_4O_2^{2-}]$ (Equation 116), $[OH^-]$ (Equation 124), $[NaHCO_3]$ (Equation 125) and $[H_2CO_3]$ (Equation 126) and removal of a common factor, on each side, gives rise to Equation 131:

$$\frac{[C_6H_6O_2]K_{a1}}{[H^+]} + 2\frac{[C_6H_6O_2]K_{a1}K_{a2}}{[H^+]^2} + \frac{K_w}{[H^+]} = \frac{[Na_2CO_3]K_{b1}[H^+]}{[K_w]} + \frac{[Na_2CO_3]K_{b1}K_{b2}[H^+]^2}{[K_w]^2} + [H^+]$$

$$\frac{[C_6H_6O_2]}{[H^+]^2}(K_{a1}[H^+] + 2K_{a1}K_{a2}) + \frac{K_w}{[H^+]} = \frac{[Na_2CO_3]}{[K_w]^2}(K_{b1}[H^+]K_w + K_{b1}K_{b2}[H^+]^2) + [H^+]$$

Equation 131

The mass balance equations of both R and Na_2CO_3 (Equation 118 and Equation 127) can then be used to reorganise Equation 131, resulting in the BATE equation, as shown in Equation 132.

$$\frac{C_a(K_{a1}[H^+] + 2K_{a1}K_{a2})}{[H^+]^2 + K_{a1}[H^+] + K_{a1}K_{a2}} + \frac{K_w}{[H^+]} = \frac{C_bK_wK_{b1}[H^+] + K_{b1}K_{b2}[H^+]^2}{K_{b1}[H^+]K_w + K_{b1}K_{b2}[H^+]^2} + [H^+]$$

Equation 132

Equation 132 describes the BATE pH equation for the reaction between an acid and base, with both having two dissociation steps, whereas Equation 111 shows the generic BATE

equation, which can be applied to variety of acids and bases with varying degrees of dissociation.

5 Methodology

"The purpose of an experiment is to answer questions. The truth of this seems so obvious, that it would not be worth emphasising were it not for the fact that the results of many experiments are interpreted and presented with little or no reference to the questions that were asked in the first place."

- *Little 1981*

5.1 Organic gel preparation

5.1.1 Hydrogel preparation

To prepare RF hydrogels all variables, with the exception of R/C ratio, were kept constant. The solid content (R + F + C) was kept constant at 20 % wt/vol, where the volume was set at approximately 60 ml (based on the actual weight of solids) and the R/F ratio was fixed at 0.5. The gels prepared in this study were labelled as X_R/C_Y, where X = catalyst, R/C = resorcinol/catalyst molar ratio and Y denotes whether the gel was dried Y=D, dried and pyrolysed Y=DP, for example a gel prepared with Na_2CO_3 with R/C ratio of 300, which had been dried and pyrolysed would be named Na_2CO_3_300_DP.

(a) Composition

Resorcinol was obtained in a plate like solid form which made it difficult to measure accurately. To ensure that all gel compositions were comparable the weight of R was measured as close to the calculated weight as possible, all other weights and volumes were then measured based on the actual weight of R used. For example, Table 5-1 indicates the calculated weight of reactants required for Na_2CO_3_300 gel. Using these calculated values R was then weighed as close as possible to 7.7490 g.

Table 5-1: Calculated weight of reactants for Na_2CO_3_300

Reactant	Equiv. Mols	Equiv. molar wt (g)	Percentage solid (%)	Calculated wt. (g)
R	1	110.110000	64.5747	7.7490
F	2	60.052400	35.2181	4.2262
C	0.00333333	0.353328	0.2072	0.02487
TOTALS		**170.515728**	**100.0000**	**12.0000**

The actual weight of R was then used to determine the weight of F required, as detailed in Equation 133:

$$Weight\ F\ (g) = \frac{\%\ F_{Table\ 1} \times Act.wt.R\ (g)}{\%\ R_{Table\ 1}}$$

Equation 133

Using the density of formalin (1.09 g/ml), which contains 37 wt % F, the volume of formalin required was calculated using:

$$1ml\ formalin = 1.09\ g\ Formalin = 37\ \%\ x\ 1.09\ g = 0.4033\ g\ F$$

$$Vol.of\ formalin\ required\ (ml) = \frac{Wt.F\ (g)}{0.4033\ g}$$

Equation 134

The weight of C was then calculated in a similar manner to the weight of F, see Equation 135.

$$Wt.C = \frac{\%\ C_{Table\ 1} \times Act.Wt.R}{\%\ R_{Table\ 1}}$$

Equation 135

The formalin solution contains both water and methanol, to determine the total volume of deionised water required (i.e. to make the total volume (H_2O + methanol) up to approximately 60 ml) the actual weight of F in the formalin solution added was first calculated (Equation 136), which using the density of F (0.815 g/ml) then allowed the volume due to F to be calculated (Equation 137):

$$1\ ml\ formalin = 0.4033\ g\ F$$

$$Actual\ wt.of\ F\ (g) = Vol.formalin\ (ml)\ \times 0.4033\ g$$

Equation 136

$$Vol.of\ formalin\ from\ F\ (ml) = \frac{Wt.F}{0.815}$$

Equation 137

Therefore, the volumes of solvents from formalin were determined using Equation 138:

$$Vol.MeOH\ \&\ H_2O\ (ml) = Total\ Vol.formalin\ (ml) - Vol.due\ to\ F\ (ml)$$

Equation 138

By Subtraction the volume of deionised water required was then calculated:

$$Vol.H_2O\ (ml) = Total\ Vol. - Vol.formalin\ due\ to\ MeOH\ and\ H_2O$$

Equation 139

Where the total volume of solution is determined based on the total solids (i.e. 5 g solids at 20 % would be 60 ml, 5.1 g solids would require a solution volume of 61.2 ml):

$$Total\ Vol. = Total\ solids_{(Act.R+F+C)} \times 5$$

Equation 140

This process was repeated for all hydrogels prepared, Table 5-1 gives the reactant weights for all hydrogels prepared.

(b) Preparation

Using the calculations set out above, the appropriate weight of R (Sigma Aldrich Reagent plus 99 %) was first added to approximately 54 ml of deionised water and stirred until all of the R was dissolved. The appropriate amount of catalyst (see Table 5-2) was then added with continuous stirring. After dissolution of all solids the appropriate volume of formalin (Sigma Aldrich Formaldehyde solution, 37 wt. % in H_2O, and containing 10-15 % methanol as stabiliser) was added. The sol was then sealed and stirred for 30 minutes before the initial pH was measured.

Table 5-2: List of catalysts used for gel preparation

Catalyst name	Chemical Formula	Product description
Sodium carbonate	Na_2CO_3	Sigma Aldrich (ACS anhydrous)
Sodium bicarbonate	$NaHCO_3$	VWR (granular)
Potassium bicarbonate	KHCO3	Sigma Aldrich (granular 99.7 % A.C.S
Potassium hydroxide	KOH	Sigma Aldrich (45 wt % solution in H_2O)
Sodium hydroxide	NaOH	Sigma Aldrich (50 % solution in H_2O)
Caesium carbonate	Cs_2CO_3	Sigma Aldrich (Reagent plus, 99 %)
Caesium bicarbonate	$CsHCO_3$	Alfa Aesar (99.99% metals basis crystalline aggregates
Ammonium carbonate	$(NH_4)_2CO_3$	Sigma Aldrich (≥ 30 % NH_3)
Magnesium hydroxide	$Mg(OH)_2$	Sigma Aldrich (Reagent grade, 95 %)
Calcium carbonate	$CaCO_3$	Sigma-Aldrich (≥99 %).
Strontium carbonate	$SrCO_3$	Aldrich (98 %)
Barium carbonate	$BaCO_3$	Sigma Aldrich (ACS reagent > 99 %)
Magnesium nitrate	$Mg(NO_3)_2.6H_2O$	Sigma Aldrich (ACS reagent, 99 %)

Table 5-3 - Part 1: Gels prepared using Group I catalysts

Gel	Equiv. Mols R:F:C	Calculated wt. R (g)	Calculated wt. F (g)	Calculated wt. C (g)
Na_2CO_3_50	1:2:0.02	7.6695	4.1828	0.14766
Na_2CO_3_100	1:2:0.01	7.6958	4.2301	0.0741
Na_2CO_3_200	1:2:0.005	7.7570	4.2306	0.01244
Na_2CO_3_300	1:2:0.00333	7.7490	4.2262	0.02487

Na_2CO_3_400	1:2:0.0025	7.7530	4.2284	0.01866
Na_2CO_3_450	1:2:0.00222	7.7543	4.2291	0.01659
Na_2CO_3_500	1:2:0.002	7.7554	4.2297	0.01493
Na_2CO_3_600	1:2:0.001667	7.7570	4.2306	0.01245
Na_2CO_3_700	1:2:0.001429	7.7581	4.2312	0.01067
Na_2CO_3_750	1:2:0.001333	7.7586	4.2314	0.00996
Na_2CO_3_800	1:2:0.00125	7.7590	4.2317	0.00934
Na_2CO_3_900	1:2:0.001111	7.7597	4.2320	0.00830
$NaHCO_3$_50	1:2:0.02	7.76891	4.1935	0.1173
$NaHCO_3$_75	1:2:0.01333	7.7143	4.2073	0.0785
$NaHCO_3$_100	1:2:0.01	7.7269	4.2141	0.0590
$NaHCO_3$_200	1:2:0.005	7.7459	4.2245	0.02955
$NaHCO_3$_300	1:2:0.00333	7.7523	4.2280	0.01972
$NaHCO_3$_400	1:2:0.0025	7.7555	4.2297	0.01479
K_2CO_3_100	1:2:0.01	7.7025	4.2008	0.09668
K_2CO_3_200	1:2:0.005	7.7336	4.2178	0.04858
K_2CO_3_300	1:2:0.00333	7.7441	4.2235	0.03240
K_2CO_3_400	1:2:0.0025	7.7493	4.2264	0.02132
K_2CO_3_500	1:2:0.002	7.7525	4.2281	0.01946
$KHCO_3$_100	1:2:0.01	7.7196	4.2102	0.0702
$KHCO_3$_200	1:2:0.005	7.7423	4.2225	0.03520
$KHCO_3$_300	1:2:0.00333	7.7499	4.2267	0.02349
$KHCO_3$_400	1:2:0.0025	7.7536	4.2287	0.01762
NaOH_100	1:2:0.01	7.7468	4.2250	0.02814
NaOH_200	1:2:0.005	7.7345	4.2514	0.01405
NaOH_300	1:2:0.00333	7.7375	4.2531	0.00937
NaOH_400	1:2:0.0025	7.7391	4.2539	0.00703
KOH_100	1:2:0.01	7.7395	4.2210	0.03944
KOH_200	1:2:0.005	7.7523	4.2280	0.01975
KOH_300	1:2:0.00333	7.7565	4.2303	0.01317
KOH_400	1:2:0.0025	7.7587	4.2315	0.00988
Cs_2CO_3_100	1:2:0.01	7.6192	4.1554	0.22545
Cs_2CO_3_200	1:2:0.005	7.6914	4.1948	0.1130
Cs_2CO_3_300	1:2:0.00333	7.7158	4.2081	0.07610
Cs_2CO_3_400	1:2:0.0025	7.7281	4.2148	0.05717
Cs_2CO_3_500	1:2:0.002	7.7354	4.2188	0.04578
$CsHCO_3$_50	1:2:0.02	7.5920	4.1406	0.26742
$CsHCO_3$_100	1:2:0.01	7.6776	4.1872	0.13521
$CsHCO_3$_200	1:2:0.005	7.7211	4.2110	0.06799
$CsHCO_3$_300	1:2:0.00333	7.7357	4.2189	0.04541

Table 5-4 - Part 2: Gels prepared using Group II metal catalysts

Gel	Equiv. Mols R:F:C	Calculated wt. R (G)	Calculated wt. F (g)	Calculated wt. C (g)
$Mg(OH)_2$_100	1:2:0.01	7.7385	4.2205	0.04099
$Mg(OH)_2$_300	1:2:0.00333	7.7562	4.2301	0.01369
$Mg(OH)_2$_500	1:2:0.002	7.7597	4.2320	0.00822
$CaCO_3$_100	1:2:0.01	7.7196	4.2102	0.07017
$CaCO_3$_200	1:2:0.005	7.7423	4.2225	0.03519
$CaCO_3$_300	1:2:0.00333	7.7499	4.2267	0.02348
$CaCO_3$_400	1:2:0.0025	7.7537	4.2287	0.01762
$CaCO_3$_500	1:2:0.002	7.7559	4.2300	0.01410

$SrCO_3$_100	1:2:0.01	7.6983	4.1985	0.10321
$SrCO_3$_200	1:2:0.005	7.7315	4..2167	0.0518
$SrCO_3$_300	1:2:0.00333	7.7427	4.2227	0.0346
$SrCO_3$_400	1:2:0.0025	7.7482	4.2258	0.02597
$BaCO_3$_100	1:2:0.01	7.6760	4.1864	0.13757
$BaCO_3$_300	1:2:0.00333	7.7352	4.2186	0.04621
$BaCO_3$_500	1:2:0.002	7.7471	4.2251	0.02777

Table 5-5 – Part 3: Gels prepared using other catalysts

Gel	Equiv. Mols R:F:C	Calculated wt. R (G)	Calculated wt. F (g)	Calculated wt. C (g)
$(NH_4)_2CO_3$_25	1:2:0.04	7.5935	4.1414	0.26507
$(NH_4)_2CO_3$_50	1:2:0.02	7.6783	4.1877	0.13401
$(NH_4)_2CO_3$_75	1:2:0.01333	7.7070	4.2033	0.08968
$(NH_4)_2CO_3$_100	1:2:0.01	7.7214	4.2112	0.06738
$(NH_4)_2CO_3$_300	1:2:0.00333	7.7505	4.2270	0.02255
$(NH_4)_2CO_3$_500	1:2:0.002	7.7563	4.2302	0.0135
NO_C	1:2:0	7.7651	4.2349	0
$Mg(NO_3)_2$_300	1:2:0.00333	7.7436	4.2227	0.03476

5.1.2 Measurement and adjustment of initial sol pH

After the 30 minute stir period the initial sol pH was measured using a Hanna pH20 bench top meter equipped with a HI 1110B pH electrode probe (see Figure 5-1). To ensure accurate measurements the pH probe was calibrated, before each batch of gels, with both neutral (pH 7.1) and alkaline (pH 4.1) HANNA pH buffers.

Figure 5-1: HANNA pH20 meter [146].

In order to study the effect of initial sol pH, batches of gels were prepared with set pH values. These controlled pH values were achieved by drop-wise addition of nitric acid, HNO_3 (Sigma Aldrich – ACS reagent 70 %), until required pH was realised. The sols were then treated as normal to produce RF gels. The gels prepared with set pHs are detailed in Table 5-6 and Table 5-7.

Table 5-6: pH adjusted Na_2CO_3 gels[1] [147]

Gel	Initial sol pH	Set pH
Na_2CO_3_150	7.28	7.00
	7.27	6.75
Na_2CO_3_200	7.18	7.00
	7.18	6.75
Na_2CO_3_250	7.10	7.00
	7.09	6.74
Na_2CO_3_300	7.02	6.98
	7.02	6.75
Na_2CO_3_350	6.91	6.91
	6.92	6.75
Na_2CO_3_400	6.94	6.94
	6.92	6.75

Table 5-7: pH adjusted $NaHCO_3$ gels[2] [148]

Gel	Initial pH	Set pH
$NaHCO_3$_50	7.22	7.00
$NaHCO_3$_75	7.11	7.00
	7.10	6.75
$NaHCO_3$_100	7.05	6.75

5.1.3 Gelation and curing

After the initial sol pH had been measured the sol was placed in an oven (Memmert) for three days at 85ºC ± 5ºC. This allows the endothermic reaction between R and F to progress at an elevated rate, to that of room temperature. Initial RF clusters form within hours, and then aggregate, resulting in a highly cross-linked structure.

5.1.4 Solvent exchange

A recent study has shown that, due to its low surface tension and polarity, solvent exchanging with t-butanol significantly reduces gel shrinkage during drying, resulting in RF gels with greater porosity than their acetone exchanged counter parts [70]. Nevertheless, to ensure that results obtained are comparable with the majority of RF xerogel literature, and due to its significantly lower cost, acetone will be employed as the exchanging solvent.

After gelation and curing, water within the gels was replaced by acetone (Sigma Aldrich). Firstly, to ensure that the solvent exchange was effective the monolithic gel structure was cut into small pieces and the excess water drained off. Approximately 100 ml of acetone was

[1] These gels were prepared by Stephnie Peat, The University of Strathclyde, during an undergraduate Masters Project

[2] These gels were prepared by Heba Razouk, The University of Strathclyde, during a postgraduate Masters Project

added and vigorously shaken with the gel pieces; this shaking process was repeated and the excess acetone drained off. 180 ml of acetone was then added, and the container was sealed and placed in a shaker (Jencons lab-line incubator and shaker) for three days.

By exchanging the residual water content with acetone the drying process can be performed at a lower temperature (b.pt of H_2O = 100 °C, b.pt acetone = 56.5 °C), and with water the cohesive forces are stronger than when acetone is used as the solvent, consequently evaporation applies more force to the pore, resulting in greater shrinkage of the RF gel structure.

(a) Effect of solvent exchange

In order to determine the effects of solvent exchange two identical Na_2CO_3_300 sols were prepared, however, upon removal from the oven one gel was exchanged with the acetone, whereas the second sol was immediately dried. Both gels were vacuum dried and analysed by N_2 adsorption/desorption analysis. When water within the pores of the gels was not exchanged with acetone increased shrinkage occurred (due to high surface tension, see Table 2-1 Section 2.6.6), resulting in decreased pore volume (0.800 cm^3/g compared to 0.740 cm^3/g) and, as a result, a reduced quantity of N_2 was adsorbed.

Although the pore volume decreases only slightly for the Na_2CO_3_300 gels, it is theorised that for weaker gel structures (i.e. higher R/C ratios) pore shrinkage would be more significant, resulting in a marked decrease in pore volume upon removal of H_2O during drying. A greater reduction in pore volume for R/C 500 gel was observed by Kraiwattanawong *et al*. [70] who reported a pore volume of 0.78 cm^3/g for a xerogel solvent exchanged with acetone compared to a pore volume of 0.32 cm^3/g for an analogous gel containing H_2O.

5.1.5 Drying – xerogel synthesis

(a) Comparison of ambient pressure evaporative drying and vacuum drying

In order to compare vacuum drying and conventional evaporative drying, two of each of the sols detailed in Table 5-8 were prepared; both were solvent exchanged with acetone and the first gel was dried under vacuum, the other was dried at ambient pressure. Figure 5-2 compares the specific surface area (S_{BET}) and the total pore volume (V_{TOT}) for each set of gels prepared.

Table 5-8: Gels prepared with both vacuum and conventional drying techniques

Gel number	Gel

1	Na_2CO_3_300
2	$NaHCO_3$_300
3	NaOH_300
4	KOH_300
5	$KHCO_3$_300

Figure 5-2 illustrates that drying RF gels at ambient pressure results in diminished pore volume and as a result surface area (on average V_{TOT} is reduced by 16 %, reducing S_{BET} by 22 %). These results indicate that ambient pressure drying results in increased shrinkage of the RF gel structure, causing collapse of some of the pores.

During both drying processes (i.e. ambient pressure and vacuum drying) liquid molecules within the pores are heated until they have sufficient kinetic energy to overcome the liquid phase intermolecular forces. As the solvent within the pores is the same, theoretically equal kinetic energy is required for both processes, however, during vacuum drying the vacuum draws liquid from the pores, therefore aiding the evaporation process and causing it to occur quicker. As molecules evaporate from the liquid surface the remaining molecules require more kinetic energy to enable them to break the liquid phase forces, consequently, the quickening of evaporation occurring during vacuum drying reduces the effects of evaporative cooling, in turn reducing the stress enforced on the molecule and reducing the observed shrinkage.

This increased shrinkage, in gels dried at ambient pressure was also reported by Kraiwattanawong *et al*. [70], who observed S_{BET} of 820 m^2/g and V_{TOT} of 0.86 cm^3/g for a vacuum dried gel compared to 680 m^2/g and 0.78 cm^3/g for the analogous gel dried at ambient pressure. Given these results, and to ensure that findings are comparable with the majority of literature, evaporative vacuum drying will be utilised to produce RF xerogels.

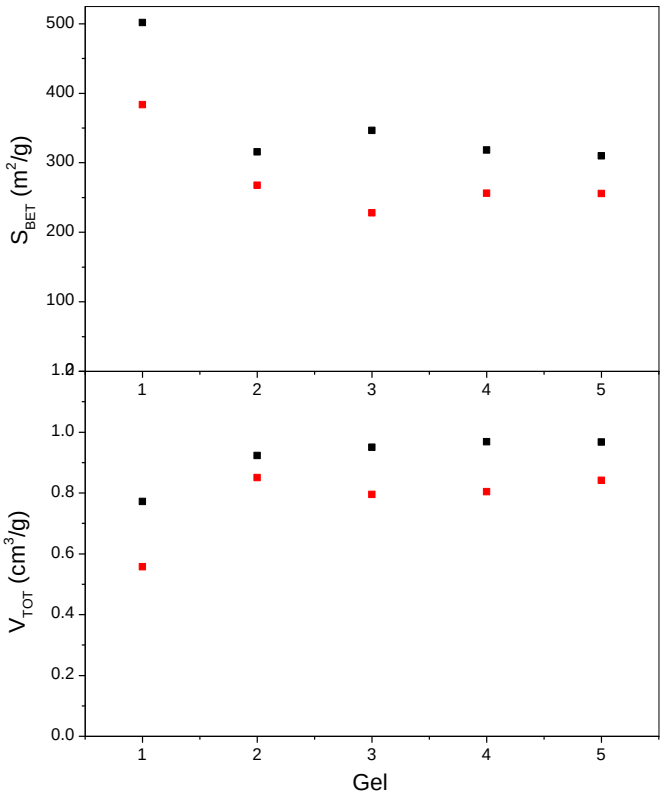

Figure 5-2: S_{BET} and V_{TOT} for gels dried at ambient pressure (red) and vacuum oven (black)

(b) Drying method

After removal from the shaker the acetone was drained off and the wet gels were placed in a vacuum oven (Townson and Mercer 1425-2), the temperature was increased to 60 °C and the pressure was decreased from 10^5 Pa to 10^3 Pa. The oven was cooled overnight, while held at full vacuum, and the gels were heated for a second time the following day, again to 60 °C. Finally the temperature was increased to 110 °C, while still under full vacuum.

5.2 Pyrolysis – carbon xerogel synthesis

5.2.1 Determination of pyrolysis conditions – Thermogravimetric analysis

In order to determine the optimal pyrolysis conditions Thermogravimetric Analysis (TGA) was performed, using a Mettler TGA/DSC system. Approximately 5 mg of dried xerogel was weighed into a small balance pan and placed onto the microbalance, within the TGA. To determine the starting weight of xerogel sample (i.e. 100 %) the sample was accurately weighed within the TGA system. To remove oxygen from the system, preventing

combustion under heating, the sample was purged with N_2 at 20 °C for 30 minutes, before the temperature was increased to 1000 °C at a rate of 10 °C min^{-1}. The results obtained (Figure 5-3) illustrate that for all gels studied approximately 50 % of mass is lost during heat treatment and there is no further mass loss above a temperature of approximately 800 °C. The 1st derivative plots indicate the temperatures at which significant mass losses occur.

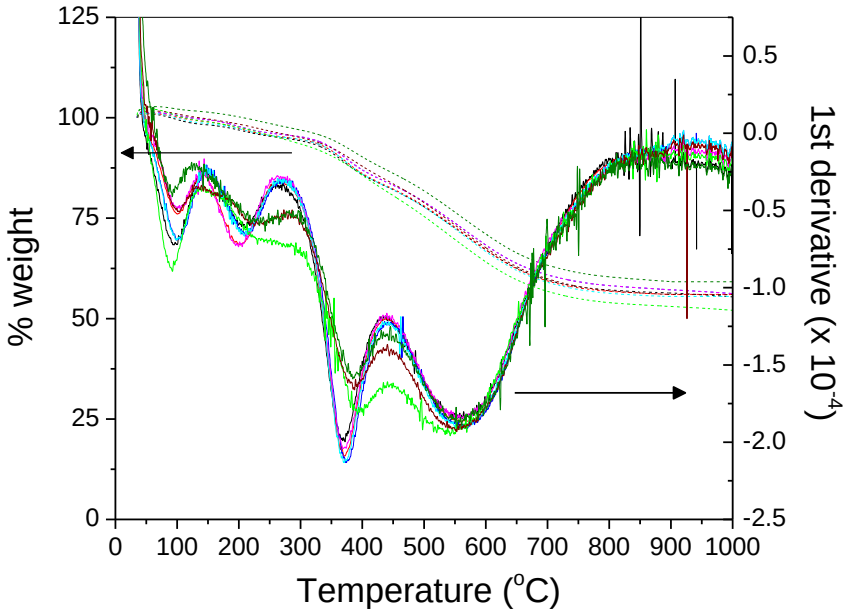

Figure 5-3: TGA results for Na_2CO_3_300 (black), $NaHCO_3$_300 (red), NaOH_300 (blue), KOH_300 (pink), $KHCO_3$_300 (cyan), $(NH_4)_2CO_3$_25 (green), $(NH_4)_2CO_3$_75 (wine) & $(NH_4)_2CO_3$_500 (olive) showing % weight loss with increasing temperature and the 1st derivative indicating temperatures at which significant weight loss occurs.

Table 5-9 summaries the temperatures at which the main mass losses occur, the results show that C-O bonds within the RF gel structure are broken before C-H bonds. This order of bond breakage has previously be reported [57] and can be explained by the strength of the bonds involved (bond strength of C-O and C-H are approximately 374 kJ mol^{-1} and 436 kJ mol^{-1}, respectively [6, 149]).

Table 5-9: Temperatures at which significant mass loss occurs

Temperature (°C)	Mechanism of mass loss
100	Desorption of residual acetone
200	Desorption of H_2O
375	Breakage of C-O bonds
550	Breakage of C-H bond

5.2.2 Pyrolysis

(a) Effect of pyrolysis temperature

As discussed in Section 2.6.8, the pyrolysis temperature can greatly affect the porous properties of RF gels. The TGA results illustrated in Figure 5-3 indicate that for the RF gels studied there was negligible weight loss above 800 °C, therefore, a pyrolysis temperature at this level would result in RF gels with optimal porous properties. Consequently, in order to determine the most effective pyrolysis temperature a sample of $NaHCO_3$_300 was pyrolysed at 800, 900 and 1000 °C. Figure 5-5 shows the N_2 adsorption/desorption isotherms and the pore size distributions for the carbons prepared and demonstrates that there is modest difference between the porous properties of the carbons prepared at different pyrolysis temperatures. However, Figure 5-6 illustrates that at a pyrolysis temperature of 1000 °C the total pore volume is slightly lower than the volumes obtained at 800 and 900 °C. As a result of this diminished pore volume the surface area is reduced. The results presented in Figure 5-6 show that pyrolysis at 800 and 900 °C result in carbon RF gels with very similar porous properties and as such either temperature could be used for pyrolysis.

(b) Pyrolysis method

Approximately 2 g of the dried gel was placed a ceramic boat and placed in a tube furnace (CARBOLITE 15/75/450 - Figure 5-4). The gel was purged with Ar flowing at 200 cm^3 min^{-1} for 30 minutes at room temperature. With the flow of Ar kept constant at 200 cm^3 min^{-1} the furnace was heated to 900 °C at a rate of 20 °C min^{-1} and held for 2 hours. After pyrolysis, the furnace was allowed to cool to room temperature under a continuous flow of Ar.

Figure 5-4: Carbolite tube furnace.

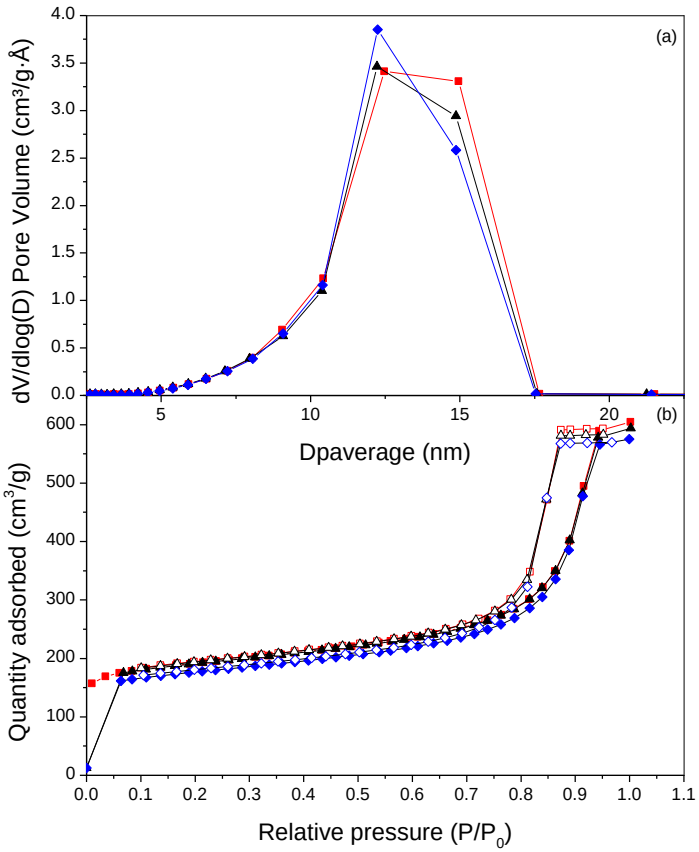

Figure 5-5: Pore size distribution (a) & N_2 adsorption (closed) and desorption (open) isotherms (b) for $NaHCO_3$_300 pyrolysed at 800 (black), 900 (red) and 1000 °C (blue).

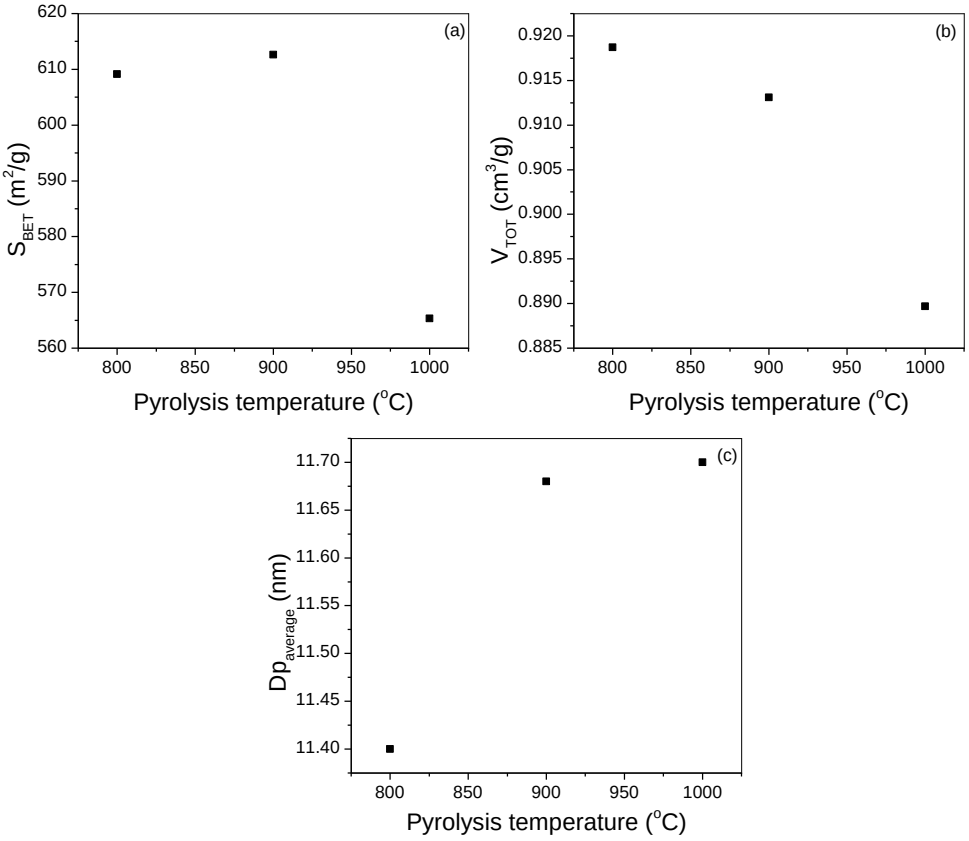

Figure 5-6: S_{BET} (a), V_{TOT} (b) and $Dp_{average}$ (c) for $NaHCO_3$_300 pyrolysed at 800, 900 and 1000 °C.

5.3 Determination of porous character – N_2 adsorption/desorption analysis

The surface area, porosity and pore volumes of both the dried and pyrolysed gels were determined by the analysis of nitrogen adsorption/desorption isotherms, which were measured using a Micromeritics ASAP 24:20 Surface Area and Porosity Analyser (Micromeritics). The Brunauer, Emmett and Teller (BET) method was utilised to determine surface area, Barrett Joyner Halenda (BJH) adsorption/desorption was used for the mesopore analysis and pore size distributions and the t-plot method, α-s plot method and Horvath Kawazoe model were used for micropore analysis. The total pore volume was determined as the volume of N_2 adsorbed closest to saturation point.

5.3.1 Standard analysis method

Approximately 0.5 g of gel was transferred to a Micromeritics sample tube and fitted to a degas port within the analysis equipment. Prior to analysis all samples were degassed,

initially by a slow vacuum at room temperature to 5 mmHg, before reducing the pressure quickly to 10 µmHg. Whilst under vacuum the samples were then heated to 50 ºC and held for 30 minutes before heating to 110 ºC, and holding for 120 minutes. This degassing process removed all adsorbed species, ensuring samples were clean for analysis. Degassed samples were then cooled to room temperature and backfilled with analysis gas before being removed, reweighed and transferred to an analysis port. The reweighed mass is used as sample mass for analysis.

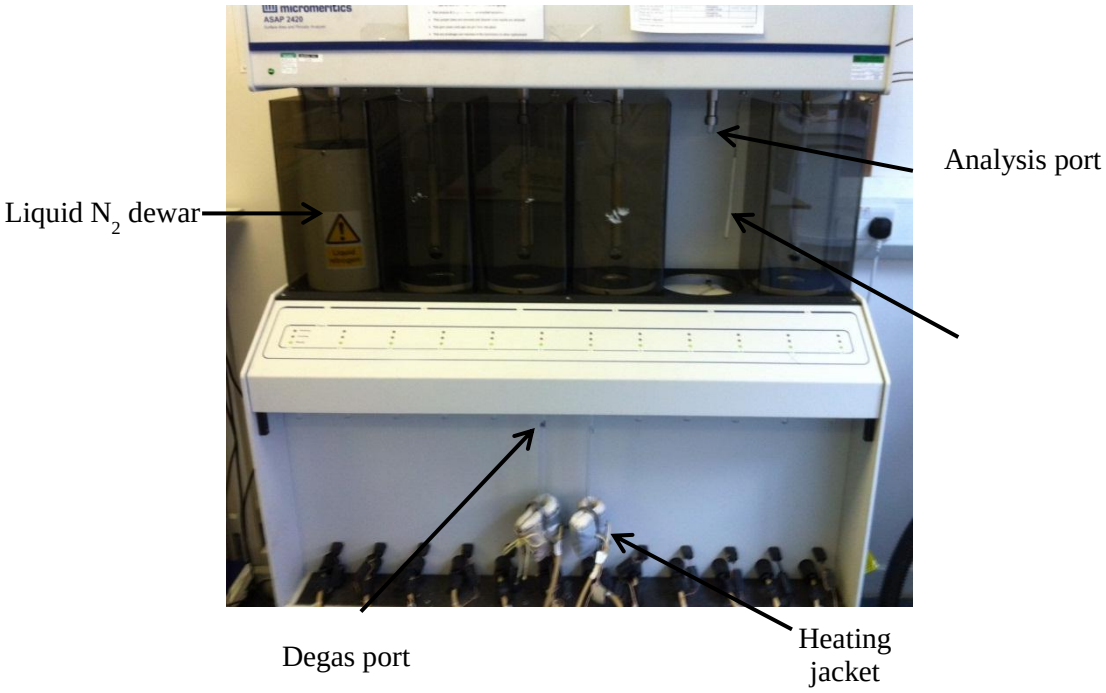

Figure 5-7: Micromeritics ASAP 24:20 Surface Area and Porosity Analyser.

Adsorption/desorption isotherms were obtained at -196 ºC (critical temperature of N_2), through the use of a coolant (liquid N_2 held in Dewars surrounding the sample tube). Adsorption of N_2 (g), from a mixture of He/N_2, was monitored over 40 points between 0.1 - 1.0 P/P_0 and desorption, from 1.00 to 0.1 P/P_0 was recorded over 30 points. At the working temperature physical adsorption of He, into the pores of the RF gels, does occur due to its high critical temperature (-268 ºC). Prior to analysis a filler rod was placed within the sample tube and an isothermal jacket was placed over the long sample tube neck, these steps reduced the volume of N_2 required and ensured a constant sample temperature was maintained, respectively.

5.3.2 Micropore analysis method

For carbons that exhibited significant microporous character under standard analysis, further micropore analysis was performed. For this procedure samples were initially degassed under the same conditions detailed for standard analysis. The samples were then reweighed and fitted with an isothermal jacket and seal frit, which prevented any unwanted particles entering the sample tube. A second degas was then completed on the analysis ports of the analyser. This degas involved the same evacuation as the standard degas, however heated the samples to 200 ºC at a rate of 10 ºC per minute, holding for 120 minutes (as illustrated in Figure 5-3 no significant weight loss occurs up to 200 ºC). The double degas process ensured that all absorbed species were removed from even the smallest pores. Adsorption/desorption isotherms were then acquired for pressures in the range of 0.005 to 1.00 P/P_0. Micropore analysis typically required 5 days of analysis time, consequently the liquid N_2 had to be checked and filled regularly to ensure that it remained at an appropriate level.

5.3.3 Instrument calibration

To ensure that accurate isotherms were obtained the analysis instrument was calibrated periodically with a Micromeritics silica-alumina standard. The obtained isotherms were analysed and the properties compared with the set characteristics detailed in Table 5-10.

Table 5-10: Properties of Micromeritics silica-alumina standard

Property	Value	Error (±)
S_{BET} (m^2/g)	205	6
V_{TOT} (cm^3/g)	0.63	0.08
$Dp_{average}$ (nm)	11.5	1.5

If the results acquired showed any variances, outwith the ranges given in Table 5-10, these were investigated and rectified before any further analyses were performed.

5.4 Determination of [R] and [HM] – Reverse phase HPLC

Reverse phase HPLC was utilised to quantitatively monitor the change in resorcinol and qualitatively monitor the HM concentration with reaction time. Due to the chemical nature of RF gels, it was found that over time the elution of R and HM derivatives changed, making reproducible results difficult to achieve. It is thought that this change was caused by irreversible bonding of RF structures, which altered the chemistry of the SP within the column. A similar problem was overcome by Datta *et al*. [114] who found that acidifying a

dilute RF residue, stirring, re-diluting, and repeating this process several times resulted in an RF solution that could be analysed on a reverse phase HPLC column, without irreversible damaging the column. This method of prolonging the column life was considered, however the objective of this study was to analyse RF samples in time sequence to monitor the progress of the reaction, therefore long sample preparation methods were not suitable, as the composition of the samples changed over time (this is discussed further in the method development section).

In this study three reverse phase columns were used, as detailed in Table 5-11. When the column chemistry appeared to change a new column was utilised.

Table 5-11: Reverse phase HPLC columns utilised

Column	Manufacturer	SP	Internal diameter (mm)	Column length (mm)
1	Waters, Spherisorb	5 µm ODS-C_{18}	2.1	150
2	Waters, Symmetry	5 µm ODS-C_{18}	3.9	150
3	Waters, Symmetry	5 µm ODS-C_{18}	3.9	150
LCMS	Zorbax, Eclipse	5 µm XDB-C_{18}	4.6	150

Samples will be named as detailed in section 5.1 with the progress stated as an additional term (as detailed in Table 5-12). For example, Na_2CO_3_100_T_9 relates to a sol prepared with Na_2CO_3 at R/C ratio of 100, with the sample taken after the sol has been in the oven for 9 minutes. For samples analysed before the sol has been heated (i.e. during the room temperature stir) the sample will be denoted with a negative time vale, e.g. Na_2CO_3_100_T_{-15}, relates to the same sol above, however, the sample is analysed 15 minutes before the sol is placed in the oven, i.e. 15 minutes into the 30 minute stir period.

Table 5-12: Sample nomenclature for LC samples

Sample name	Description
Na_2CO_3_100_R+C	Before addition of F
Na_2CO_3_100_T_{-30}	At start of 30 minute stir period
Na_2CO_3_100_T_{-20}	10 minutes into 30 minute stir
Na_2CO_3_100_T_{-10}	20 minutes into 30 minute stir
Na_2CO_3_100_T_0	Point when sol is placed in oven

Na_2CO_3_100_T_{10}	10 minutes in the oven

5.4.1 Method development

(a) Determination of detection wavelength:

The detection of R and HM derivatives has previously been carried out using UV-Vis detection at both 254 nm [150] and 273 nm [151] , consequently to ensure the optimum wavelength was chosen an aqueous R solution was tested at both wavelengths. The acquired chromatograms are shown in Figure 5-8, demonstrating that detection is significantly more sensitive at 273 nm. As a result 273 nm was chosen as the fixed detector wavelength.

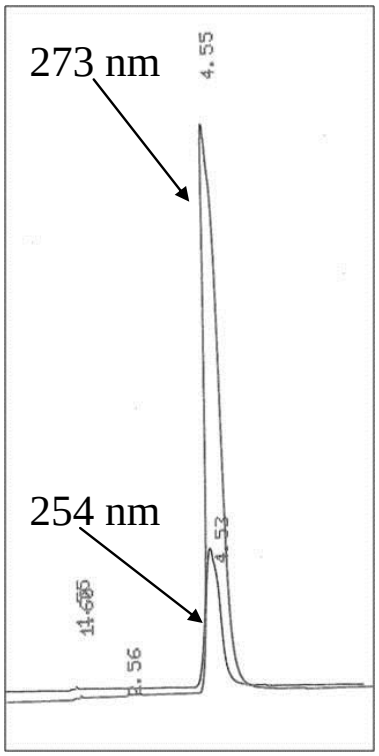

Figure 5-8: LC chromatograms for R/W standard solution with detection at 254 nm and 273 nm (analysed on column 1).

(b) Effect of standing time on RF sol samples

The final LC method will be used to analyse reacting systems, consequently, it was worthwhile to determine whether aliquots could be removed from the oven and left for a period of time, or whether they had to be analysed immediately. Figure 5-9 demonstrates that the chromatogram changes with time; consequently to give an accurate representation of

the system analysis must be carried out immediately after the aliquot is removed from the oven.

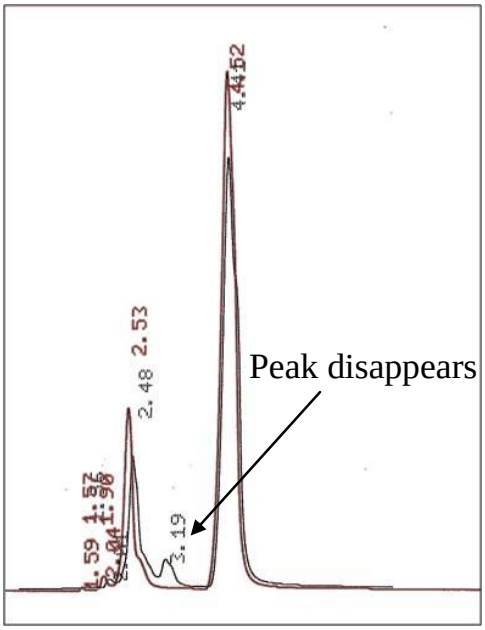

Figure 5-9: LC chromatogram for Na_2CO_3_100_T_0, shows analyte peak with R.T 3.19 and chromatogram for Na_2CO_3_100_T_0 analysed after a couple of hours, showing no peak at 3.19 minutes (column 2, MP 10 % acetonitrile, flow rate 0.3 ml/min, sample dilution 15 µl/10 ml).

(c) Choice of column

Previous LC studies on the formation of RF gels have typically utilised a C_{18} reverse phase system [114, 152, 153], however, initial work using a similar column showed that on this type of system the HM derivatives elute with very similar retention times, resulting in overlapping peaks. Figure 5-10 shows a chromatogram obtained using a C_{18} reverse phase system, where the peaks at 1.09 – 1.63 minutes are caused by HM derivatives and the peak at 2.31 minutes is caused by R (peaks identified using mass spectrometry, see section 5.5).

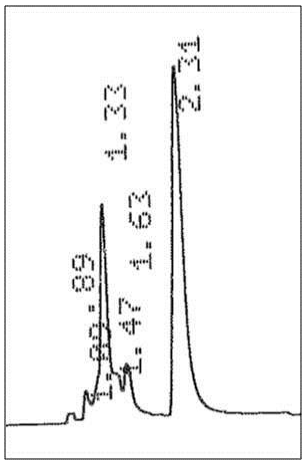

Figure 5-10: LC chromatogram for Na2CO3_100_T9, analysed on column 1, with 15 % acetonitrile aqueous MP (Flow rate 0.5 ml/min, sample dilution 15 µl/20 ml and attenuation 1024).

Due to the decreased hydrocarbon chain length a reverse phase C_8 column is less non polar than the C_{18} reverse phase column, therefore, it was theorised that the polar analytes (HM and R) would interact more favourably and remain in the C_8 column longer, resulting in increased separation between the HM derivatives. In order to test this theory an R/C_100 reacting system was analysed at T_9 (9 minutes in the oven), on a C_8 column (Sphereclone 5 µm, with an internal diameter of 4.6 mm and column length of 150 mm), however, as illustrated by Figure 5-11, HMs were not retained with this system. This non retention can be explained due to decreased steric interaction with decreasing chain length, subsequently when the C_8 column is used the HM remain in the polar MP and elute immediately, escaping detection. Whereas in the C_{18} column the increased hydrocarbon chain length on the SP hold the HM derivatives within the column for a short period of time. Based on the chemistries of both columns and the known interactions that occur, it can be concluded that there is no chemical interaction between the HM and the reverse phase column and HM retention in the C_{18} column is based only on steric hindrance.

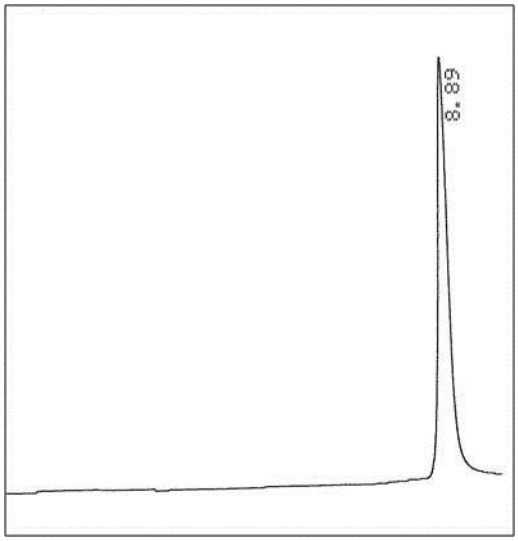

Figure 5-11: LC chromatogram for Na_2CO_3_100_T_9, analysed on C_8 column with 15 % acetonitrile aqueous MP, indicating only R detection (Flow rate 0.5 ml/min, sample dilution 15 µl/20 ml and attenuation 1024).

(d) Dimer/trimer detection

LC-MS results (section 5.5) indicate that dimers/trimers are less polar than monomers and R, therefore it is expected that these analytes will have a higher affinity for the non-polar SP. Given that the C_8 column is less non polar than the C_{18} column, retention of these

dimers/trimers should be decreased in the C_8 system. To test whether the C_8 column could be used for separation of dimers/trimers the polarity of the MP was decreased by increasing the acetonitrile concentration. Altering the MP adjusts the distribution of the analytes between the two phases, consequently, it was expected that the affinity of the dimer/trimer analytes for the SP would decrease, resulting in decreased retention time. The MP was changed to 30 % acetonitrile in H_2O and Na_2CO_3_100_T_9 was analysed. The acquired chromatogram is shown in Figure 5-12.

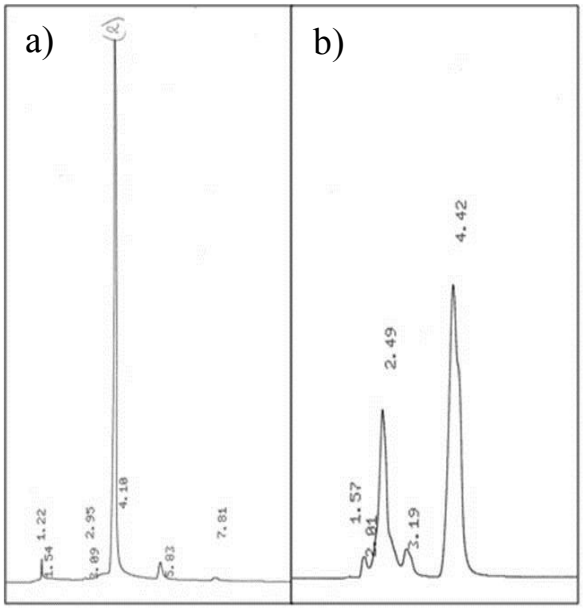

Figure 5-12: (a) LC chromatogram for Na_2CO_3_100_T_9, analysed on C_8 column and (b) LC chromatogram for Na_2CO_3_100_T_9, analysed on column 2 (MP (a) 30 % acetonitrile in H_2O (b) 10 % acetonitrile, flow rate 0.5 ml/min, sample dilution 15 µl/20 ml and attenuation 1024).

Figure 5-12 shows that some dimers can be observed in this system (peak with retention time of 5.83 minutes, to the right of the main R peak), but only in very low concentration. Given the poor results obtained, for both monomer and dimer detection, on the C_8 column, the C_{18} column was chosen for monitoring the initial RF reaction.

(e) Retention time optimisation - Effect of flow rate & MP composition

In order to alter the retention times, there are two main options, the first is changing the MP composition, which alters the distribution of analytes between the mobile and SP, i.e. increasing the acetonitrile content decreases the polarity of the MP, in turn decreasing the affinity the polar analytes have for the MP, resulting in increased retention times. It was found that altering the composition of the MP had little effect on the analyte retention times, and the MP was fixed at 15 % acetonitrile for column 1 and 10 % acetonitrile for columns 2 & 3.

As expected, increasing the flow rate causes the analytes to be carried through the column quicker, resulting in decreased retention times. Consequently, decreasing the flow rate can improve separation. In this study it was important to optimise the flow rate to ensure the best possible separation was obtained, however the flow rate had to be appropriate for the column used and run time had to be kept within a time limit, allowing significant time between samples, to remove the sol from the oven, measure and dilute the correct sample amount and acquire the chromatogram. To allow significant time a total analysis time of approximately 6 minutes was required.

Column 1 had an internal diameter of 2.1 mm, consequently, to maintain optimal column pressure it is advised that the flow rate should be about 0.2 ml/min [154], however, it was found that a flow rate of 0.3 ml/min provided adequate peak separation, keeping the run time within 6 minutes. To keep the retention time of R at approximately 4.5 minutes, and a total run time of approximately 5 minutes (as illustrated by Figure 5-12 b), columns 2 and 3required a flow rate of 0.5 ml/min.

(f) Setting sensitivity and sample dilution – column specific

In order to obtain the best separation a balance between the sample dilutions, the detector range setting and the integrator attenuation value had to be obtained. A small sample volume (increased dilution), with high sensitivity makes sample preparation difficult and increases the errors involved, whereas large sample volume sand low sensitivity reduces the sensitivity of the detector and reduces the height of the observed peaks.

For column 1 dilution was set at 15 µl/10 ml of H_2O, detector range was set at 0.2 AUFS, and the integrator attenuation was set at 512, increasing the sample volume to 30 µl with a reduced integrator sensitivity (attenuation of 1024) reduced the sensitivity, resulting in the loss of monomer peaks.

For columns 2 and 3, the columns were found to be slightly more sensitive, than column 1, consequently the dilution was set at 30 µl/25 ml (1.2×10^{-3} M, compared to 1.5×10^{-3} M) with an attenuation of 512.

(g) Setting the detector rise time

The time required for the detector to go from 10 % to 90 % output is defined as the detector rise time. If the rise time is set too high, early peaks lose peak height and begin to tail and peak resolution between adjacent peaks is lost [155]. In this study it was found that there

were no immediately eluting peaks (< 1 minute), therefore this was not a significant problem. Rise time was set at 1.0 second.

(h) Column degradation

As discussed in Section 5.4, over time the separation of HM and R appeared to change. Given that dimer/trimer molecules are not eluted from the LC columns it is likely that they were irreversibly bonding to the SP, resulting in alteration of the column chemistry, consequently, affecting analyte separation. This irreversible bonding could have been prevented by sample pre-treatment and/or cleaning of the column, with a non-polar MP, after each sample run. However, due to the strict time scales involved neither of these options were feasible for this study. In order to prolong the column life as long as possible, the columns were flushed out daily with a 70 % acetonitrile MP, nevertheless the columns were still found to degrade and change over time. Figure 5-13 shows the chromatogram acquired for Na_2CO_3_400_T_{100}. This chromatogram demonstrated an increased retention time for R and shows a large spike with a retention time of 0.63 minutes. Initially it was considered that this peak was a reaction peak, however there were no trends in appearance and it was present within samples that had previously shown no peak at this retention time.

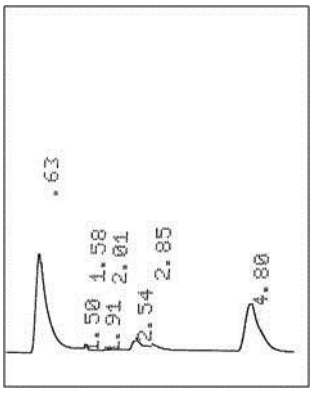

Figure 5-13: LC chromatogram for Na_2CO_3_400_T_{100}, analysed on column 1 (MP 10 % acetonitrile, flow rate 0.3 ml/min, sample dilution 15 µl/10 ml and attenuation 512).

The column was then flushed with a 70 % acetonitrile solution and the chromatogram was monitored, as illustrated in Figure 5-14. The acquired chromatogram showed a large broad peak eluting early, suggesting that the early peak within the reaction chromatograms was a result of something within the column, which could be removed with a less polar MP. In order to determine whether the cleaning process had removed the contaminants from the column the sample was analysed, see Figure 5-15.

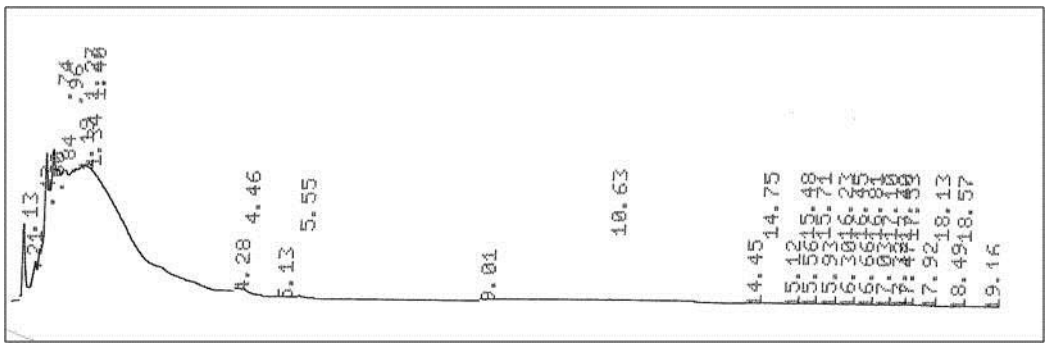

Figure 5-14: LC chromatogram acquired during cleaning of column 1 with 70 % aqueous acetonitrile column (N.B no sample present).

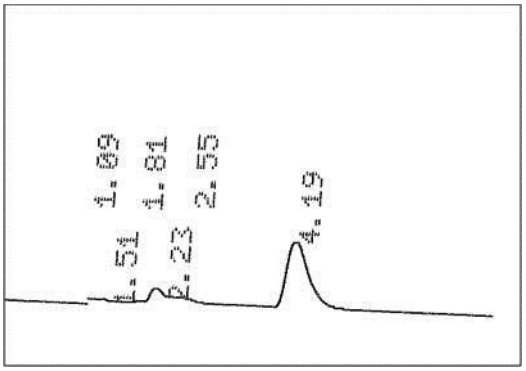

Figure 5-15: LC chromatogram for Na_2CO_3_400_T_{100}, analysed on column 1 after column cleaning (MP 10 % acetonitrile, flow rate 0.3 ml/min, sample dilution 15 µl/10 ml and attenuation 512).

Cleaning with 70 % acetonitrile MP appears to remove the contaminant from the column, as demonstrated by sample chromatogram obtained before and after cleaning (Figure 5-13 and Figure 5-15 respectively). It is likely that this peak is caused by dimers which remain trapped in the LC column, where the 10 % acetonitrile MP is not polar enough to remove these and when a sample containing bulky reaction products is injected the dimers within the column are knocked off causing a peak to appear at the beginning of the spectra. A sample of R/W was injected to determine whether this removed the bulk contaminant from the column and it was found that no elution occurred, thus larger analytes must be required to remove them from the column.

Although this column cleaning process appeared to remove the contaminant it proved only to be a temporary measure as the contamination peak reappeared after a few more analyses were carried out. Due to this column degradation the LC column had to be replaced regularly.

5.4.2 Method validation

For clarity the IUPAC definitions of repeatability and reproducibility are given as follows [156]:

Repeatability – *"The closeness of agreement between independent results obtained with the same method on identical test material, under the same conditions (same operator, same apparatus, same laboratory and after short intervals of time)."* Reproducibility – "*The closeness of agreement between independent results obtained with the same method on identical test material but under different conditions (different operators, different apparatus, different laboratories and/or after different intervals of time)".*

Ideally, method validation would have been carried out on all three columns used in this study, however, due to time constraints and given that most analyses were carried out on a Waters Symmetry, 5 µm ODS C_{18} 3.9mm x 150 mm column, validation was carried out on column 2.

(a) LC system repeatability – standard solution

In order to determine the repeatability of the LC system, an R/W standard solution was analysed 8 times on three different days, the peak areas were the compared to determine if LC would produce repeatable results. The peak areas obtained and the ANOVA results are given in Table 15-1 (Chapter 15 Appendix C). The ANOVA results indicate that there is no significant difference between chromatograms obtained on different days (i.e. $F_{calc} < F_{crit}$), demonstrating that peak areas are repeatable. The calculated relative standard deviation (RSD) is 1.39 %, which is within the expected RSD for HPLC of standard solutions, which in most cases should be within 2.0 % [157].

(b) LC method Reproducibility – standard solution

The reproducibility of the LC method was tested by measuring the effect of different R/W standards and different MPs on the R peak area. The results for three different R/W solutions and three different MPs (all 10 % acetonitrile), with ten analyses for each one, are given in Appendix C (see Table 15-3 to Table 15-6 in Appendix C – LC validation (ANOVA). The results presented show that for both, changing R/W and changing MP, F_{calc} is less than F_{crit}, indicating that there is no significant difference between the peak areas obtained, therefore it can be concluded that the LC method is reproducible. The RSD's for changing R/W and changing MP are 1.65 % and 1.52 %, respectively, which is again within the expected variance for HPLC standard analysis.

(c) LC method repeatability – Reacting system

The repeatability of LC results, for a reacting system, was determined by comparing the R peak area from the time resolved chromatograms for seven solutions of Na_2CO_3_200. The peak areas obtained over the course of the reaction are given in Table 15-7 Appendix C). The chromatograms were acquired on column 2, with a 10 % acetonitrile MP, a flow rate of 0.5 ml/min, attenuation of 512, rise time of 1.0 second and a range of 0.2 Absorbance Units Full Scale (AUFS). The relative standard deviations given in Table 15-8 (Appendix D), show that the maximum variance observed was 16.69 %, with an average RSD of 7.20 %.

In general, a RSD of within 5 % is considered acceptable, however given the nature of the samples studied and considering the large number of error sources involved (i.e. sample volume, sample and analysis timing, varying sol compositions due to weighing differences, varying MP compositions and oven temperature variations) an average RSD of 7.2 % is acceptable. Figure 5-16 shows the change in [R] for the Na_2CO_3_200 repeats and compares these to Na_2CO_3_100 and 400. Figure 5-16 demonstrates that early in the reaction (up to ten minutes) there is large variance between the results, however as the reaction progresses the HPLC method becomes more repeatable and produces profiles that are significantly different to profiles acquired for different sol compositions.

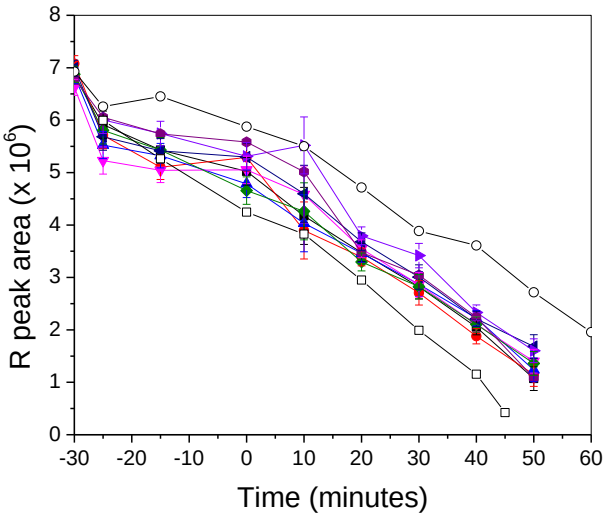

Figure 5-16: Change in LC R peak area with reaction time for Na_2CO_3_200 repeats (closed symbols) showing standard deviation error bars, Na_2CO_3_100 (open symbol-square) & Na_2CO_3_400 (open symbol-circle).

It is assumed that as the chemistry of all columns is similar the repeatability will be similar for columns 1 to 3.

5.4.3 Column calibration – [R]

To enable the method to be quantitative and to allow comparisons between the different columns, calibration was carried out using aqueous solutions of R. R was weighed out (specific weights given in Table 5-13) and dissolved in 60 ml of H_2O. For column 1, 15 µl was diluted into 10 ml of H_2O, whereas for columns 2 and 3, 30 µl was diluted with 25 ml of H_2O and the sample was analysed using the HPLC method discussed below. The molar volume of R (Table 5-13) was then plotted against the peak area obtained, as shown in Figure 5-17.

Table 5-13: Weight of R used to make calibration standards for each column

Weight R (g)	Mols R (MW = 110.11 g)	[R]/M
Column 1		
0.61	0.0055	0.0923
1.0542	0.0096	0.1596
2.2633	0.0206	0.3426
3.2235	0.0293	0.4879
4.5321	0.0412	0.6860
5.6061	0.0509	0.8486
6.4877	0.0589	0.9820
7.7623	0.0705	1.1749
8.9012	0.0808	1.3473
Column 2		
0.6101	0.0056	0.0923
1.0522	0.0096	0.1593
2.2539	0.0205	0.3412
3.2125	0.0292	0.4863
4.5181	0.0410	0.6839
5.6063	0.0509	0.8486
6.4928	0.0590	0.9828
7.7563	0.0704	1.1740
8.8986	0.0808	1.3469
Column 3		
0.611	0.0055	0.0925
1.0782	0.0098	0.1632
2.2520	0.0205	0.3409
3.2097	0.0292	0.4858
4.5150	0.0410	0.6834
5.6091	0.0509	0.8490
6.4915	0.0590	0.9826
7.7521	0.0704	1.1734
8.8989	0.0808	1.3470

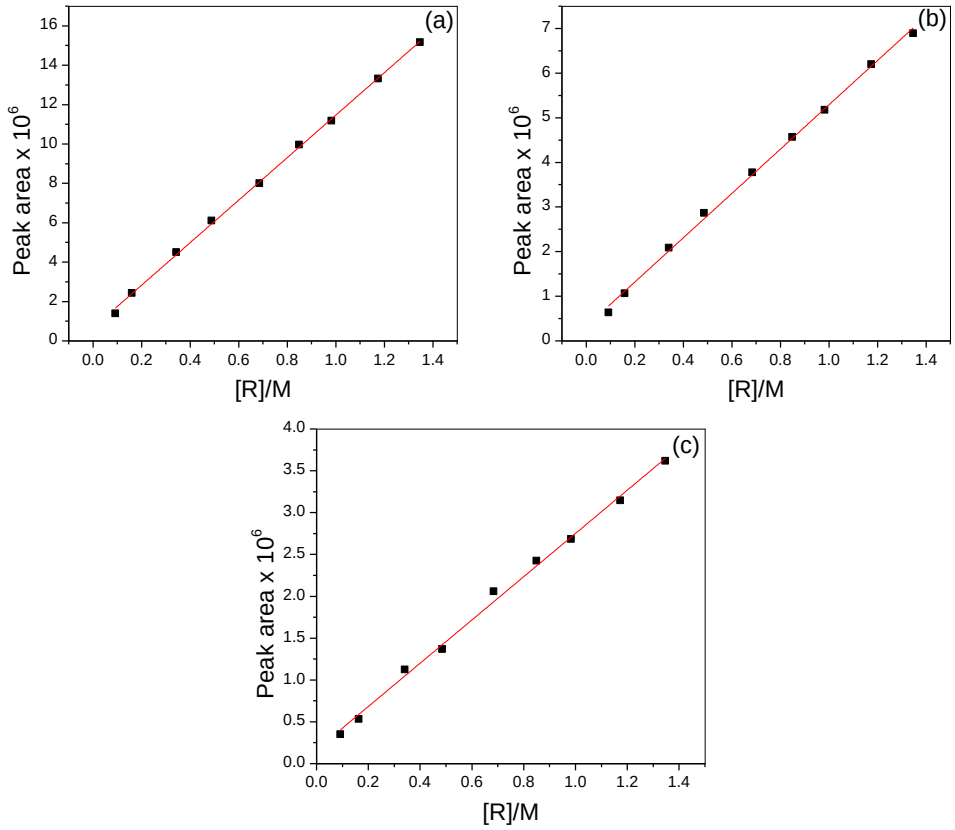

Figure 5-17: Resorcinol calibration graphs for column 1 (a), 2 (b) and 3 (c).

5.4.4 [HM] determination

HMs are formed from the initial reaction between R and F, however, once formed they react quickly to form dimers, trimers and so on. Due to the nature of HM's and due to the fact that they cannot be easily purchased and/or made, the change in HM concentration could not be used quantitatively to monitor the progress of the condensation reaction. As the concentration of HM within the sol is constantly changing, comparison of HM peak areas for different sol compositions is also difficult, consequently the HM peaks will only be used qualitatively.

5.4.5 HPLC method

RF sols were prepared using the traditional method discussed in section 5.1.1. A representative aliquot (15 µl for column 1, 30 µl for columns 2 and 3) was removed from the sol and diluted with H_2O (10 ml for column 1, 25 ml for columns 2 and 3). To monitor the progress of the reaction this process was repeated every ten minutes and the sample was analysed immediately upon abstraction from the bulk solution. The sample was then injected into an acetonitrile aqueous MP (15 % for column 1, 10 % for columns 2 and 3),

through a 50 µl rheodyne valve. The MP, carrying the sample analytes, was pumped into the reverse phase column at a flow rate of 0.3 ml/min or 0.5 ml/min using a Varian 2510 HPLC pump. Once eluted from the column analytes were detected at 273 nm, using a Spectra Series UV 100 detector and the LC chromatogram was constructed by an Spectra Physics SP4290 integrator. To ensure optimum sensitivity the detector range and rise time were set at 0.2 AUFS and 1.0 sec, respectively; the integrator attenuation was set at 512.

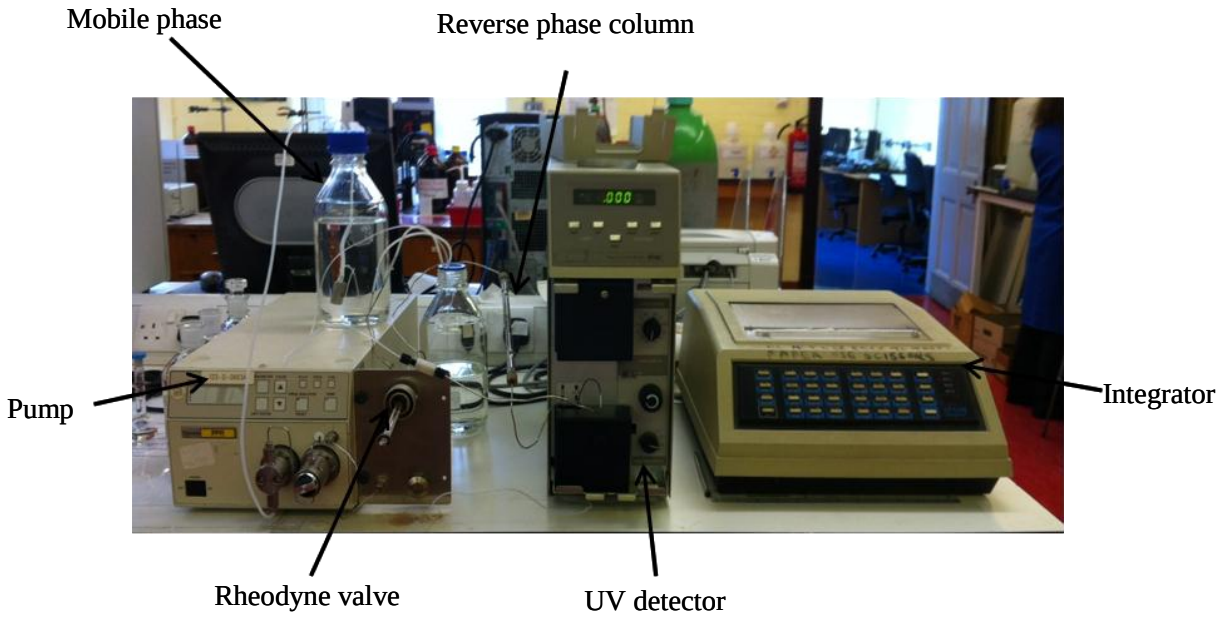

Figure 5-18: HPLC set up, illustrating key components; MP solution, Varian HPLC pump, rheodyne injection valve, reverse phase column, Spectra Series UV 100 detector and integrator.

5.5 LCMS[3]

In order to determine the order of elution of RF polymerisation products a selection of RF sols were analysed using LCMS. The LC stage utilised a reverse phase column with similar chemistry to that employed for the determination of R disappearance and HM formation, consequently the order of elution will be very similar. The samples were passed through a 150 mm x 4.6 mm Zorbax Eclipse XDB – C_{18} column, with a two component MP (A – 5mM ammonium acetate in H_2O, B – 5mM ammonium acetate in acetonitrile) at a flow rate of 1 ml/min and a run time of 36 minutes. A gradient pump was used to alter the composition of MP composition as follows; 0 – 17 min 95 % A and 5 % B, 17 – 27 min 100 % A, 27 – 3 min 100 % B and 33 – 36 min 95 % A and 5 % B. This MP gradient from polar, to non-polar and back to polar, ensured that all polymerisation products were eluted from the

[3] This work was carried out by the Analytical Suite, Department of Pure and Applied Chemistry, University of Strathclyde, Glasgow

column and prevented the significant shortening of column lifetime observed in the LC method discussed in Section 5.4.1(h).

After elution from the LC column, analytes were ionised at atmospheric pressure by electrospray ionisation and detected using a mass spectrometer. Interpretation of the mass spectra produced allowed polymerisation products to be identified and the order of elution, in the LC method discussed in Section 5.4, to be determined.

5.6 Determination of free [F]

The concentration of free F in RF sols/gels was determined using a pre described titration method [12, 158, 159]. Initially 10 ml of sol/gel sample was dissolved in a 90 % ethanol solution. To prevent further reaction of F with R^-, the solution was titrated against 0.2 N hydrochloric acid (HCl). The end point was observed as a green/yellow colour using bromophenol blue indicator, signifying a pH of approximately 4.0.

25 ml of 5 % w/v hydroxylamine hydrochloride solution (5 % hydroxyl amine hydrochloride dissolved in small volume of hot water and made up with ethanol) was added and the prepared solution left to stand for 30 min. This period allowed HCl from reaction of F with hydroxylamine hydrochloride (Equation 141 [160]) to be liberated and prevented underestimation of the F concentration [158].

$$CH_2O + NH_2OH \cdot HCl \rightarrow H_2O + CH_2NOH + HCl$$

Equation 141

The liberated HCl was then titrated with 1.0 N NaOH to a pH endpoint of 3.40. 1 mole of NaOH reacts with 1 mole HCl as shown in Equation 142 and as F reacts with hydroxylamine hydrochloride in a 1:1 ratio, 1 ml 1.0 N NaOH indicates the presence of 0.001 M F, consequently, 1 ml NaOH is equal to 0.0303 g F [12].

$$NaOH + HCl \rightarrow NaCl + H_2O$$

Equation 142

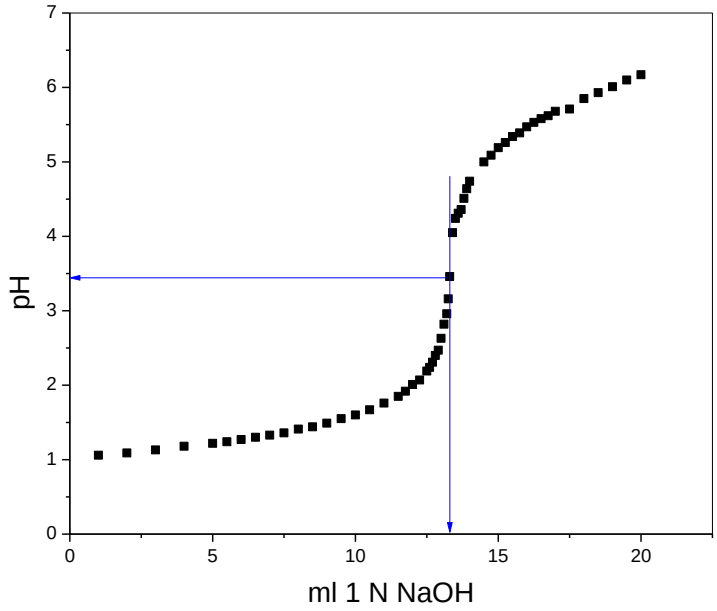

Figure 5-19: Titration curve showing the equivalence point for titration of HCl with NaOH.

5.6.1 Example calculation

For Na_2CO_3_200 at T_{45}, 7.35 ml of 1 N NaOH were required to reach a pH of 3.40. This therefore equates to 0.2227 g F (7.35 ml x 0.0303 g), which is equal to 0.00742 mols F in the 10 ml sol/gel sample. The number of mols, in 10 ml of sample, was then multiplied by 100 to determine the molar quantity of 0.742 M.

5.6.2 Reproducibility

The reproducibility of the formaldehyde titration method was tested by monitoring the decrease in F concentration for six repeats of Na_2CO_3_200. The concentration of F determined at each time interval is given in Table 5-14. The RSD at each time interval is within 5 % indicating that the method is reproducible.

Table 5-14: Remaining F concentration for Na_2CO_3_200 repeats

Time	Remaining [F]/M						
(min)	1	2	3	4	5	6	RSD (%)
0	1.745775	1.735684	1.745775	1.796231	1.745775	1.745775	1.24
15	1.432949	1.422857	1.402675	1.463222	1.412766	1.493496	2.38

30	1.14535	1.110031	1.221034	1.175623	1.140304	1.210942	3.71
45	0.741702	0.681155	0.671064	0.696292	0.67611	0.72152	4.03

Figure 5-20 illustrates the [F] profiles and shows that the titration method produces reproducible results that are significantly different from sols prepared with different sol compositions.

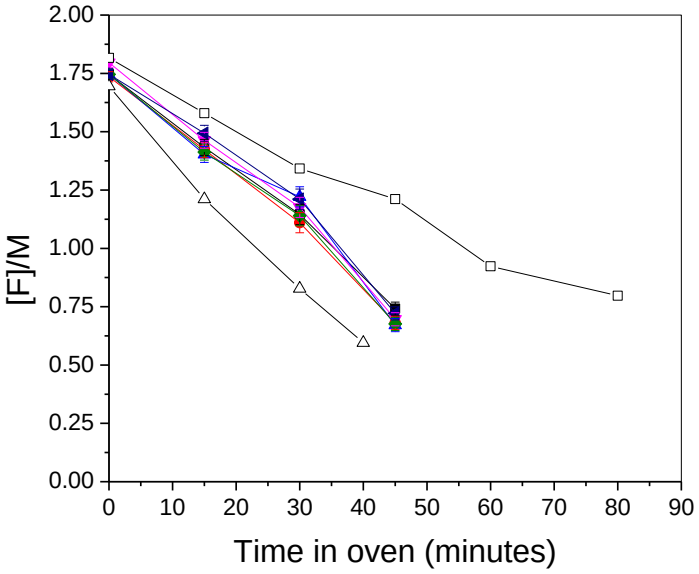

Figure 5-20: F titration results for 6 Na_2CO_3_200 repeats (closed coloured symbols), Na_2CO_3_100 (open symbol-triangle) & Na_2CO_3_400 (open symbol-square).

5.7 DLS - Particle growth[4]

Particle growth in the initial stages of the RF reaction was monitored using DLS. The system employed utilised an ALV/CGS 3 Compact Goniometer System in conjunction with an ALV/LSE 5004 Multiple Tau Digital Correlator, with a He:Ne laser operating at 632.8 nm, as the light source. The system was arranged to measure the scattered intensity at an angle of 90° to the beam path.

For all compositions analysed the RF sol was prepared as described in Section 5.1 and in order to remove any undesired particulates was subsequently passed through a 0.2 μm PTFE filter (Whatman™ Puradisc™). Eleven sample cells were then filled with equal volumes of the filtered sol. One of the cells was placed directly in the cell holder of the DLS equipment, allowing a measurement at time zero to be obtained. The other cells were placed in an oven

[4] These measurements were performed by Stewart Taylor, Department of Chemical and Process Engineering, University of Strathclyde, Glasgow

at 85 ± 5 °C to begin gelation and were removed sequentially at time intervals of 10 % of the total gelation time, quenched to room temperature, before the scattered intensity was measured.

5.7.1 Data analysis

For each sample analysed, the scattered intensities were used to generate autocorrelation functions, which were processed with a third order cumulant fit that yielded the diffusion coefficients of the samples. These values were substituted into the Stokes Einstein Equation (Equation 12) to give the hydrodynamic radii of the particles at each stage of the gelation process.

$$d(H) = \frac{kT}{3\pi nD}$$

Equation 143

Where *d(H) = hydrodynamic radius (m)*

D = translational diffusion coefficient (m^2 s^{-1})

k = Boltzmann's coefficient (m^2 Kg s^{-2} K^{-1})

T = absolute temperature (K)

H = viscosity (Pa s)

5.8 Determination of surface morphology – SEM

To investigate the surface morphology and estimate the average particle size, RF gel products were imaged using SEM. A Hitachi SU6600 Analytical Variable Pressure Field Emission SEM was utilised for all samples.

Figure 5-21: Hitachi SU6600 SEM.

To enable good quality imaging the specimen must be conductive (as discussed in Section 3.1.6) consequently, prior to analysis all samples were gold coated using an Edwards S150 Sputter Coater.

Figure 5-22: Edwards S150 sputter coater.

Prior to sputtering, the samples were ground into small particles, which allowed even gold coverage. Early analysis indicated that, even after gold coating, SEM analysis of dried RF xerogels resulted in poor quality images (Figure 5-23). It is likely that the cause of these poor quality images is the low conductivity of the dried gels, whereas pyrolysed gels will be better conductors and consequently provide high quality SEM images. Similar low quality images were presented in the literature for dried gels [31, 161], with most authors opting to present SEM images for carbonised and activated samples [80, 162-164]. Due to the low quality images obtained for dried xerogels SEM analysis focused on pyrolysed samples.

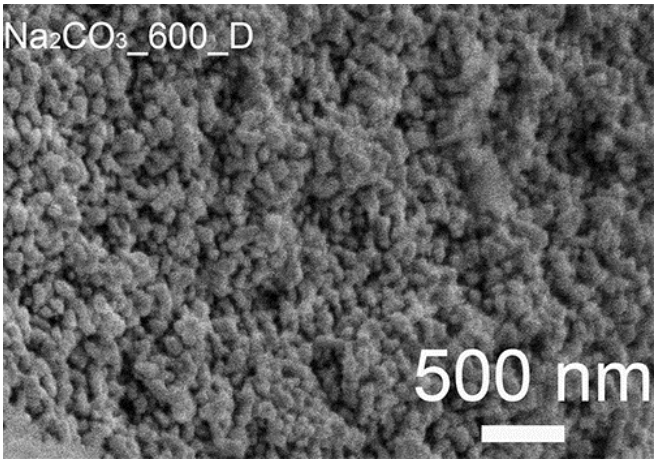

Figure 5-23: SEM image for Na_2CO_3_600_D at a working distance of approximately 10 mm.

After the sample had been coated, the sample chamber was vented and the sample inserted into the chamber. This chamber was evacuated and the sample inserted into the high

vacuum chamber of the SEM; the stage was positioned at a working distance of approximately 10 mm. The vacuum was switched on and the RF carbon samples were bombarded with a beam of electrons accelerating at 20 keV. Each sample was imaged at three different sites and at magnifications of 30000, 100000 and 300000 X, allowing surface morphology to be investigated and permitting estimation of the average particle size, hence, comparison with published data [31, 47, 80, 162-164]. Table 5-15 provides an estimation of the sample area imaged. A small probe lens was used, in order to decrease the beam diameter and increase the depth of field, allowing the varied surface of the RF carbons to be imaged in high quality.

Table 5-15: Area sampled as a function of magnification [117].

Magnification	Area on sample
10	1 cm^2
100	1 mm^2
1,000	100 μm^2
10,000	1 μm^2
100,000	100 nm^2

5.9 UV-Visible spectroscopy

The UV-Vis absorbance spectra for RF sols prepared from Na_2CO_3, Cs_2CO_3 and $CaCO_3$ with molar R/C rations of 200 and 400, were obtained by measuring the log of the sample reflectance (R), using a Varian Cary 5000 UV-Vis-NIR spectrometer (Figure 5-24). The sample reflectance is related to the absorbance, A, as shown in Equation 144 [165]. As expected, as the reflectance increases the absorbance of light will decrease, consequently the log of the reciprocal of reflectance is proportional to the sample absorbance.

$$A = \log\left(\frac{1}{R}\right)$$

Equation 144

The Varian Cary 5000 is capable of measuring absorbance at either a single wavelength or over a range, and can measure between 175 nm and 3500 nm. Consequently absorbance can be studied over the full visible to NIR range, however, Berho *et al*. [166] studied the UV-Vis absorbance of non-absorbing species and illustrated that for particles less than 1 µm, absorbance was inversely proportional to the wavelength of light. Given that the RF particles are much smaller than 1 µm and given that MS analysis and literature indicates that RF sols absorb strongly at 273 nm, a shorter wavelength region of 200 nm to 800 nm was chosen. This range ensures that sensitive absorbance in the UV range was observed, however also allowed the visible absorbance to be studied.

Prior to analysis a background spectra was measured, which was then subtracted from the sample spectrum. RF sols were made following the general synthesis procedure discussed in section 5.1.1. After the 30 minute stir at room temperature, a small sub sample of the sol was extracted into a 2mm wide quartz cuvette. The absorbance spectrum obtained was classified as T_0. The remaining sol was placed immediately in the oven and small samples were extracted at sequential time intervals and the absorbance measured, allowing time resolved spectra to be obtained. Samples were measured until the viscosity was such that the sample could not be extracted into the quartz cell, at this stage the sols were close to the gelation point.

Figure 5-24: Varian Cary 5000 UV-Vis-NIR spectrometer [111].

5.10 IR spectrometry

In order to determine the IR adsorption of both dried and carbonised samples a small amount of gel/carbon was ground into a fine powder, using a mortar and pestle. A small spatula was used to transfer the sample onto the single reflection diamond/ZnSe ATR crystal, held within the ABB MIRacle sampling kit, and IR spectra were acquired with an ABB MB3000 FT-IR laboratory spectrometer (Figure 5-25). 32 scans were taken in the range of 4000 to 600 cm^{-1} with a detector resolution of 4 cm^{-1}.

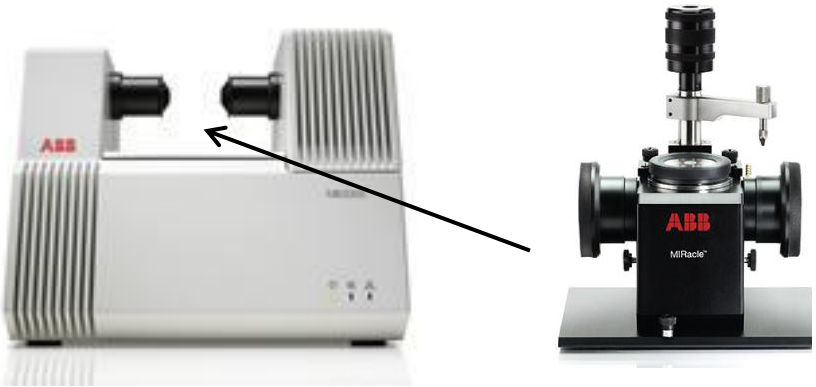

Figure 5-25: ABB MB3000 FT-IR laboratory spectrometer, and ABB MIRacle™ [167].

.

6 Results Part 1 – General synthesis

6.1 Gel preparation repeatability

In order to determine the repeatability of gel preparation seven Na_2CO_3_300 gels and four Na_2CO_3_600 gels were prepared under identical conditions and the properties of each R/C group compared. The comparison of properties for R/C 300 and 600 are illustrated in Table 6-1 and Table 6-2 respectively.

Table 6-1: Gel properties for Na_2CO_3_300 repeats

Gel	S_{BET} (m^2/g)	V_{TOT} (cm^3/g)	V_{MIC} (cm^3/g)	V_{MES}(cm^3/g)	$Dp_{average}$
1	494	0.800	0.036	0.764	6.98
2	517	0.786	0.038	0.748	6.55
3	516	0.811	0.041	0.770	6.86
4	490	0.743	0.032	0.710	6.4
5	488	0.755	0.033	0.722	6.61
6	514	0.794	0.045	0.749	6.84
7	494	0.714	0.034	0.680	6.06
Mean	502	0.772	0.037	0.735	6.61
Stdev	13.1	0.035	0.005	0.032	0.317
RSD	0.026	0.046	0.128	0.044	0.048
% RSD	2.61	4.59	12.8	4.39	4.79

Table 6-2: Gel properties for Na_2CO_3_600 repeats

Gel	S_{BET} (m^2/g)	V_{TOT} (cm^3/g)	V_{MIC} (cm^3/g)	V_{MES}(cm^3/g)	$Dp_{average}$
1	340	0.982	0.040	0.943	15.2
2	355	1.07	0.038	1.04	15.3
3	325	0.970	0.028	0.951	15.1
4	363	1.02	0.034	0.986	13.78
Mean	346	1.01	0.035	0.976	4.8
Stdev	16.9	0.047	0.005	0.045	0.706
RSD	0.049	0.046	0.149	0.045	0.048
% RSD	4.88	4.61	14.9	4.57	4.76

The results presented demonstrate that the gel preparation process is repeatable, with all properties, with the exception of V_{MIC}, repeatable to within 5 %. As the gels are mainly mesoporous, and given the number of experimental variables involved this repeatability is considered reasonable. The repeatable properties, of analogous RF gels, are demonstrated by the N_2 adsorption/desorption isotherms and PSD illustrated in Figure 6-1.

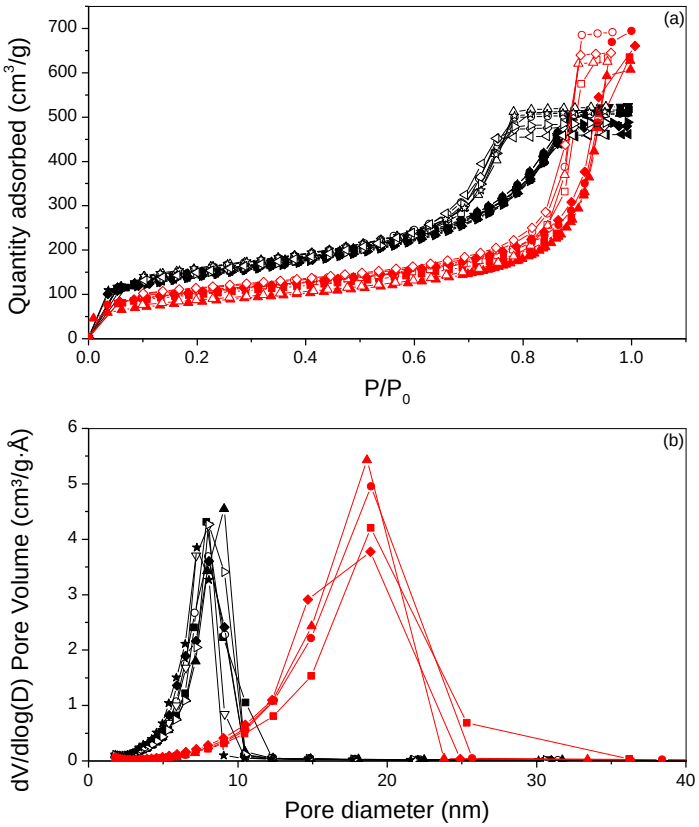

Figure 6-1: (a) N_2 adsorption (closed symbols) and desorption (open symbols) and (b) PSDs for Na_2CO_3_300 (black) and Na_2CO_3_600 (red).

Figure 6-2 and Figure 6-3 illustrate the normal probability distributions for the gel characteristics for Na_2CO_3_300 and Na_2CO_3_600 repeats, respectively. All displayed probability plots show relatively straight lines, indicative of normally distributed data. Consequently, it can be concluded that all properties follow a normal Gaussian distribution, for gels prepared under the same experimental conditions, demonstrating that the gel preparation process is repeatable producing RF gels with comparable properties.

This repeatability, for gels prepared with analogous R/C ratios, suggests that gels prepared with varying R/C ratios will have dissimilar properties allowing comparisons to be carried out.

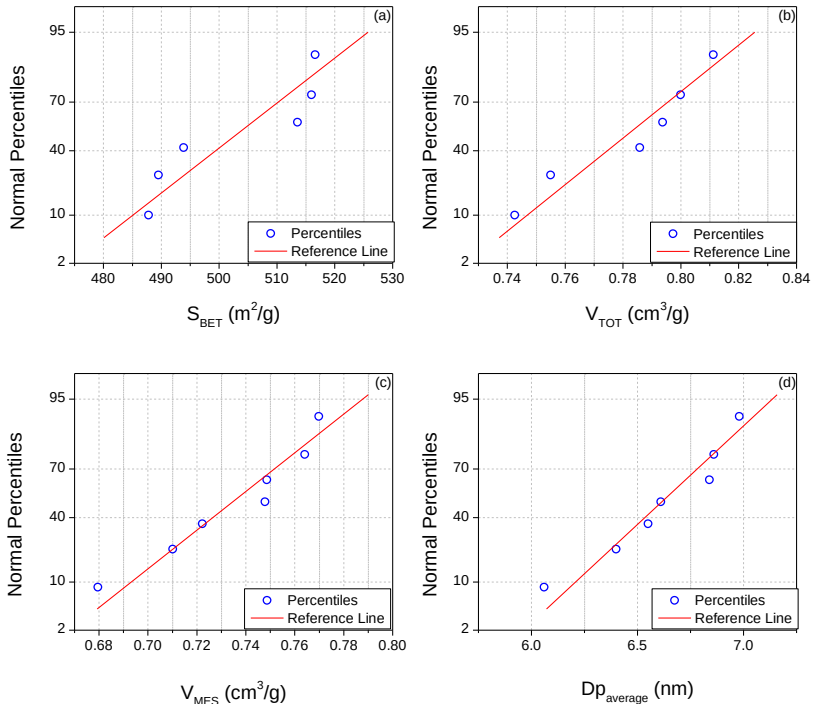

Figure 6-2: Normal probability distribution for (a) S_{BET}, (b) V_{TOT}, (c) V_{MES} and (d) $Dp_{average}$ for Na_2CO_3_300 repeats.

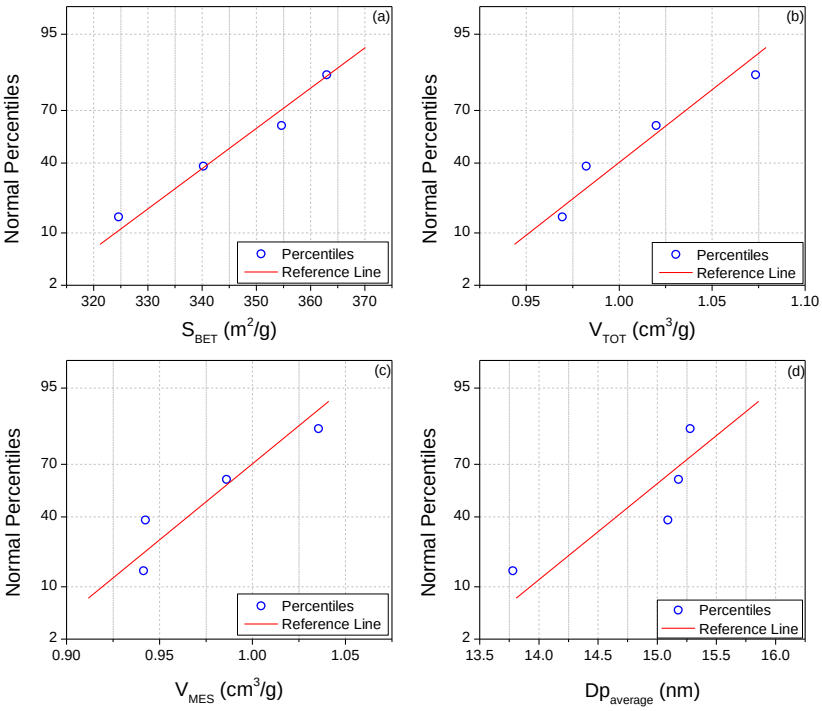

Figure 6-3: Normal probability distribution for (a) S_{BET}, (b) V_{TOT}, (c) V_{MES} and (d) $Dp_{average}$ for Na_2CO_3_600 repeats.

6.2 Effect of R/C ratio

The nitrogen adsorption/desorption isotherms and pore size distributions (PSDs) for xerogels prepared using Na_2CO_3 and $NaHCO_3$ are shown in Figure 6-4. The isotherms are all Type IV, indicating that they are mainly mesoporous in nature, and the hystereses progress from Type H2 to Type H1 with increasing R/C ratio, which is likely to be caused by a decrease in pore depth [168].

The effects of changing R/C ratio on the properties of xerogels are as expected, with the average pore size and total pore volume generally decreasing and specific surface area increasing as R/C ratio decreases (i.e. catalyst concentration increases) [15, 65, 67, 78]. This is indicative of the mechanism discussed previously in section 2.6.1.

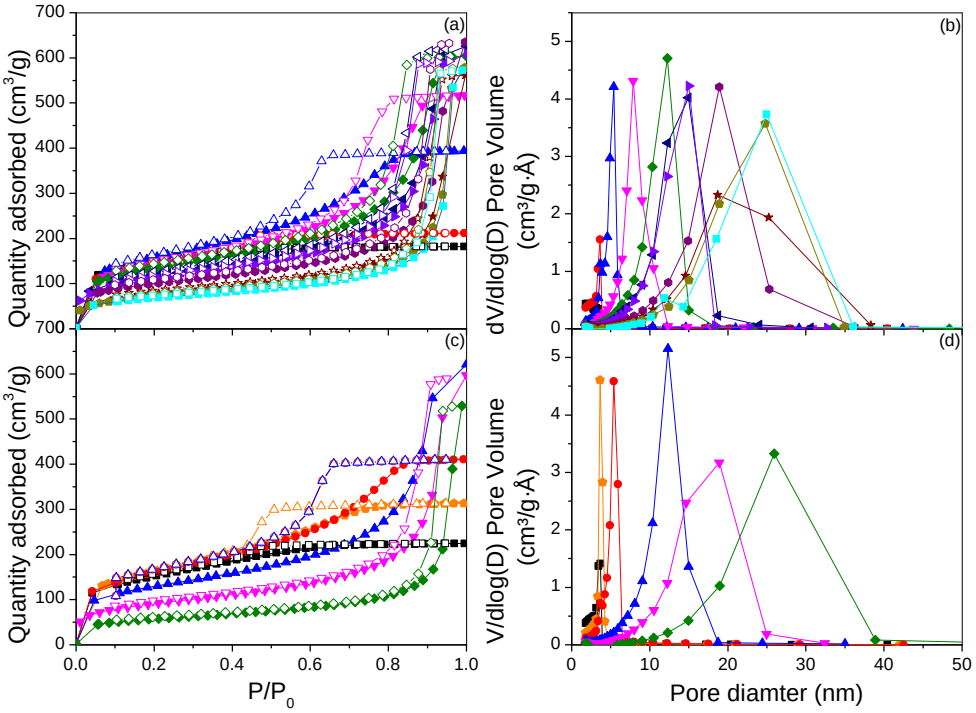

Figure 6-4: (a) N_2 adsorption (closed symbols) and desorption isotherms (open symbols) and (b) PSD for Na_2CO_3_50_D (!), Na_2CO_3_100_D (,), Na_2CO_3_200_D (7), Na_2CO_3_300_D (B), Na_2CO_3_400_D (Λ), Na_2CO_3_450_D (β), Na_2CO_3_500_D (Ω), Na_2CO_3_600_D (,), Na_2CO_3_700_D (ξ), Na_2CO_3_750_D (□), Na_2CO_3_800_D (!) and (c) adsorption (closed symbols) and desorption isotherms (open symbols) and (d) PSD for $NaHCO_3$_50_D (!), $NaHCO_3$_75_D (□), $NaHCO_3$_100_D (,), $NaHCO_3$_200_D (7), $NaHCO_3$_300_D (B) and $NaHCO_3$_400_D (Λ).

Similar trends with changing R/C ratio are observed for all catalysts used (see Chapter 16 Appendix D).

6.2.1 R/C ratio limits

Figure 6-5 displays the N_2 adsorption and desorption isotherms for Na_2CO_3 gels prepared with R/C ratios in the region of 5 – 50. The isotherms indicate that below R/C 50 the quantity of N_2 adsorbed diminishes significantly, indicating that the surface areas and resultant pore volumes decrease considerably, with declining R/C ratios. This decrease in surface area results from a lack of cross-linking within the gel structure, caused by reduced gelation times. The isotherms for pyrolysed R/C 50 and 100 gels demonstrate that although the dried xerogels exhibit porous characteristics, the structures are not strong enough (i.e. cross-linked enough) to withstand the harsh pyrolysis conditions, and subsequently collapse into non porous carbons.

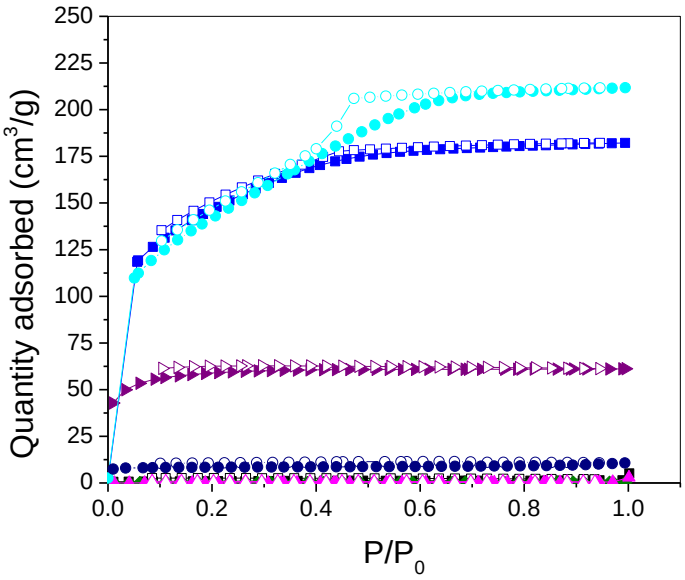

Figure 6-5: N_2 adsorption (closed symbols) and desorption isotherms (open symbols) for Na_2CO_3_100_D (,), Na_2CO_3_100_DP (,) Na_2CO_3_50_D (!), Na_2CO_3_50_DP (!), Na_2CO_3_25_D (β), Na_2CO_3_10_D (7) and Na_2CO_3_5_D (Λ).

This increased shrinkage for low R/C gels results from the variances in particle interconnection observed at different R/C ratios [15, 18, 169, 170]. At low R/C ratios, particles are small and are connected by large necks, which results in the gel having a fibrous rigid appearance, whereas at high R/C ratios the larger particles are interconnected by small necks and adopt a 'string of pearls appearance. Consequently, when stress is exerted on the structures the fibrous (low R/C) structures cannot adjust their structure, resulting in significant shrinkage, whereas the string of pearls structure has more mobility and is, therefore, able to contend with a higher level of stress. Given these results, the lower R/C limit for gel synthesised using Na_2CO_3 was set at R/C 50 for dried xerogels and R/C 200

for pyrolysed gels (this carbon has surface area of 481 m^2/g compared to 25.6 m^2/g for the pyrolysed R/C 100).

The upper R/C limit for Na_2CO_3 gels was set at 800, above this ratio the gelation time extended beyond 24 hours and the gel structure became weak due to the large mesopores/macropores within the structure, as demonstrated by Figure 6-6.

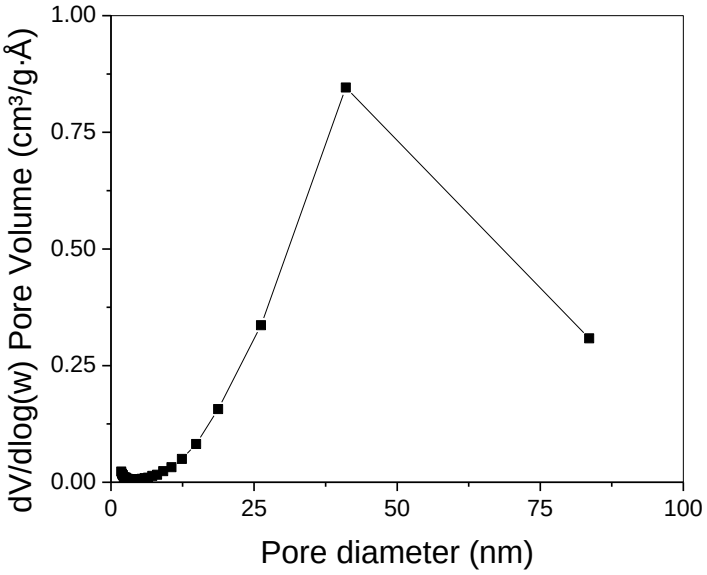

Figure 6-6: PSD for Na_2CO_3_900_D.

K_2CO_3 reacts in a similar manner to Na_2CO_3, therefore similar R/C limits will exist. For reasons, discussed in Chapter 7, the R/C limits for $NaHCO_3$, $KHCO_3$, NaOH and KOH would be half of the limits obtained for the Na_2CO_3 catalysed gels, i.e. a lower limit of 25 and an upper limit of 400. Xerogels prepared from Cs_2CO_3 and $CsHCO_3$ have smaller R/C ranges, when compared to their Group I counterparts (Cs_2CO_3 R/C range 100 – 500 and $CsHCO_3$ range of, 50 – 300), this is caused by increased particle size within the gel structure, which results is weaker structures. It should be noted that only a selection of R/C ratios were prepared and carbonised (see Table 7-1). For the Group II catalysts, the pore sizes within the xerogel structures increased significantly when compared to the analogous Group I prepared gels, consequently, the R/C range was found to be approximately between 100 and 500 (again only a selection of xerogels were prepared and only some were carbonised, as detailed in Table 8-1).

6.2.2 Disappearance of reactants with changing R/C ratio

The consumption of R and F for different R/C ratios are illustrated in Figure 6-7 (a) and (b), respectively. These figures show that as the R/C ratio increases ([C] deceases) the rate of consumption of both R and F decreases. The disappearance of R indicates the formation of HMs, i.e. one R molecule forms one HM, thus the reduced consumption of R, with increasing R/C ratio, indicates that fewer HMs are forming. This is in-line with the reports by Pekala *et al*. [11], who reported that at higher [C] more anions are formed initially, forming more HM and, as a result, more small clusters.

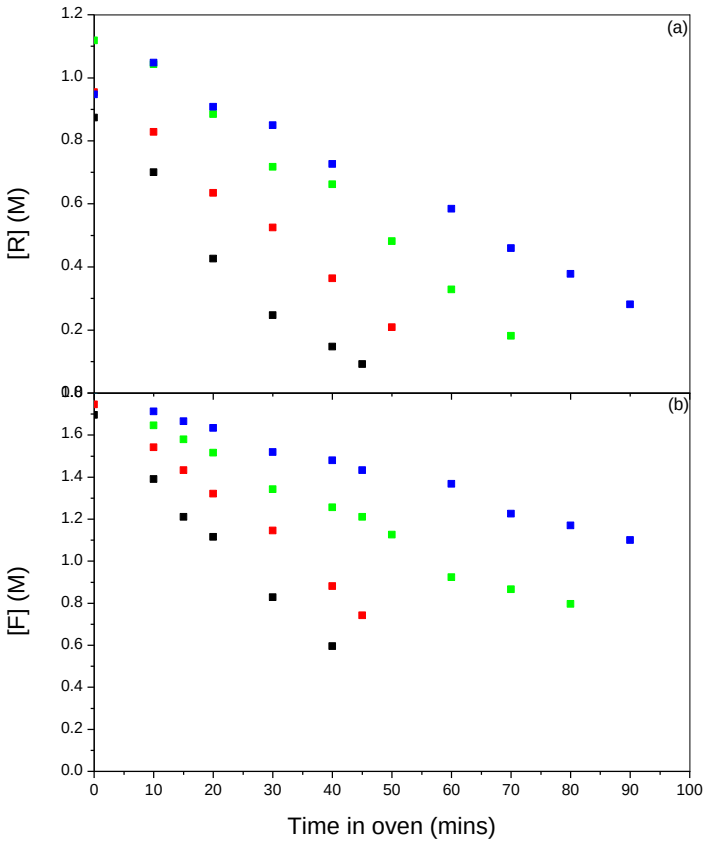

Figure 6-7: Consumption of R (a) and F (b) as a function of time in the oven for Na_2CO_3_100 (black), Na_2CO_3_200 (red), Na_2CO_3_400 (green) and Na_2CO_3_600 (blue).

Figure 6-8 displays the ratio of F to R consumption (F consumptions were interpolated to allow direct comparison with R consumption – see Chapter 14 Appendix B) for Na_2CO_3_100, 200, 400 and 600. This figure shows that in general the ratio of [F]/[R] lies between 1 and 1.5, indicating that a mixture of mono and di-substituted HM are likely to be forming. This value of between 1 and 1.5 is similar to that shown by Pekala *et al*. [11] for RF system with an R/C ratio of 200. Figure 6-8 shows that, with the exception of R/C 100, the ratio of F to R consumption generally decreases, with increasing R/C ratio. This is

consistent with the proposed *'preferential growth'* theory, as it is expected that substitution would decrease, as aggregation increases, resulting in a reduction in F consumption and, in turn, a decrease in F/R consumption. The reaction between R and F, within the R/C 100 gel, will be limited by gelation time, and consequently, a reduced F/R consumption is observed.

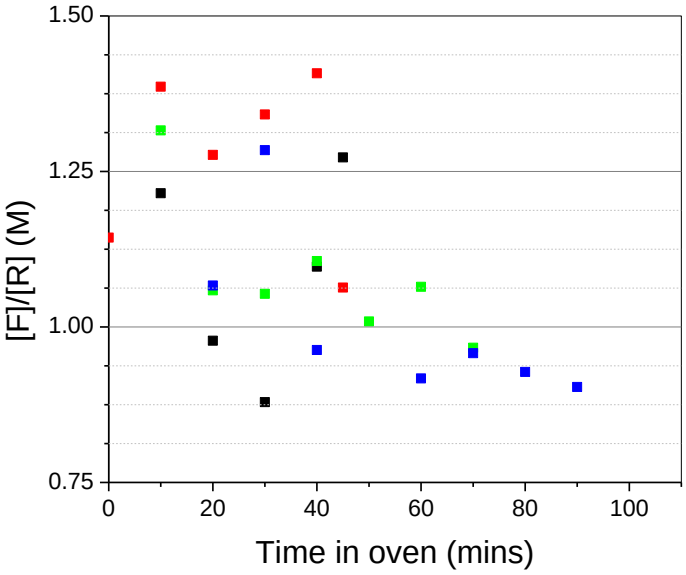

Figure 6-8: Ratio of consumption of F to R for Na_2CO_3_100 (black), Na_2CO_3_200 (red), Na_2CO_3_400 (green) and Na_2CO_3_600 (blue).

6.2.3 Particle growth – DLS

As displayed in Figure 6-4, the average pore diameter increases with increasing R/C ratio, which, as discussed in Section 2.6.1, is indicative of the '*auto-catalytic growth mechanism'* proposed by Pekala *et al*. [11], whereby higher concentrations of C result in enhanced concentrations of anions leading to small clusters, small pores and reduced particle size, whereas lower concentrations of C result in '*preferential growth of polymer clusters'* resulting in the presence of larger pores and larger particles. In the higher R/C gels less R anions will form and as a result less HM will form. As these HM are more reactive than R they will preferentially aggregate forming larger particles. Figure 6-9 shows the change in primary particle size with reaction time for Na_2CO_3 gels, prepared with a variety of R/C ratios (where time 0 indicates when sols were placed in the oven). Figure 6-9 demonstrates that, as expected, the particle size peaks at larger values with increasing catalyst concentration, confirming that initial particles, prior to aggregation, are larger in high R/C gels.

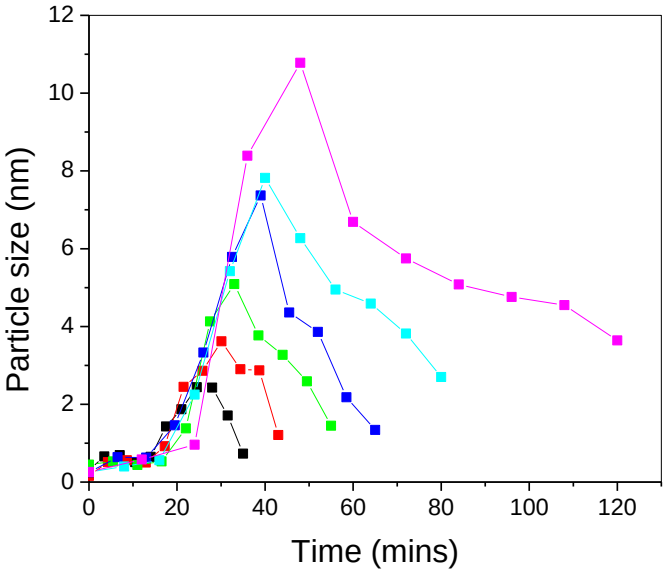

Figure 6-9: DLS results for Na_2CO_3 gels prepared with R/C ratio of 100 !, 200 !, 300 !, 400 !, 500 !, and 600 ! [171].

As will be discussed in Chapter 7, the average pore diameter increases linearly with increasing R/C ratio (see Figure 7-1), from the results presented in Figure 6-9, it is clear the that average particle size shows a similar trend and Figure 6-11 demonstrates that this relationship is also linear. Considering Pekala's proposed synthesis theory [11], it follows that the pore size should be directly dependent on particle size. Figure 6-11 demonstrates that this is true, with primary RF particle size and pore diameter exhibiting a correlation of 99.6 % (r^2 = 0.99106). Consequently it can be concluded that average pore diameter is directly dependent on particle aggregation during the sol-gel transition.

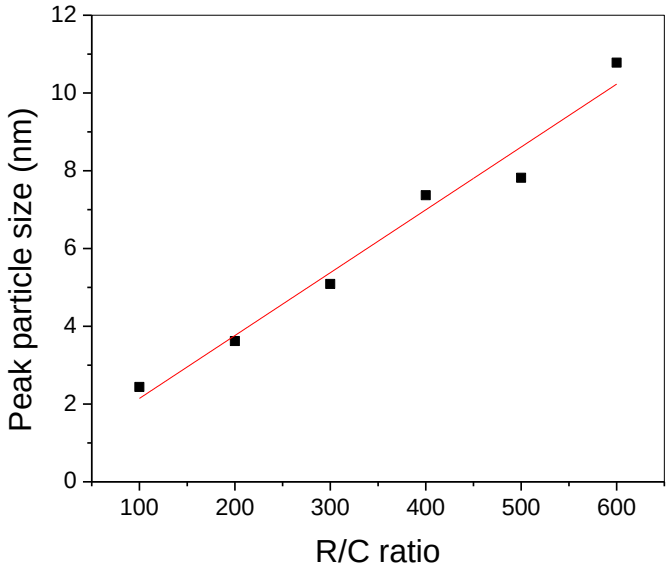

Figure 6-10: DLS peak particle size with R/C ratio for Na_2CO_3 gels.

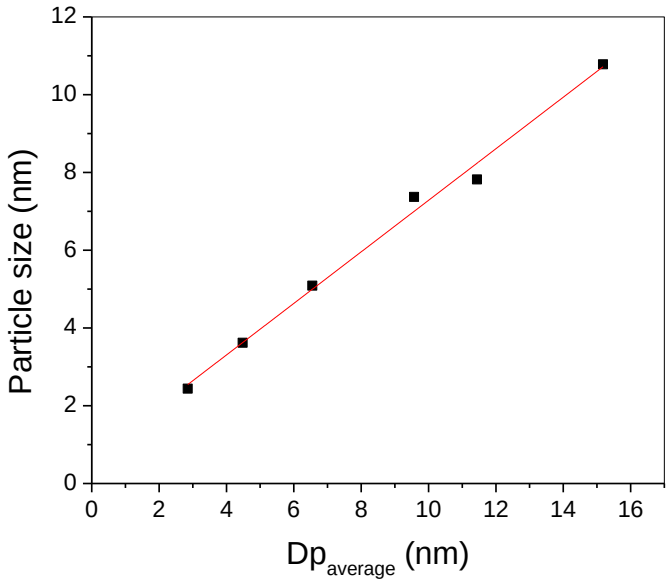

Figure 6-11: Relationship between $Dp_{average}$ (nm) and primary particle size.

6.2.4 SEM

SEM images for Na_2CO_3_200, Na_2CO_3_400 and Na_2CO_3_600 demonstrate that, in line with the DLS results and as expected, the particle size increases with increasing R/C ratio

(decreasing [C]). Magnification at 300 k allows the best comparison of particle size, demonstrating small densly packed particles of approximately 25 nm (Figure 6-14), for R/C 200, larger particles of approximately 50 nm, for R/C 400 (Figure 6-17) and less dense particles of approximately 100 nm for Na_2CO_3_600 (Figure 6-20).

(a) Na_2CO_3_200_DP

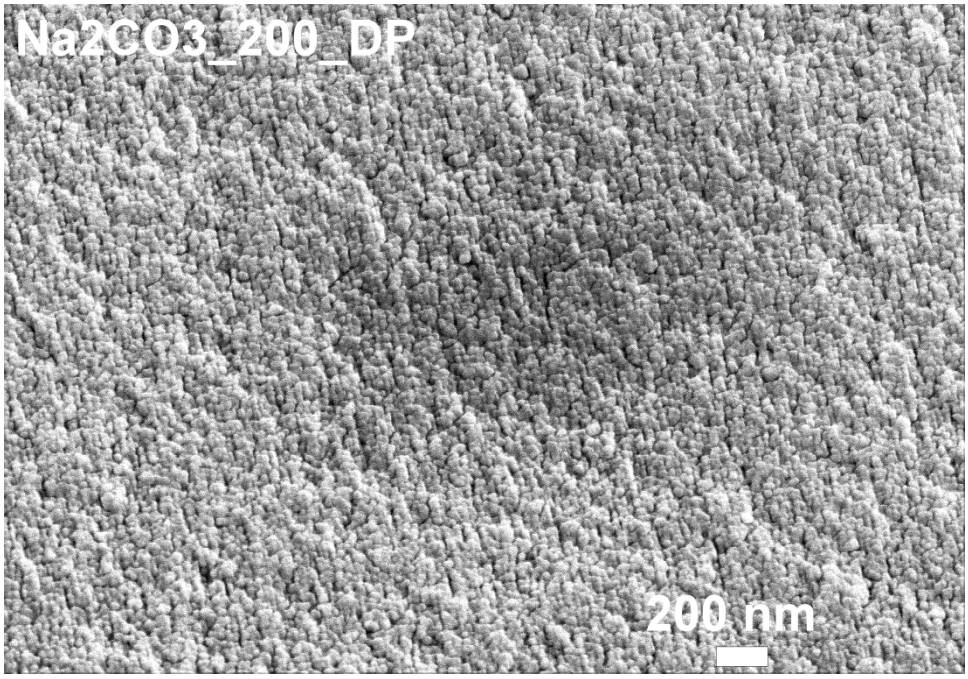

Figure 6-12: SEM images for Na_2CO_3_200_DP with magnification of 30 k.

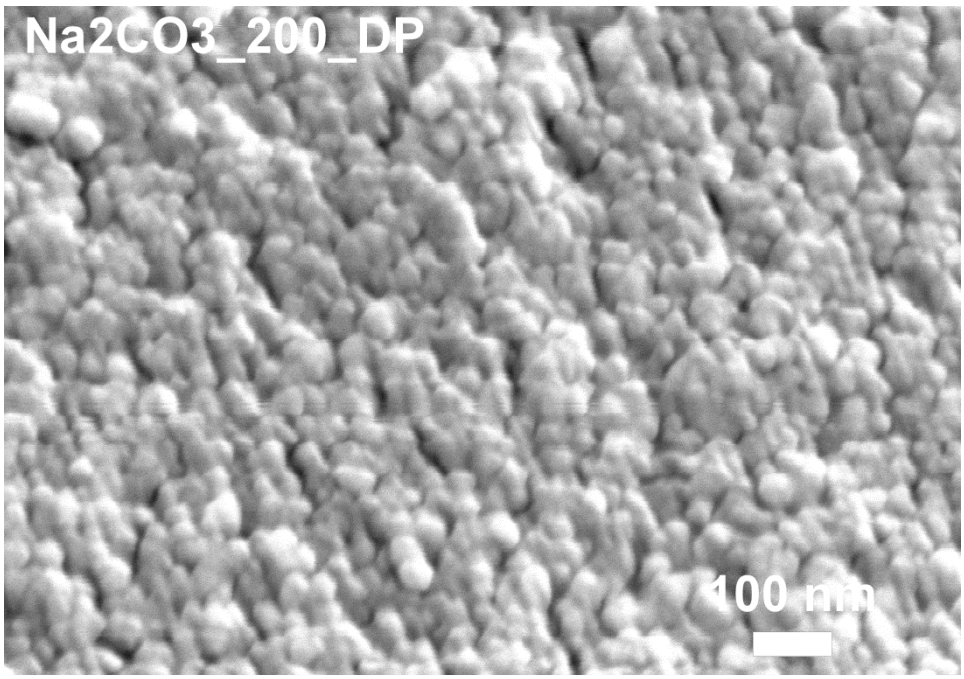

Figure 6-13: SEM images for Na_2CO_3_200_DP with magnification of 100 k.

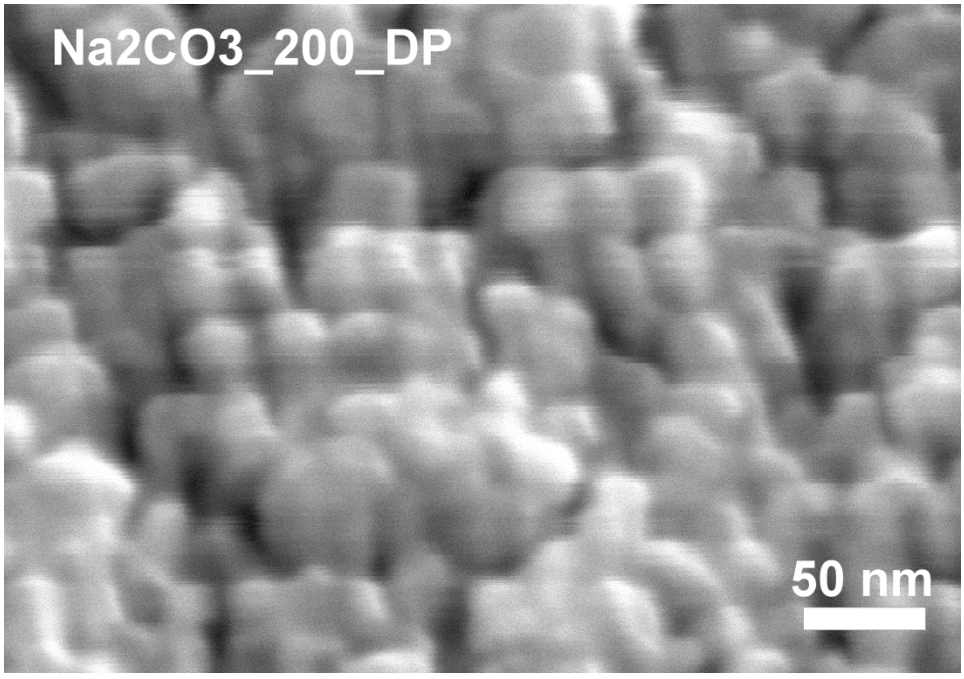

Figure 6-14: SEM images for Na_2CO_3_200_DP with magnification of 300 k.

(b) ***Na_2CO_3_400_DP***

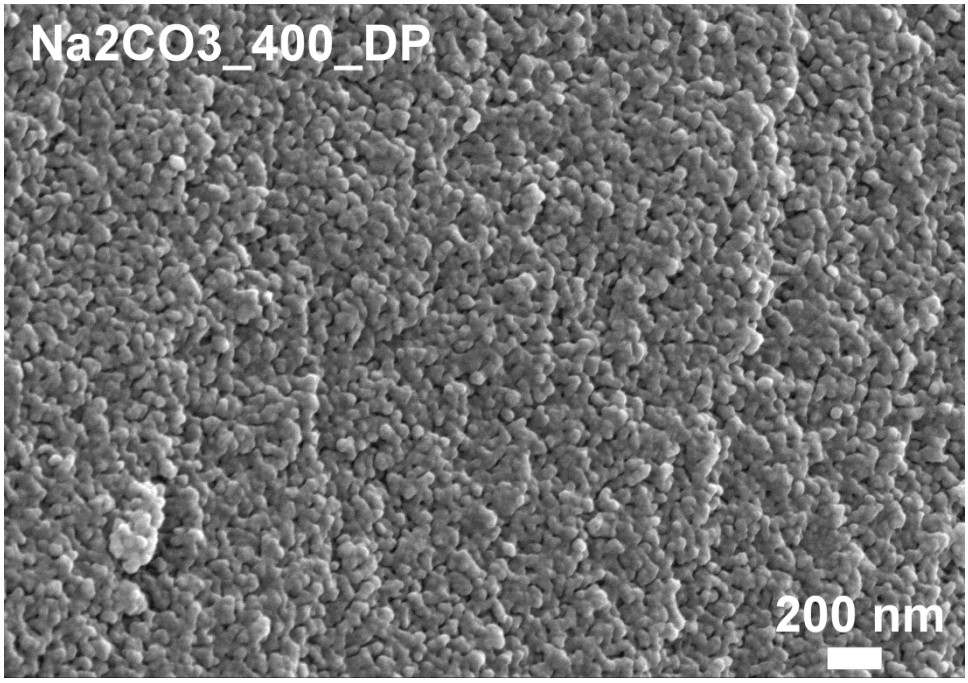

Figure 6-15: SEM images for Na_2CO_3_400_DP with magnification of 30 k.

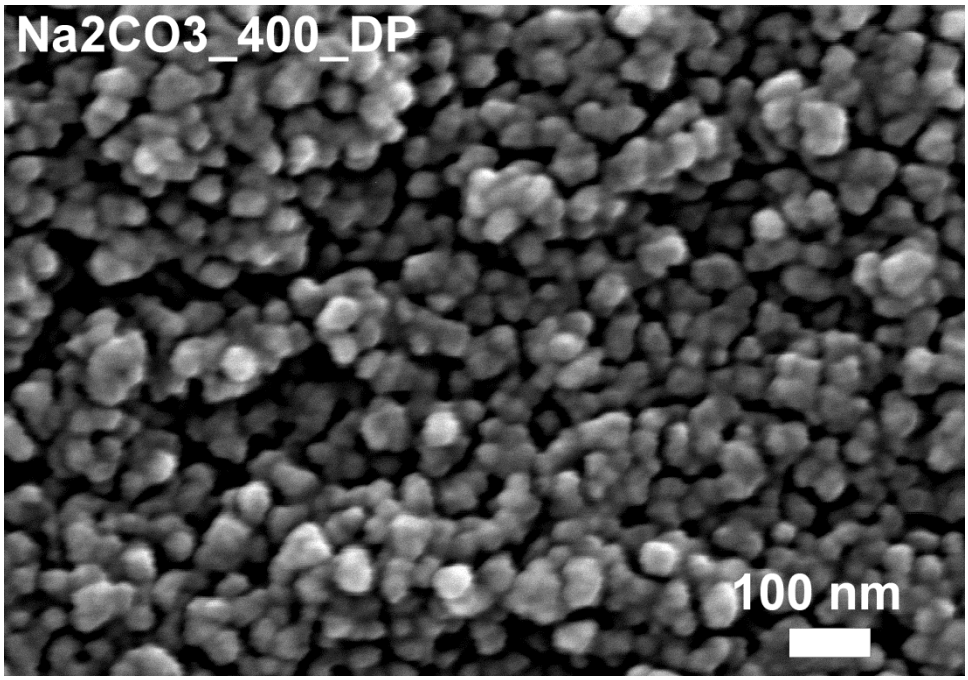

Figure 6-16: SEM images for Na_2CO_3_400_DP with magnification of 100 k.

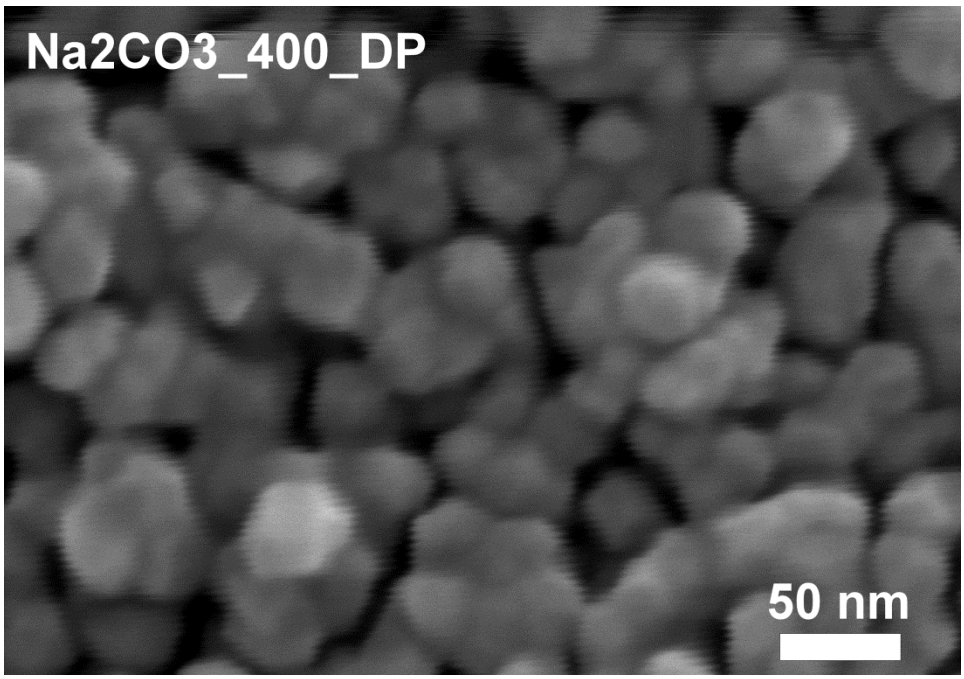

Figure 6-17: SEM images for Na_2CO_3_400_DP with magnification of 300 k.

(c) Na_2CO_3_600_DP

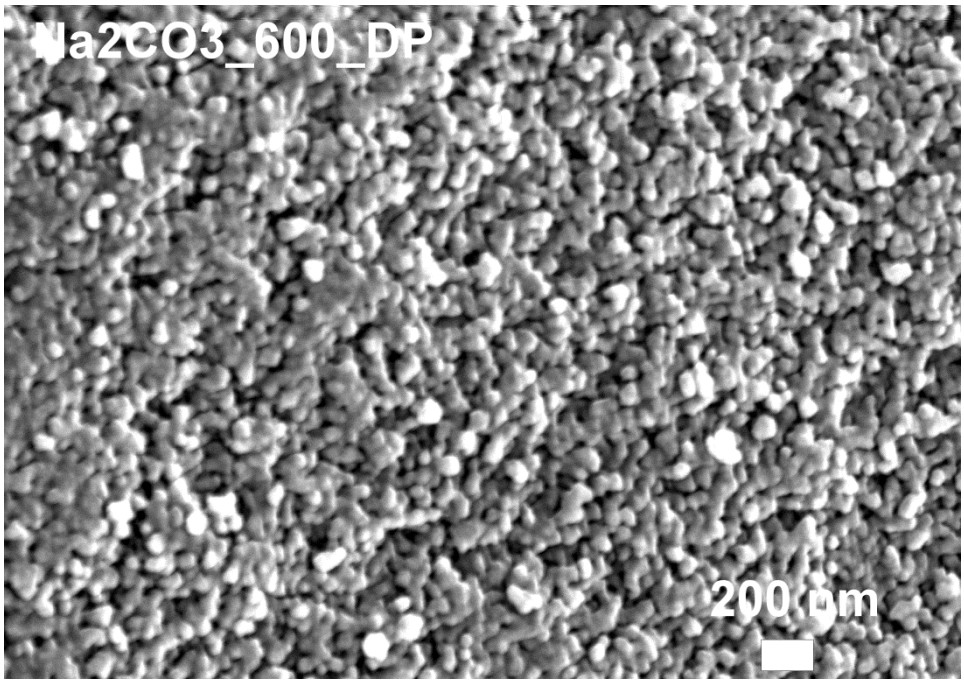

Figure 6-18: SEM images for Na_2CO_3_600_DP with magnification of 30 k.

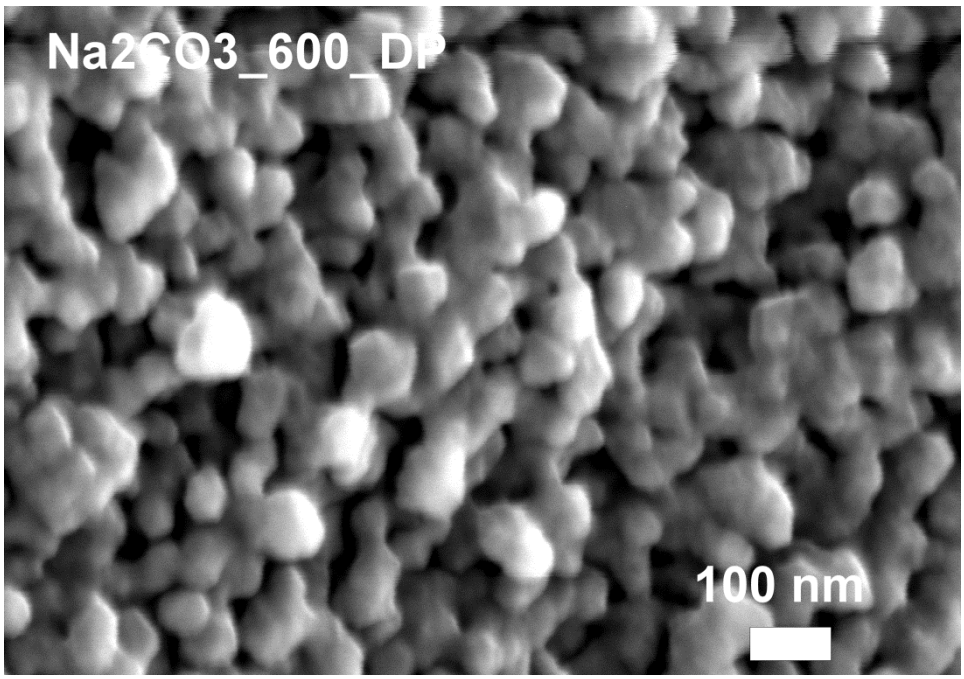

Figure 6-19: SEM images for Na_2CO_3_600_DP with magnification of 100 k.

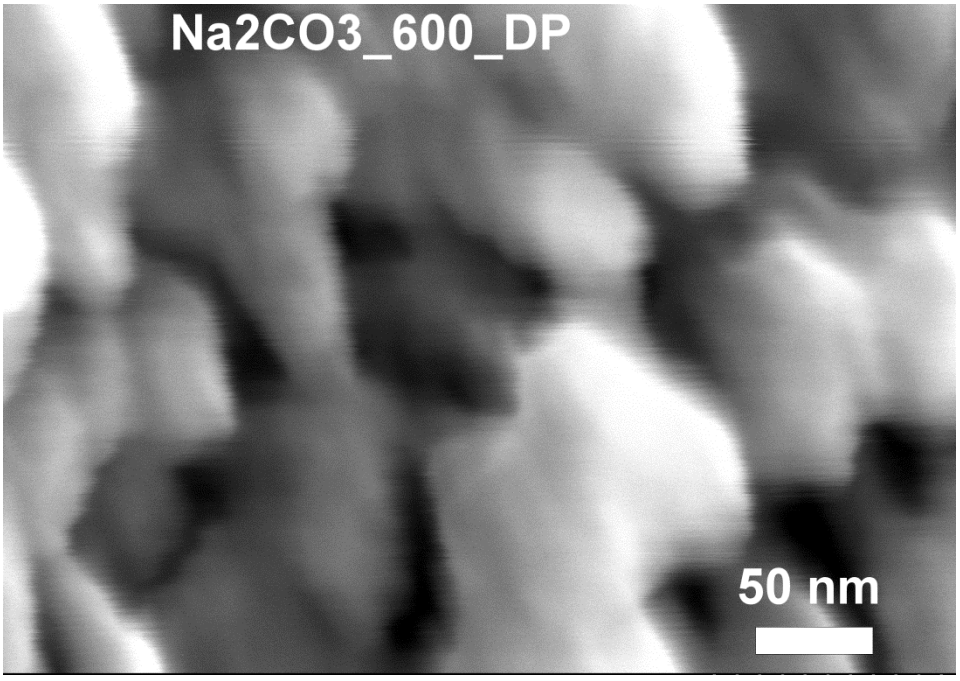

Figure 6-20: SEM images for Na_2CO_3_600_DP with magnification of 300 k.

6.3 IR

The IR absorbance spectra of dried xerogels prepared from Na_2CO_3, $NaHCO_3$ and $CaCO_3$ are displayed in Figure 6-21. These compounds exhibit strong absorbance due to aromatic C=C stretches (1600 cm^{-1}), aliphatic stretches (1450 – 1470 cm^{-1}), C-O stretching (1090 cm^{-}

^{1}) and broad O-H absorption (3000 cm^{-1}). This absorption pattern is typical of dried RF xerogels [164] and confirms that the chemical structure is as expected.

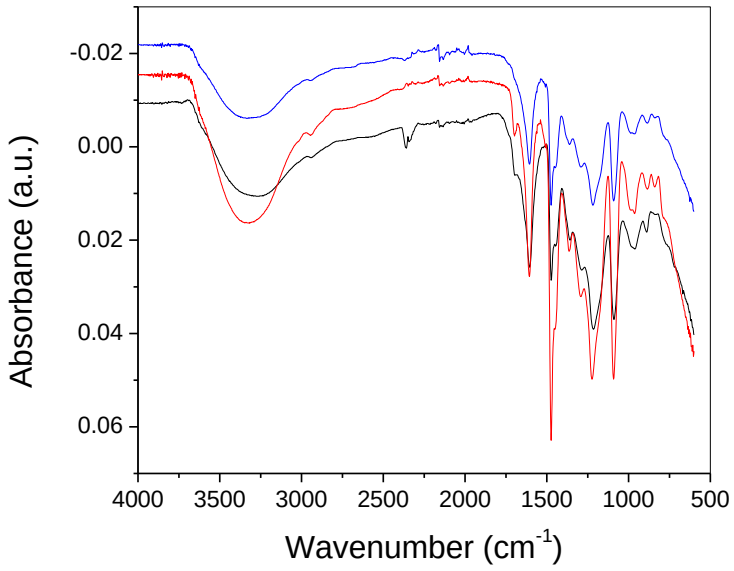

Figure 6-21: IR spectra for Na_2CO_3_300_D (black), $NaHCO_3$_300_D (blue) and $CaCO_3$_300_D (red).

After pyrolysis the RF structures are transformed into carbonised materials, consequently they will contain very few dipole moments. As a result there is minimal stretching and bending and very little absorbance occurs [164]. This is demonstrated by Figure 6-22, which shows the IR spectra for the pyrolysed derivatives of the xerogels shown in Figure 6-21.

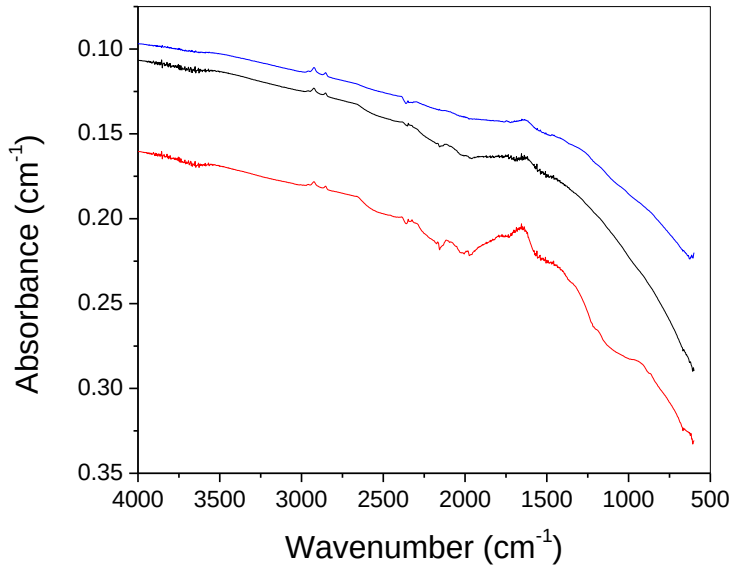

Figure 6-22: IR spectra for Na_2CO_3_300_DP (black), $NaHCO_3$_300_DP (blue) and $CaCO_3$_300_DP (red).

6.4 Sol pH

In order to determine the repeatability and reproducibility of sol pHs, a number of repeat measurements for Na_2CO_3_100 and 300 were obtained using two different operators. The obtained pHs are given in Table 6-3.

Table 6-3: Obtained pHs for repeat measurements

	Na_2CO_3_100 Operator 1	Na_2CO_3_100 Operator 2[5]	Na_2CO_3_300 Operator 1	Na_2CO_3_300 Operator 25
	6.96	7.00	7.37	7.39
	6.98	7.00	7,37	7.43
	6.98	7.02	7.38	7.37
	7.02	7.05	7.37	7.42
	6.98	-	-	7.42
	-	-	-	7.35
Mean	6.98	7.02	7.37	7.40
Stdev	0.022	0.024	0.005	0.032
RSD	0.0032	0.0034	0.00068	0.0043
% RSD	0.32	0.34	0.068	0.43

The ANOVA results for R/C 100 and 300 are given in Table 6-4 and Table 6-5 respectively, and demonstrate that the difference between the within sample and between sample variance is not significant (i.e. $F_{calc} < F_{crit}$), which shows that measurements obtained from different operators are within similar variance to pH measurements obtained by one single operator.

Table 6-4: ANOVA results for Na_2CO_3_100 repeats

SUMMARY

Groups	*Count*	*Sum*	*Average*	*Variance*
Operator 1	4	29.55	7.3875	0.000825
Operator 2	6	44.38	7.396667	0.001027

ANOVA

Source of Variation	*SS*	*df*	*MS*	*F*	*P-value*	*F crit*
Between Groups	0.000202	1	0.000202	0.212048	0.657425	5.317655
Within Groups	0.007608	8	0.000951			
Total	0.00781	9				

Table 6-5: ANOVA results for Na_2CO_3_300 repeats

SUMMARY

[5] These gels were prepared by Stewart Taylor, Department of Chemical and Process Engineering, University of Strathclyde, Glasgow.

Groups	*Count*	*Sum*	*Average*	*Variance*
Operator 1	5	34.92	6.984	0.00048
Operator 2	4	28.07	7.0175	0.000558

ANOVA

Source of Variation	*SS*	*df*	*MS*	*F*	*P-value*	*F crit*
Between Groups	0.002494	1	0.002494	4.855973	0.063391	5.591448
Within Groups	0.003595	7	0.000514			
Total	0.006089	8				

The RSD of the all pH measurements are within 1 % demonstrating that sol pH is repeatability to within 1 %.

6.4.1 Reduction in sol pH with reaction

Previous studies have maintained that the initial sol pH is a critical factor for controlling RF gel properties and it is theorised that this dependence is due to the initial sol pH controlling the extent of the condensation reaction between R and F [3]; with too high an initial sol pH (low R/C) hindering the condensation reaction and too low a pH (high R/C) hampering the formation of R anions.

Recent work by Gaca [172] has demonstrated that during the initial stages of reaction (for most R/C ratios), the pH of the RF sol drops to approximately 5. These results are illustrated in Figure 6-23, which demonstrates that for low R/C ratios (50 & 100) the high catalyst concentration results in rapid gelation at a higher pH than normal, which is consistent with the results discussed in Section 6.2.1. For R/C ratios greater than 100 the pH drops significantly during the reaction and gelation occurs between a pH of 4.75 and 5.5.

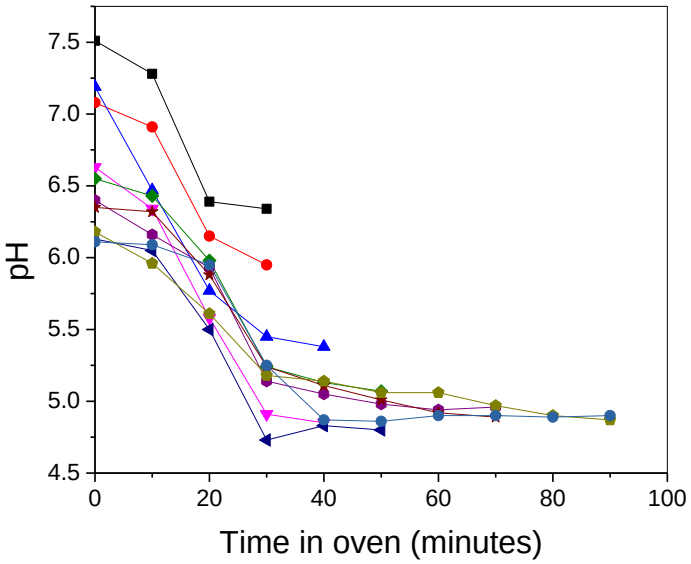

Figure 6-23: Change in sol pH with reaction time for Na_2CO_3_50 (!), Na_2CO_3_100 (,), Na_2CO_3_150 (7), Na_2CO_3_200 (B), Na_2CO_3_250 (Λ), Na_2CO_3_300 (Ω), Na_2CO_3_450 (,), Na_2CO_3_500 (ξ), Na_2CO_3_550 (□), Na_2CO_3_600 (,).

These results are consistent with previous proposed theories and demonstrate that, if the initial pH is too high rapid reaction hinders the condensation reaction and results in a gel with limited porous structure. Gaca's results demonstrate that the pH drops to a consistent level for R/C ratios between 200 and 600; however, no theory was proposed to explain these results.

Qualitative LC results obtained in this study, for the change in HM concentration, appear to coincide with the drop in sol pH (see Figure 6-24). This figure demonstrates that after approximately 20 minutes in the oven the HM concentration rises to a peak, which coincides with the drop in sol pH. These results suggest that the increase in polar HMs causes a significant drop in pH, which then stabilises as the HMs react on, to form bridged compounds. From this it can be concluded that the RF gel properties are dependent on the formation of HM derivatives and their subsequent inter-reaction. If the catalyst concentration is too high, HMs form rapidly, resulting in gelation occurring before HMs have cross-linked. Consequently, it appears that the RF gel properties are dependent on the extent of the initial reaction between R and F and the subsequent formation of a cross-linked gel structure.

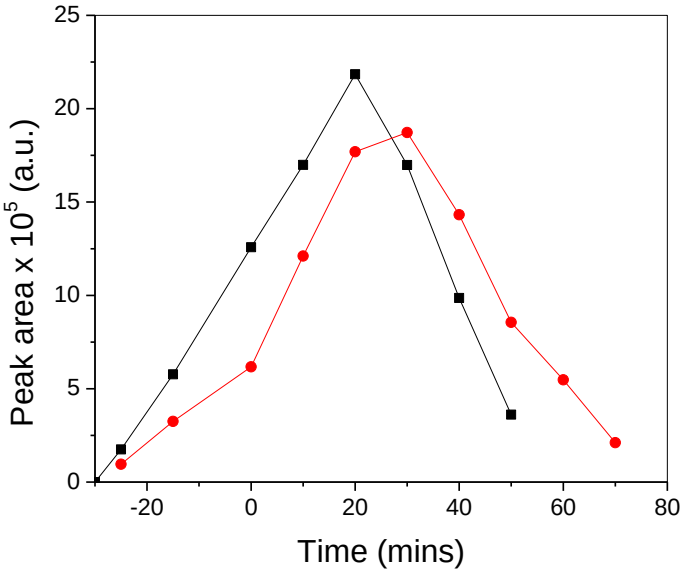

Figure 6-24: Change in HM peak area for Na_2CO_3_200 (black) and Na_2CO_3_400 (red) monitored on LC column 3, where T_0 is when the gel is placed in the oven.

7 Results Part 2 – Effect of Group I catalysts

7.1 Effect of R/C ratio

As discussed in section 6.2.1, there are R/C limits within which RF xerogels can be prepared. Consequently, to study the effect of this variable, the working limits were applied to the ratios studied. Table 7-1 summarises the gel characteristics for all xerogel/carbon gels made.

Table 7-1: Xerogel/carbon properties for all gels prepared using Group I catalysts

Gel	Initial sol pH	S_{BET} (m^2/g)	V_{TOT} (cm^3/g)	V_{MES} (cm^3/g)	V_{MIC} (cm^3/g)	$Dp_{average}$ (nm)
Na_2CO_3_50	7.64	497/3.17	0.282/0.008	0.214/0.008	0.068/0	2.49/3.20
Na_2CO_3_100	7.43	494/25.6	0.328/0.017	0.289/0.005	0.040/0.012	2.85/2.34
Na_2CO_3_200	7.22	546/481	0.609/0.361	0.572/0.223	0.037/0.138	4.48/3.61
Na_2CO_3_300	6.98	517/603	0.786/0.555	0.748/0.389	0.038/0.166	6.55/4.86
Na_2CO_3_400	6.91	461/597	0.936/0.794	0.892/0.629	0.043/0.164	9.57/8.30
Na_2CO_3_450	6.83	401/610	0.968/0.839	0.936/0.664	0.032/0.175	11.10/9.27
Na_2CO_3_500	6.69	379/536	0.916/0.762	0.886/0.598	0.0310.164	11.44/10.09
Na_2CO_3_600	6.57	340/591	0.982/0.974	0.943/0.788	0.0400.187	15.18/13.10
Na_2CO_3_700	6.54	264/576	0.869/0.920	0.843/0.727	0.026/0.193	16.77/14.22
Na_2CO_3_750	6.54	244/545	0.894/0.899	0.870/0.706	0.023/0.192	18.84/14.87
Na_2CO_3_800	6.51	231/526	0.282/0.008	0.214/0.008	0.026/0.196	20.05/15.94
K_2CO_3_100	7.43	520/42.8	0.367/0.027	0.329/0.009	0.039/0.019	3.00/3.09
K_2CO_3_200	7.21	536/525	0.658/0.416	0.622/0.269	0.036/0.147	5.02/3.81
K_2CO_3_300	7.00	476/581	0.849/0.671	0.812/0.513	0.037/0.158	7.91/6.79
K_2CO_3_400	6.91	431/586	1.030/0.857	0.987/0.695	0.043/0.162	11.51/9.59
K_2CO_3_500	6.78	350/594	0.980/0.965	0.946/0.784	0.033/0.181	14.06/12.29
Cs_2CO_3_100	7.16	466/497	0.833/0.610	0.801/0.496	0.032/0.114	8.06/6.67
Cs_2CO_3_200	7.11	399/587	1.107/0.956	1.078/0.798	0.029/0.158	12.91/10.62
Cs_2CO_3_400	6.85	234/545	1.327/1.003	1.307/0.827	0.020/0.176	26.45/22.66
Cs_2CO_3_500	6.47	106/523	0.463/0.914	0.451/0.704	0.012/0.210	25.11/29.26
$NaHCO_3$_50	7.23	522/38.1	0.348/0.023	0.300/0.018	0.047/0.005	2.86/2.69
$NaHCO_3$_75	7.13	562/191	0.485/0.112	0.445/0.066	0.041/0.046	3.46/2.83
$NaHCO_3$_100	6.92	552/506	0.635/0.397	0.594/0.142	0.041/0.256	4.72/3.8
$NaHCO_3$_200	6.80	441/606	0.961/0.807	0.920/0.169	0.041/0.639	10.11/8.26
$NaHCO_3$_300	6.79	316/613	0.923/0.935	0.896/0.191	0.027/0.744	14.00/11.67
$NaHCO_3$_400	6.53	196/550	0.819/0.893	0.788/0.205	0.021/0.689	22.09/16.34

Table 7-1 continued: Xerogel/carbon properties for all gels prepared

Gel	Initial sol pH	S_{BET} (m^2/g)	V_{TOT} (cm^3/g)	V_{MES} (cm^3/g)	V_{MIC} (cm^3/g)	$Dp_{average}$ (nm)
$KHCO_3$_100	6.89	506/467	0.570/0.367	0.543/0.224	0.027/0.143	4.43/3.65
$KHCO_3$_200	6.77	446/614	0.991/0.855	0.949/0.684	0.042/0.171	10.59/9.01
$KHCO_3$_300	6.52	310/589	0.968/0.948	0.940/0.076	0.028/0.183	15.38/12.74
$KHCO_3$_400	6.48	188/523	0.865/0.822	0.844/0.615	0.022/0.207	24.47/17.15
$CsHCO_3$_50	7.29	465/526	0.745/0.549	0.714/0.419	0.031/0.130	7.21/6.18
$CsHCO_3$_100	6.84	392/576	1.012/0.845	0.983/0.692	0.029/0.153	11.91/10.01
$CsHCO_3$_200	6.86	242/555	1.237/1.290	1.216/1.114	0.021/0.176	25.78/21.53
$CsHCO_3$_300	6.43	110/515	0.698/0.963	0.686/0.758	0.012/0.205	35.91/31.06
NaOH_100	7.41	531/516	0.662/0.429	0.625/0.024	0.037/0.014	5.11/4.03
NaOH_200	6.92	458/602	0.952/0.779	0.916/0.613	0.036/0.166	9.48/7.97
NaOH_300	6.75	346/598	0.951/0.852	0.921/0.668	0.029/0.184	13.31/10.59
NaOH_400	6.54	274/553	0.871/0.910	0.843/0.719	0.028/0.191	16.28/14.03
KOH_100	7.39	558/463	0.621/0.355	0.583/0.222	0.037/0.133	4.51/3.63
KOH_200	7.04	420/591	0.905/0.796	0.874/0.635	0.032/0.160	9.71/8.44
KOH_300	6.75	318/567	0.969/0.906	0.941/0.730	0.027/0.177	14.71/11.95
KOH_400	6.56	214/548	0.903/0.948	0.882/0.751	0.021/0.198	21.19/17.28

As presented in section 6.2 and Appendix D it is evident that there are general trends with R/C ratio for each individual Group I catalyst used. In general, as the R/C ratio increases the pore size increases, resulting in a decrease in surface area and overall increase in pore volume.

In order to compare the effect of R/C ratio, for all Group I catalysts, the average pore diameter, surface area, total and micropore volumes were plotted as illustrated in Figure 7-1. The relationship between R/C ratio and average pore diameter is approximately linear for all catalysts used (as R/C increases $Dp_{average}$ increases), see Figure 7-1 (a). For the gels prepared using carbonate catalysts the specific surface area remains approximately constant between R/C 50 and 400 and then decreases in a linear manner, see Figure 7-1 (b). In contrast the total pore volume increases linearly between R/C 50 and 400 and then remains constant, as the maximum pore volume is reached, see Figure 7-1 (c). These results indicate that the increase in pore volume between 50 and 400 corresponds to the creation of larger pores that have little or no effect on the surface area; above R/C 400, however, erosion of micropores into mesopores results in a decrease in surface area. For gels prepared with bicarbonates, the drop in surface area is observed at a lower R/C ratio (200), suggesting that micropores are lost at lower R/C ratios, this is confirmed in Figure 7-1 (d), which shows that the micropore volume for the bicarbonate gels decreases at a faster rate than the carbonate gels. The carbonised derivatives show similar trends as displayed in Appendix D.

From Figure 7-1 (a), (b) and (c), it is evident that there are two clear groupings between the Na and K carbonates and the Na and K bicarbonates/hydroxides, whereas the xerogels prepared using Cs catalysts demonstrate distinctive properties dissimilar to their Na or K counterparts. This will be discussed later in the chapter.

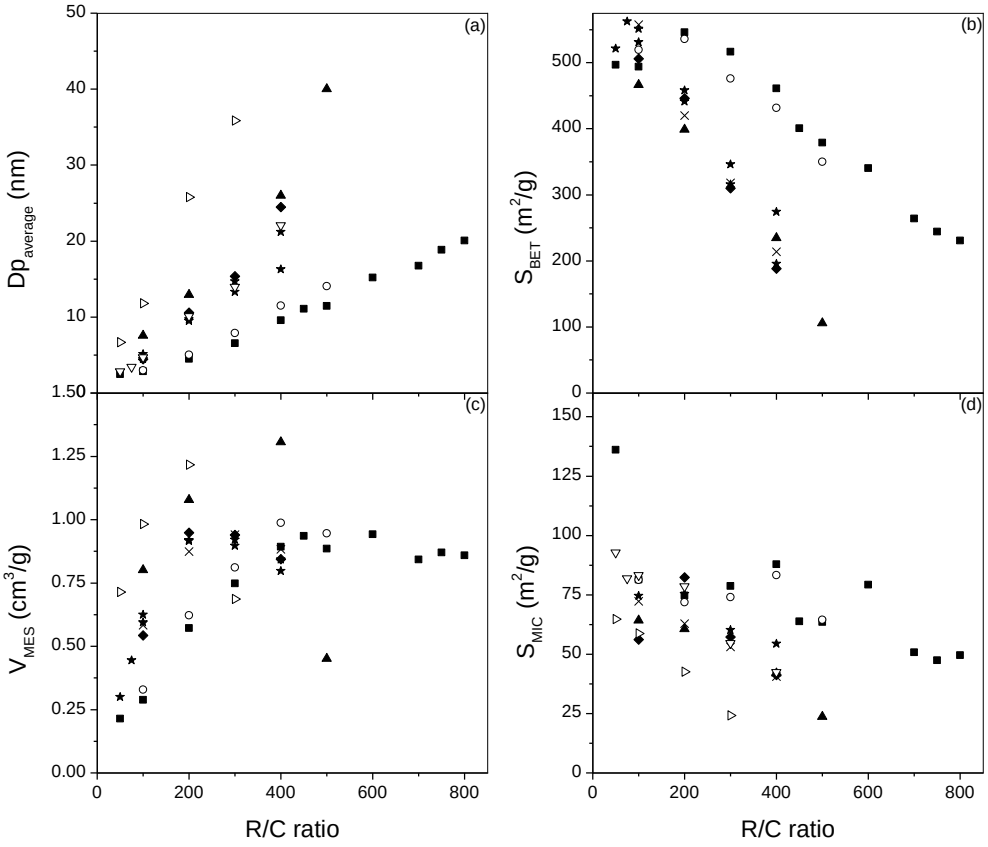

Figure 7-1: Trend of (a) $Dp_{average}$, (b) specific surface area, (c) mesopore volume and (d) micropore surface, with R/C ratio, for dried xerogels prepared with, Na_2CO_3 (!), K_2CO_3 (–), Cs_2CO_3 (7), $NaHCO_3$ (X), $KHCO_3$ (Λ), CsHCO3 (χ), NaOH (ξ), KOH (□).

Previous studies have suggested that the variances, in RF gel properties, observed between xerogels prepared using different catalyst types (i.e. carbonate, bicarbonate and hydroxide) are caused by differences in the initial sol pH, with Job *et al*. [1] and Sharma *et al*. [2] describing the catalyst as a pH adjuster only, concluding that it does not undertake a typical catalytic role.

7.2 Effect of initial sol pH

In order to study the effect of the initial sol pH, the expected initial pH was calculated using the BATE pH equation (Equation 111 or Equation 132), by substituting the pK_b values, given in Table 7-2, and experimental concentrations. Figure 7-2 shows both the calculated

BATE pHs and experimentally measured pHs, illustrating that they show similar trends, with the carbonate catalysts giving the highest pHs, above the hydroxide and finally the bicarbonate catalysts.

Table 7-2: Catalyst p_{kb} values [6]

Catalyst	p_{Kb1}	p_{Kb2}
$Na_2CO_3/K_2CO_3/Cs_2CO_3$	3.65	7.64
$NaHCO_3/KHCO_3/CsHCO_3$	7.64	-
NaOH	0.2	-
KOH	0.5	-

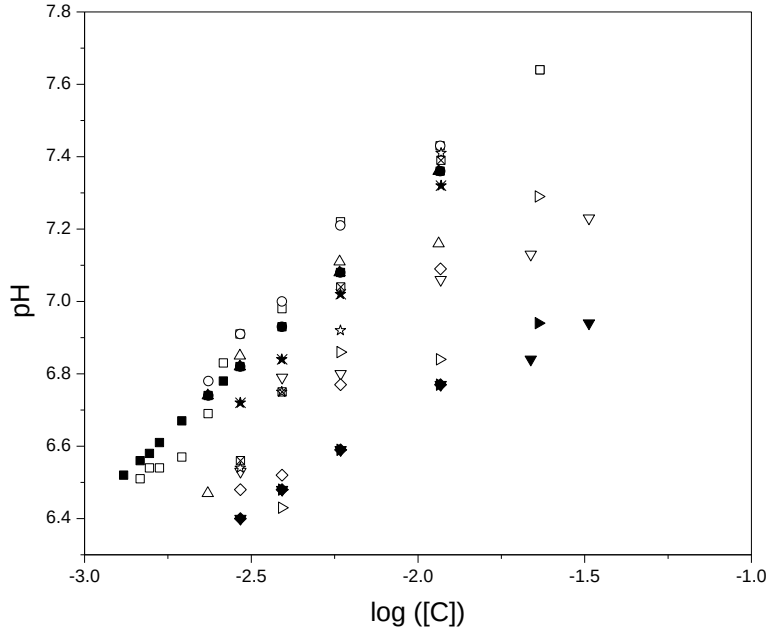

Figure 7-2: Calculated BATE (closed symbols) and experimental (open symbols) pHs for Na_2CO_3 (!,∀); K_2CO_3 (,,–); Cs_2CO_3 (7,8), $NaHCO_3$ (B,X); $KHCO_3$ (Λ,M); $CsHCO_3$ (β,χ)NaOH (ξ,ψ); KOH (□,%).

Given that the hydroxide bases have significantly lower pK_b values, it was first expected that the hydroxide sols would have the highest pH, however investigation using the BATE equation demonstrated that due to its 2^- charge, some CO_3^{2-} molecules dissociate R twice. Consequently the remaining [R] is reduced when compared to a sol prepared with an analogous concentration of OH^-, resulting in a more basic pH (a comparison of the calculations for Na_2CO_3_100 and NaOH_100 are given in Chapter 17 Appendix F). With the bicarbonate catalysts the lower pK_b values result in higher remaining [R] and lower pH.

Figure 7-3 illustrates that trends between initial sol pH and dried xerogel characteristics are as expected from previous findings [1, 3, 15, 18, 60, 65]. With increasing catalyst

concentration; the initial sol pH rises, resulting in a decrease in average pore diameter (a), which, in turn, leads to an increase in specific surface area and decrease in total pore volume; as the materials are mainly mesoporous, the total and mesopore volumes follow similar trends, so only the mesopore volume is shown (c). The pyrolysed gels show similar trends (see Appendix D).

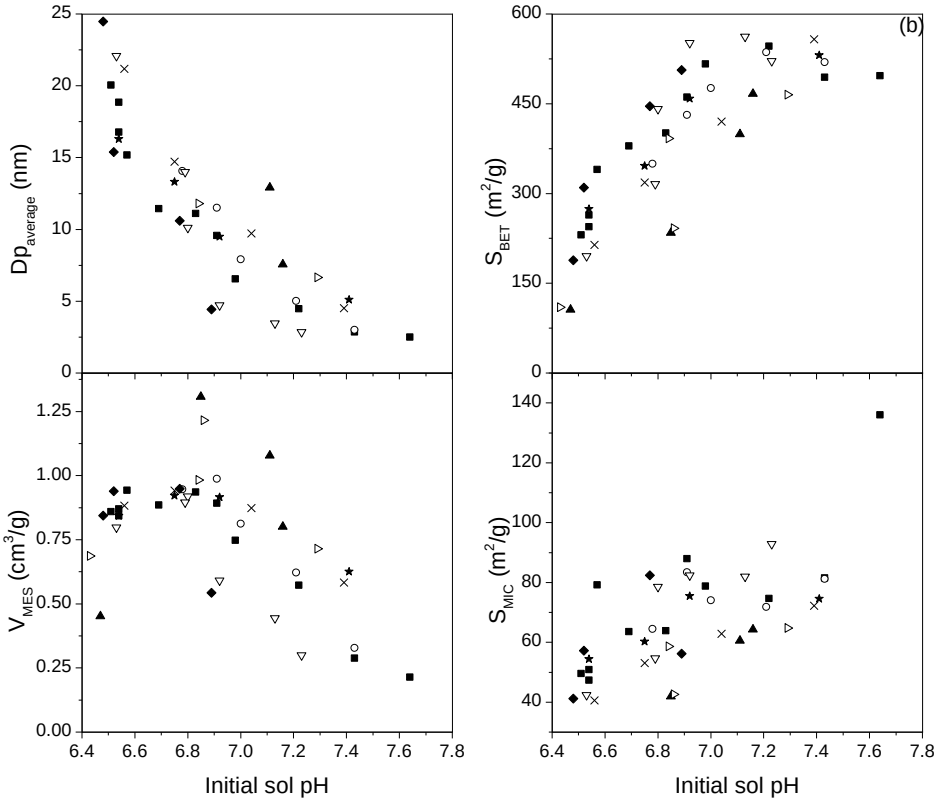

Figure 7-3: Trend of (a) $Dp_{average}$, (b) specific surface area, (c) mesopore volume and (d) micropore surface, with initial sol pH, for dried xerogels gels prepared with, Na_2CO_3 (!), K_2CO_3 (–), Cs_2CO_3 (7), $NaHCO_3$ (X), $KHCO_3$ (Λ), $CsHCO_3$ (χ), NaOH (ξ), KOH (□).

From Figure 7-3, it is evident that the characteristics of RF xerogels are, to some extent, dependent on the initial sol pH, which supports theories within the literature that pH governs the extent of each reaction step (i.e. step 1 – addition, requires basic pH, step 2 – condensation, requires acidic pH).

For the Group I catalysts studied, sols prepared with an initial pH of less than 6.45 did not form cross-linked gel structures, indicating that there is possibly a defined pH range during which RF gels are formed (this will be discussed further in later chapters). Lin *et al*. [3] reported a working pH range of 5.45 to 6.9, whereas Job *et al*. [1] reported a range of 5.45 to 6.25; as these studies used different reaction conditions, it can be concluded that the pH range is dependent on the conditions used.

Like Horikawa *et al*. [25], this study investigates the effect of different catalysts on the final gel properties. Horikawa *et al.* explained that differences between carbonate and bicarbonate prepared sols, were based solely on the alkalinity effects of the catalysts present. It was reported that the stronger carbonate bases would result in a higher sol pH, and it was theorised that this would directly affect the porous properties of the gels. However, given the results presented in this study, this does not explain why gels with equivalent initial pHs have significantly different properties, for example KOH and K_2CO_3 gels prepared with a pH of ~6.9 have pore volumes of 0.57 and 1.03 cm^3/g, surface areas of 506 and 431 m^2/g and average pore diameters of 4.43 and 11.51 nm, respectively.

7.3 Effect of deprotonating ability

Assuming that all catalysts fully dissociate within a sol system, the potential of each catalyst to deprotonate R can be calculated. For example 1 mol of carbonate base is potentially able to deprotonate R twice, i.e. it is able to react with 2 mols of H as shown in Equation 145. Consequently, the deprotonating ability can be expressed as Equation 146:

$$CO_3^{2-} + 2H \rightarrow H_2CO_3$$

Equation 145

$$DPA_{Na_2CO_3} = 2 \times [CO_3^{2-}]$$

Equation 146

With bicarbonate and hydroxide bases, as they have a charge of negative 1, they are only able to deprotonate R once. An example is given for hydroxide in Equation 147. Thus the DPA is equal to the base concentration (Equation 148).

$$OH^- + H \rightarrow H_2O$$

Equation 147

$$DPA_{NaHCO_3/NaOH} = [HCO_3^-] or [OH^-]$$

Equation 148

Table 7-3 illustrates the abilities of the different catalysts, at varying experimental concentrations, to deprotonate R, a term herein referred to as the Deprotonation Ability (DPA). The values indicate that, theoretically, the carbonate bases have the ability to abstract double the amount of hydrogen ions as the bicarbonate and hydroxide bases, at the same R/C ratio.

Table 7-3: Calculated equivalent deprotonation abilities

DPA (M x 10^{-3})	Catalyst							
	CO_3			HCO_3			OH	
	Na_2	K_2	Cs_2	Na	K	Cs	Na	K
46.4	50	-	-	-	-	-	-	-
23.3	100	100	100	50	-	50	-	-
15.6	-	-	-	75	-	-	-	-
11.7	200	200	200	100	100	100	100	100
7.82	300	300	-	-	-	-	-	-
5.85	400	400	400	200	200	200	200	200
5.22	450	-	-	-	-	-	-	-
4.7	500	500	500	-	-	-	-	-
3.92	600	-	-	300	300	300	300	300
3.34	700	-	-	-	-	-	-	-
3.13	750	-	-	-	-	-	-	-
2.94	800	-	-	400	400	-	400	400

The isotherms and pore size distributions (PSDs) for the xerogels given in Table 7-3, are shown in Figure 7-4 and Figure 7-5. All of the xerogels exhibit type IV isotherms, meaning that the materials are mainly mesoporous, and exhibit mainly Type H2 hysteresis loops, indicative of wide pore size distributions. As DPA decreases (catalyst concentration decreases), the hysteresis loops become larger and shift to higher relative pressures, indicating an increase in the amount of nitrogen adsorbed (i.e. increase in pore volume and pore size).

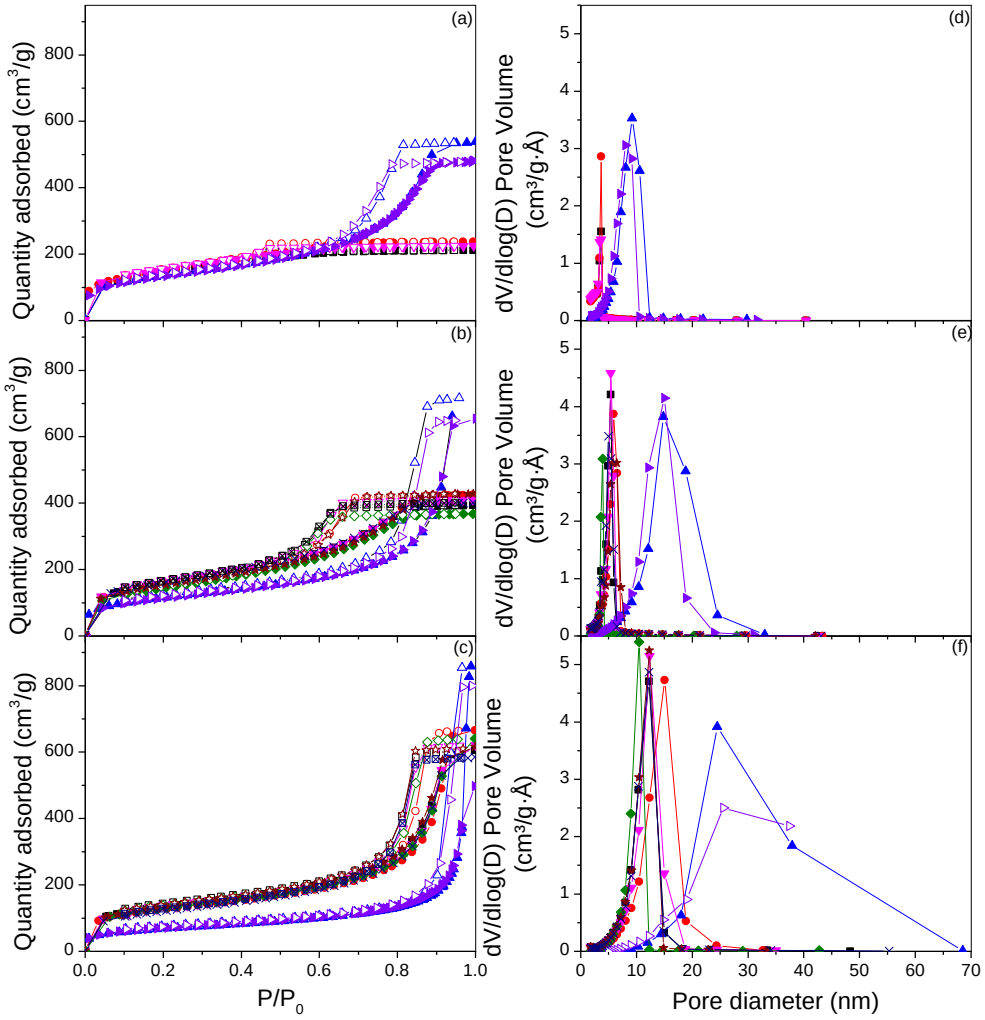

Figure 7-4: N_2 adsorption (closed symbols) and desorption (open symbols) isotherms for dried xerogels prepared with (a) DPA of 23.3 x 10^{-3} M, (b) 11.7 x 10^{-3} M, (c) 5.85 x 10^{-3} M, and PSD for xerogels prepared with (d) DPA of 23.3 x 10^{-3} M, (e) 11.7 x 10^{-3} M, and (f) 5.85 x 10^{-3} M for Na_2CO_3 (!), K_2CO_3 (,), Cs_2CO_3 (7), $NaHCO_3$ (B), $KHCO_3$ (Λ), $CsHCO_3$ (β), NaOH (ξ) and KOH (□).

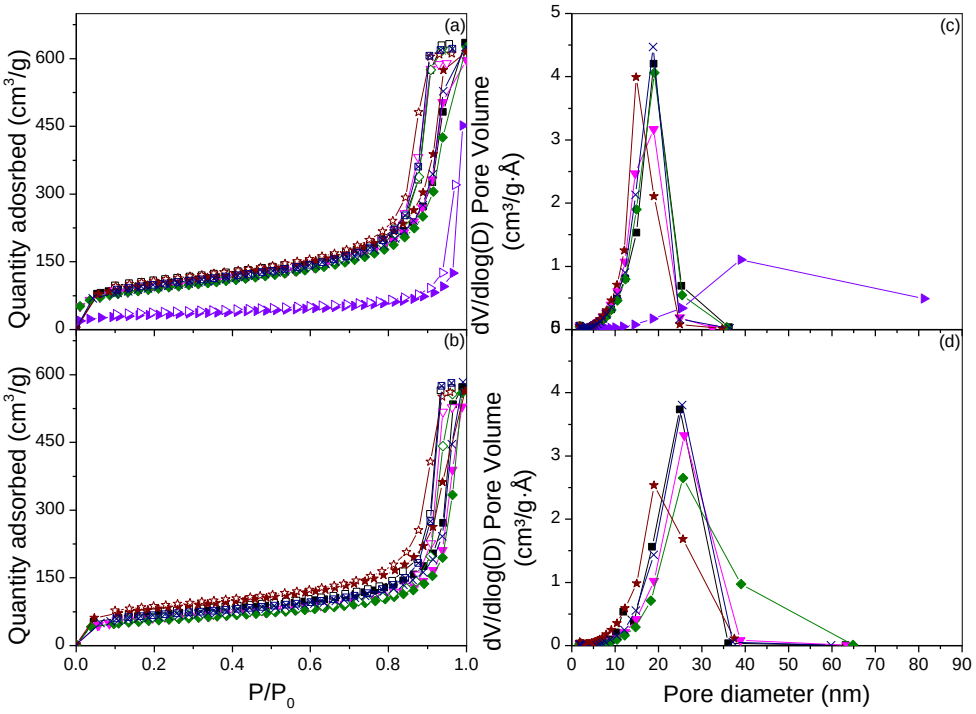

Figure 7-5: N_2 adsorption (closed symbols) and desorption (open symbols) isotherms for dried xerogels prepared with DPA of 3.92 x 10^{-3} M (a), 2.94 x 10^{-3} M (b), and PSD for xerogels prepared with DPA of 3.92 x 10^{-3} M (c), 2.94 x 10^{-3} M (d), for Na_2CO_3 (!), K_2CO_3 (,), Cs_2CO_3 (7), $NaHCO_3$ (B), $KHCO_3$ (Λ), $CsHCO_3$ (β), NaOH (ξ) and KOH (□).

Consideration of the xerogel gel characterisation data, with respect to DPA rather than pH, shows the relationships to be more pronounced. The isotherms, PSDs and porous properties displayed in Figure 7-6 illustrate that, with the exception of those catalysed by Cs catalysts (discussed further in section 7.5), gels prepared from catalysts with the same DPA (e.g. Na_2CO_3_R/C400 and $NaHCO_3$_R/C200) have very similar properties, thus, indicating that carbonate catalysts are twice as reactive as their bicarbonate and hydroxide counterparts. Figure 7-6 (a) shows that, as expected, the average pore diameter initially decreases rapidly, with increasing DPA (increasing catalyst concentration), before levelling off at DPA > 0.01. Specific surface area, Figure 7-6 (b), demonstrates the opposite trend, with a rapid increase as pore size decreases. Initially, as the material becomes more porous, there is a small increase in mesopore volume and, consequently, total volume; as DPA increases further, pore diameter decreases and pore size distributions narrow resulting in decreases in meso and total pore volumes (c). At high DPA the materials become more microporous (d) and pore volumes begin to level off. Again the trends are similar for carbon xerogels as displayed in Appendix D.

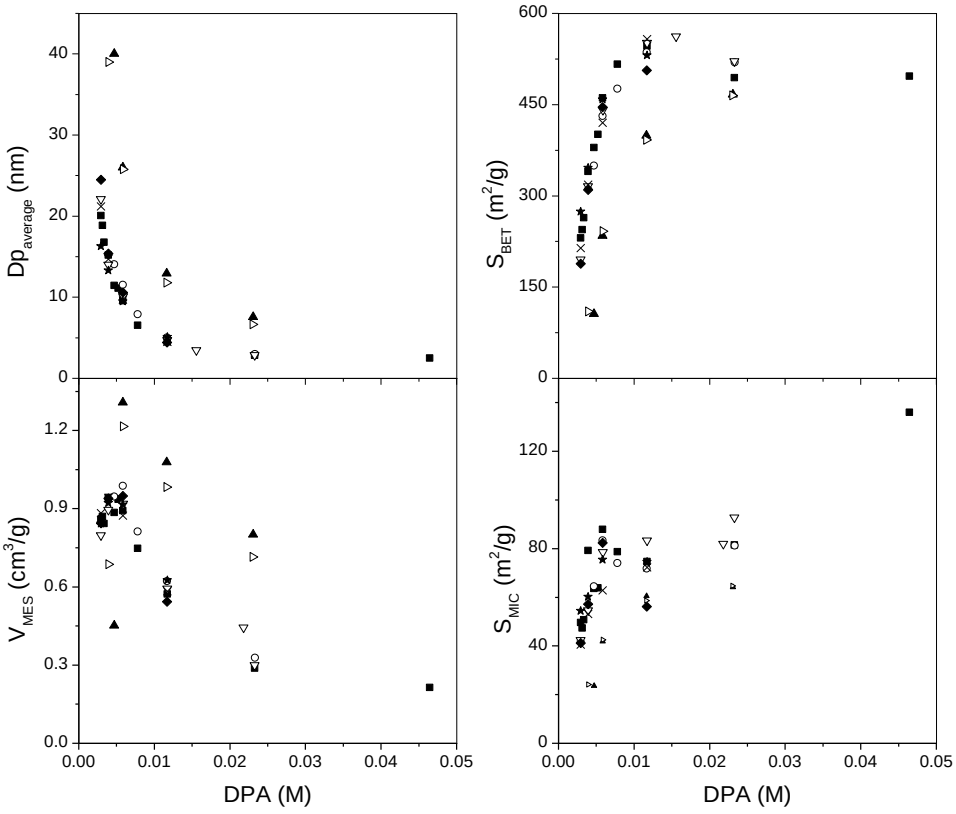

Figure 7-6: Trend of $DP_{average}$ (a), specific surface area (b), mesopore volume (c) and micropore surface area (d) with DPA, for dried xerogels prepared using, Na_2CO_3 (!), K_2CO_3 (–), Cs_2CO_3 (7), $NaHCO_3$ (X), $KHCO_3$ (Λ), $CsHCO_3$ (χ), NaOH (ξ), KOH (□).

Tamon *et al*. [71] previously investigated the use of different catalysts for RF gel syntheses and, inspection of the results obtained in their study, show that gels produced using Na_2CO_3_25 and $NaHCO_3$_12.5 had very similar properties (S_{BET}, V_{MES} and $Dp_{average}$), which agrees with the data presented here. Tamon *et al*. [71] did not discuss the similarities observed for these gels but it is suggested here that the DPA of the catalyst concentrations used explains the analogous properties of these RF gels.

Consideration of the calculated BATE pH with DPA values, Figure 7-7 (a), demonstrates that sols prepared with equivalent DPA values are not expected to have the same initial sol pH, with the bicarbonate sols expected to have a lower pH than their analogous carbonate and hydroxide. The experimentally measured pHs follow similar trends to those predicted, however, the variance between the different catalysts is reduced.

The results presented for initial sol pH, Figure 7-3, and DPA, Figure 7-6, imply that, although the sol pH is important, the gel properties appear to be more reliant on DPA. As

proposed by Sharma *et al*. [2], and illustrated in Section 6.4.1, the pH will continue to change throughout the reaction, consequently, it is proposed here that RF gel properties are dependent on the overall ability of the catalyst to react with R, with different catalysts activating R, towards reaction with F, at differing rates.

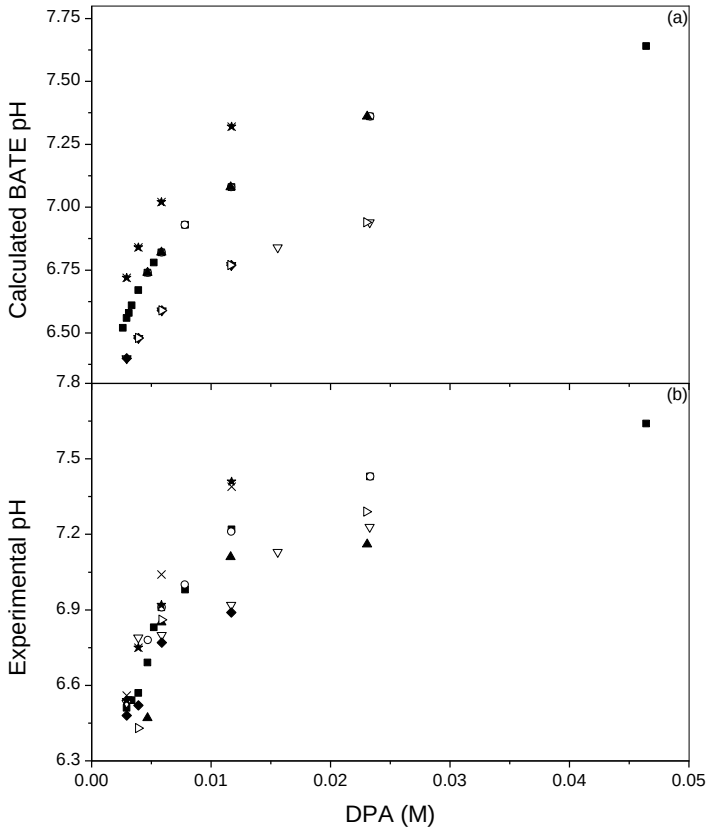

Figure 7-7: Trend in (a) calculated BATE pH and (b) experimental pH with DPA for dried xerogels prepared using, Na_2CO_3 (!), K_2CO_3 (–), Cs_2CO_3 (7), $NaHCO_3$ (X), $KHCO_3$ (Λ), $CsHCO_3$ (χ), NaOH (ξ), KOH (□).

7.3.1 Liquid chromatography and titration results

In order to investigate the differing catalyst effects the reaction was studied using liquid chromatography and a titration method, allowing R and F concentrations to be monitored, respectively. Figure 7-8 shows an example HPLC chromatogram, illustrating reaction peaks. MS results indicated (see Chapter 18 Appendix G) that the peak at approximately 4.46 min is attributable to R and peaks eluting before R were identified, as more polar, HM compounds. This elution was similar to that reported by Kendal *et al*. [173] who studied the characterisation of phenol formaldehyde resins using a similar LC column. The authors also reported [173] the separation of a tetramer [174], which eluted before phenol, however, MS

results obtained in this study, indicate that HM dimers are less polar than R, thus would elute later, but these HM dimers could not be resolved on the HPLC system used.

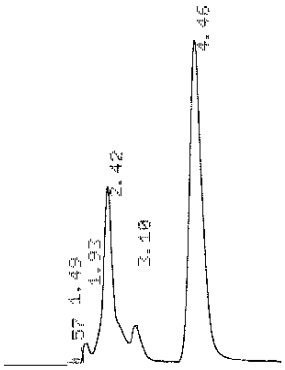

Figure 7-8: Example HPLC chromatogram (Na_2CO_3_300_T_{15} monitored on column 1).

For a variety of dried xerogels the change in R and F concentrations were monitored from when the sol was placed in the oven (zero minutes – T_0). The changes in both concentrations, as the reactions proceed, are illustrated in Figure 7-9 and Figure 7-10 (all calculated [R], obtained using linear regression analysis of LC results, are given in Chapter 20 Appendix H). These figures show that initially there is large variation in the concentration of R and F within the RF sol and there appears to be no trends between the different catalysts and R/C ratios. However, as the reaction proceeds and reaction equilibrium is reached the decrease in R and F appears to be similar for gels with equal DPA values, indicating that gels with equivalent DPAs follow similar reaction pathways. These results again suggest that carbonate catalysts are twice as reactive as their corresponding bicarbonates and hydroxides.

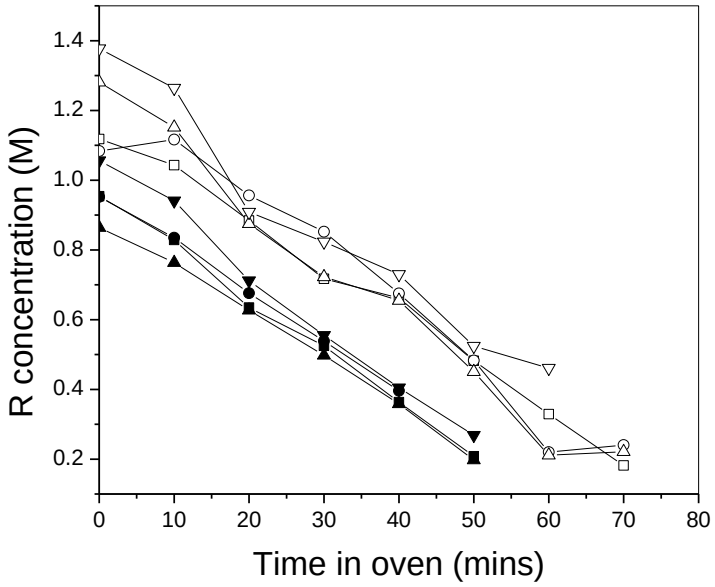

Figure 7-9: LC results showing disappearance of R for gels prepared with DPA of 11.7 x 10^{-3} M (Na_2CO_3_200 !, Cs_2CO_3_200 „, $NaHCO_3$_100 7 and NaOH_100 B) and 5.85 x 10^{-3} M (Na_2CO_3_400 ∀, Cs_2CO_3_400 –, $NaHCO_3$_200 8, and NaOH_200 X). All measured on Column 2, with the exception of NaOH, which was measured on Column 1.

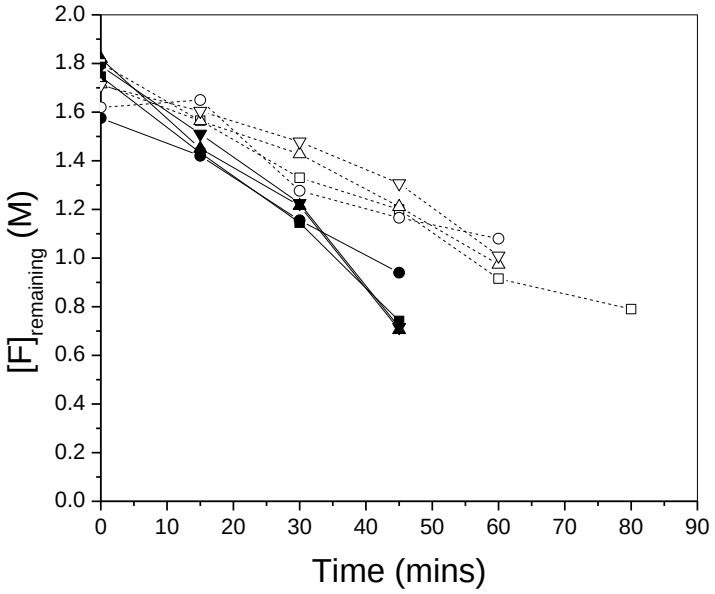

Figure 7-10: Titration data showing the disappearance of F for gels prepared with DPA of 11.7 x 10^{-3} M (Na_2CO_3_200 !, Cs_2CO_3_200 „, $NaHCO_3$_100 7 and NaOH_100 B) and 5.85 x 10^{-3} M (Na_2CO_3_400 ∀, Cs_2CO_3_400 –, $NaHCO_3$_200 8, and NaOH_200 X).

7.4 Effect of setting initial sol pH using acid

The results presented in section 7.3 indicate that the RF gel properties are not dependent on initial sol pH; in order to test this theory further a number of R/F sols were prepared as normal using Na_2CO_3 or $NaHCO_3$ at varying R/C ratios, however, after the 30 minute stir period, nitric acid (HNO_3) was added to fix the sol pH at 7.00. The sols were then treated as normal to produce RF gels. Comparison of the porous properties of these gels allows the effect of the initial sol pH to be studied in more detail.

Table 7-4: Properties of Na_2CO_3 and $NaHCO_3$ gels prepared with a set pH of 7.00 [148, 175]

Na_2CO_3				
R/C ratio	S_{BET} (m^2/g)	V_{TOT} (cm^3/g)	V_{MES} (cm^3/g)	Dp_{ave} (nm)
150	518	0.820	0.779	7.00
200	490	0.796	0.760	6.93
250	490	0.826	0.789	7.41
300	558	0.901	0.857	7.22
$NaHCO_3$				
50	522	0.458	0.427	3.50
75	491	0.509	0.486	4.03

As shown in Table 7-4, the $NaHCO_3$ gels have smaller average pore diameters, and as a result, lower mesopore volumes. These characteristics are illustrated by the PSDs and N_2 adsorption/desorption isotherms, shown in Figure 7-11 (a) and (b), respectively, which show two clear groupings for the Na_2CO_3 and $NaHCO_3$ gels. The PSDs for the bicarbonate gels demonstrate significantly smaller pores, and narrower distributions, confirmed by the bicarbonate isotherms, with hystereses appearing at lower relative pressures and shrinking in height.

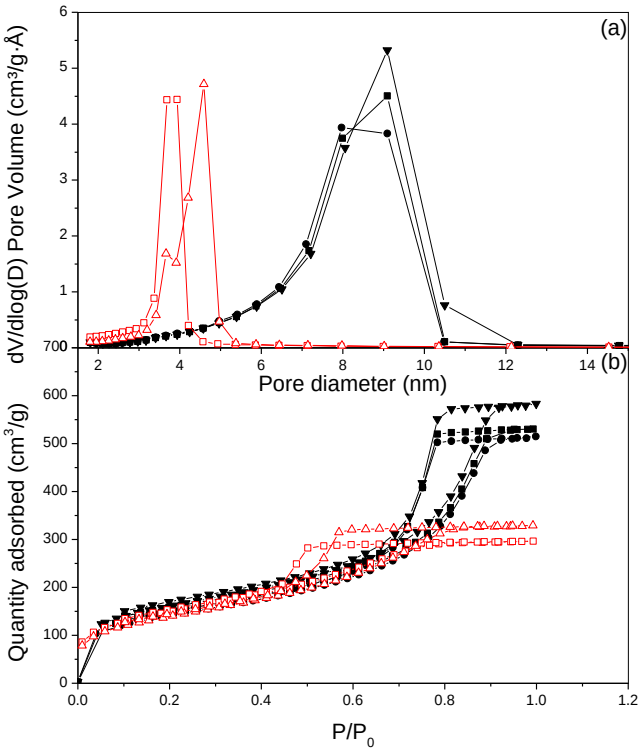

Figure 7-11: PSD (a) and N_2 adsorption/desorption isotherms (b) for Na_2CO_3 (black) and $NaHCO_3$ (red) gels prepared with a set pH of 7.00.

These results are further verified by comparing gels prepared with a set initial sol pH to 6.75 (again the pH was set using addition of HNO_3). $NaHCO_3$ gels again demonstrate smaller average pore diameters and, as a result, slightly lower mesopore volumes (see Table 7-5), which is again illustrated by the PSDs and isotherms shown in Figure 7-12.

Table 7-5: Properties of Na_2CO_3 and $NaHCO_3$ gels prepared with a set pH of 6.75 [175]

R/C ratio	S_{BET} (m^2/g)	V_{TOT} (cm^3/g)	V_{MES} (cm^3/g)	Dp_{ave} (nm)
Na_2CO_3				
150	387	1.183	1.145	15.65
200	356	1.260	1.226	18.04
250	336	1.027	0.993	16.17
300	388	1.260	1.224	16.80
350	326	1.266	1.232	19.90
400	315	1.137	1.105	18.43
$NaHCO_3$				
75	408	1.004	0.975	11.14
100	424	1.020	0.988	11.12

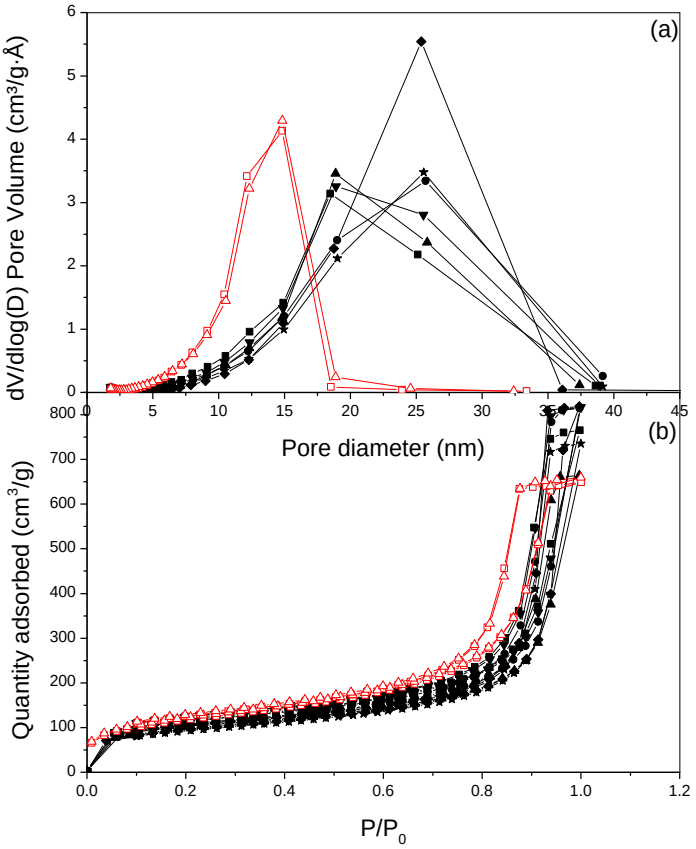

Figure 7-12: PSD (a) and N_2 adsorption/desorption isotherms (b) for Na_2CO_3 (black) and $NaHCO_3$ (red) gels prepared with a set pH of 6.75.

This method of setting the sol pH using acid has been used previously to study the effect of the sol pH on the porous properties of RF gels [3, 60, 65, 66], however, these studies have focused on the use of only one catalyst (Na_2CO_3) or one catalyst type (carbonates), therefore, no significant differences were reported for gels prepared with the same initial sol pH. The results presented here demonstrate that when different catalyst types are used the initial sol pH does not determine the porous properties of RF gels and that the catalyst plays a specific role in the reaction of R with F.

The smaller pore diameters and pore volumes observed in bicarbonate gels can be explained by considering, and simplifying, the main equilibria occurring during the initial RF reaction and pH adjustment stage, namely the preliminary reaction between catalyst and R to form anions and then the reaction of HNO_3 with the free catalyst within the sol.

Using the BATE equation and BATE pH calculator [145], equilibria for Na_2CO_3_200 were compared to $NaHCO_3$_50 at set pHs of 7.00 and 6.75. In these systems the initial reaction of

R with C occurs, as shown in Equation 149 and Equation 150, where Na_2CO_3 is capable of deprotonating twice, therefore, it will follow both equations and $NaHCO_3$ will react with R as described in Equation 150:

$$Na_2CO_3 + C_6H_6O_2 \overset{pK_{b1}=3.65}{\Longleftrightarrow} CO_2 + H_2O + C_6H_5O_2{}^-Na^+ + NaHCO_3$$

Equation 149

$$NaHCO_3 + C_6H_6O_2 \overset{pK_b=7.64}{\Longleftrightarrow} CO_2 + H_2O + C_6H_5O_2{}^-Na^+$$

Equation 150

For Na_2CO_3_200, [C] is equal to 5.85 x 10^{-3} M, using this concentration and the pk_b values, given in Table 7-2, the BATE equation predicts that after reaction with R a negligible amount of Na_2CO_3 remains, with a remaining [$NaHCO_3$] of 0.004918 M; whereas when $NaHCO_3$_50 is used as the catalyst, [C] is equal to 23.3 x 10^{-3} M and 0.00345 M of $NaHCO_3$ remain after reaction with R. Using these concentrations the reaction of remaining catalyst with the added acid was investigated (Equation 151), where the pKa value of HNO_3 is -1.3 [176]:

$$NaHCO_3 + HNO_3 \xrightarrow{pK_a=-1.3} 2NaNO_3 + H_2CO_3$$

Equation 151

According to the BATE equation, Na_2CO_3_200 sol has 0.004918 M of $NaHCO_3$ that remains after reaction with R, which requires 0.00092 M HNO_3 to set the sol pH to 7.00, following this acid-base reaction, 0.003998 M $NaHCO_3$ remains. Comparing this with a $NaHCO_3$_50 sol, which requires 0.00345 M HNO_3 to react with the 0.003998 M of base, the remaining $NaHCO_3$ concentration is 0.01499 M. Consequently, after addition of the pH adjusting acid the $NaHCO_3$ sol has a higher concentration of $NaHCO_3$ remaining (3.75 x more). This higher concentration of catalyst allows a larger quantity of R to be activated towards reaction with F, resulting in increased cross-linking and as a result smaller pores and pore volumes. With the sols set to a pH of 6.75, similar equilibria are observed, however, the difference in remaining $NaHCO_3$ concentration is smaller (i.e. comparing $NaHCO_3$_75 and Na_2CO_3_200, the remaining $NaHCO_3$ concentrations, after addition of HNO_3, are 8.22 x 10^{-3} M and 3.998 x 10^{-3} M respectively, therefore $NaHCO_3$_75 has 2.05 x more remaining base) and, as a result, the differences between the final gel properties become less significant.

7.5 Effect of cation radius

Average pore diameters for dried xerogels prepared using different Group I catalysts are illustrated in Figure 7-13. These graphs show that, as ionic radius increases, from Na to Cs, average pore diameter within the gel increases. The significant increase in pore diameter, from Na to Cs, results in lower specific surface areas and higher pore volumes (see Table 7-1).

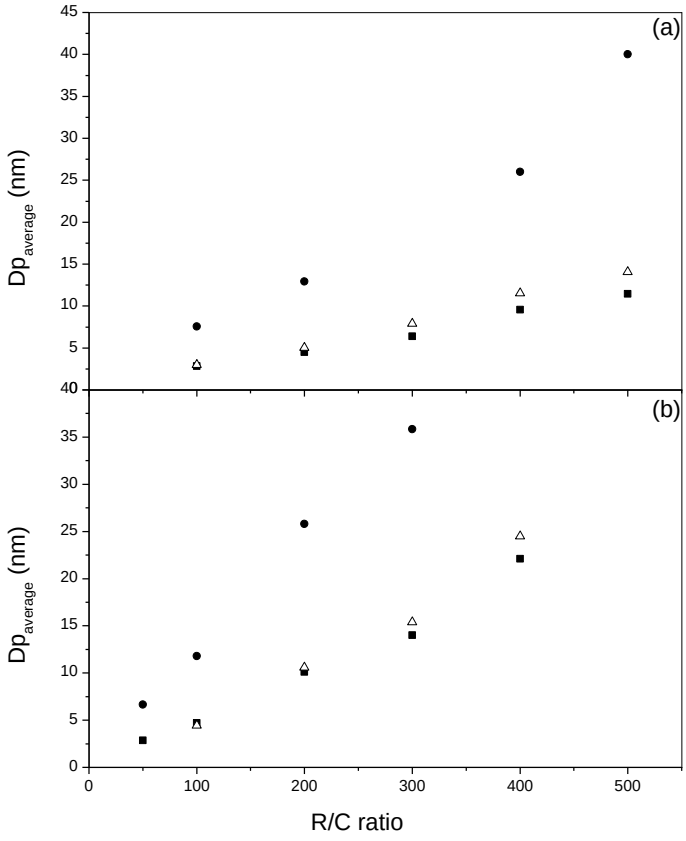

Figure 7-13: $Dp_{average}$ for gels prepared from Na (!), K (8) and Cs (,) carbonate (a) and bicarbonate (b).

This increase in pore diameter with ionic radius was previously reported by Torres *et al*. [62], who found that RF gels became less compact going from Li to Cs catalysts. They theorised that increasing cation size resulted in decreased interaction with the oxygenated functionalities of RF clusters. Utilising this theory, given the proposed transition state (Figure 7-14) for HM formation [151], it would be expected, due to decreased interaction with oxygen of R, that an increase in cation size would cause a decrease in the rate of HM formation.

However, LC and titration data for Na_2CO_3_200 and Cs_2CO_3_200 indicate that this is not the case and HMs are formed at a similar rate, F disappearance is also comparable until after 20 minutes of reaction time.

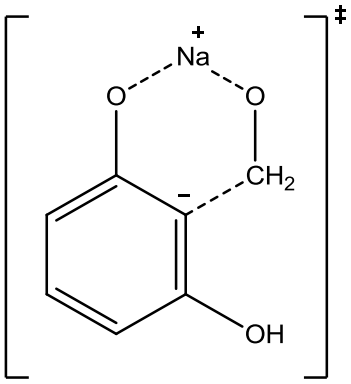

Figure 7-14: Proposed transition state for HM formation.

Torres *et al*. [62] stated that the theorised lower interaction of Cs results in increased gelation time, which favours the aggregation and formation of primary particles, subsequently resulting in larger pores. In order to test this theory the gelation time for a variety of Cs and Na gels were monitored and compared, it was found that although Na gelation times were repeatable, Cs gels demonstrated random gelation times, which could not be repeated. In some instances the gelation time of the Cs gel was longer than the corresponding Na gel and in others shorter. Thus, it can be concluded that the porous properties of the Cs gels could not be explained due to differing gelation times, when compared to Na gels. Consequently, as the disappearance of reactants to form primary particles has been shown to be similar (for the different cations used), the differences in porous structure are likely to be caused by the interaction and aggregation of these primary particles, as the reaction proceeds.

To test this theory the sol-gel transition was monitored using DLS and the final carbonised gels were imaged using SEM. The DLS results illustrate that particle growth is more significant in Cs gels when compared to their Na counterparts, as shown in Figure 7-15. This is confirmed further by SEM images (Figure 7-16 and Figure 7-17), which indicate larger particles and less dense structures when compared to Na gels (see Figure 6-16 and Figure 6-17). These findings suggest that when Cs catalysts are used, colloidal particles grow and aggregate quicker, demonstrating that interaction between particles is favoured.

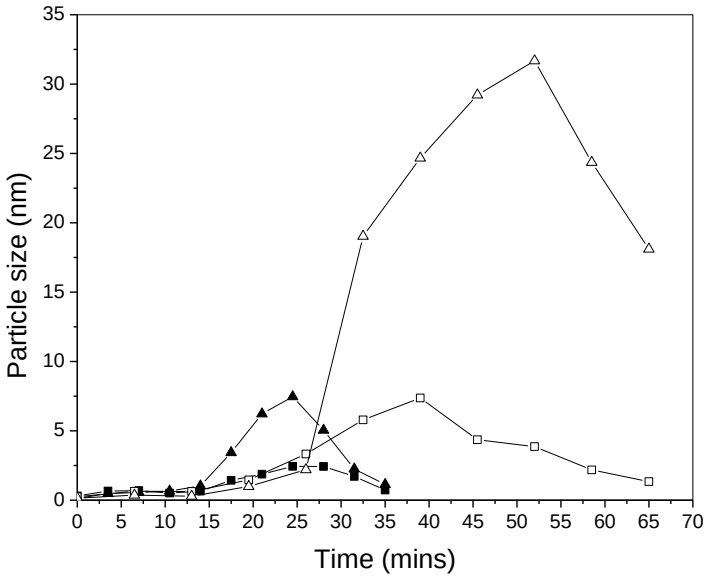

Figure 7-15: DLS results showing particle formation for Na_2CO_3_100 (!), Na_2CO_3_400 (∀) Cs_2CO_3_100 (7), and Cs_2CO_3_400 (8) [171].

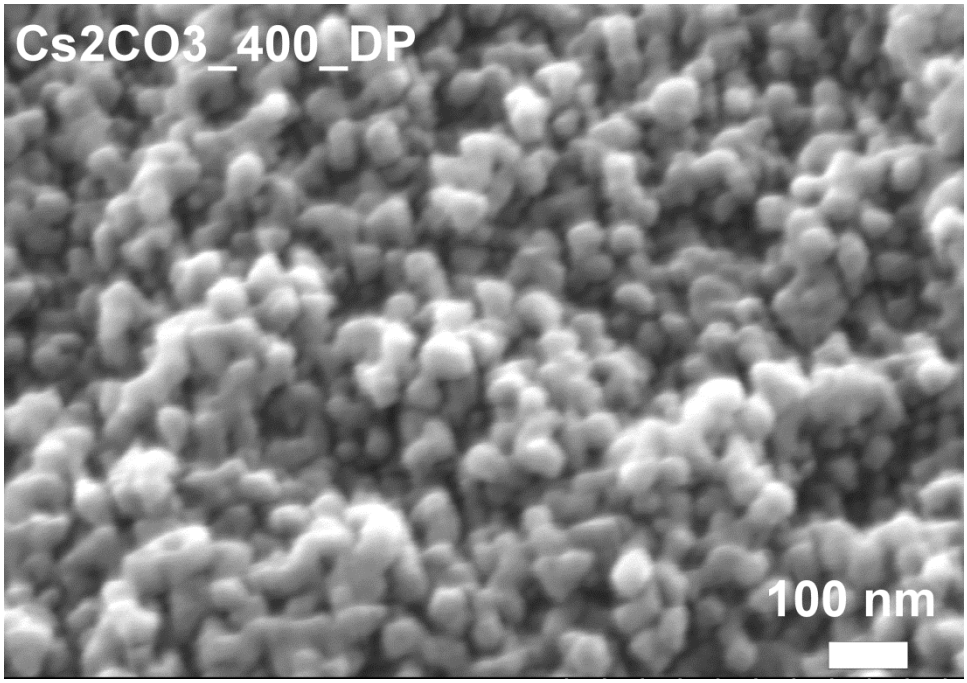

Figure 7-16: SEM images for Cs_2CO_3_400_DP with magnification of 100 k.

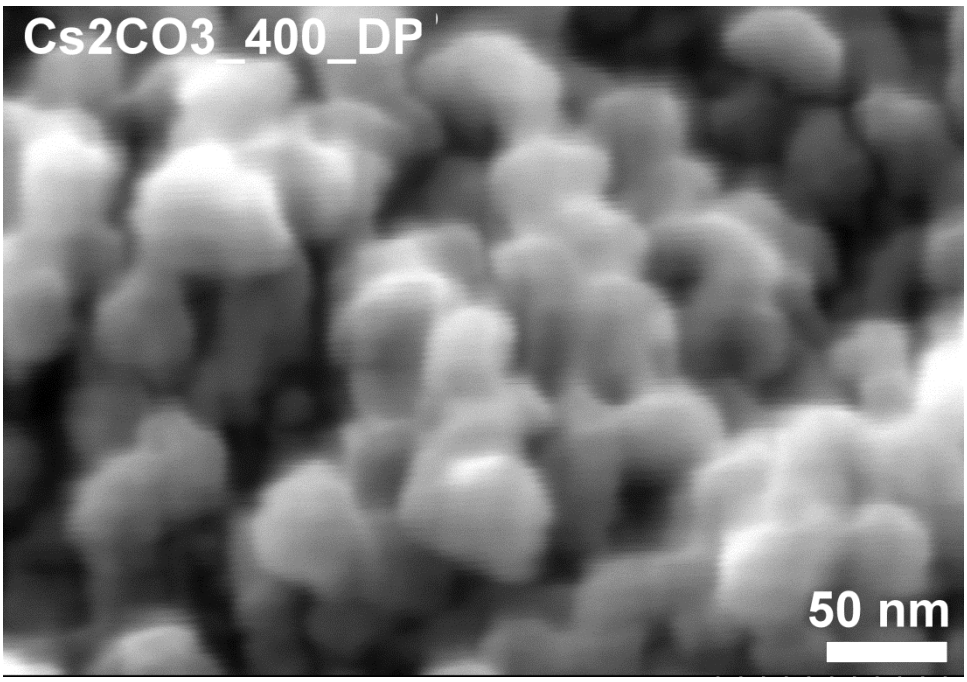

Figure 7-17: SEM images for Cs_2CO_3_400_DP with magnification of 300 k.

Job *et al*. [63] reported that due to a decrease in the Debye Huckle screening length, Group II metal catalysts caused increased stabilisation of the RF colloidal suspension. This effect would favour particle aggregation and Job *et al*. [63] found that this resulted in gelation occurring more quickly, at a lower degree of cross-linking, consequently, resulting in larger pores (it should be noted that this effect is the opposite of that reported by Torres *et al*. [62] who stated that increased gelation time allowed particle aggregation resulting in larger pores, whereas Job *et al*. [62] have stated that a decreased gelation time results in larger pores due to reduced cross-linking).

As discussed by Brinker [24], a similar screening effect is observed with cations with small hydrated radii. It was reported that smaller hydrated cations (larger ionic cations - see Figure 7-18) are able to pack more densely around colloidal particles, resulting in a reduction in the length of the double layer. As the screening length decreases, attraction between colloidal particles is enhanced and repulsion is reduced, consequently, the total potential energy of colloidal interaction decreases, as illustrated in Figure 7-19. Thus, in comparison to Na and K, when Cs catalysts are used, it is likely that colloidal particles are more reactive towards each other, resulting in increased interaction between particles, causing particle size to increase more rapidly.

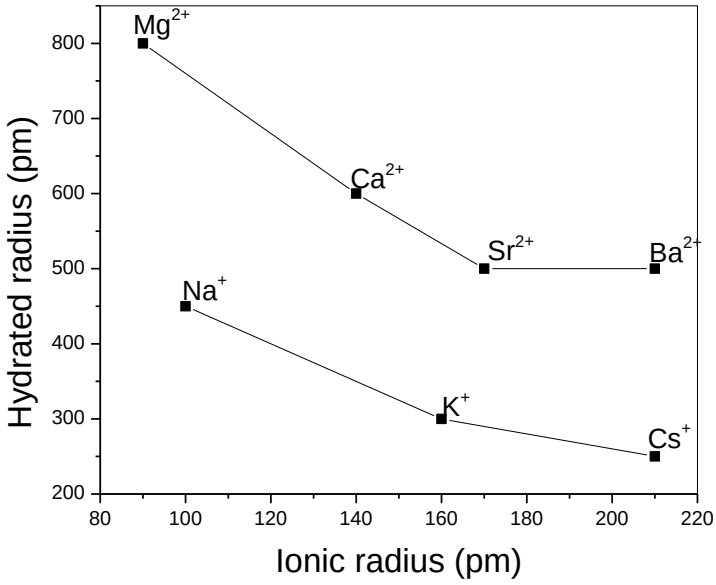

Figure 7-18: Ionic and hydrated radii for Group I and Group II metals [177]

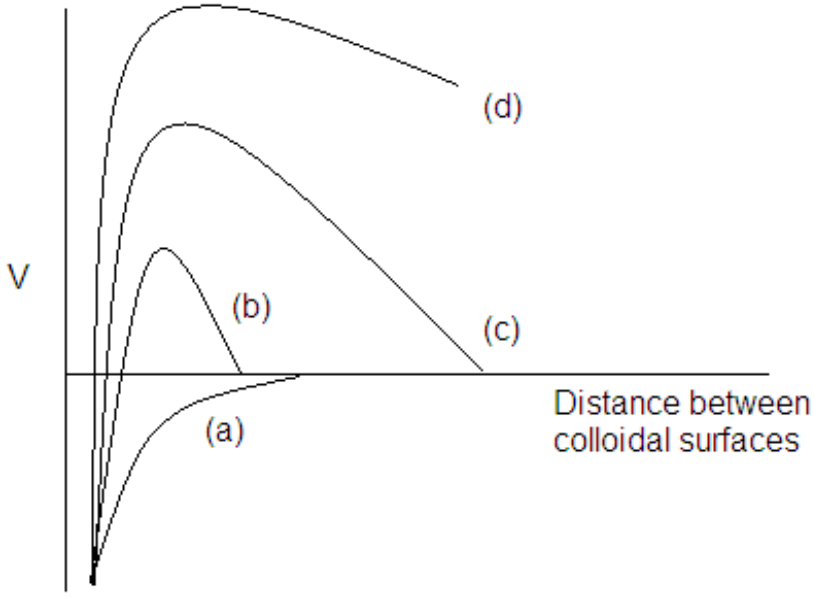

Figure 7-19: Total interaction energy (V) of two colloidal particles in aqueous media, with Debye screening lengths of 10^{-7} cm (a), 10^{-6} cm (b), 10^{-5} cm (c) and 10^{-4} cm (d). Redrawn from [37].

Bernards [33] stated that the sol-gel transition occurs when one cluster is large enough to span the total volume of solution, as depicted in Figure 7-20. The DLS results shown in Figure 7-15 demonstrate that for both Cs and Na gels the particle size begins to increase

when the concentration of HMs reaches a maximum and begins to drop off (as illustrated in Figure 6-24 for Na_2CO_3 sols). At this stage, Cs gels show significant particle size growth compared to Na gels. At this point in the reaction HMs condense together to form RF clusters. In Cs gels, where particle interaction is favoured the RF clusters react together to form larger clusters (larger particles). This reaction, between clusters, hinders further reactions of F with free activated positions on RF clusters (2, 4 and 6 position), consequently a higher F concentration remains in the Cs gels (see titration data - Figure 7-10). The aggregation of larger particles results in larger voids causing the larger pore diameters observed in the Cs gels.

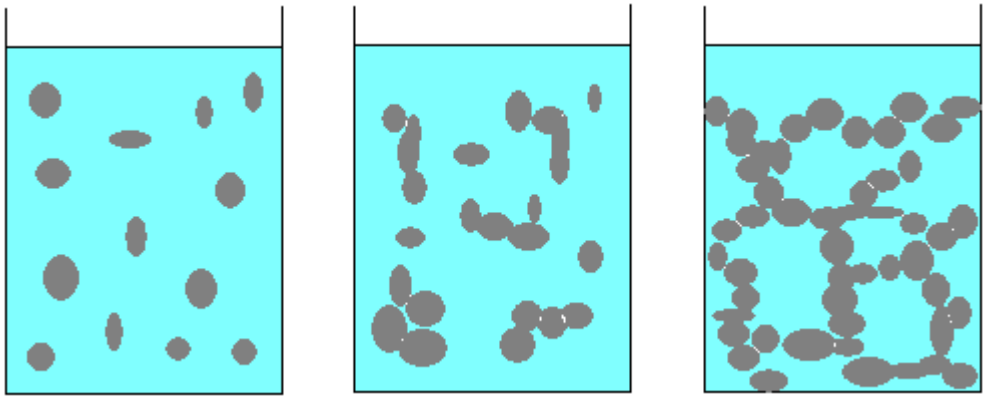

Figure 7-20: Schematic representation of the typical sol-gel transition. Redrawn from [33].

In Na and K gels the RF clusters are more stable towards each other (i.e. screening length is larger and interaction is reduced) thus the concentration of small clusters will continue to rise. This increase in concentration reduces the separation distance between particles, which will ultimately lead to aggregation of clusters and subsequent gelation. Consequently the gelation time is dependent mainly on the formation of primary particles, thus, is dependent on the DPA of the catalyst.

Conversely, due to increased interaction, the RF clusters formed in Cs gels will continue to react together and will eventually span the volume of the solution causing gelation. Therefore, in Cs catalysed gels the gelation time will be dependent not only on DPA of the catalyst but also on orientation of RF clusters.

7.6 Group I catalysts – summary

The effect of Group I catalysts, on the properties of RF xerogels has been studied in detail, through the investigation of the sol-gel transition of gels prepared using various Group I metal catalysts. The results presented show that gel properties are not directly dependent on

initial sol pH, however, the fact that gels cannot be formed from sols prepared with pH of less than 6.45, this minimum value will be studied further in Chapter 8, suggests that there may be a pH range, within which both the reaction between R and F and subsequent cross-linking can proceed.

Assuming each catalyst is able to fully dissociate R, allowed DPA values to be calculated. Consideration of the data with respect to this parameter, rather than pH, produces defined relationships, with the data indicating that gels prepared from catalyst compositions with equivalent DPA have similar properties; suggesting that the extent of reaction is not based on catalyst strength (pK_b values), but that twice as much bicarbonate and hydroxide are required to react in the same manner as one equivalent of carbonate. This theory is supported by HPLC and titration results which show that reaction concentrations follow similar trends for gels prepared from catalysts with equivalent DPA, indicating reaction pathways are similar.

Given the effect of DPA, it is possible that the cut-off point for gel formation may be an effect of the catalyst rather than sol pH, i.e. there may be a range of catalyst concentrations that allow gels to be formed. Too much catalyst (high DPA) causes the formation of a large number of R anions, which will subsequently form high concentration of HMs resulting in phase separation without a cross-linked network. Low concentrations of catalyst (low DPA), form limited HMs, which are unable to react (interact together) and sol-gel transition does not occur.

It should be noted that at equal DPA values, carbonate, bicarbonate and hydroxide catalysts also have equal concentrations of metal cations, thus the effect of metal and the effect of base cannot be considered separately. Subsequent results chapters investigate these effects further, through the use of Group II metal catalysts and catalysts with no metal cations, allowing the effect of initial sol pH, metal concentration, base concentration and the proposed transition state [151, 178] for HM formation to be investigated further.

To summarise the main points for RF xerogels catalysed with Group I metal catalysts:

(1) There may be a pH range, during which RF gels are produced.

(2) However, gel properties are not directly dependent on the initial sol pH but are dependent on DPA and ionic radius of the catalyst used.
(3) Consequently, production of RF xerogels may be possible within a range of catalyst concentrations rather than a pH range.
(4) Carbonate catalysts are twice as reactive as bicarbonate and hydroxide catalysts.
(5) As a result of (4), twice as much bicarbonate and hydroxide are required to react in the same manner as one equivalent of carbonate to produce analogous gels.

8 Results Part 3 – Gels prepared with Group II catalysts

8.1 Xerogels prepared using Group II catalysts

The properties of RF xerogels prepared using Group II catalysts are given in Table 8-1, with corresponding isotherms and PSDs given in Appendix D. The displayed properties indicate that xerogels prepared from Group II metal catalysts have similar properties to those prepared with both Cs_2CO_3 and $CsHCO_3$, demonstrating larger pores, increased porosity and decreased surface area, to their analogous Na and K prepared gels.

It was proposed in, Section 7, that RF gel properties are dependent on the ability of the catalyst to deprotonate R, however, gels studied in Section 7 with equal DPA values also had the same concentration of metal, and therefore, it is possible that the metal concentration also affects the final gel properties. The Group II prepared sols, which have similar DPAs to the Group I sols, but have different metal concentrations, will allow both parameters; metal concentration and DPA, to be investigated, while also allowing the effects of initial sol pH and cation size to be considered further.

Table 8-1: Xerogel/carbon properties for all gels prepared using Group II catalysts

Gel	Sol pH	S_{BET} (m^2/g)	V_{TOT} (cm^3/g)	V_{MES} (cm^3/g)	V_{MIC} (cm^3/g)	$Dp_{average}$ (nm)	[C] (M x 10^3)	DPA (M x 10^3)
$Mg(OH)_2$_100	6.88	463	0.965	0.928	0.037	9.43	11.7	23.4
$Mg(OH)_2$_300	6.24	226	0.964	0.930	0.024	22.8	3.9	7.8
$Mg(OH)_2$_500	5.86	131	0.413	0.399	0.014	40.1	2.3	4.7
$CaCO_3$_100	7.08	408/608	1.08/1.04	1.04/0.862	0.03/0.178	13.2/14.1	11.7	23.4
$CaCO_3$_200	7.02	407/600	1.14/1.17	1.10/1.00	0.039/0.17	14.2/14.6	5.9	11.7
$CaCO_3$_300	6.96	333/564	1.46/1.52	1.42/1.35	0.035/0.17	22.5/23.6	3.9	7.8
$CaCO_3$_400	6.83	216	1,41	1.40	0.020	33.9	2.9	5.8
$CaCO_3$_500	6.79	169/528	0.37/0.614	0.351/0.41	0.020/0.19	39.3/13.1	2.3	4.7
$SrCO_3$_100	6.82	384	1.05	1.02	0.031	12.8	1.7	2.3
$SrCO_3$_200	6.45	386	1.40	1.36	0.040	18.8	5.9	11.7
$SrCO_3$_300	6.49	150	0.434	0.418	0.016	16.1	3.9	7.8
$SrCO_3$_400	6.43	197	0.586	0.562	0.023	41.0	2.9	5.8
$BaCO_3$_100	6.98	378	0.867	0.847	0.020	9.69	11.7	23.3
$BaCO_3$_300	6.88	252	1.05	1.03	0.020	28.8	3.9	7.8
$BaCO_3$_500	6.66	130	0.418	0.407	0.011	60	2.3	4.7

8.2 Initial sol pH

The broad range of initial sol pHs (5.86 – 7.08), observed for Group II prepared gels, allows the effect of sol pH on the final gel properties to be further studied. Figure 8-1 illustrates the trends observed for Group II xerogels and compares them with analogous Group I xerogels. The isotherms and PSD for Group II prepared xerogels and carbons are given in Appendix D.

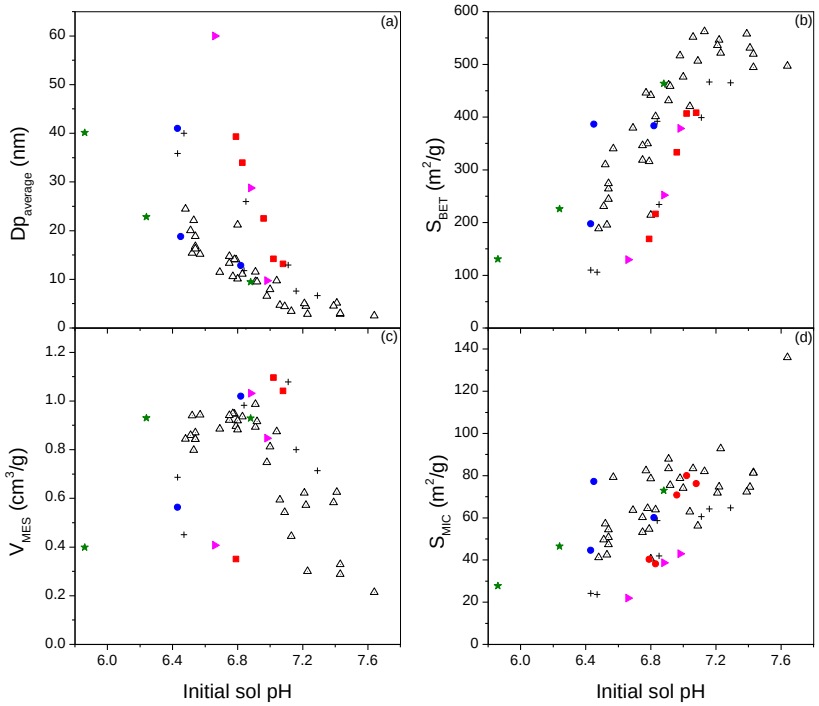

Figure 8-1: Trend of (a) $Dp_{average}$, (b) specific surface area, (c) mesopore volume and (d) micropore surface, with R/C ratio, for dried xerogels prepared with Group I catalysts (9 excluding Cs), Cs_2CO_3 & $CsHCO_3$ (□), $Mg(OH)_2$ (ξ), $CaCO_3$ (!), $SrCO_3$ (,) and $BaCO_3$ (β).

The results presented demonstrate even broader variances, in gel characteristics, for xerogels prepared with the same initial sol pH. For example, a $CaCO_3$ gel, which had an initial sol pH of approximately 6.8, has $Dp_{average}$ of 39.8 nm, S_{BET} of 169 m^2/g and V_{TOT} of 0.37 cm^3/g, whereas, the xerogels prepared with Group I catalysts, with initial pHs of approximately 6.8, have $D_{paverage}$ ~ 10 nm, S_{BET} ~ 300 m^2/g and V_{MES} ~ 0.9 cm^3/g. Consequently, the Group II prepared RF xerogels provide further evidence that the porous properties are not directly dependent on initial sol pH.

8.3 Effect of DPA and metal concentration

The metal concentrations for Group I catalysts are equal to the DPA values given in Table 7-3, whereas, for Group II catalysts, due to the 2^+ charge, metal concentrations are half the DPA values, i.e. metal concentration is equal to the total base concentration (see Table 8-1). Figure 8-2 displays trends in average pore diameters, for both Group I and Group II catalysts, with (a) DPA and (b) metal concentration. The results presented indicate that $Dp_{average}$ appears to be more dependent on the metal concentration than on DPA.

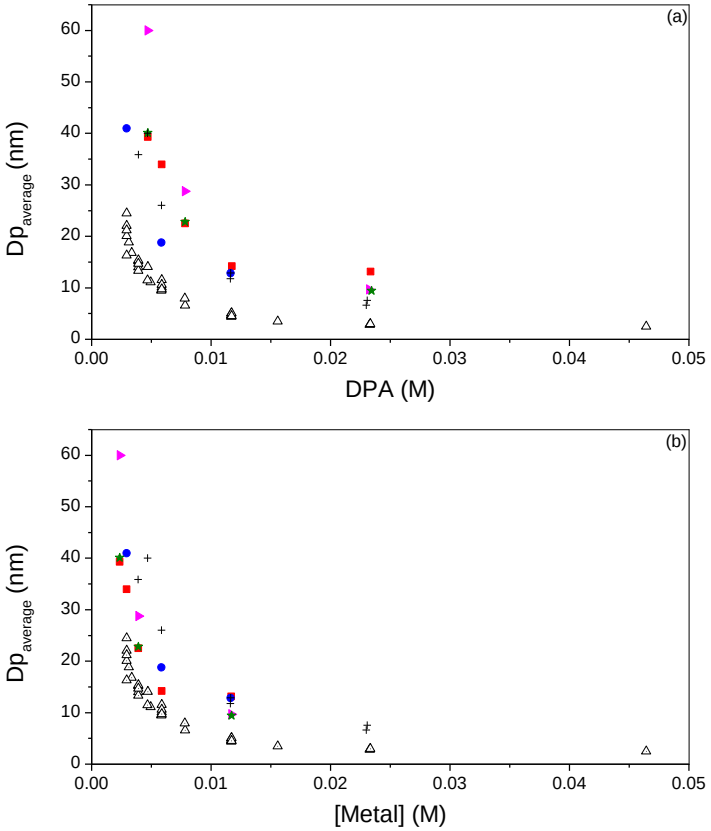

Figure 8-2: Trend in $Dp_{average}$ with (a) DPA and (b) metal concentration for xerogels prepared with Group I catalysts (9 excluding Cs), $CsCO_3$ & $CsHCO_3$ (□), $Mg(OH)_2$ (ξ), $CaCO_3$ (!), $SrCO_3$ (,) and $BaCO_3$ (β).

The trends in S_{BET} (Figure 8-3) show similar results, i.e. S_{BET} appears to be more dependent on metal concentration than DPA. Nonetheless, both Figure 8-2 (a) and Figure 8-3 (a) show two clear groupings in the trends for xerogels properties with DPA. Therefore, it is still possible that this is the main factor in determining the porous properties of RF xerogels (this will be discussed further in Section 8.4).

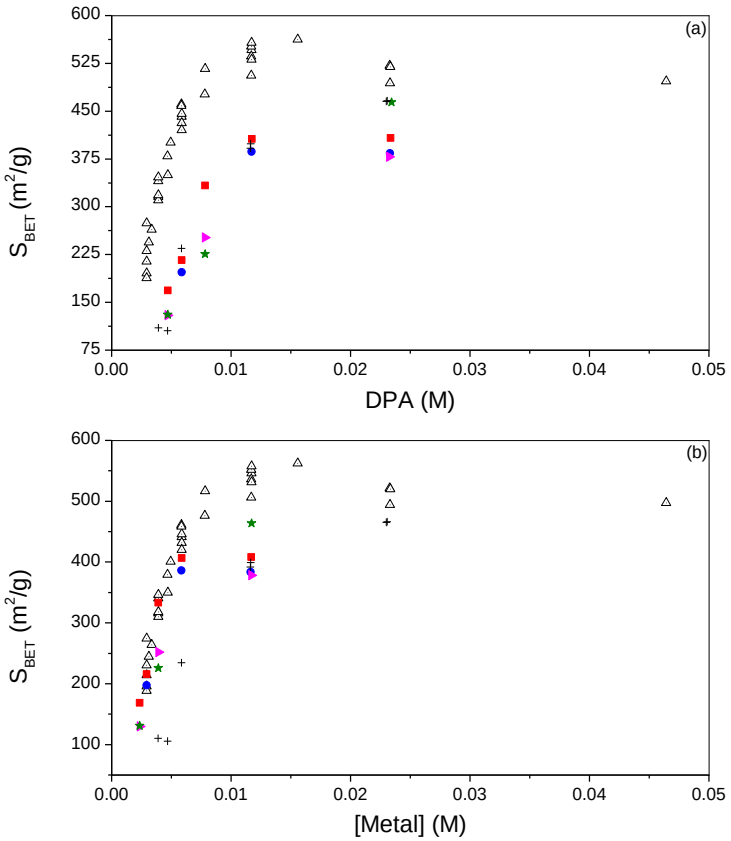

Figure 8-3: Trend in S_{BET} with (a) DPA and (b) metal concentration for xerogels prepared with Group I catalysts (9 excluding Cs), $CsCO_3$ & $CsHCO_3$ (□), $Mg(OH)_2$ (ξ), $CaCO_3$ (!), $SrCO_3$ (,) and $BaCO_3$ (β).

As previously discussed, S_{BET} and V_{MES} are dependent on pore size, i.e. as average pore diameter increases, surface area will, in general, decrease and pore volume will increase (in this case as the xerogels are mainly mesoporous, V_{MES} will increase) until the number of pores significantly decreases, due to significantly increased pore diameters (as represented in Figure 8-4). As expected, with decreasing pore diameters, the number of micropores within the structure will increase, resulting in an increase in S_{MIC}, as illustrated by Figure 8-5.

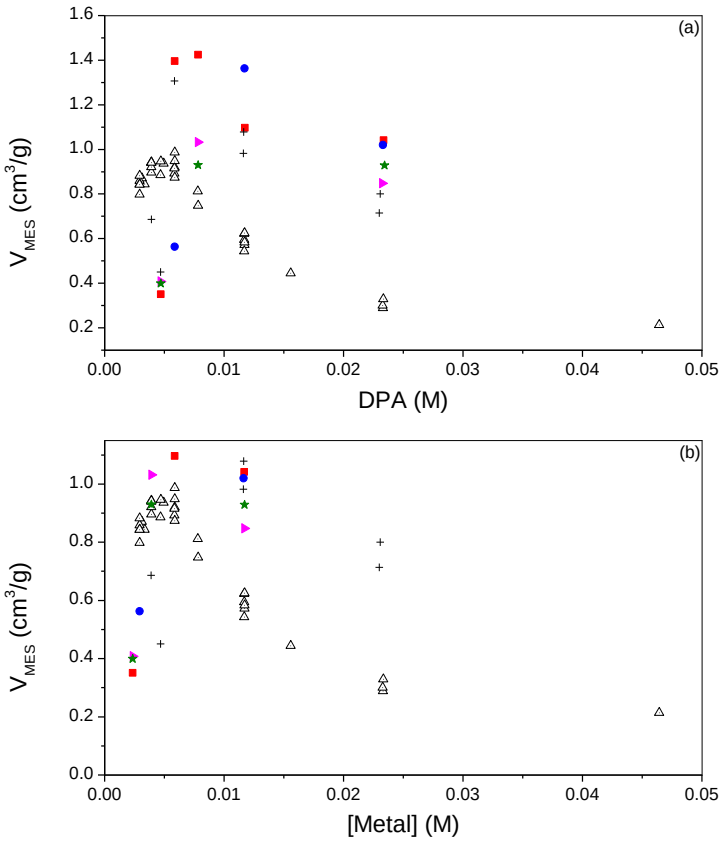

Figure 8-4: Trend in V_{MES} with (a) DPA and (b) metal concentration for xerogels prepared with Group I catalysts (9 excluding Cs), $CsCO_3$ & $CsHCO_3$ (□), $Mg(OH)_2$ (ξ), $CaCO_3$ (!), $SrCO_3$ (,) and $BaCO_3$ (β).

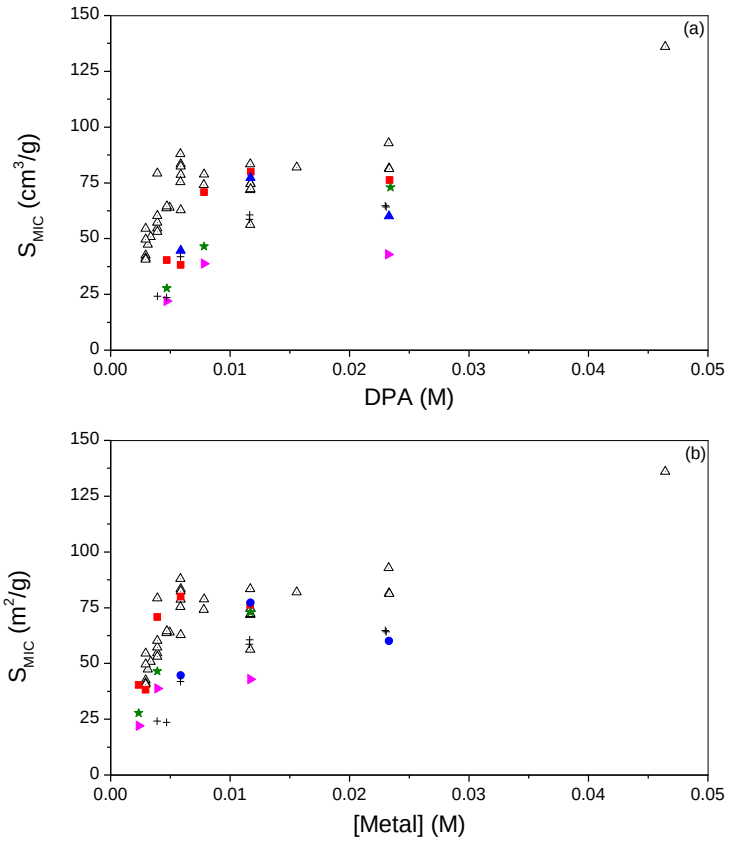

Figure 8-5: Trend in S_{MIC} with (a) DPA and (b) metal concentration for xerogels prepared with Group I catalysts (9 excluding Cs), $CsCO_3$ & $CsHCO_3$ (□), $Mg(OH)_2$ (ξ), $CaCO_3$ (!), $SrCO_3$ (,) and $BaCO_3$ (β).

8.4 The reaction - LC & titration results

When comparing gels prepared using Na, Cs and Ca catalysts, LC results indicate that, for equal R/C ratios (equal DPAs), R disappears at very similar rates. These results suggest that, for sols prepared with all three catalysts, R reacts with F to form similar concentrations of HM derivatives (see Figure 8-6). All calculated [R], obtained using linear regression analysis of LC results, are given in Appendix H.

For Na and Cs prepared sols (R/C 200 and 400), during the early stages of the reaction F consumption is similar, as illustrated in Figure 8-7, however, as the sol nears gelation, F consumption within the Cs sol diminishes. Given that R disappears similarly, the differing F consumption suggests that HMs and their aggregated forms are less substituted when Cs is used as a catalyst, i.e. the concentration of HMs formed are equal, however, when Na and K are used there are more di and tri-substituted molecules. This is consistent with the

increased aggregation (see DLS results - Figure 8-8), and resultant larger particles (see SEM images, and larger pores (Figure 8-9), observed within Cs sols (as discussed in Section 7).

F consumption within the Ca sols varies significantly from their Na and Cs counterparts; with the $CaCO_3$_200 sol, F disappearance is reduced significantly and is more akin to Na and Cs R/C 400 sols. DLS results for $CaCO_3$_200 sol (Figure 8-8) indicate that, during the sol to gel transition, there is a large increase in particle size, with DLS detecting particle sizes of up to 100 nm. The increased particle size, for Ca sols, is illustrated by the SEM images shown in Figure 8-10 and Figure 8-11, which can be compared to Na sols (Figure 6-16 and Figure 6-17) and Cs sols (Figure 7-16 and Figure 7-17). These larger particles are indicative of increased aggregation, which in a similar manner to the Cs sols, results in decreased substitution of HM derivatives and, in turn, decreased F consumption. Reduced F consumption, in comparison to its analogous Na and Cs sols, is also observed for $CaCO_3$_400 sol, which can again be explained due to increased aggregation (this will be discussed further in Section 8.8).

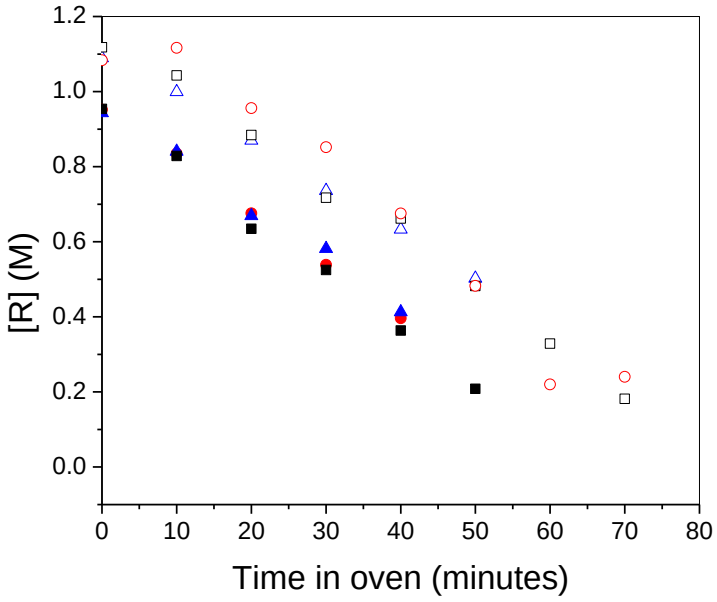

Figure 8-6: LC results obtained on Column 2 for Na_2CO_3_200 (!), Na_2CO_3_400 (∀), Cs_2CO_3_200 (,), Cs_2CO_3_400 (.), $CaCO_3$_200 (7) and $CaCO_3$_400 (8).

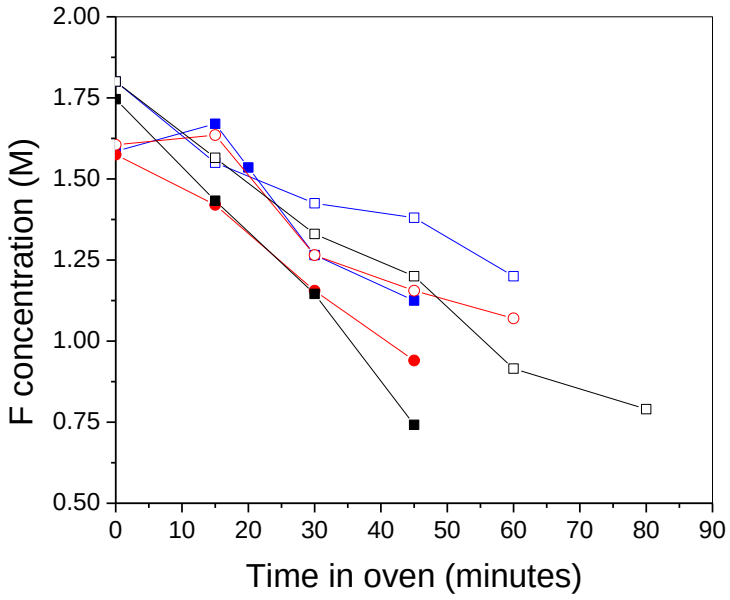

Figure 8-7: Titration data showing the disappearance of F for Na_2CO_3_200 (!), Na_2CO_3_400 (∀), Cs_2CO_3_200 (,), Cs_2CO_3_400 (.), $CaCO_3$_200 (!) and $CaCO_3$_400 (∀).

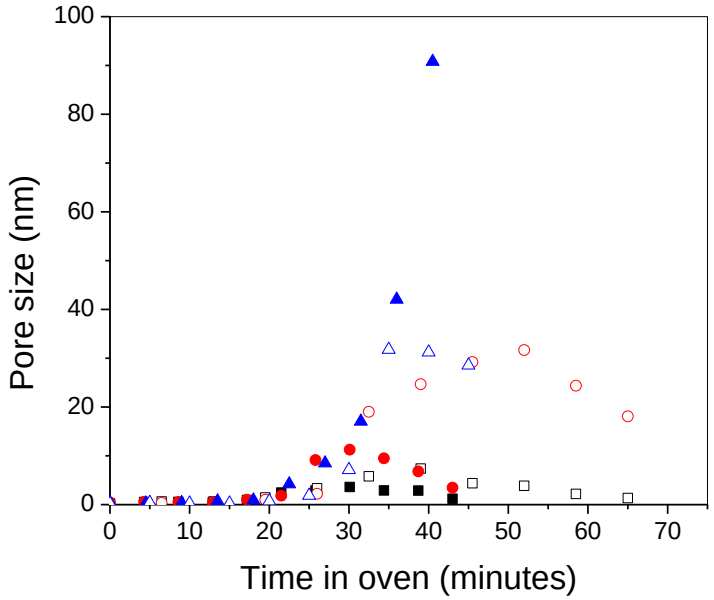

Figure 8-8: DLS results for sols prepared with Na_2CO_3_200 (!), Na_2CO_3_400 (∀), Cs_2CO_3_200 (,), Cs_2CO_3_400 (.), $CaCO_3$_200 (7) and $CaCO_3$_400 (8).

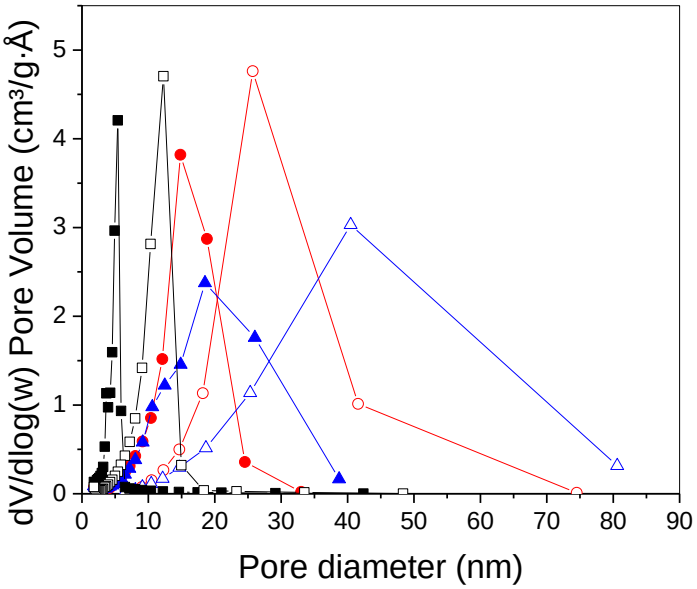

Figure 8-9: PSD for xerogels prepared Na_2CO_3_200 (!), Na_2CO_3_400 (∀), Cs_2CO_3_200 (,), Cs_2CO_3_400 (.), $CaCO_3$_200 (7) and $CaCO_3$_400 (8).

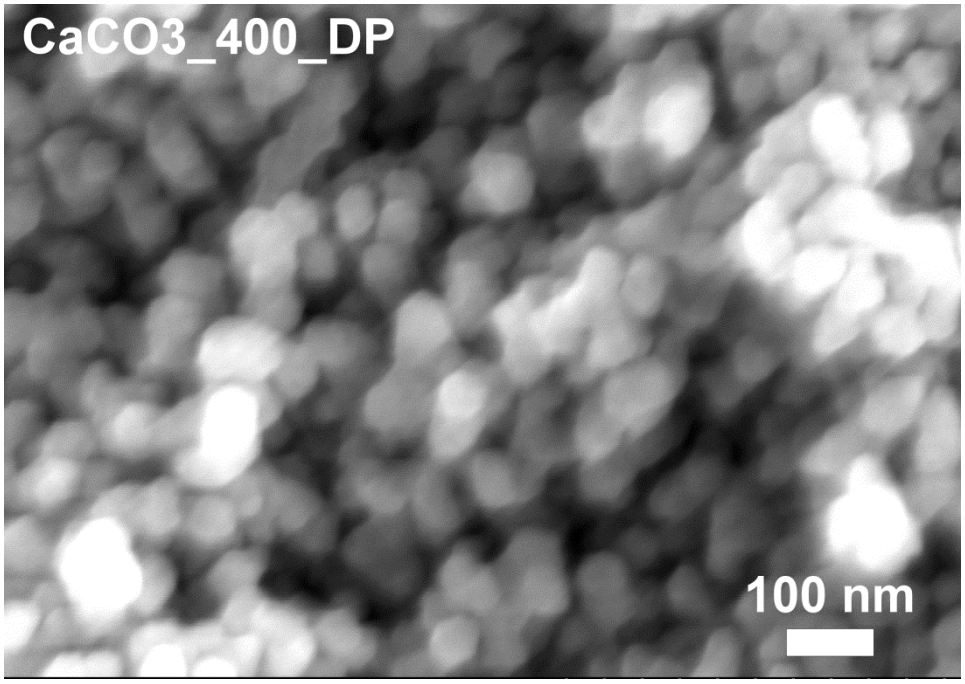

Figure 8-10: SEM image for $CaCO_3$_400_DP with magnification of 100 k (demonstrating larger particles than Na counterparts – see Figure 6-16).

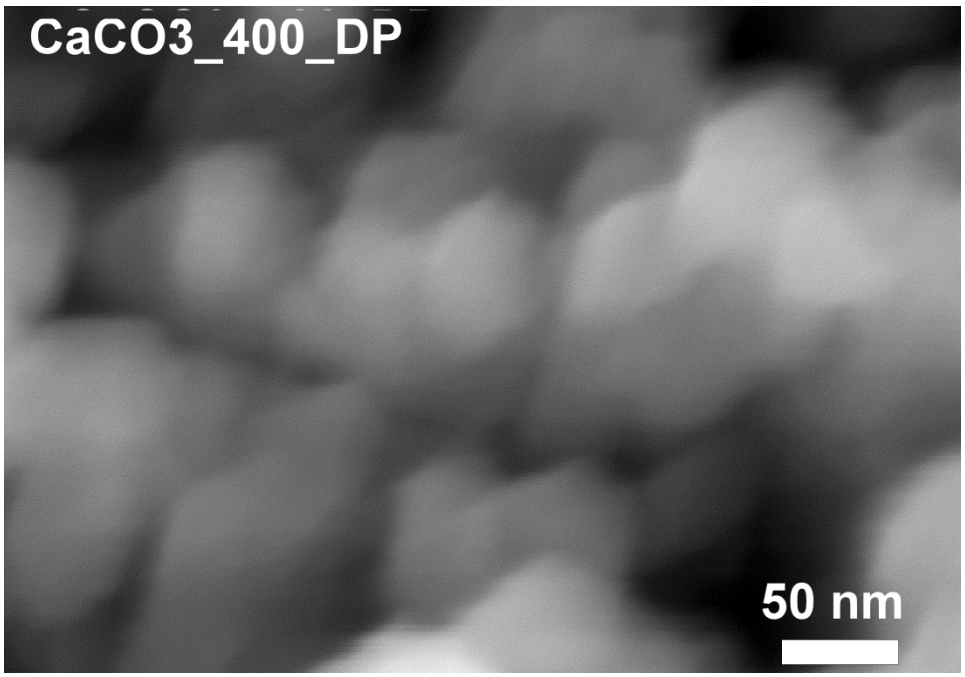

Figure 8-11: SEM image for $CaCO_3$_400_DP with magnification of 300 k (demonstrating larger particles than Na counterparts – see Figure 6-17).

8.5 Effect of cation radius

As you descend Group II, the number of electron shells increases, which in turn causes the ionic radius to expand, as discussed in Section 2.4.4 with increasing ionic radii the hydrated radii decreases. The smaller hydrated cations (larger ionic cations - see Figure 7-18) pack more densely around colloidal particles, resulting in a reduction in screening length [24]. In a similar manner to Group I catalysts, it is expected that as the ionic radii increases and hydrated radii decreases (as the Group is descended), attraction between colloidal particles is enhanced and repulsion is reduced. Consequently, it is expected that xerogel particle size should increase in the order Mg < Ca < Sr < Ba.

Figure 8-12 shows that, in general, analogous Mg and Ca gels have similar pore sizes and as the hydrated ionic radius increases, the pore size increases further, with Sr and Ba gels displaying similar average pore diameters. These results are similar to the trends displayed with Group I catalysed sols, with Na and K showing similar pore diameters and Cs prepared sols exhibiting significantly larger pore sizes.

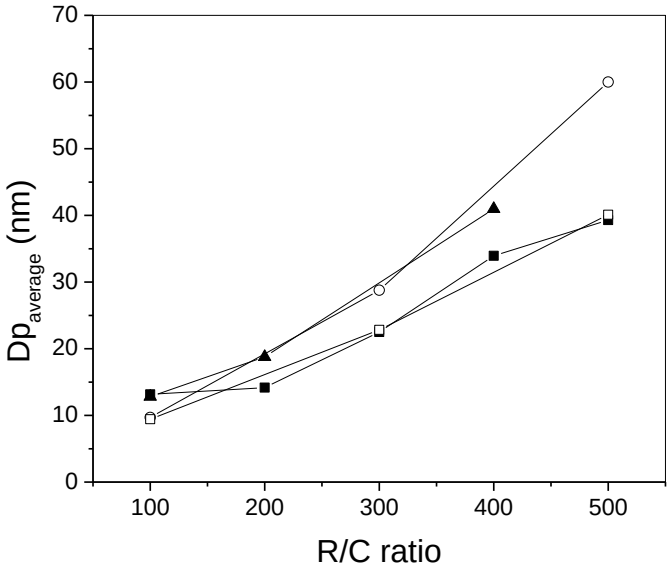

Figure 8-12: Trend in Dpaverage for $Mg(OH)_2$ (∀), $CaCO_3$ (!), $SrCO_3$ (7) and $BaCO_3$ (.).

8.6 Effect of the cation charge

The results obtained for RF xerogels prepared with Group II catalysts are consistent with the screening length theory proposed in Chapter 7; as the charge on the cation increases, the cations are able to pack more densely around the RF particles, resulting in a decrease in screening length ($1/\kappa$), where κ, is determined using Equation 6 [24].

For analogous concentrations of Group I and Group II metal catalysts (i.e. Cs_2CO_3_200 and $CaCO_3$_200), the screening length, based on metal cations only, is ~ 1.5 times smaller for Group II catalysts. Consequently, the energy barrier for coagulation is reduced and it is expected that colloidal particles will come closer together, resulting in particle aggregation [24]. This coagulation is demonstrated by DLS results (Figure 8-8), which show significantly larger particle sizes for $CaCO_3$_200 sol, when compared to its Cs_2CO_3 counterpart.

Estimating the Debye Huckel screening length, based on only the metal cations, gives similar screening lengths for Cs_2CO_3_200 and $CaCO_3$_400 sols, however, from the results presented it is evident that gel characteristics, disappearance of reactants and particle size growth, vary between these two sols. From the LC results displayed (Figure 8-6), it appears that the disappearance of R is based on the DPA, consequently, despite similar screening lengths for Cs_2CO_3_200 and $CaCO_3$_400 sols, the DPA value of the Cs sol is higher, which

will result in an increased R^- concentration. This higher R^- concentration will result in increased primary particle formation, which upon aggregation will result in smaller pores within the gel structure (as demonstrated by DLS results and gel characteristics).

8.7 Comparison of gel times

Table 8-2: Comparison of gel time for analogous, Na, Cs and Ca prepared sols

Gel	Gel time (min)	Gel	Gel time (min)	Gel	Gel time (min)
Na_2CO_3_200	50	**Cs_2CO_3_200**	50	**$CaCO_3$_200**	55
Na_2CO_3_400	70	**Cs_2CO_3_200**	70	**Cs_2CO_3_400**	70

8.8 Group II catalysts – Summary

Several RF xerogels were prepared using various different Group II catalysts. The initial sol pH, reaction pathways, particle aggregations and gel properties were studied and compared to xerogels prepared with analogous Group I catalysts. The results presented support those discussed in Section 7, demonstrating that initial sol pH has little effect on the overall properties of the final gel structure (Figure 8-2).

LC data, comparing disappearance of R, indicated that sols prepared with similar DPAs displayed comparable R consumption. As R reacts with F to form HM derivatives, the LC results presented (Figure 8-6) suggest that DPA is responsible for the formation of primary HM particles.

DLS results (Figure 8-8) indicate increased particle aggregation, for Cs based sols and Group II catalysed sols, which, as expected, resulted in reduced F consumption (Figure 8-7), caused by decreased HM substitution. The increased aggregation observed can be explained by a decrease in screening length, with increasing ionic radius (decreasing hydrated radius), charge and concentration of metal cation. Cation charge appears to be the dominant parameter, with low R/C Group II catalysed sols i.e. $CaCO_3$_200 (approximate hydrated radii 600 pm and cation concentration 5.87 x 10^{-3} M), exhibiting significantly increased aggregation, even when compared to considerably smaller hydrated cations at higher concentrations i.e. Cs_2CO_3_200 (approximate hydrated radii 250 pm and cation concentration 11.17 x 10^{-3} M). However, as the cation concentration decreases the charge has a reduced effect and Cs_2CO_3_400 and $CaCO_3$_400 show more comparable results.

Similar results were reported by Job *et al*. [63], who theorised that the decrease in Debye Huckle screening length, observed for Group II metal catalysts, favoured particle aggregation, resulting in gelation occurring more quickly. They concluded that this faster

gelation occurred at a lower degree of cross-linking, resulting in larger pores. However, the results presented in this study, demonstrate similar gelation times for analogous Group I and Group II catalysed gels (section 8.7) with LC (disappearance of R) and titration (disappearance of F) results indicating differing reaction pathways, for Group I and Group II catalysts. These results, along with the differing particle aggregations observed (DLS), demonstrate that gel properties are dependent on the reactions and interactions occurring, and not on quickened gelation times.

To summarise:

(1) Initial sol pH appears to have little effect on the final properties of RF gels.
(2) The formation of primary HM particles is dependent on the DPA of the catalyst involved, which is related to the concentration of base.
(3) Aggregation and further reaction of the primary HM particles are dependent on the metal cations present and the ability to screen colloidal surface charges. This screening ability decreases with increasing charge, concentration and ionic radius of the metal cation.

9 Results Part 4 - Gels prepared with $(NH_4)_2CO_3$ and no catalyst

In order to investigate the role of the metal cation in RF gel formation, reactions were followed for both RF sols prepared using ammonium carbonate, $(NH_4)_2CO_3$, and a sol prepared with no catalyst. $(NH_4)_2CO_3$ has previously been used as a catalyst [179], with the authors investigating R/C ratios ranging from 465 to 13,200. Reuss *et al*. [179] also studied a mass ratio of approximately 0.52, where the mass ratio was defined as the mass of water plus C to the total mass of solution, thus 50 % of the mass is mainly water and the other 50 % is made up of R plus F, this equates to approximately 100 % w/v solids (R + F + C). This high reactant concentration makes it difficult to compare to other systems in the literature, which in general have percentage solids between 5 and 40 %. To allow direct comparisons to be made, between metal catalysed gels and $(NH_4)_2CO_3$ catalysed gels, the R/C ratios investigated here range from 25 to 300 with constant percentage solids of 20 % w/v.

9.1 Gel properties

Table 9-1 presents the properties for dried and carbonised RF gels, indicating that both micro- and meso-porosity is introduced during pyrolysis. As expected the observed increase in surface area is due to a significant increase in micropores within the structure [80, 180, 181].

Table 9-1: RF xerogel and carbon properties for gels prepared from $(NH_4)_2CO_3$ and no catalyst

R/C	pH	S_{BET} (m^2/g)	V_{TOT} (x 10^{-3} cm^3/g)	S_{MIC} (m^2/g)	V_{MIC} (x 10^{-3} cm^3/g)	V_{MES} (x 10^{-3} cm^3/g)	$Dp_{average}$ (nm)
25	7.14	3.03	4.32	0.675	0.340	4.02	12.1
50	7.12	1.49	2.01	0.252	0.182	1.83	35.6
75	7.09	1.21	1.157	1.76	0.971	0.213	32.6
100	6.50	1.81	2.30	1.11	0.360	1.94	26.9
300	6.37	1.64	0.908	0.658	0.370	0.538	36.8
500	6.23	0.777	0.540	0.650	0.338	0.160	35.8
NO_C	3.89	2.38	4.70	-	-	4.70	27.0
PYROLYSED GELS							
R/C	**pH**	S_{BET} (m^2/g)	V_{TOT} (cm^3/g)	S_{MIC} (m^2/g)	V_{MIC} (cm^3/g)	V_{MES} (cm^3/g)	$Dp_{average}$ (nm)
25	7.14	459	0.256	430	0.223	0.033	0.66
75	7.09	463	0.249	425	0.224	0.025	0.66
100	6.50	472	0.251	429	0.226	0.025	0.66
300	6.37	469	0.249	440	0.232	0.017	0.67
500	6.23	466	0.246	436	0.229	0.017	0.68
NO_C	3.89	448	0.236	418	0.215	0.021	<2

N.B micropore analysis for NO_C_DP has not been carried out therefore exact pore diameter cannot be determined, however PSD indicates it is less than 2 nm, consequently,

given the similarities between the properties of NO_C_DP and $(NH_4)_2CO_3$ pyrolysed gels, it is expected that the average pore diameter of NO_C_DP will in the region of 0.6-0.7 nm.

Figure 9-1 (a) shows that before pyrolysis gels prepared with either no catalyst or with $(NH_4)_2CO_3$ show very little porosity. Figure 9-1 (b) shows that after pyrolysis all gels show very similar adsorption behaviour resulting in Type I isotherms, indicative of microporous materials. The carbons show very little adsorption above 0.1 and have no hysteresis loops, indicating that there are few mesopores within the carbon structures, as confirmed by the very high percentage of micropores (Table 9-1). The small slope of adsorption between 0.1 and 0.3 also demonstrates low external surface area.

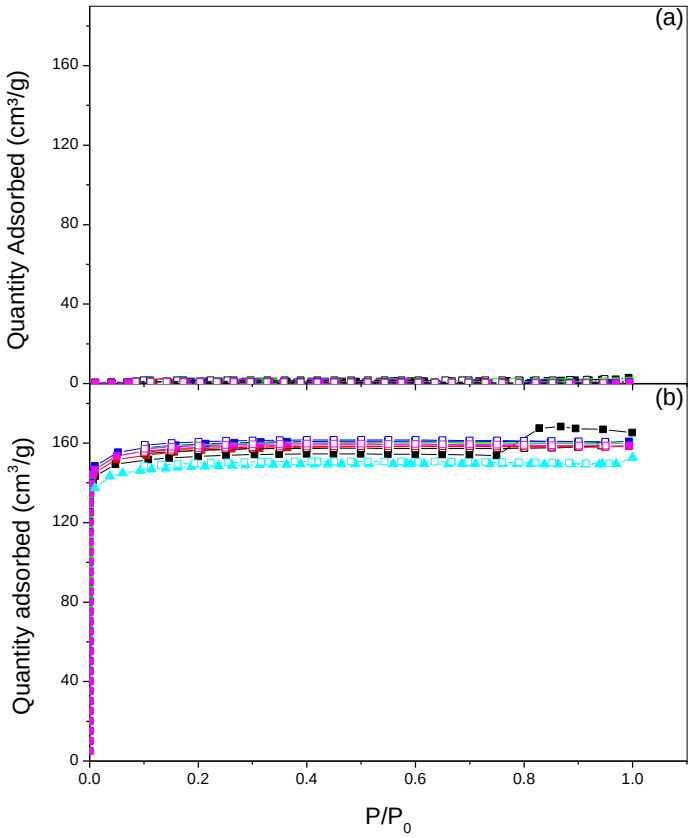

Figure 9-1: N_2 adsorption (closed symbols) and desorption (open symbols) isotherms for (a) dried and (b) carbonised gels prepared with $(NH_4)_2CO_3$ with R/C ratios of 25 (!), 50 (!), 75 (!), 100 (!), 300 (!) and 500 (!) and for gel prepared with no catalyst (!).

The Horvath Kawazoe and BJH PSDs are shown Figure 9-2, demonstrating that, unlike gels prepared with a metal bearing catalyst, carbons made using $(NH_4)_2CO_3$ show monomodal pore sizes and exhibit no mesoporous character.

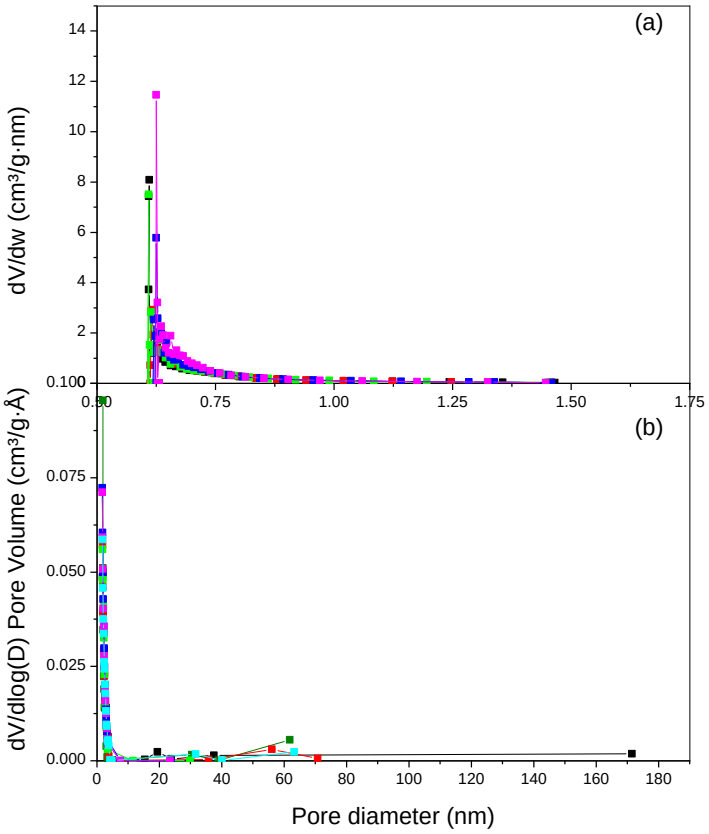

Figure 9-2: (a) Horvath Kawazoe and (b) BJH pore size distributions for carbonised gels prepared with $(NH_4)_2CO_3$ with R/C ratios of 25 (!), 50 (!), 75 (!), 100 (!), 300 (!) and 500 (!) and for a gel prepared with no catalyst (!).

Similar to previously reported values for RF carbon materials [182-185], the carbons prepared using no catalyst and $(NH_4)_2CO_3$ all demonstrate ~ 90 % microporosity, however, the PSD is usually broader, showing micropores and mesopores. In most RF carbons, micropores and smaller diameter mesopores result from small erosions in the carbon particles, and larger diameter mesopores and macropores result from channels between closely packed and loosely packed particles, respectively [162], as illustrated in Figure 9-3. Obviously, as particle size increases, interparticle separation will increase resulting in larger pores.

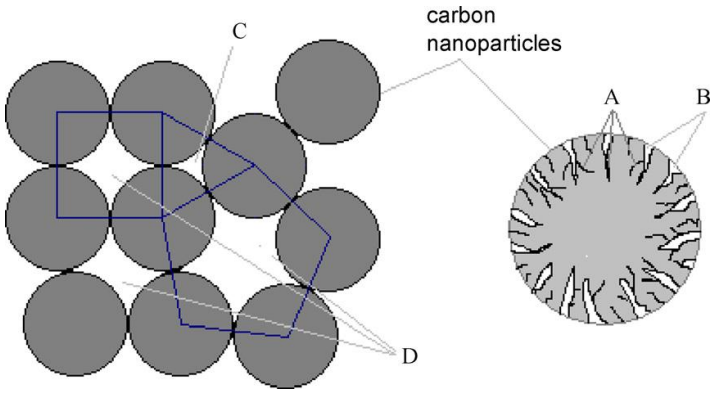

Figure 9-3: Carbon particles showing micropores (A), mesopores (B & C) and macropores (D) [162].

Given the narrow pore size distribution displayed for the carbons reported here, it is likely that all particles are exclusively microporous and the fact that minimal mesopores are detected suggests that particles are large, resulting in considerable pores that are undetectable by N_2 sorption experiments [80] (i.e. they are outside the experimental limits of the equipment used). In order to test this $(NH_4)_2CO_3$_75_DP and NO_C_DP were imaged using SEM; the results are shown in Figure 9-4 and Figure 9-5.

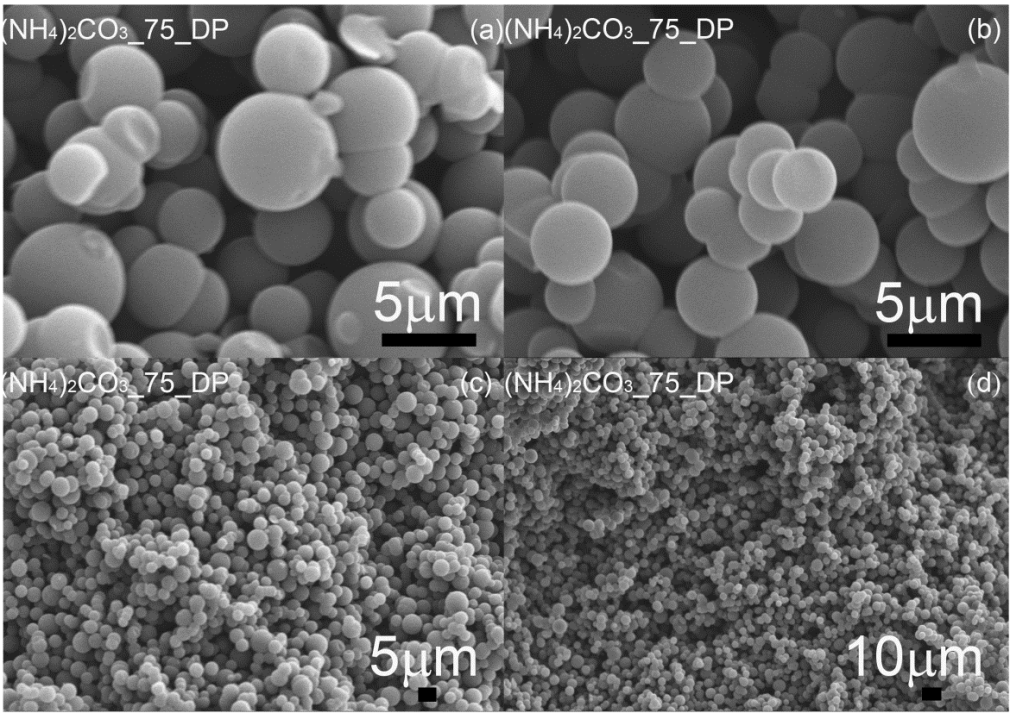

Figure 9-4: SEM images for $(NH_4)_2CO_3$_75_DP at magnifications of 4.5 k at (a) site 1 and (b) site 2, 800 at (c) site 1 and 450 at (d) site 1.

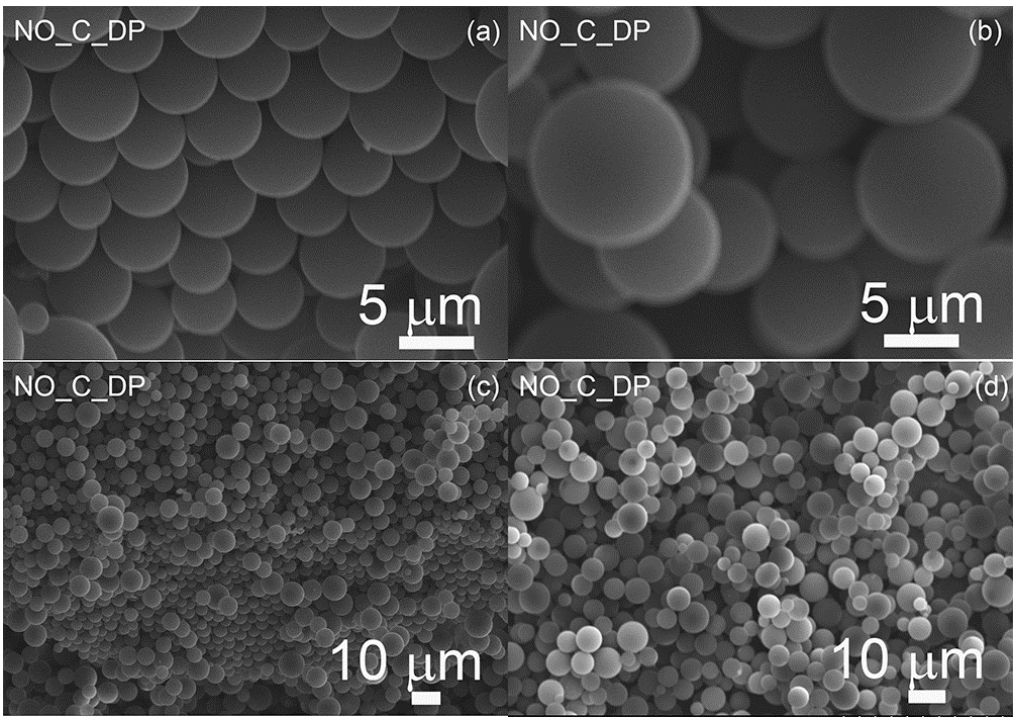

Figure 9-5: SEM images for NO_C_DP at magnifications of 4.5 k at (a) site 1 and (b) site 2 (b), 800 at (c) site 1 and 800 at (d) site 1.

Figure 9-4 and Figure 9-5 show that, in contrast to RF gels synthesised using metal bearing catalysts, $(NH_4)_2CO_3$ catalysed gels and gels prepared with no catalyst are composed of individual spherical particles. These structures are very similar to those reported by Scherdel *et al*. [80] for low catalyst systems. The authors demonstrated that, as the catalyst concentration was reduced, the particle size increased and the particles became less aggregated. They reported Equation 152 to determine parameter (x), which estimates whether the particles are aggregated or randomly packed spheres. For values of x close to 1, the material is composed of randomly packed polydisperse spheres, whereas values of <<1 indicate that the material consists of aggregated particles. When the interparticle voids are large macropores (> 50 nm), which are undetectable by N_2 adsorption, the value of x greatly exceeds 1.

$$\frac{V_{particle}/V_{mes}}{V_{sphere}/V_{interparticle}} = x$$

Equation 152

$V_{particle}$ is defined as the total volume of particles, which can be determined by calculating the external surface area of one particle, $S_{ext,\ particle}$, and using the total external surface area, S_{ext}, to determine the number of particles. The volume of one particle, $V_{single,\ particle}$, is then multiplied by the number of particles to determine $V_{particle}$, as shown in Equation 153 to Equation 155.

$$S_{ext,particle} = 4\pi r^2$$

Equation 153

$$No.of\ particles = S_{ext}/S_{ext,particle}$$

Equation 154

$$V_{particle} = No.of\ particles \times V_{single,particle}$$

Equation 155

Schaerti *et al*. [186] stated that for a random packing of spheres the packing density is 0.7, consequently for $(NH_4)_2CO_3$_75_DP, $V_{sphere}/V_{interparticle\ (pore\ volume)}$ can be calculated as 0.7/1.157 x 10^{-3} = 605. From the SEM images shown in Figure 9-4, the average particle diameter for $(NH_4)_2CO_3$_75_DP can be determined as approximately 2.5 μm, using this value, and the properties given in Table 9-1, the x parameter can be calculated as follows:

$$S_{ext,particle} = 4\pi r^2 = 4\pi\ (1.25\ \times 10^{-6})^2 = 1.96\ \times 10^{-11} m^2$$

$$No.of\ particles = \frac{463.132 - 424.862\ (\frac{m^2}{g})}{1.96\ \times 10^{-11}\ m^2} = 1.54 \times 10^{12}$$

$$V_{single,particle} = \frac{4}{3}\pi r^3 = \frac{4}{3}\pi(1.25 \times 10^{-6})^3 = 8.18 \times 10^{-18}\ m^3$$

$$V_{particle} = 8.18 \times 10^{-18}\ m^3 \times 1.54 \times 10^{12} = 1.26\ \times 10^{-5}\ m^3$$

$$\frac{V_{particle}/V_{mes}}{V_{sphere}/V_{interparticle}} = \frac{(1.26\ \times 10^{-5} m^3/(2.12\ \times 10^{10} m^3/g))}{605} = 98$$

Consequently, it can be deduced that $(NH_4)_2CO_3$_75_DP consists of randomly packed polydisperse spheres and, due to their large size, the interparticle voids are large macropores.

Scherdel *et al*. [80] demonstrated that RF gels with larger external surface areas tended to be more aggregated and gels with similar porous properties showed similar morphologies. Given the similarity of the porous properties of the non-catalysed and $(NH_4)_2CO_3$ gels, it would be expected that the morphology would be similar. Thus it can be concluded that non-catalysed and $(NH_4)_2CO_3$ gels consist of randomly packed polydisperse spheres, separated by large interparticle voids.

9.2 Sol sedimentation

Scherdel *et al*. [80] also reported that, when the particle size exceeded 200 nm, visible sedimentation was observed about 24 hours into gelation. The $(NH_4)_2CO_3$ gels synthesised here displayed strong sedimentation within minutes of being placed in the oven, and the

non-catalyst gel showed visible sedimentation after a couple of hours. This indicated that large particles were forming early into gelation, in contrast to the metal catalysed sols which displayed a uniform transition from sol to gel. The DLS results for sols prepared with $(NH_4)_2CO_3$_200 and no catalyst are illustrated in Figure 9-6. The DLS results show that, for the $(NH_4)_2CO_3$_200 sol, large particles form instantly upon heating, which is consistent with visible sedimentation. For the non-catalyst sol, where sedimentation appears to occur more gradually, the DLS results demonstrate more gradual particle growth.

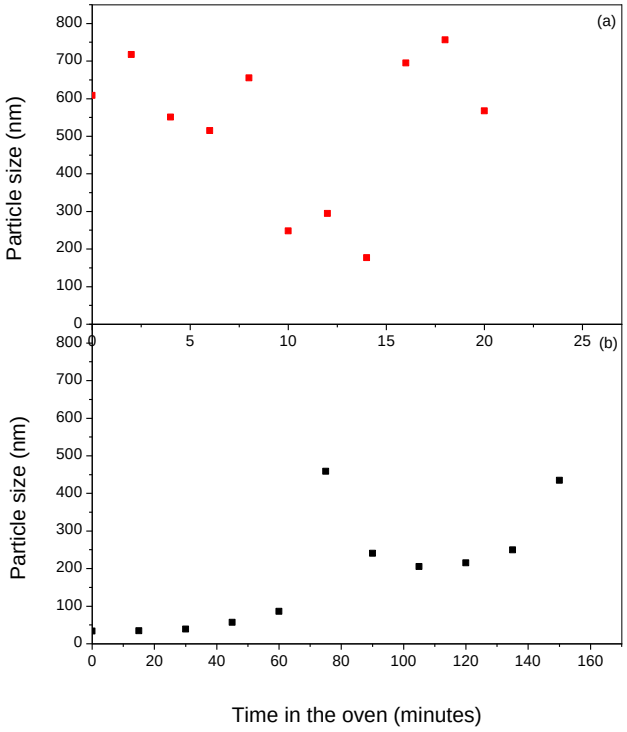

Figure 9-6: DLS results for (a) $(NH_4)_2CO_3$_200 sol and (b) sol prepared with no catalyst.

Given that $(NH_4)_2CO_3$ gels were prepared with very similar base concentrations, hence pHs to metal catalysed RF gels, the different structures observed and the visible particle formation suggest that the reaction for $(NH_4)_2CO_3$ sols may be different. In order to investigate this, the reaction was followed using LC and titration methods.

9.3 The reaction

The consumption of R and F for gels prepared with $(NH_4)_2CO_3$ and no catalyst are illustrated in Figure 9-7, the results for Na_2CO_3_200 are also shown for comparison. The results indicate that when $(NH_4)_2CO_3$ is used R disappears in a very similar manner to when a comparable concentration of Na_2CO_3 is present. When $(NH_4)_2CO_3$ is utilised the initial consumption of R occurs at a slightly slower rate than when Na_2CO_3 is present, suggesting

that there is less base present for deprotonation, and as the reaction progresses the rate of consumption of R remains slightly faster for the Na_2CO_3 prepared gels, compared to gels made using $(NH_4)_2CO_3$, where the rate of consumption is represented by the slope, m, of the consumption trendline (m = -0.0118 M/min for $(NH_4)_2CO_3$_200, and = -0.0151 M/min Na_2CO_3_200). However, due to the increased aggregation observed in the $(NH_4)_2CO_3$ sols, reaction of R and F is hindered, resulting in significantly reduced F consumption; with the rate of F consumption being 0.01033 M/min for $(NH_4)_2CO_3$_200, compared to 0.022 M/min for Na_2CO_3_200.

As illustrated in Figure 9-7, for gels prepared with no catalyst there appears to be very little change in [R] and [F] until after approximately 75 minutes in the oven, at this stage R then disappears at a rate of 0.0084 M/min and F disappears at a rate of 0.0088 M/min.

From LC and titration results for gels prepared with no catalyst it appears that something else in the synthetic mixture triggers the reaction, instigating a significant increase in the rate of consumption of both R and F. Although monitoring the hydroxyl-methyl (HM) concentration using LC cannot be used quantitatively, examination of the results obtained for gels prepared with no C show that, at approximately 50 minutes, the concentration of HMs increases slightly, see Figure 9-8, and it is at this stage that the reaction between R and F appears to be activated. These results suggest that, once a critical concentration of HM is reached, condensation reactions occur, forming RF polymeric products. This would also explain why [HM], with no catalyst, appears to increase and then drop off as the monomers further react to form dimers, trimers etc. This was tested further through the use of LCMS, as presented in Figure 9-9 and Table 9-2, which show LC spectra and associated MS identification, respectively. MS results obtained prove that growing polymeric products, from HM monomers to tetramers, are present in the sol. LCMS results obtained for $(NH_4)_2CO_3$ sol are given in Appendix F.

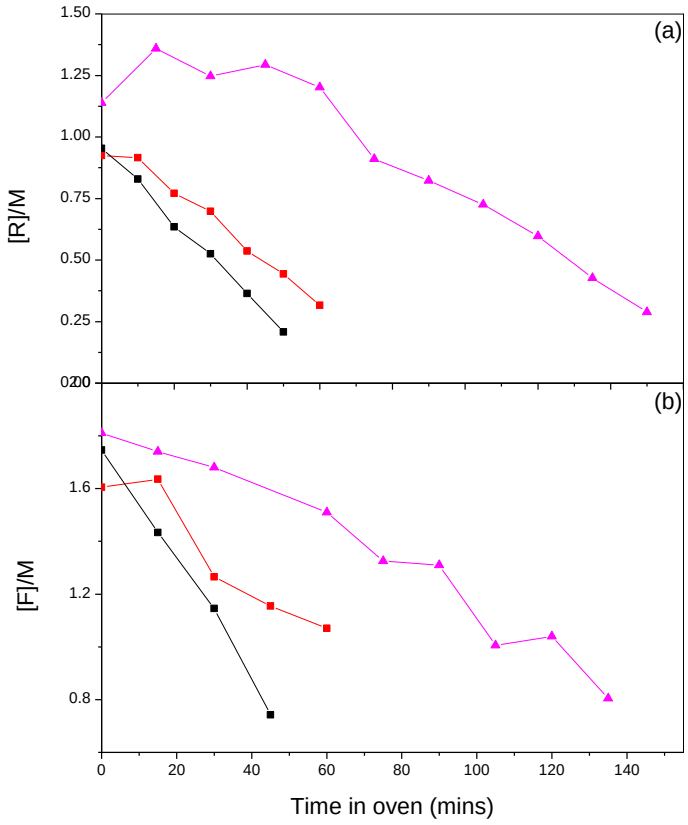

Figure 9-7: LC results showing (a) consumption of R, measured on LC column 2, and (b) titration data showing the consumption of F (b) for Na_2CO_3_200 (!), $(NH_4)_2CO_3$_200 (!) and NO_C (7).

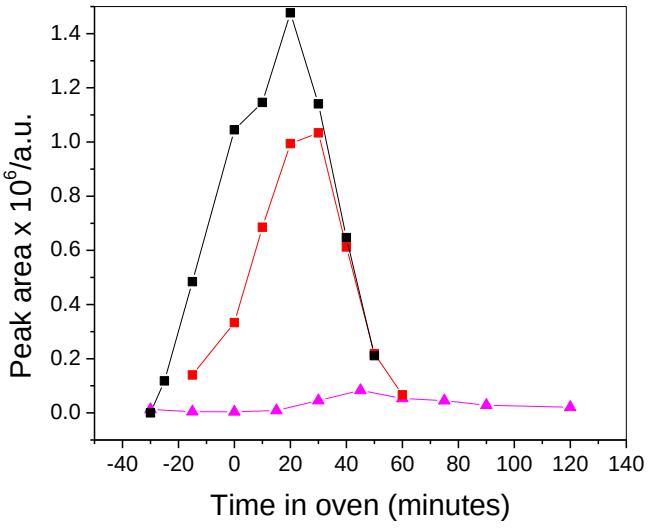

Figure 9-8: Change in LC peak area of hydroxyl-methyl peak, measured on column 2, for Na_2CO_3_200 (!), $(NH_4)_2CO_3$_200 (!) and NO_C (7).

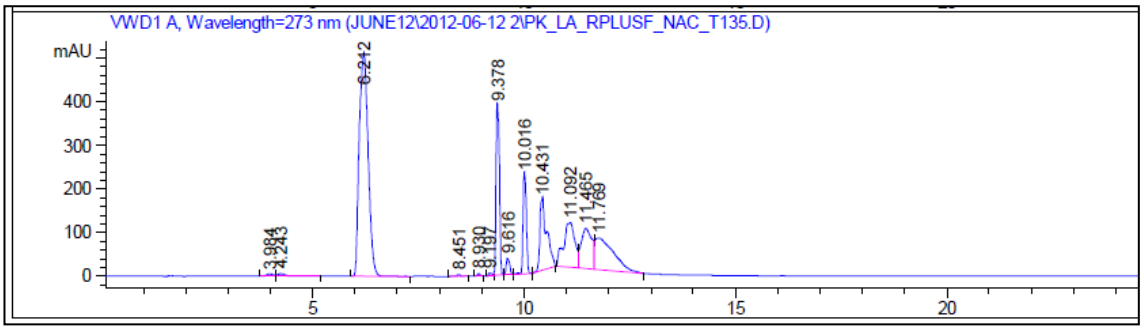

Figure 9-9: LC spectra for sol prepared with no C at T_{135}.

Table 9-2: MS identification of reaction products at T_{135} for sol prepared with no C

Retention time (minutes)	Molecular weight (g)	Identification (see Appendix G)
4.255	139.1	Monomer
6.235	109.2	Resorcinol
8.475, 9.217	261.1	Dimer
9.399, 9.637	231.1	Dimer
10.041	353.0	Trimer
10.414	353.1, 475.1	Trimer & Tetramer
10.586	353.1	Trimer
10.874	475.1	Tetramer
11.102	597.0	Pentamer

The reaction products formed, i.e. dimers, trimers and tetramers with MS peaks at 232, 354 and 476 result from reaction of HM monomers with other monomers and with unreacted R (see Appendix G). Consequently, it can be concluded that small concentration of HMs formed activate unreacted R to form dimers etc. The LCMS results show that dimers with a mass of 232 are in the highest concentration (approximately 10 – 20x more than the other products displayed in Table 9-2), it is likely that further reactions are hindered by the low HM concentration.

LCMS results also display a peak with a m/z of 169, given the disappearance of F and results previously reported by Raff *et al*. [14] and Ingram *et al*. [13], it is likely that this peak results from the formation of hemiacetals, which are formed via the reaction of F with HM. This reaction reduces the concentration of F and prevents further formation of HMs. Although this reaction will occur in all sols, the increased concentration of activated R will prevent it from limiting the RF reaction.

9.4 Discussion

The results presented indicate that, even although R consumption is similar for both $(NH_4)_2CO_3$ and Na_2CO_3 catalysed gels, when $(NH_4)_2CO_3$ is present, the RF colloidal

suspension is destabilised, resulting in salting out; flocculated particles subsequently clump together forming a mass of spherical particles, as illustrated by SEM (Figure 9-4 and Figure 9-5).

Initially, it was theorised that catalytic cations affect stability of xerogel polymer molecules following a Hofmeister like trend. However, examination of gel properties, prepared using Group I and Group II metal carbonates/bicarbonates demonstrates that metal cations do not follow a typical Hofmeister series, namely Cs^+ appears to act in a manner similar to Group II metals, where the presence Group II ions make the RF colloidal suspension less stable (i.e. polymeric macromolecules are more stable and, as a result, less soluble, resulting in flocculation), than when other Group I cations are present. The cations studied result in the following Hofmeister-like series:

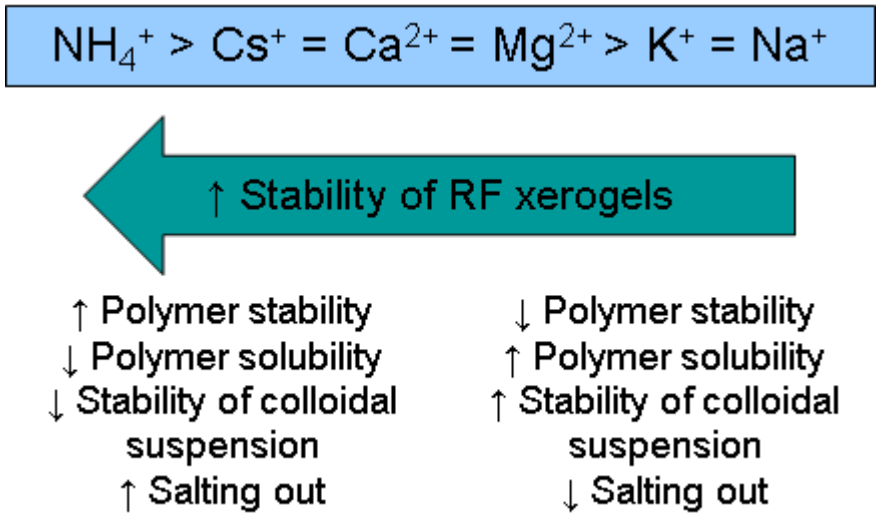

Figure 9-10: Effect of cations on RF xerogel stability.

As illustrated in Figure 9-10, when NH_4^+ is utilised the RF xerogel particles visibly salt out, in comparison to Na^+ and K^+, which appear to stabilise RF colloidal suspensions, allowing aggregation of polymer clusters in suspension. In contrast to this series, most work into the stability of colloidal suspensions has indicated that highly charged ions stabilise such colloidal suspensions, by destabilising the polymer molecules, which are salted in, and Cs^+ is normally reported as causing more stability in colloidal suspensions than that observed when K^+ and Na^+ are present. A typical Hofmeister series is illustrated in Figure 9-11.

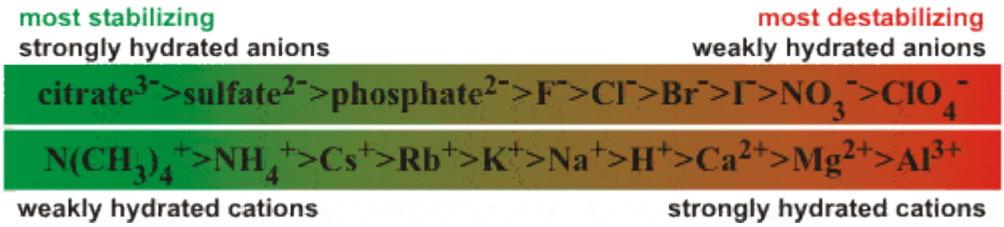

Figure 9-11: Typical Hofmeister series [40].

Comparison of gels catalysed with $(NH_4)_2CO_3$ and gels prepared with no catalyst have very similar properties, DLS findings show that the salting out effect is observed at similar levels for both syntheses. This suggests that metal cations are capable of stabilising RF colloidal suspensions, whereas NH_4^+ ions are not. Given that the hydrated radius of the NH_4^+ cation is 250 pm [177], which is identical to that of Cs^+ (see Figure 7-18), it would be expected that ammonium ions would have a similar repulsive and aggregative effect; however, if the decomposition of $(NH_4)_2CO_3$ is considered, it is clear that, with heat, ammonium carbonate will decompose initially into ammonium bicarbonate, with decomposition into ammonia gas, carbon dioxide and water:

$$(NH_4)_2CO_3 \rightarrow NH_4HCO_3 + NH_3(g)$$

Equation 156

$$NH_4HCO_3 \rightarrow NH_3(g) + H_2O + CO_2(g)$$

Equation 157

Consequently, during gel formation, most of the $(NH_4)_2CO_3$ is converted into gaseous ammonia, water and carbon dioxide. As described in Section 5.1, the reaction process involves initially reacting the reactants on the bench at room temperature. At standard temperature and pressure $(NH_4)_2CO_3$ undergoes the first stage of decomposition, consequently some base will be released to the surrounding atmosphere as gaseous ammonia. The remaining ammonium bicarbonate and carbonate react with R forming R^-, a small amount of which will react with F to form HM derivatives. The release of some NH_3, at room temperature, will result in a lower content of R^- than that of an analogous Na_2CO_3 gel, explaining why the reaction is slower when the sol is placed in the oven. Once placed in the oven, $(NH_4)_2CO_3$ will fully decompose, resulting in further release of NH_3, removing the majority of NH_4^+ ions from solution and, ultimately, removing the repulsive force that allows colloidal stability. However, $[R^-]$ present from the room temperature reaction is

sufficient to promote the reaction at a much faster rate than the corresponding non catalysed gel.

9.5 Summary

The results presented for non-catalysed and $(NH_4)_2CO_3$ gels indicate that these materials consist of randomly packed polydisperse spheres, separated by large interparticle voids. After pyrolysis, their carbon derivatives display very high levels of microporosity, which is borne from erosion of large particles. This is in comparison to RF gels prepared with a metal bearing catalyst, which display mainly mesoporous structures, resulting from densely packed, highly aggregated, monolithic RF gels, exhibiting increased microporosity after pyrolysis, however, remaining mainly mesoporous.

The significant differences, in RF structures, were investigated by studying the possibility of a varying reaction mechanism; however, LC and LCMS results show similar reaction pathways and products. These results contradict the theory put forward by Loustalot *et el*. [151], who proposed that a metal cation was required to produce a transition state (Figure 7-14) during the formation of HM derivatives.

The LCMS results presented for non-catalysed gels indicate the formation of HM monomers, dimers and trimers, and LC results indicate that a critical [HM] triggers the reaction. Therefore, it can be concluded that the reaction, between R and F, is not dependent on the presence of a metal cation, and reaction products will form even when a metal is not present. However, the stability of the colloidal suspension appears to be dependent on the presence of a metal, where metal cations allow the colloidal suspension to remain in solution resulting in the formation of many colloidal particles and subsequent aggregation, whilst suspended, resulting in a highly cross-linked gel (as discussed in Sections 7.5 and 8.6).

To summarise:

(1) RF carbons prepared with $(NH_4)_2CO_3$ are significantly more microporous than RF carbons catalysed with a metal bearing catalyst.
(2) The reaction between R and F is similar for both $(NH_4)_2CO_3$ catalysed gels and gels catalysed with Group I and Group II metallic bases.
(3) The stability of the colloidal suspension is increased in the presence of a metal cation, therefore when $(NH_4)_2CO_3$ is used the colloidal suspension is significantly less stable and salts out.

9.6 Application of $(NH_4)_2CO_3$ carbons

The tuneable porous nature of Na_2CO_3 xerogels/carbons suggested that they would be suitable inclusions for gas separation membranes and preliminary studies; utilising Na_2CO_3_300 dried and pyrolysed at 5 % loading, indicated that, with this filler, increased sensitivities were observed for CO_2/O_2 and CH_4/N_2 gas mixtures, when compared to unfilled membranes [187]. However, for high kinetic diameter gases and low molecular weight gases (i.e. slow gases – N_2 and CH_4) diffusion into the large mesopores occurs, resulting in significant increases in the normalised fluxes and reduced sensitivities. The brittle monolithic nature of the Na_2CO_3 derivatives also made the fillers difficult to handle and the membranes brittle.

The microporous nature of $(NH_4)_2CO_3$ carbons indicated that, when used as a membrane filler, they would display reduced diffusion and as a result increased sensitivity, for both low (CO_2 and O_2) and high kinetic diameter gases. The results obtained were as expected with $(NH_4)_2CO_3$ filled membranes displaying comparable or increased sensitivities for all gas mixtures studied, compared to the unfilled, and interestingly displayed an increased normalised flux for CO_2 gas (i.e. when compared to unfilled membranes the filled membranes would display increased purification in the same time period). In contrast to their Na_2CO_3 counterparts, the soft nature of the $(NH_4)_2CO_3$ carbons also makes the materials easier to handle and the membranes more elastic and less prone to breakage [187]. These preliminary results present $(NH_4)_2CO_3$ carbons as useful fillers for gas separation, and work on tuning the porous properties and optimising the milling process may improve their separation abilities further.

10 Results Part 5 – Relationship between UV-Vis absorbance and particle size

As discussed in Section 2.7.1 a number of parameters influence RF particle size and, in turn, impact the final porosity of the organic gels, it is, therefore, of significant importance that the process of aggregation can be easily monitored. Traditional methods for particle size determination include Dynamic Light Scattering (DLS), Small Angle X-Ray Scattering (SAXS) and microscopic techniques, for example Scanning Electron Microscopy (SEM) and Transmission Electron Microscopy (TEM). Schaefer *et al*. [32] and Horikawa *et al*. [25] have demonstrated that the reactions and structure formations occurring during the sol-gel transition are critical, subsequently, in order to study RF particle growth, the measurement technique must be capable of measuring solutions. For this reason microscopic methods, SEM and TEM, are not suitable.

As discussed in Section 3.1.1, DLS is a spectroscopic technique that involves determination and interpretation of a time autocorrelation function for scattered light, upon interaction with a sample. Although DLS can be carried out on RF sol samples [28, 188, 189], with no required sample preparation, obtaining particle size information from the auto correlation function can be complex and time consuming. SAXS is a similar technique and can also be utilised with solutions. This method involves recording the scattering of X-rays but, like DLS, this technique requires intricate data analysis [27]. The complex data analysis required for these procedures makes it difficult to compare different sols as they are prepared. Consequently, the aim of this work is to investigate the use of UV-Vis spectrometry as a means of rapidly monitoring RF particles, thus eliminating the need for sample preparation and complex data manipulation.

10.1 Introduction

Suspended particles in solution can interact with incident light in a number of different ways as illustrated in Figure 10-1. Particles can display absorption, refraction, diffraction or reflection and these physical phenomena all contribute to the collection of a UV-Vis spectrum [166]. The physical and chemical nature of the particles involved will affect which interactions occur.

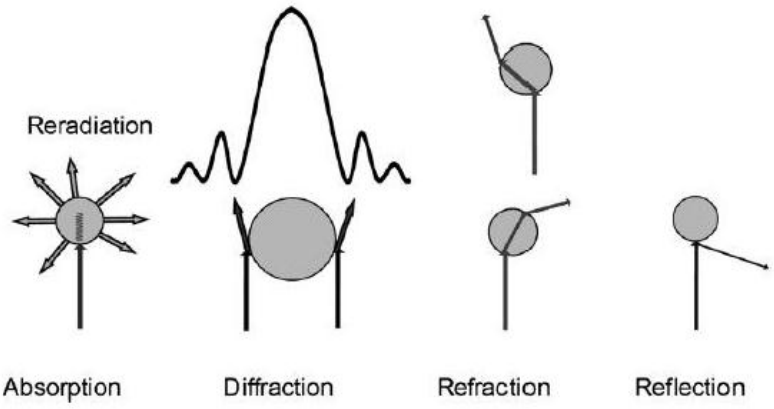

Figure 10-1: Schematic showing different types of interaction of light with suspended particles [190].

As well as being dependent on particle diameter, d, the type of light scattering involved is also dependent on the wavelength, λ, of incident light. To simplify this, a size parameter, α, has been identified as shown in Equation 158 [166] .

$$\alpha = \frac{\pi d}{\lambda}$$

Equation 158

The different types of scattering with changes in the size parameter, are displayed in Figure 10-2. It is clear from this diagram that when the particle diameter is much smaller (less than a tenth) than the wavelength of light, Rayleigh scattering occurs; this type of scattering tends to occur with soluble particles and light is scattered in all directions (Figure 10-3). When the particle diameter and wavelength are approximately equal Mie scattering occurs, where a combination of scattering in all directions and forward scattering is observed (Figure 10-3). As the particle diameter exceeds the wavelength Fraunhofer scattering/diffraction is observed, with light scattered mainly in the forward direction (Figure 10-3).

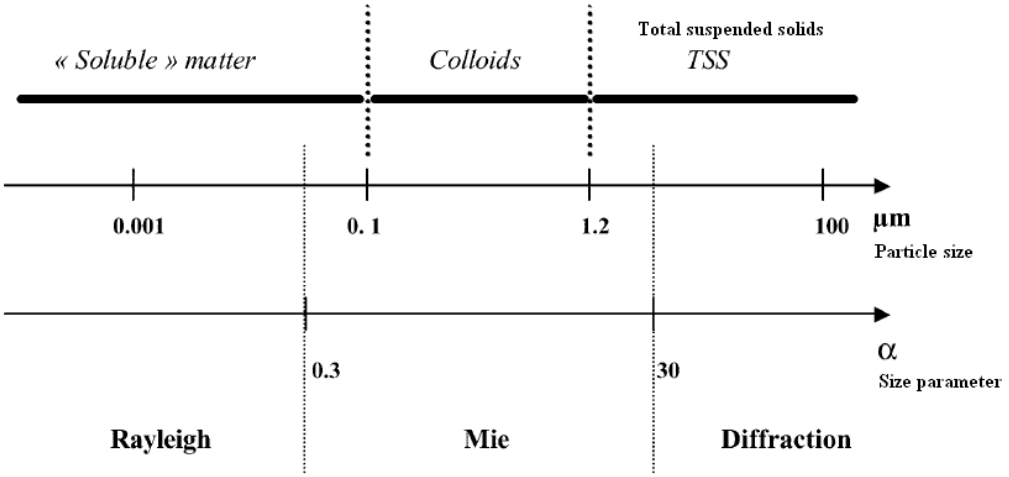

Figure 10-2: Diagram showing the different scattering types for varying size parameters and particle sizes [166].

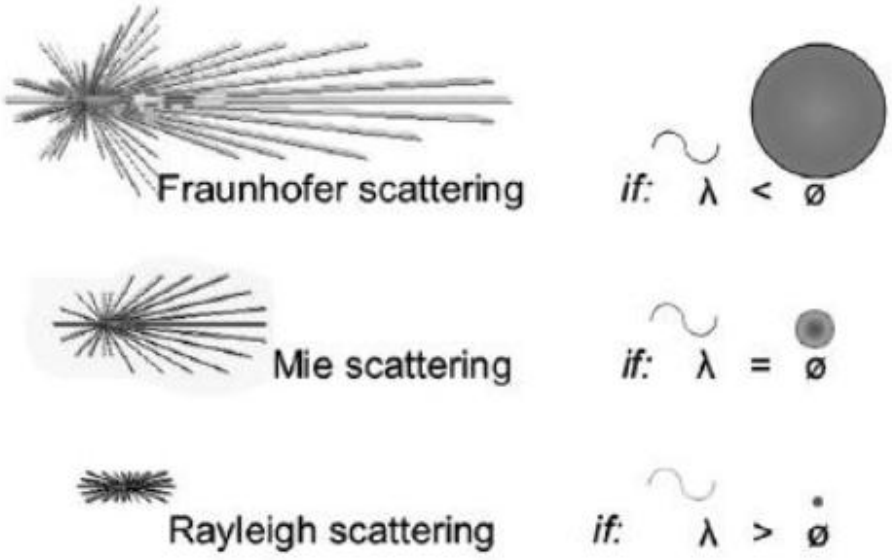

Figure 10-3: Diagram showing the different scattering types and the relationship between scattering and particle size [190].

The RF particles that form prior to gelation have radii in the region of 1 – 40 nm, therefore, they have diameters in the region of 2-80 nm. At 200 nm this gives rise to size parameters between 0.0314 and 1.256, and at 800 nm gives values between 0.00785 and 0.314. Consequently, mainly Rayleigh scattering is observed, however, some Mie scattering will also occur.

Given that different types of interaction (i.e. absorption, refraction, diffraction and reflection) can occur simultaneously, the effect of particle size on the absorption spectrum can be difficult to interpret.

10.2 Relationship between absorbance and RF particle size

An example UV-Vis spectrum for an RF sol is given in Figure 10-4, and the time resolved spectra for all RF sols studied are given in Figure 10-6. Figure 10-4 clearly illustrates three main absorbance peaks, which can be assigned using absorption bands given in the literature. The peak at approximately 280 nm is ascribed to phenol and aldehyde groups within the forming gel, and the peaks at approximately 220 nm and 350 nm result from conjugated benzene rings [191]. Similar scattering, as a result of conjugation, is observed in the spectrum for fullerene (C_{60}) solutions, as shown in Figure 10-5 [192, 193].

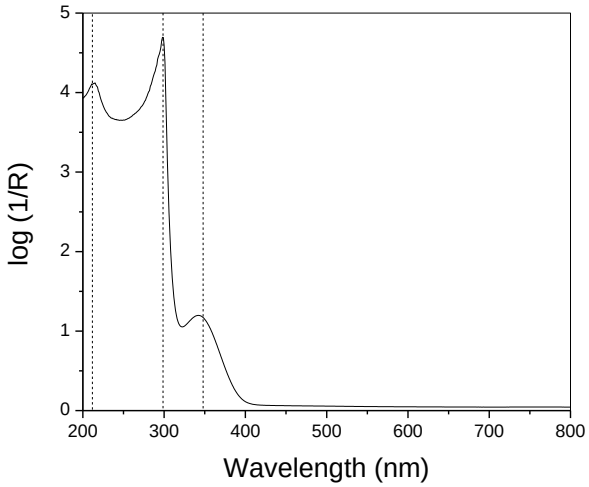

Figure 10-4: UV-Vis absorbance spectrum for Na_2CO_3_200 at T_{12}.

The results shown in Figure 10-6 demonstrate that absorbance at 350 nm appears to intensify with increasing reaction time. This increased absorbance results from a change in the sol colour, from colourless to red, as polymerisation reactions proceed; where colour change is indicative of increasing particle size, which results in increased conjugation across the larger clusters [19] and dense packing of RF particles.

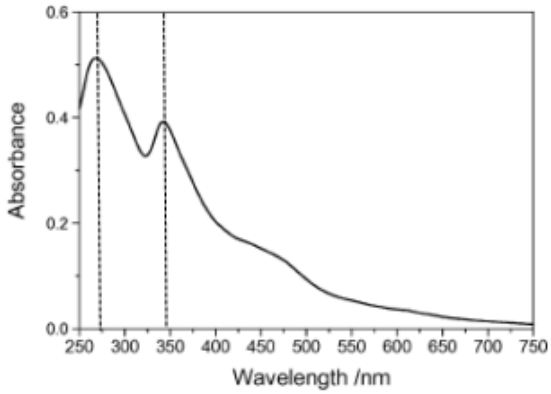

Figure 10-5: UV-Vis absorbance spectrum of colloidal C_{60} particles in water [193].

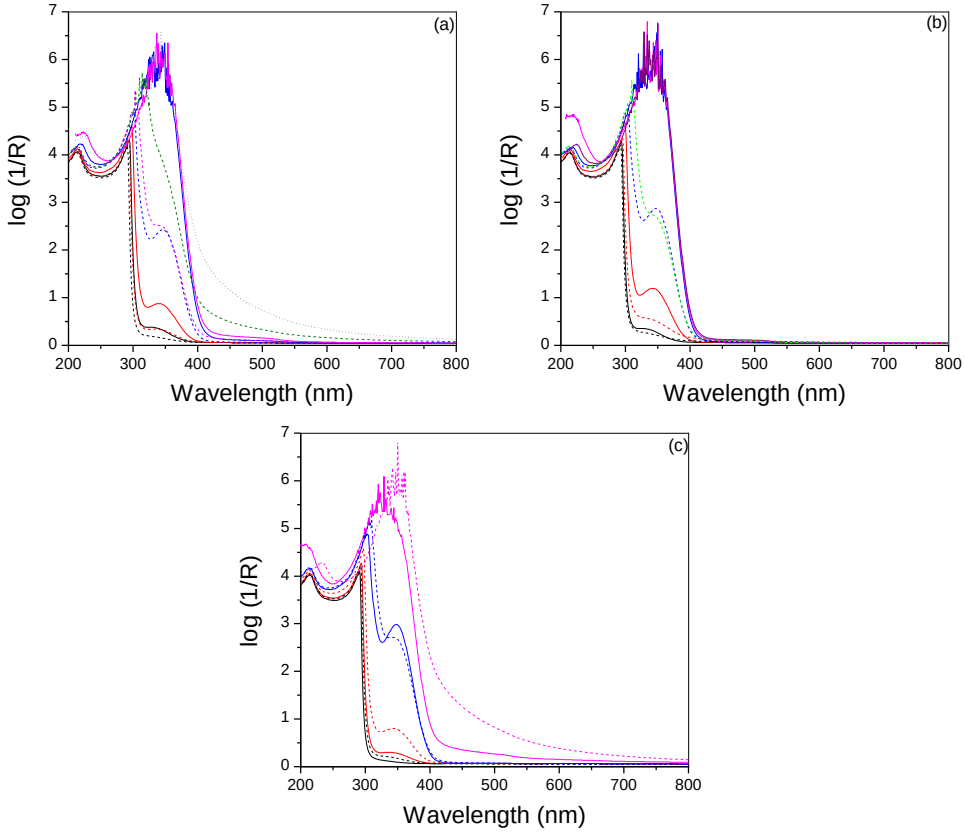

Figure 10-6: UV-Vis spectra for (a) Na_2CO_3_200 (solid lines) at T_0 (black), T_{12} (red), T_{25} (blue), T_{30} (pink) and T_{37} (purple), and Na_2CO_3_400 (dotted lines) at T_0 (black), T_{12} (red), T_{25} (blue), and T_{40} (green); (b) Cs_2CO_3_200 (solid lines) at T_0 (black), T_{12} (red), T_{30} (blue), and T_{40} (pink), and Cs_2CO_3_400 (dotted lines) T_0 (black), T_{12} (red), T_{25} (blue), T_{30} (pink), T_{40} (green), and T_{45} (purple); (c) $CaCO_3$_200 (solid lines) T_0 (black), T_{12} (red), T_{25} (blue), and T_{40} (pink), and $CaCO_3$_400 (dotted lines) at T_0 (black), T_{12} (red), T_{30} (blue), and T_{40} (pink).

Similar results were demonstrated by Kato *et al*. [193] who showed that, as the particle size of colloidal C_{60} increased, the UV-Vis absorbance changed significantly (Figure 10-7) and they suggested that this variation was caused by a change in the colour of the solution with increasing particle size. Kato *et al*. reported an almost linear relationship between the ratio of absorbance at 340 nm to the absorbance at 270 nm for particle sizes in the region of 100 - 250 nm, and given that the absorbance at 270 nm does not change significantly with particle size this ratio is effectively the change in absorbance at 340 nm [193].

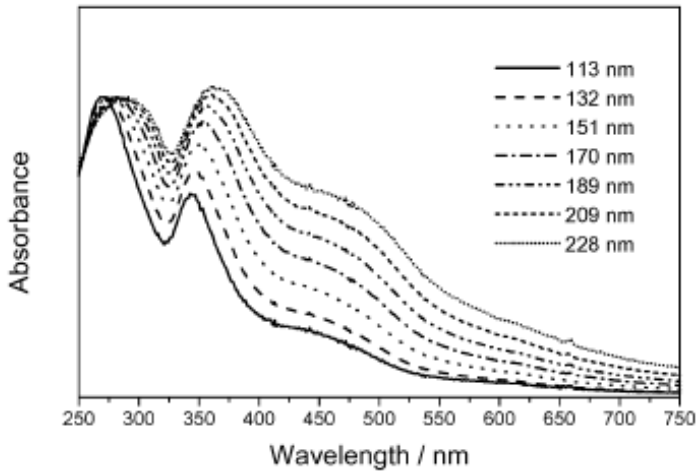

Figure 10-7: UV-Vis spectra for various different sizes of colloidal C_{60} particles [193].

To investigate whether a similar relationship, between RF particle size and absorbance exists, DLS particle size (Figure 10-8) was plotted against UV-Vis absorbance observed at 350 nm, as illustrated in Figure 10-9. 350 nm was chosen, as this is the wavelength where the peak maximum is observed (see Figure 10-6).

Figure 10-9 shows that there is no correlation between the particle size and UV-Vis scattering at 350 nm. One explanation for this is that the surface area of the RF particles also has an effect on the amount of light absorbed by the sol. This effect was demonstrated by Fu *et al*. [194], who reported that as the particle size of a pigment dispersion decreased, the absorption increased, this was attributed to the increase in surface area of the particles with decreasing particle size. In order to test this theory absorbance spectra for Na, Cs and Ca catalysed gels were directly compared (Figure 10-10). The spectra for R/C 200 sols at T_{12} indicate that, absorbance at 350 nm is in the order Na > Cs > Ca.

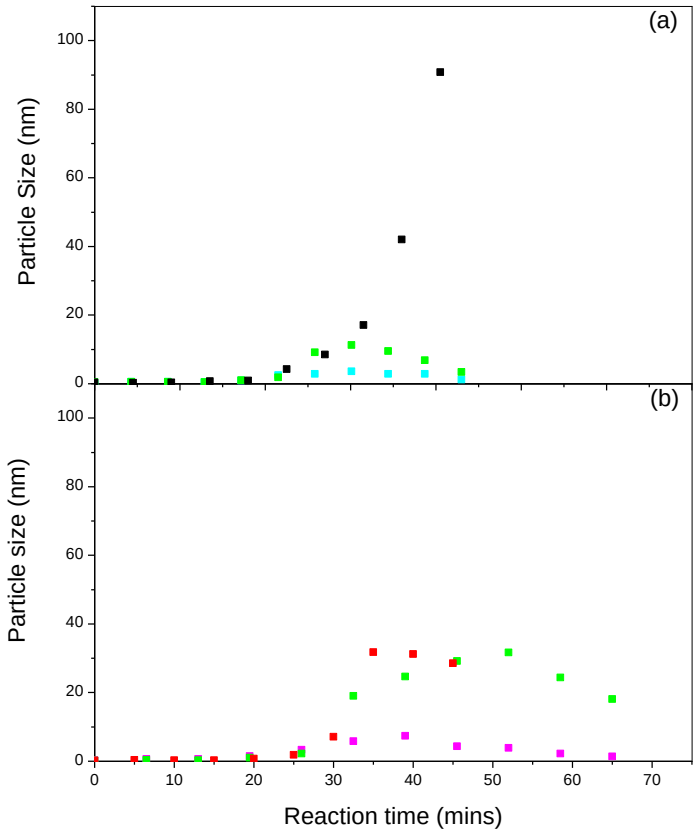

Figure 10-8: DLS particle size as a function of reaction time (a) for Na_2CO_3_200 (!), Cs_2CO_3_200 (!), $CaCO_3$_200 (!) and (b) Na_2CO_3_400 (!), Cs_2CO_3_400 (!) and $CaCO_3$_400 (!).

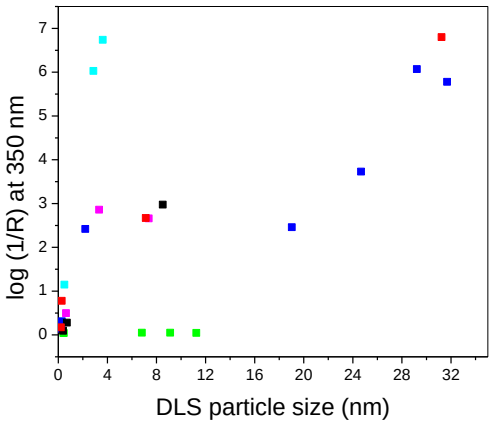

Figure 10-9: UV-Vis absorbance at 350 nm for Na_2CO_3_200 (!), Na_2CO_3_400 (!), Cs_2CO_3_200 (!), Cs_2CO_3_400 (!), $CaCO_3$_200 (!) and $CaCO_3$_400 (!).

In the Cs and Ca sols particle aggregation is favoured, resulting in larger colloidal particles within the solution, whereas Na sols consist of smaller colloidal particles. These smaller colloidal particles will have a larger surface area and will scatter incident light in all

directions, limiting the amount of light passing through the solution, which increases absorbance. However, the spectra for sols prepared with R/C 400 at T_{40}, display the opposite trend, with Na_2CO_3_400 displaying lower absorbance than Cs_2CO_3_400 and $CaCO_3$_400. At this increased reaction time the effect of particle surface area is less significant and UV absorption is based on particle size, with absorbance in the order of increasing pore diameter (Na_2CO_3_400_T_{40} = 7.37 nm, Cs_2CO_3_400_T_{40} = 24.67 nm, $CaCO_3$_400_T_{40} = 31.78 nm). From these results it appears that there are two opposing factors contributing to the UV-Vis scattering of RF gels (i.e. decreasing particle size increases surface area, which increases absorbance, but in general absorbance increases with increasing particle size) and as a result the absorbance at approximately 350 nm cannot be used to determine particle size within the sol.

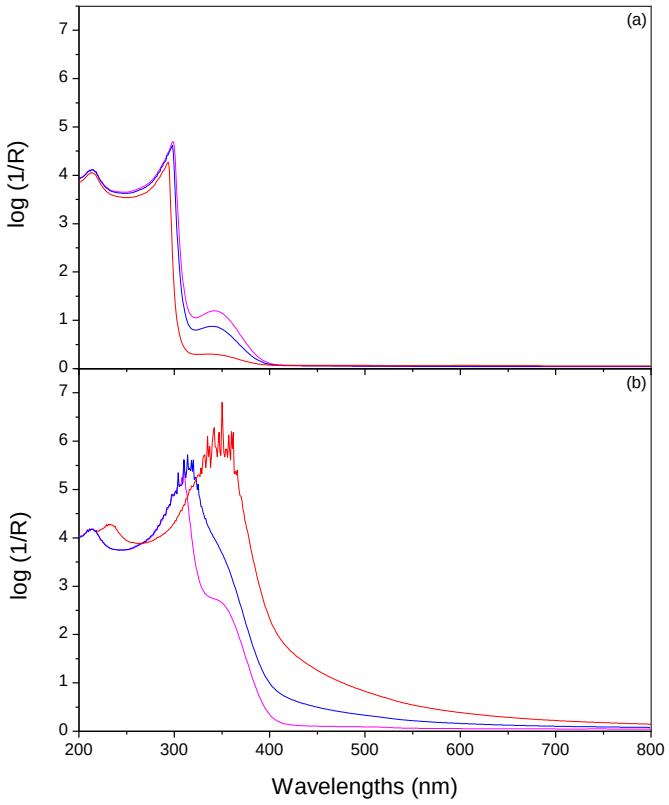

Figure 10-10: UV-Vis spectra for (a) Na_2CO_3_ 200 (pink), Cs_2CO_3_200 (blue) and $CaCO_3$_200 (red) sols at T_{12}, and (b) Na_2CO_3_ 400 (pink), Cs_2CO_3_400 (blue) and $CaCO_3$_400 (red) sols at T_{40}.

However, a study by K. Goodner [195, 196], on the estimation of turbidity, of tea samples, from absorbance, demonstrated that change in absorption in the red region was dependent only on the turbidity of the sample and not on the sample chemistry. Consequently, samples with the same chemical structure but different turbidities displayed varying absorbance at

750 nm. Goodner was able to demonstrate a linear relationship between the absorbance at 750 nm and sample turbidity.

Inspection of RF absorbance spectra obtained (Figure 10-6) shows that, as the reaction proceeds, absorbance in the green to red region (500 to 800 nm) increases. If the first region of decay in DLS is considered (i.e. the initial reaction, where particles grow gradually, before clusters aggregate quickly causing a significant increase in particle size), and the average particle size is plotted against UV-Vis absorbance (log 1/R), at 500, 600 and 750 nm, it is evident that there is a relationship between particle size and absorbance. Figure 10-11 illustrates that there is little change in the absorbance as the particles grow to approximately 20 nm. As the reaction proceeds, further particles grow and aggregate, resulting in a significant increase in turbidity (cloudiness) of the sample and a change in colour from pale yellow to deep red. At this stage there is a linear relationship between particle size and absorbance at 500, 600 and 750 nm, as shown in Figure 10-11.

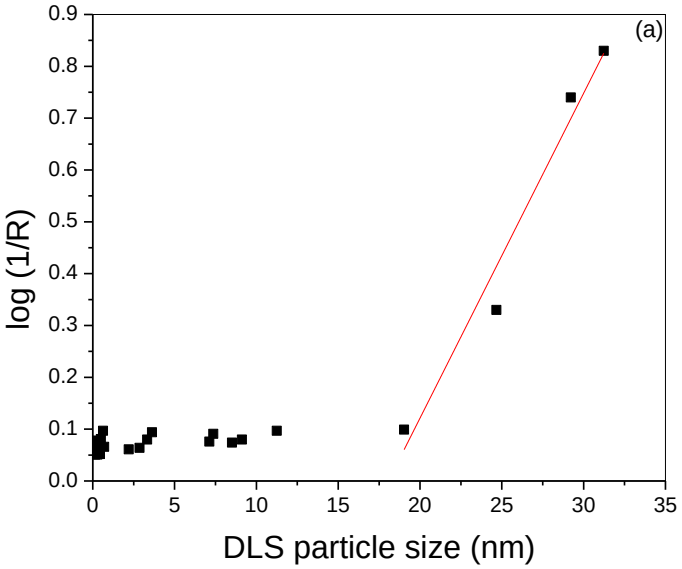

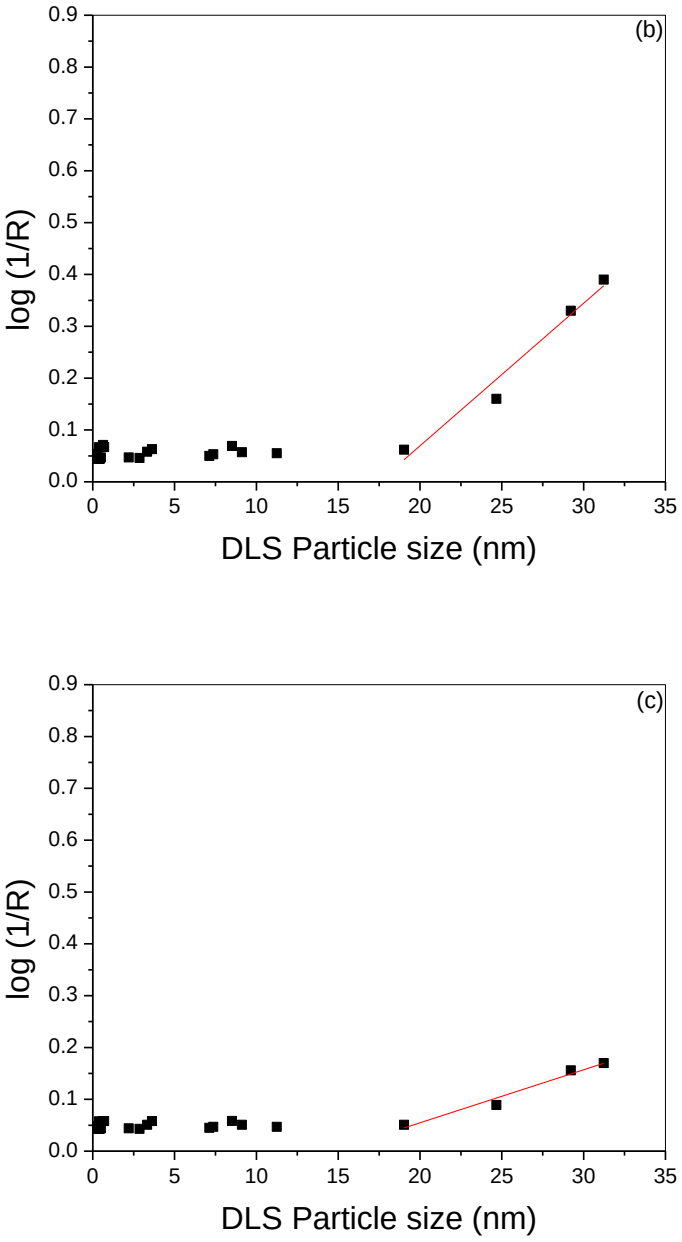

Figure 10-11: Plot of log (1/R) as a function of DLS particle size at (a) 500 nm, (b) 600 nm and (c) 750 nm, for $CaCO_3$, Cs_2CO_3 and Na_2CO_3 at R/C ratios of 200 and 400.

10.3 Summary

UV-Vis absorbance measurements take only a few minutes and the method used in this study allowed samples to be analysed at line (i.e. sol samples were taken straight from the oven and no further sample preparation or dilution was required). Subsequently, as

demonstrated by Figure 10-11, UV-Vis spectrometry could be used as a quick analysis tool to determine whether there are significant changes in particle size during the RF gelation stage. The results presented demonstrate the use of this technique to compare sols prepared with different catalysts showing that variations in the particle aggregation during the sol-gel transition can be monitored using sample absorbance at various wavelengths. These results indicate that the technique could be applied to different RF sol compositions or used to compare varying synthesis processes, providing an insight into the particle aggregation occurring.

The linear relationships shown for these preliminary results also suggest that, with the collation of a reference library of particle sizes, it may possible to use UV-Vis spectrometry to determine RF particle sizes above 20 nm. In comparison to other methods used for particle size determination, i.e. DLS, SAXS and microscopic techniques, this method is simple and rapid allowing sol samples to be analysed straight from the oven, and for results to be obtained in a matter of minutes.

To summarise:

(1) UV-Vis absorbance at 500, 600 and 750 nm can be used to determine variations in RF particle size. Given that absorbance at 500 nm is higher than 600 and 500 nm this wavelength would be the easiest to monitor.
(2) With the collation of a reference library, it may be possible to use this technique to calculate RF particle sizes above 20 nm, thus providing a rapid and simple method requiring no specific sample preparation.

11 Conclusion

RF xerogels were prepared using a wide range of Group I and Group II metal catalysts at varying concentrations, with initial sol pHs in the region 5.86 to 7.64. Comparison of xerogel and carbon properties demonstrated that, in general, as molar ratio of R/C, and resultant sol pH, increased the structure became more cross-linked, resulting in decreased pore diameters and pore volumes, and increased surface areas. Although these main trends existed, there were significant variations between the properties of gels prepared with similar initial pHs, indicating that RF gel properties are not directly dependent on initial sol pH.

It is known that the initial stage of RF polymerisation involves the catalyst abstracting a proton from R, producing more reactive R^- [11], which subsequently react with F, forming hydroxy-methyl derivatives. Consequently, it follows that the reaction, and subsequent gel properties, are highly dependent on the formation of these R anions. Given this relationship, it was theorised that RF gel properties would be dependent on the ability of each catalyst to deprotonate R. By assuming all catalysts are able to fully dissociate, the deprotonation ability (DPA) of each catalyst was determined, i.e. carbonate bases have DPAs equal to 2 x their concentration, whereas DPAs of bicarbonates and hydroxides are equal to their concentration. LC results demonstrated that changes in [R] were similar for RF sols prepared from Group I and Group II catalysts, with equal DPAs, indicating that hydroxyl-methyl derivatives are formed at similar rates. From these results it can be concluded that RF polymerisation is dependent on base concentration, however, it is also independent of the type of base utilised.

Although, LC results indicate similar changes in [R], titration results, and comparison of gel properties confirm variances between gels prepared with equal DPAs; illustrating two clear groupings:

a) *Gels prepared with Group I catalysts, with the exception of catalysts containing Cs*
b) *Gels prepared with Group II catalysts and Cs catalysts*

These variances were investigated using DLS and it was found that the presence of Group II and Cs bases results in increased particle size, during the sol-gel transition, indicating that their presence causes increased colloidal aggregation, which in turn decreases HM substitution resulting in slower F consumption. Following on from results reported by Job *et al*. [63] it can be concluded that this increased aggregation results from a decrease in the

Debye Huckle screening length, caused by an increase in cation charge and, to a lesser extent, cation size.

Gels catalysed with $(NH_4)_2CO_3$ and uncatalysed gels display significantly different structures to their metallic base catalysed counterparts; exhibiting considerably increased pore diameters. These differences were initially thought to be caused by varying reaction pathways, however, for gels prepared using $(NH_4)_2CO_3$, LC and titration results demonstrate reactant consumptions that are very similar to Na_2CO_3 catalysed sols, therefore, showing that HM compounds form at similar rates. DLS results, for $(NH_4)_2CO_3$ sols, indicate that large particles (~ 700 nm) are present even before the sol is subjected to heat. Given that visible sol sedimentation occurs after a few minutes in the oven, these large particles can be attributed to the poor stability of the RF colloidal suspension, which results in salting out of RF particles, prior to cross-linking. A similar salting out effect is observed in uncatalysed sols, however, due to the decreased reaction rate between R and F, this occurs much later. These results indicate that a metal cation is required to stabilise RF colloidal suspensions, preventing salting out, prior to the formation of a cross-linked nanostructure.

Throughout this study gels were prepared with varying particle sizes and pore sizes, which lead to the development of a rapid and simple UV-Vis method, showing promise for identifying changes in particle sizes above 20 nm.

In summary, this comprehensive study surrounding the specific role of the catalyst during RF polymerisation has allowed the following conclusions to be drawn:

1) Final gel properties are not directly dependent on initial sol pH.
2) Type of base employed to catalyse the reaction is not important, as long as it bears a metal cation.
3) Porosity of RF xerogels is dependent on the DPA of the catalyst, which is directly linked to the base concentration.
4) Stability of the RF colloidal suspension decreases with increasing cation size, resulting in increased polymer aggregation and, as a consequence, large particles/pores.
5) To a greater extent than cation size, increasing cation charge decreases colloidal stability, which, in turn, enhances aggregation.
6) UV-Vis absorption can be utilised to monitor changes in particle sizes above 20 nm.

7) In the absence of a metal cation the RF colloidal suspension becomes very unstable, resulting in considerably enhanced aggregation and salting out prior to formation of a cross-linked network.

By identifying and differentiating between the effects of initial sol pH and the specific effects of the catalyst, a full investigation into the effects and interactions of all experimental variables can be carried out. This will be vital to the field of RF sol gels as it will allow gels to be prepared with specific gel properties for anticipated applications.

12 Future work

12.1 Development of LC method

The LC method could be developed further to allow dimers to be detected. This could be achieved through the use of a gradient pump, which would allow the polarity of the MP to be altered during the chromatographic run. A polar mobile phase (i.e. more H_2O) allows HMs and R to be eluted from the column, however increasing the methanol concentration (decreasing polarity) would then potentially fully elute less polar analytes from the column, allowing RF polymerisation reaction to be investigated further.

In this study MS was only carried out on a few samples, however if this was directly attached to the LC measurement system, mass spectrometry results could be obtained for all runs, allowing HM formation/disappearance to be studied in more detail.

12.2 UV-Vis model for particle size determination

The UV-Vis results presented in Chapter 10 indicate that UV-Vis could be used as an alternative method for determining particle sizes above 20 nm. These preliminary results demonstrate that there is a linear relationship between particle size and absorbance at 500, 600 and 750 nm. Following the results presented in Chapter 10 further work within the Group has established that the linear relationship appears to exist for particle sizes above 15 nm [197]. Consequently, this method would only be useful for RF gels prepared with higher R/C ratios or those prepared with catalysts containing larger or highly charged cations (i.e. Cs or Group II bases).

To date, UV-Vis measurments have only been evaluated for Group I and $CaCO_3$ base catalysed sols, this work should be expanded to cover additional Group II bases as they generally produce RF gels with larger particles (see Section 8.1). The UV-Vis absorbanvce results could then be compiled into a database and test sols could be prepared to determine whether absorbance is equal for gels with equivalent particle sizes even when prepared with different catalysts.

12.3 Design of Experiments (DoE)

This study has comprehensively investigated the specific effects of the catalyst in the polymerisation of RF xerogels, differentitating the effects of the initial sol pH and R/C ratio.

These results will allow a broad study on the effects of all experimental parameters, on the final RF gel properties, to be carried out using a DoE approach.

A previous DoE study by Awadallah *et al*. [65] attempted to investigate the effects of both R/C ratio and initial sol pH, however, the initial pH was set using nitric acid, which in turn would affect the R/C ratio. Subsequently, only the effect of initial sol pH was investigated as the R/C ratio becomes redundant after the adition of acid.

As discussed previously there are a number of factors involved in the synthesis of RF gels, through the use of DoE all factors and their interactions can be investigated simultaneously developing a model, which will allow the synthesis of RF gels to be optimised for a given application.

12.3.1 Introduction

DoE involves two main processes:

1. *Modelling* - performing a series of experiments to build a model that describes how the experimental results are dependent on the factors involved
2. *Optimistation* - determining the set of factors and the levels of each factor that give rise to optimal properties

The most efficient way of modelling a number of effects and their interactions is through the use of a Factorial design. This type of design allows all possible combinations between factors at each level to be examined. All factorial designs are given as a base raised to a power, i.e. B^k, where the base (B) is the number of levels and the power (k) is the number of factors.

The efficiency of factorial designs can be easily demonstrated by considering two factors, A and B at two levels, high and low. The effects of both factors can be calculated by varying the factors one at a time, where the overall effects of factor A and B can be determined using Equation 159 and Equation 160:

$$Effect\ of\ factor\ A = \mathrm{A}^{+}B^{-} - \mathrm{A}^{-}B^{-}$$

Equation 159

$$Effect\ of\ factor\ B = \mathrm{A}^{-}B^{+} - \mathrm{A}^{-}B^{-}$$

Equation 160

Where A^+/B^+ = *Factor A and B at high levels*

A^-/B^- = *Factor A and B at low levels*

Due to experimental error two replicates are required, thus 6 experiments are required (A^+B^-, A^-B^- and A^-B^+ x 2). However, in a factorial experiment an extra treatment combination is added (A^+B^+), thus effect A can be calculated from both A^+B^+ - A^-B^+ and A^+B^- - A^-B^- and effect B can be determined from both A^+B^+ - A^+B^- and A^-B^+ - A^-B^-. The two estimates for each main effect can then be averaged to give average main effects. Therefore only 4 experiments are required and the efficiency of the factorial design can be given as 4/6 = 1.5 [198].

12.3.2 Two level factorial designs (2^k) – Screening Experiment

The simplest factorial design is a two level factorial design, which is often denoted 2^k factorial design. These are commonly used for screening, as they allow *k* factors to be investigated using the smallest number of experiments, where the total number of experiments is determined as 2^k, i.e. for 8 factors the number of experiments = 2^8 = 256. Thus they can be used to determine which factors and interactions are significant in a process before a full factorial design is applied. The response over the two levels (high and low) is assumed as linear over the range being tested. The effect of a Factor can be summarised using Equation 161 and the interaction effects can be determined using Equation 162 [198]:

$$Effect = \frac{[\sum responses + level\ exps] - [\sum responses - level\ experiments]}{2^{k-1}\ (n)}$$

Equation 161

$$Interaction\ Effect = \frac{[\sum responses + \ level\ exp.] - [\sum responses\ - level\ exp.]}{2^{k-1}(n)}$$

Equation 162

Where n = *number of replicates*

12.3.3 Application of DoE to the study of RF xerogels

As discussed in Section 2.6 there are many factors affecting RF gel properties (i.e. pore volume, pore size and surface area), with previous work indicating that the most significant variables were the initial sol pH, R/C ratio (catalyst concentration), solid content and pyrolysis conditions. The work in this study has established that, rather than the initial sol pH and R/C ratio, the main factors affecting RF xerogel properties are the DPA of the

catalyst, cation size and cation charge. Consequently, these factors should be studied along with the solid content and pyrolysis temperature.

Given that cation size naturally increases with charge, in order to study the effect of both cation size and cation charge two separate DoE studies are required. Therefore, two 2^4 factorial designs are required, with the factors and levels shown in Table 12-1:

Table 12-1: *2^4* Factorial designs for studying RF gel synthesis

Factorial design 1		Factorial design 2	
Factor	**Levels**	**Factor**	**Levels**
DPA	5.85 10^{-3} M 11.7 x 10^{-3} M	DPA	5.85 10^{-3} M 11.7 x 10^{-3} M
Cation size	Na = 100 pm Cs = 210 pm	Cation charge	1^+ 2^+
Solid content	5% 40 %	Solid content	5% 40 %
Pyrolysis temp.	600 ˚C 900 ˚C	Pyrolysis temp.	600 ˚C 900 ˚C

These models will require 16 gels to be prepared; therefore the effects and interaction effects for all 5 variables can be investigated through the production of 32 gels. The design matrix for a simple 2^4 factorial design is illustrated in Table 12-2, where each experiment, or gel, is denoted by a treatment combination (TC), which indicates the factors at the high level (i.e. abc indicates that factors a,b and c are at the high level with factor d at the low level).

The effects of each variable and the interactions, on the final gel properties, can then be investigated using either, the equations given in Section 12.3.2 or using a regression model (Chapter 22 Appendix J), which allows the significance of each variable to be determined using statistical F testing. Probability plots can be prepared by ranking experimental observations (i.e. pore volume, pore size and surface area) from smallest to largest and plotting against the calculated cumulative frequency [66]. A straight line is then drawn through the points (focussing on the points in the middle, i.e. 25 % to 75 %) and points which do not lie on the line generally have a significant effect.

Table 12-2: DoE matrix for a basic 2^4 factorial design

Exp no.	***Basic design 2^4***				**TC**
	A	B	C	D	
1	+	-	-	-	a
2	-	+	-	-	b
3	+	+	-	-	ab
4	-	-	+	-	c

5	+	-	+	-	ac
6	-	+	+	-	bc
7	+	+	+	-	abc
8	-	-	-	+	d
9	+	-	-	+	ad
10	-	+	-	+	bd
11	+	+	-	+	abd
12	-	-	+	+	cd
13	+	-	+	+	acd
14	-	+	+	+	bcd
15	+	+	+	+	abcd
16	-	-	-	-	1

13 Appendix A – Statistical F table

Table 13-1: Extract of statistical F table at 95 % significance level [199].

df_2	df_1									
	1	**2**	**3**	**4**	**5**	**6**	**7**	**8**	**9**	**10**
1	161.45	199.5	215.707	224.583	230.162	233.99	236.768	238.883	240.543	241.88
2	18.513	19	19.1643	19.2468	19.2964	19.33	19.3532	19.371	19.3848	19.396
3	10.128	9.552	9.2766	9.1172	9.0135	8.9406	8.8867	8.8452	8.8123	8.7855
4	7.7086	6.944	6.5914	6.3882	6.2561	6.1631	6.0942	6.041	5.9988	5.9644
5	6.6079	5.786	5.4095	5.1922	5.0503	4.9503	4.8759	4.8183	4.7725	4.7351
6	5.9874	5.143	4.7571	4.5337	4.3874	4.2839	4.2067	4.1468	4.099	4.06
7	5.5914	4.737	4.3468	4.1203	3.9715	3.866	3.787	3.7257	3.6767	3.6365
8	5.3177	4.459	4.0662	3.8379	3.6875	3.5806	3.5005	3.4381	3.3881	3.3472
9	5.1174	4.257	3.8625	3.6331	3.4817	3.3738	3.2927	3.2296	3.1789	3.1373
10	4.9646	4.103	3.7083	3.478	3.3258	3.2172	3.1355	3.0717	3.0204	2.9782
11	4.8443	3.982	3.5874	3.3567	3.2039	3.0946	3.0123	2.948	2.8962	2.8536
12	4.7472	3.885	3.4903	3.2592	3.1059	2.9961	2.9134	2.8486	2.7964	2.7534
13	4.6672	3.806	3.4105	3.1791	3.0254	2.9153	2.8321	2.7669	2.7144	2.671
14	4.6001	3.739	3.3439	3.1122	2.9582	2.8477	2.7642	2.6987	2.6458	2.6022
15	4.5431	3.682	3.2874	3.0556	2.9013	2.7905	2.7066	2.6408	2.5876	2.5437
16	4.494	3.634	3.2389	3.0069	2.8524	2.7413	2.6572	2.5911	2.5377	2.4935
17	4.4513	3.592	3.1968	2.9647	2.81	2.6987	2.6143	2.548	2.4943	2.4499
18	4.4139	3.555	3.1599	2.9277	2.7729	2.6613	2.5767	2.5102	2.4563	2.4117
19	4.3807	3.522	3.1274	2.8951	2.7401	2.6283	2.5435	2.4768	2.4227	2.3779
20	4.3512	3.493	3.0984	2.8661	2.7109	2.599	2.514	2.4471	2.3928	2.3479
21	4.3248	3.467	3.0725	2.8401	2.6848	2.5727	2.4876	2.4205	2.366	2.321
22	4.3009	3.443	3.0491	2.8167	2.6613	2.5491	2.4638	2.3965	2.3419	2.2967
23	4.2793	3.422	3.028	2.7955	2.64	2.5277	2.4422	2.3748	2.3201	2.2747
24	4.2597	3.403	3.0088	2.7763	2.6207	2.5082	2.4226	2.3551	2.3002	2.2547
25	4.2417	3.385	2.9912	2.7587	2.603	2.4904	2.4047	2.3371	2.2821	2.2365
26	4.2252	3.369	2.9752	2.7426	2.5868	2.4741	2.3883	2.3205	2.2655	2.2197
27	4.21	3.354	2.9604	2.7278	2.5719	2.4591	2.3732	2.3053	2.2501	2.2043
28	4.196	3.34	2.9467	2.7141	2.5581	2.4453	2.3593	2.2913	2.236	2.19
29	4.183	3.328	2.934	2.7014	2.5454	2.4324	2.3463	2.2783	2.2229	2.1768
30	4.1709	3.316	2.9223	2.6896	2.5336	2.4205	2.3343	2.2662	2.2107	2.1646
40	4.0847	3.232	2.8387	2.606	2.4495	2.3359	2.249	2.1802	2.124	2.0772
60	4.0012	3.15	2.7581	2.5252	2.3683	2.2541	2.1665	2.097	2.0401	1.9926
120	3.9201	3.072	2.6802	2.4472	2.2899	2.175	2.0868	2.0164	1.9588	1.9105
inf	3.8415	2.996	2.6049	2.3719	2.2141	2.0986	2.0096	1.9384	1.8799	1.8307

14 Appendix B – Interpolated [F]

This appendix interpolates the F consumption to allow direct comparison with the consumption of R.

Figure 14-1 illustrates the F consumption for Na_2CO_3 gels prepared with R/C ratios of 100 to 600, and demonstrates the lines of best-fit calculated using Equation 163.

$$y = mx + c$$

Equation 163

Where y = *[F] (M)*

x = *time in oven (min)*

c = *[F] at time 0*

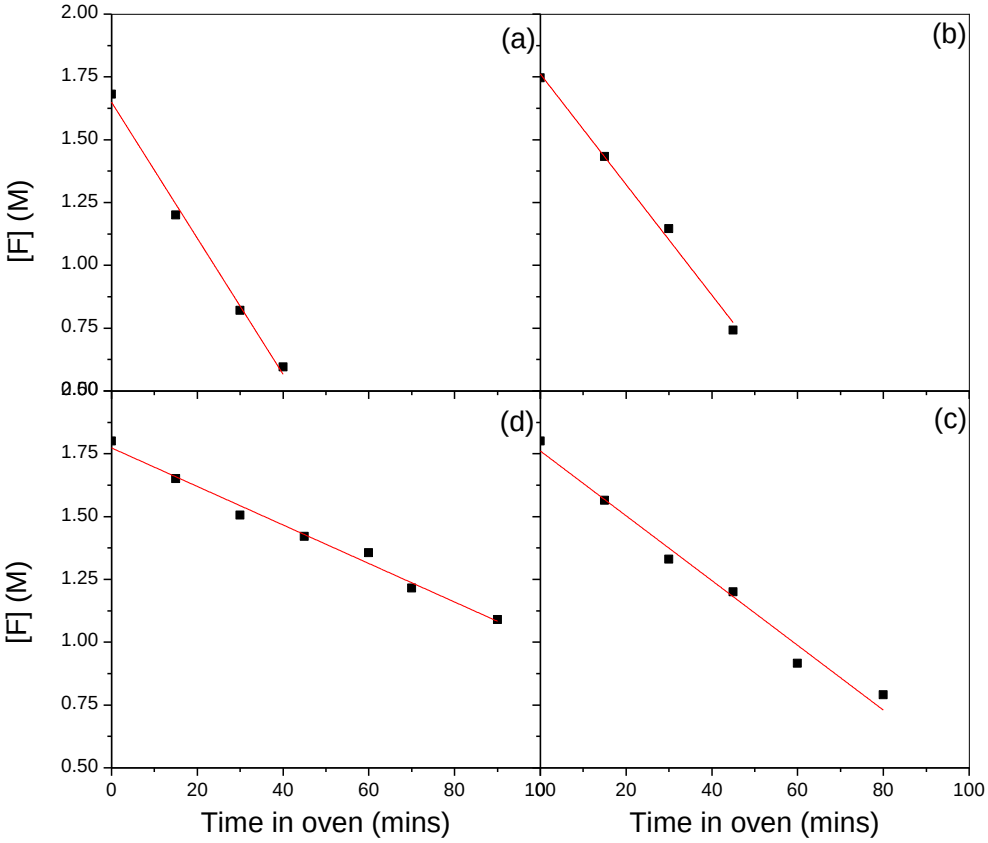

Figure 14-1: F consumption as a function of time in the oven for Na_2CO_3_100 (a), Na_2CO_3_200 (b), Na_2CO_3_400 (c) and Na_2CO_3_600 (d), showing lines of best fit for interpolation.

Table 14-1 provides the calculated linear regression data for each gel. The linear equations were then used to interpolate the F consumption and the calculated values are given in Table 14-2.

Table 14-1: Linear regression data for Na_2CO_3 gels prepared with R/C ratios of 100, 200, 400 and 600

R/C ratio	Gradient (m)	Intercept	R^2
100	-0.0271	1.649	0.991
200	-0.0220	1.761	0.992
400	-0.0077	1.773	0.985
600	-0.0129	1.761	0.978

Table 14-2: Interpolated F consumptions

Time (min)	R/C ratio			
	100	**200**	**400**	**600**
	[F] (M)			
10	1.378	1.541	1.696	1.632
20	1.107	1.321	1.619	1.503
40	-	0.881	1.465	1.245
50	-	-	1.388	-
70	-	-	1.311	-
80	-	-	-	0.729

15 Appendix C – LC validation (ANOVA)

This Appendix statistically calculates the repeatability and reproducibility of the titration method used to determine F consumption.

15.1 LC system repeatability

Table 15-1: Peak areas obtained for R/W1 standard solution analysed on three different days

Peak Area (a.u)		
Day 1	**Day 2**	**Day 3**
14314142	14826286	14311118
14305554	14596313	14389163
14389112	14573150	14463825
14571159	14665104	14486923
14426179	14940611	14590102
14438604	14004757	14643030
14401708	14833243	14576010
14441711	14635194	14701934

The within group sum of squares is then calculated using Equation 61:

$$SS_W = \sum (x_i - \bar{x})^2$$

Equation 61

The sum of the mean – dataset mean for day 1, 2 and 3 therefore gives SS_W as follows:

$$SS_W = 4.87 \times 10^{10} + 5.73 \times 10^{11} + 1.21 \times 10^{11} = 7.43 \times 10^{11}$$

The mean square value is then determined using Equation 62, where the degrees of freedom are 24 – 3 = 21 (i.e. the total number of samples, less the number of datasets).

$$MS_W = \frac{7.43 \times 10^{11}}{21} = 3.54 \times 10^{10}$$

Equation 164

The between sample variance is determined using Equation 63:

$$SS_B = \sum n(\bar{x} - \bar{X}_{SET})^2$$

Equation 63

Where the sum of $n(\bar{x} - \bar{X}_{SET})^2$ for days 1, 2 and 3 is as follows:

$$SS_B = 9.83 \times 10^{10} + 1.01 \times 10^{11} + 2.07 \times 10^{7} = 1.995 \times 10^{11}$$

The mean square value is then calculated, where the degrees of freedom are equal to 3 – 1 = 2 (i.e. the number of datasets -1).

$$MS_W = \frac{1.995 \times 10^{11}}{2} = 9.98 \times 10^{10}$$

The ANOVA results are summarised in Table 15-2

Table 15-2: Summary and ANOVA results for R/W_1 analysed on three different days

SUMMARY

Groups	*Count*	*Sum*	*Average*	*Variance*
Day 1	8	1.15E+08	14411021	6.95E+09
Day 2	8	1.17E+08	14634332	8.18E+10
Day 3	8	1.16E+08	14520263	1.73E+10

ANOVA

Source of Variation	*SS*	*df*	*MS*	*F*	*P-value*	*F crit*
Between Groups	2E+11	2	9.98E+10	2.820644	0.082219	3.4668
Within Groups	7.43E+11	21	3.54E+10			
Total	9.42E+11	23				

15.2 LC method reproducibility

15.2.1 Changing R/W

Table 15-3: Peak areas obtained with changing R/W standard

Peak area (a.u)		
R/W_1	**R/W_2**	**R/W_3**
14690093	14432819	14382406
14983714	14682719	14596187
14807459	14468239	14221585
14607105	14073460	14517991
14560693	14180747	14429159
14153371	14259502	14530350
14217207	14393932	14649335
14442360	14052864	14423925
14284919	14023483	14069683
14387832	14344092	14072593

Table 15-4: Summary and ANOVA results with changing R/W standards

SUMMARY

Groups	*Count*	*Sum*	*Average*	*Variance*
R/W1	10	1.45E+08	14513475	7.11E+10
R/W2	10	1.43E+08	14291186	4.52E+10
R/W3	10	1.44E+08	14389321	4.23E+10

ANOVA

Source of Variation	*SS*	*df*	*MS*	*F*	*P-value*	*F crit*
Between Groups	2.48E+11	2	1.24E+11	2.346842	0.114889	3.354131
Within Groups	1.43E+12	27	5.29E+10			
Total	1.68E+12	29				

15.2.2 Changing MP

Table 15-5: Peak areas obtained with changing MP

Peak area (a.u)		
MP_1	**MP_2**	**MP_3**
14311118	14690093	14818907
14389163	14983714	14358620
14463825	14807459	14532268
14486923	14607105	14475709
14590102	14560693	14301507
14643030	14153371	14369602
14576010	14217207	14192978
14701934	14442360	14247242
14342581	14284919	14319442
14367600	14387832	13988531

Table 15-6: Summary and ANOVA results with changing MP

SUMMARY

Groups	*Count*	*Sum*	*Average*	*Variance*
MP1	10	1.45E+08	14487229	1.84E+10
MP2	10	1.45E+08	14513475	7.11E+10
MP3	10	1.44E+08	14360481	4.86E+10

ANOVA

Source of Variation	*SS*	*df*	*MS*	*F*	*P-value*	*F crit*
Between Groups	1.34E+11	2	6.69E+10	1.454018	0.251347	3.354131
Within Groups	1.24E+12	27	4.6E+10			
Total	1.38E+12	29				

15.2.3 LC method repeatability

Table 15-7: R peak areas obtained, over time, for seven Na_2CO_3_200 sols

Time (minutes)	**Peak area (a.u)**						
	Na_2CO_3_200 prepared on						
	24.5.12	**29.5.12**	**30.5.12**	**30.5.12**	**31.5.12**	**12.6.12**	**14.6.12**
-30	6843781	7076863	6850454	6625958	6875684	6989734	-
-25	5914305	5713138	5524781	5230200	5805041	5683844	6005895
-15	5429786	5102395	5323886	5044414	5430007	5414179	5744881

0	5024346	5291116	4785968	5052158	4656517	5296698	5311069
10	4173734	3896231	4033577	4583246	4260840	4594958	5519043
20	3473533	3390319	3462149	3546655	3294584	3679491	3792891
30	2821290	2706251	2869258	2860727	2824489	3007437	3417023
40	2050983	1878377	2221625	2107614	2103415	2208668	2331555
50	1069773	1148536	1237381	1401433	1359490	1681974	1602449

Table 15-8: Comparison of LC peak areas for Na_2CO_3_200 repeats

Time	Standard deviation (a.u)	Mean (a.u)	RSD (%)
-30	153288	6877079	2.23
-25	258942	5696743	4.55
-15	233797	5355650	4.37
0	261948	5059696	5.18
10	543550	4437376	12.25
20	170173	3519946	4.83
30	232626	2929496	7.94
40	144894	2128891	6.81
50	226605	1357291	16.70
		Average	**7.20**

16 Appendix D – Group I & II xerogel/carbon properties

This section illustrates the isotherms and PSD for gels and carbons that are not displayed in the main body of text.

16.1 Group I gels

16.1.1 Dried xerogels

(a) K_2CO_3 & $KHCO_3$ isotherms & PSD

Figure 16-1 illustrates the isotherms and PSDs for K_2CO_3 and $KHCO_3$ xerogels. The isotherms are all Type IV, indicative of mesoporous materials, and like their Na counterparts the hystereses shift to higher relative pressures and progress from Type H2 to Type H1with increasing R/C ratio.

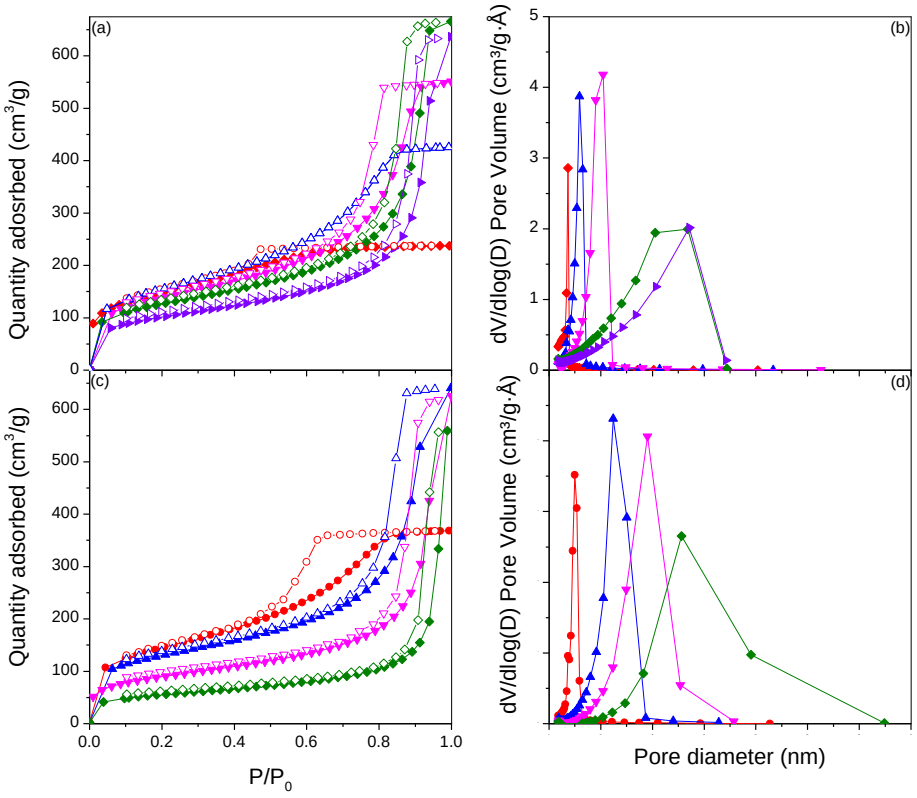

Figure 16-1: (a) N_2 adsorption (closed symbols) and desorption isotherms (open symbols) and (b) PSD for K_2CO_3_100_D (,), K_2CO_3_200_D (7), K_2CO_3_300_D (B), K_2CO_3_400_D (Λ) and K_2CO_3_500_D (Ω)and (c) adsorption (closed symbols) and desorption isotherms (open symbols) and (d) PSD for $KHCO_3$_100_D (,), $KHCO_3$_200_D (7), $KHCO_3$_300_D (B) and $KHCO_3$_400_D (Λ).

(b) Cs_2CO_3 & $CsHCO_3$ isotherms & PSD

The isotherms and PSD for Cs_2CO_3 and $CsHCO_3$ xerogels (Figure 16-2) illustrate that, compared to their Na and K counterparts the structures contain a lower proportion of micropores (lower absorption at low P/P_0) and although the hyseteres follow similar trends (Type H2 to Type H1 with increasing R/C), a higher quantity of N_2 is adsorbed and the hyseteres are shifted right. This shift is indicative of the increase in pore volume and pore size observed for the Cs prepared xerogels.

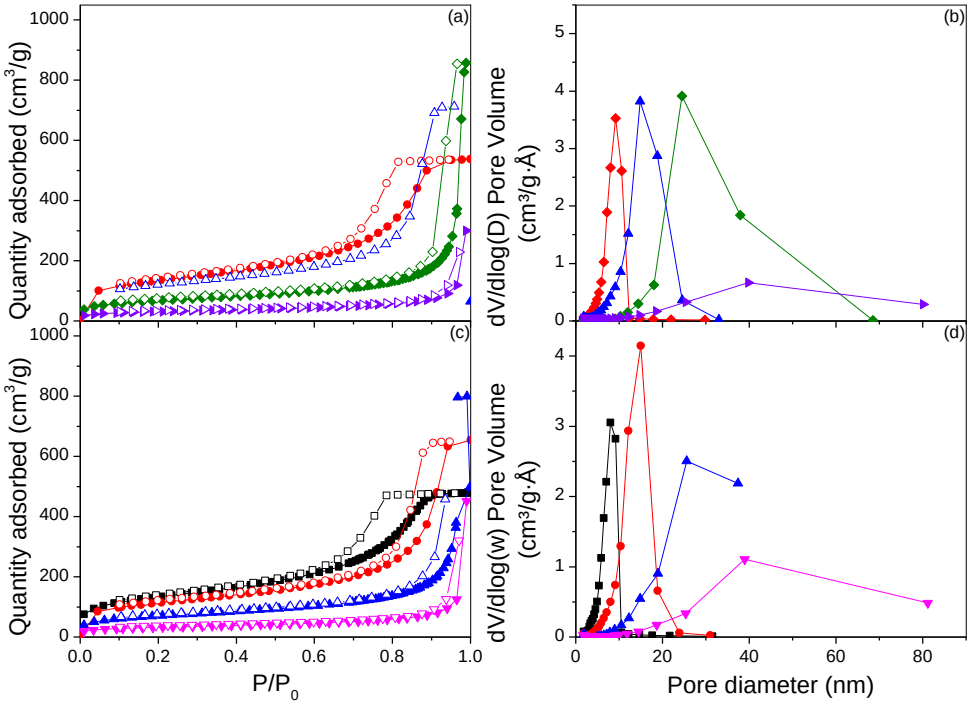

Figure 16-2: a) N_2 adsorption (closed symbols) and desorption isotherms (open symbols) and (b) PSD for Cs_2CO_3_100_D (,), Cs_2CO_3_200_D (7), Cs_2CO_3_300_D (B) and Cs_2CO_3_400_D (Λ) and (c) adsorption (closed symbols) and desorption isotherms (open symbols) and (d) PSD for $CsHCO_3$_50_D (!) $CsHCO_3$_100_D (,), $CsHCO_3$_200_D (7) and $CsHCO_3$_300_D (B).

16.1.2 Carbonised gels

Pyrolysis increases the microporosity within the RF xerogels, therefore it is expected that adsorption at low relative pressures will increase.

Indicative of the increase in micro-porosity, the adsorption at low P/P_0 is increased after pyrolysis in all carbonised Group I gels (Figure 16-3Figure 16-5 a & c). The increase in micropores is also represented by the general decrease in average pore diameters (Figure 16-3Figure 16-5 b & d), when compared the dried xerogels. Although pyrolysis has resulted

in an increase in microporosity the xerogels are still mainly mesoporous and therefore still display Type IV isotherms with Type H2 and H1 hystereses.

As discussed in Section 6.2.1, at low R/C ratios ($NaHCO_3$_50 and 75) the dried xerogels have weak structures that cannot withstand significant stress resulting in significant shrinkage, and as a result decreased pore volume leading to a significant decrease in the quantity of N_2 adsorbed. Due to the larger pore sizes observed in the Cs prepared gels, compared to equivalent Na and K gels, the Cs_2CO_3_100 and $CsHCO_3$_50 do not exhibit significant shrinkage during pyrolysis (Figure 16-5).

(a) Na_2CO_3 & $NaHCO_3$ isotherms & PSD

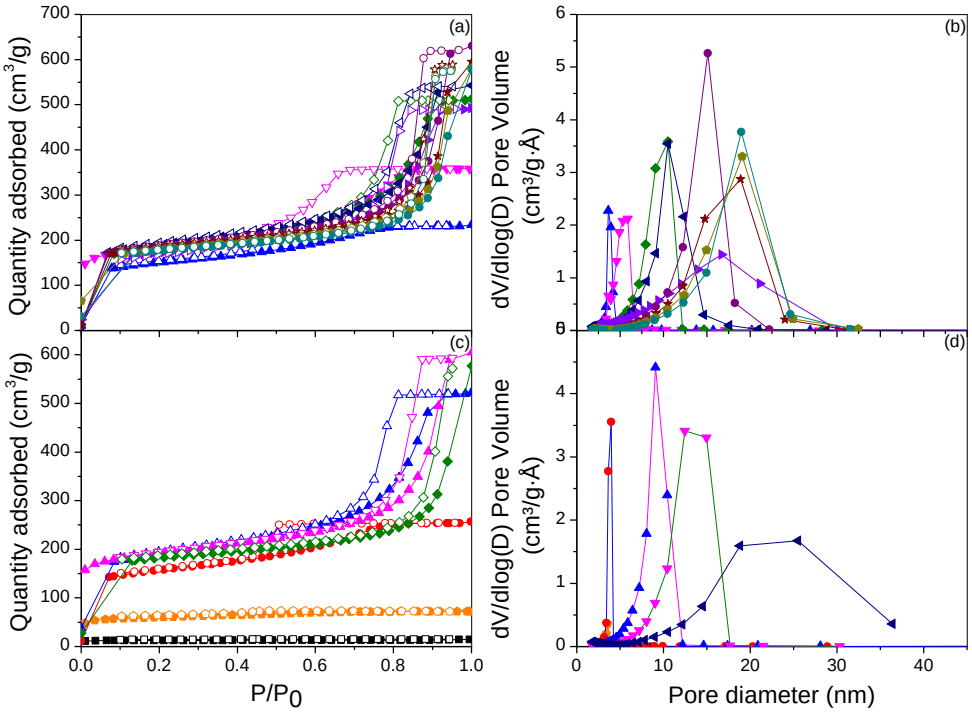

Figure 16-3: (a) N_2 adsorption (closed symbols) and desorption isotherms (open symbols) and (b) PSD for Na_2CO_3_200_DP (7), Na_2CO_3_300_DP (B), Na_2CO_3_400_DP (Λ), Na_2CO_3_450_DP (β), Na_2CO_3_500_DP (Ω), Na_2CO_3_600_DP (,), Na_2CO_3_700_DP (ξ), Na_2CO_3_750_DP (□), Na_2CO_3_800_DP (!) and (c) adsorption (closed symbols) and desorption isotherms (open symbols) and (d) PSD for $NaHCO_3$_50_DP (!), $NaHCO_3$_75_DP (□), $NaHCO_3$_100_DP (,), $NaHCO_3$_200_DP (7), $NaHCO_3$_300_DP (B) and $NaHCO_3$_400_DP (Λ).

(b) K_2CO_3 & $KHCO_3$ isotherms & PSD

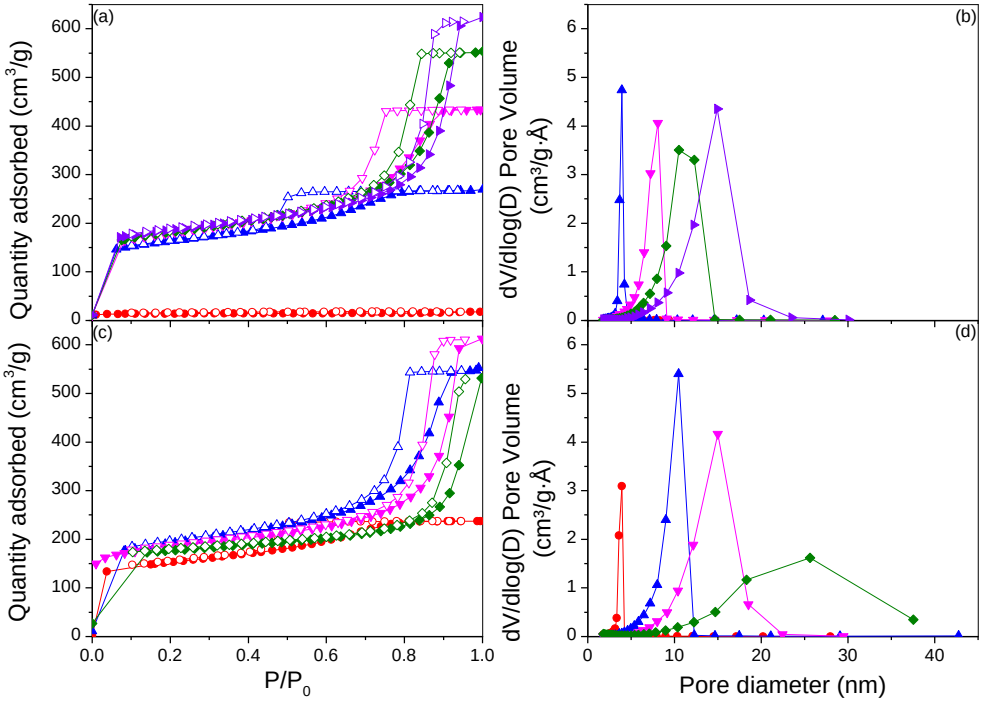

Figure 16-4: (a) N_2 adsorption (closed symbols) and desorption isotherms (open symbols) and (b) PSD for K_2CO_3_100_DP (,), K_2CO_3_200_DP (7), K_2CO_3_300_DP (B), K_2CO_3_400_DP (Λ) and K_2CO_3_500_DP (Ω)and (c) adsorption (closed symbols) and desorption isotherms (open symbols) and (d) PSD for $KHCO_3$_100_DP (,), $KHCO_3$_200_DP (7), $KHCO_3$_300_DP (B) and $KHCO_3$_400_DP (Λ).

(c) Cs_2CO_3 & $CsHCO_3$ isotherms & PSD

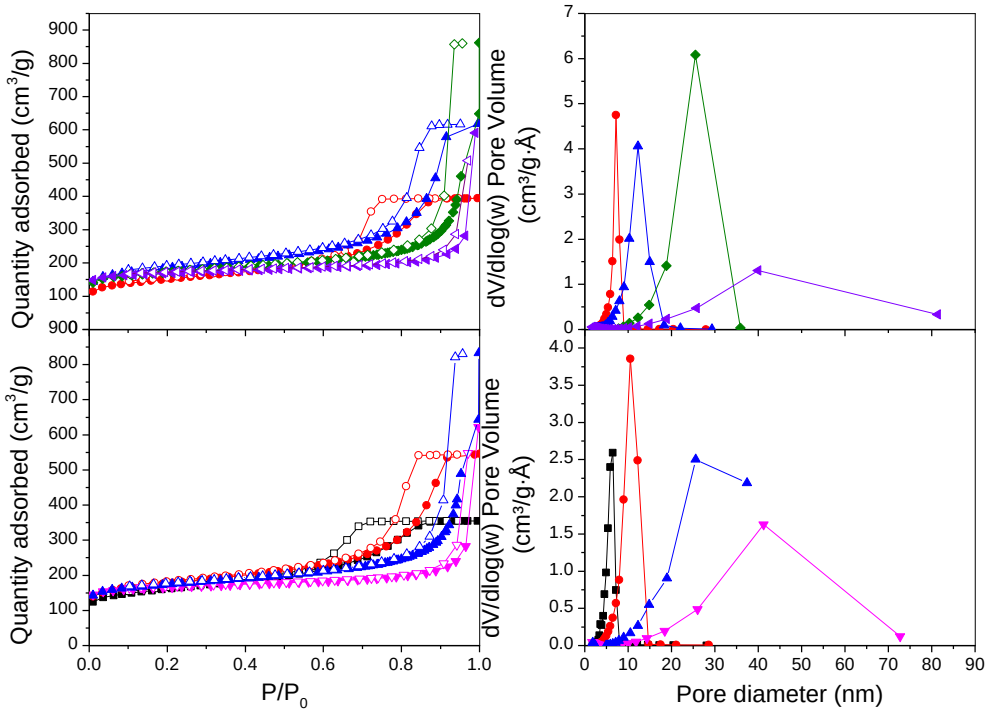

Figure 16-5: N_2 adsorption (closed symbols) and desorption isotherms (open symbols) and (b) PSD for Cs_2CO_3_100_DP (,), Cs_2CO_3_200_DP (7), Cs_2CO_3_300_DP (B) and Cs_2CO_3_400_DP (Λ) and (c) adsorption (closed symbols) and desorption isotherms (open symbols) and (d) PSD for $CsHCO_3$_50_DP (!) $CsHCO_3$_100_DP (,), $CsHCO_3$_200_DP (7) and $CsHCO_3$_300_DP (B).

16.1.3 Trends with carbon gels

The trends for carbonised gels, with R/C ratio (Figure 16-6) and initial sol pH (Figure 16-7), demonstrate similar results to the dried xerogels. However, due to the processes involved during pyrolysis; shrinkage resulting in a general decrease in average pore diameter, erosion of existing pores and creation of new pores, more uniform pore volumes and surface areas arise for carbons prepared with varying catalysts and R/C ratios.

In a similar manner to the dried xerogels, the trends become more pronounced when considered with the initial sol pH; however the most superior relationship is observed when carbon properties are considered with DPA (Figure 16-8) of the catalysts utilised in carbon preparation.

(a) Trends with R/C ratio

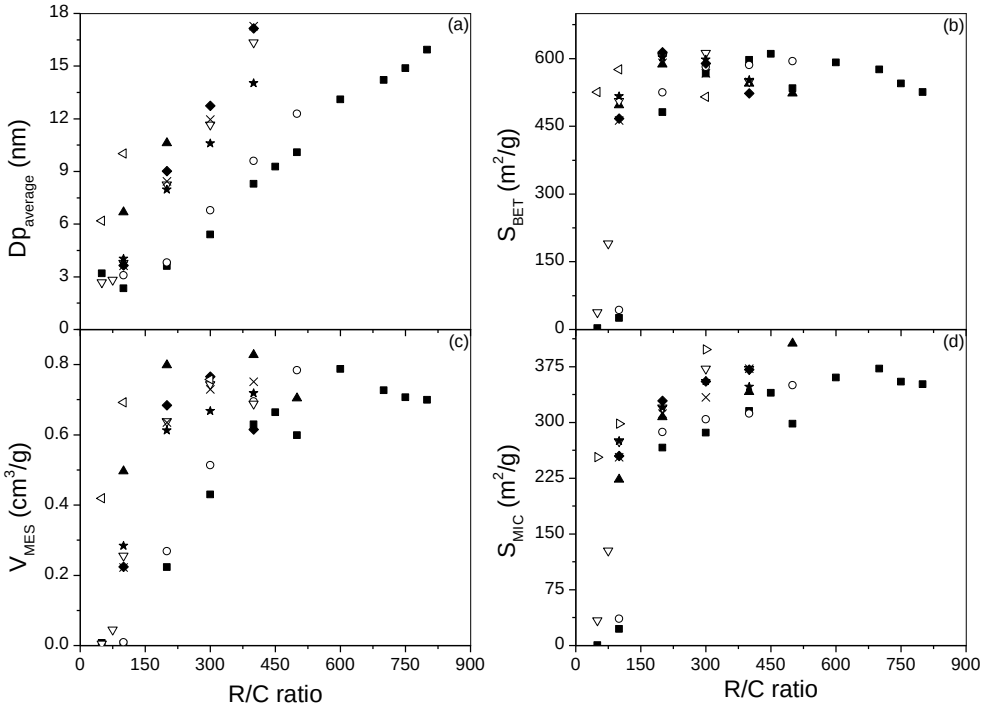

Figure 16-6: Trend of $DP_{average}$ (a), specific surface area (b), mesopore volume (c) and micropore surface area (d) with R/C ratio, for carbon xerogels prepared using, Na_2CO_3 (!), K_2CO_3 (–), Cs_2CO_3 (7), $NaHCO_3$ (X), $KHCO_3$ (Λ), $CsHCO_3$ (χ), NaOH (ξ), KOH (□).

(b) Trends with initial sol pH

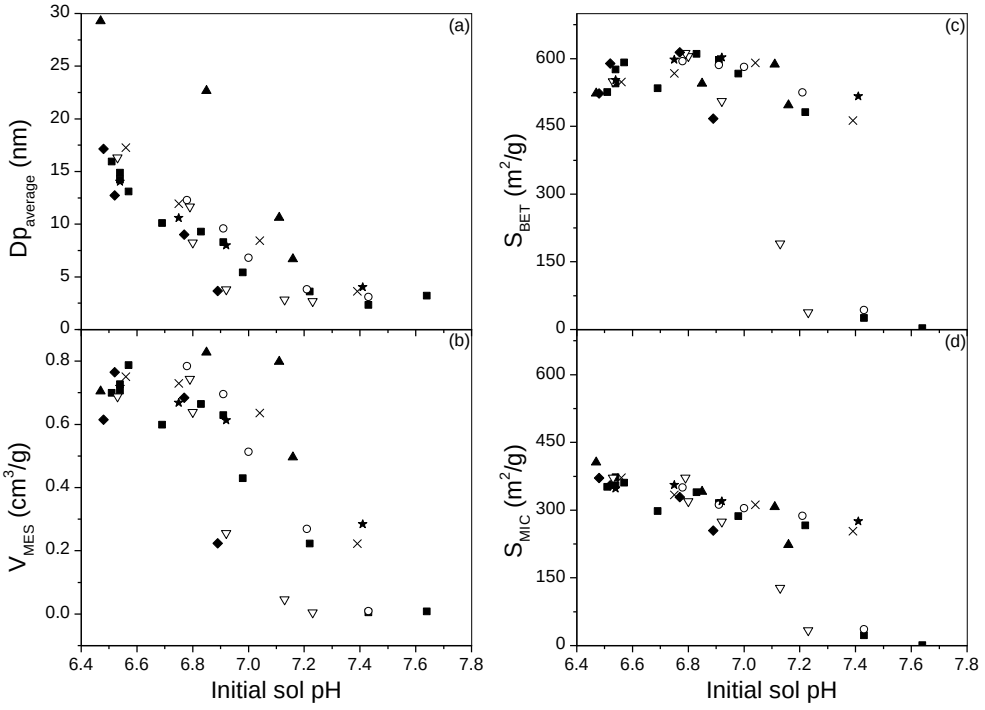

Figure 16-7: Trend of $DP_{average}$ (a), specific surface area (b), mesopore volume (c) and micropore surface area (d) with initial sol pH, for carbon xerogels prepared using, Na_2CO_3 (!), K_2CO_3 (–), Cs_2CO_3 (7), $NaHCO_3$ (X), $KHCO_3$ (Λ), $CsHCO_3$ (χ), NaOH (ξ), KOH (□).

(c) Trend with DPA

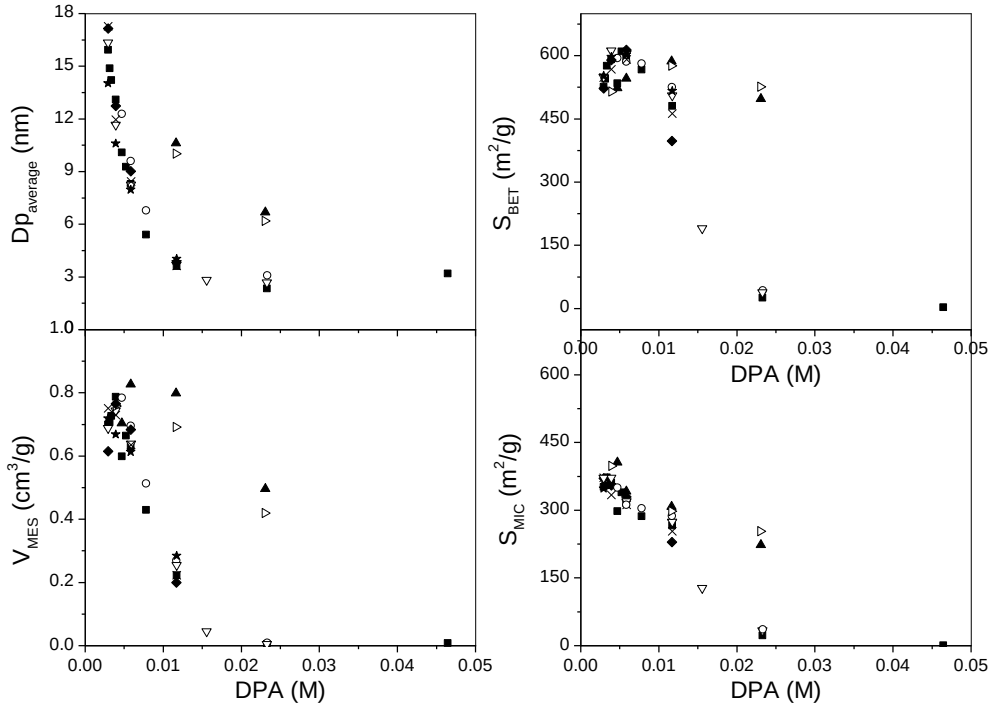

Figure 16-8: Trend of $DP_{average}$ (a), specific surface area (b), mesopore volume (c) and micropore surface area (d) with DPA, for carbon xerogels prepared using, Na_2CO_3 (!), K_2CO_3 (–), Cs_2CO_3 (7), $NaHCO_3$ (X), $KHCO_3$ (Λ), $CsHCO_3$ (χ), NaOH (ξ), KOH (□).

16.2 Group II gels

16.2.1 Dried xerogels

As discussed in Chapter 8, favoured aggregation, with Group II catalysts, results in larger RF particles and larger average pore diameters. These increased pore sizes are illustrated by the increased N_2 adsorption and shift in the PSD to larger pore diameters, observed for Ca, Sr and Ba prepared xerogels (Figure 16-10 Figure 16-12).

Again the gels are mainly mesoporous and therefore display Type IV isotherms with Type H1 and Type H2 hystereses.

(a) $CaCO_3$ isotherms & PSD

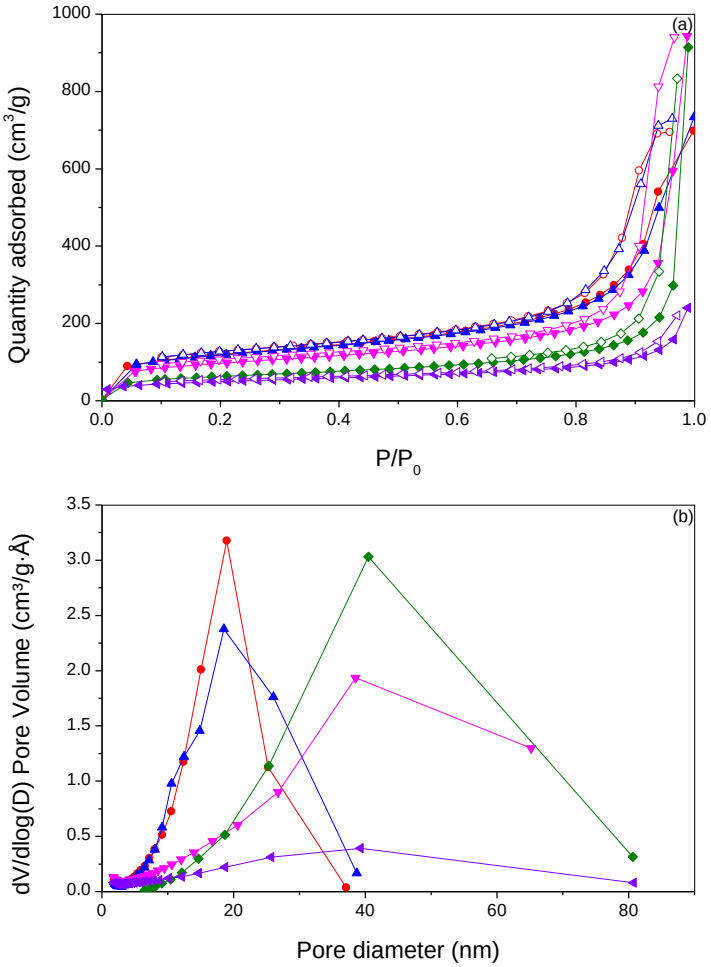

Figure 16-9: (a) N_2 adsorption (closed symbols) and desorption isotherms (open symbols) and (b) PSD for $CaCO_3$_100_D (,), $CaCO_3$_200_D (7), $CaCO_3$_300_D (B), $CaCO_3$_400_D (Λ) and $CaCO_3$_500_D (Ω).

(b) $SrCO_3$ isotherms and PSD

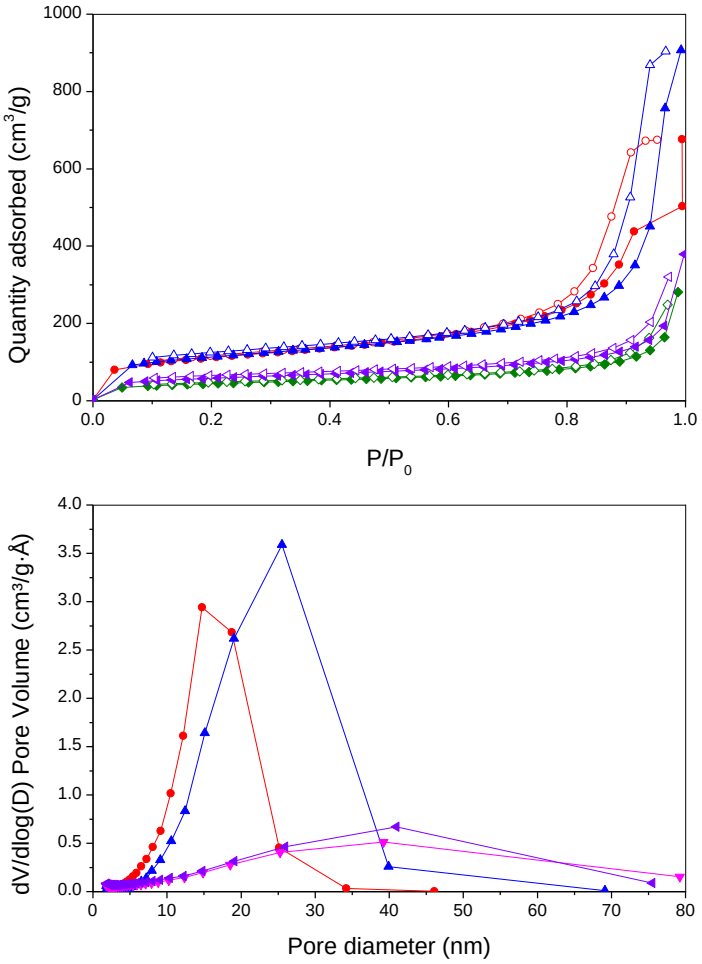

Figure 16-10: (a) N_2 adsorption (closed symbols) and desorption isotherms (open symbols) and (b) PSD for $SrCO_3$_100_D (,), $SrCO_3$_200_DP (7), $SrCO_3$_400_D (Λ) and $SrCO_3$_500_D (Ω).

(c) $BaCO_3$ isotherms and PSD

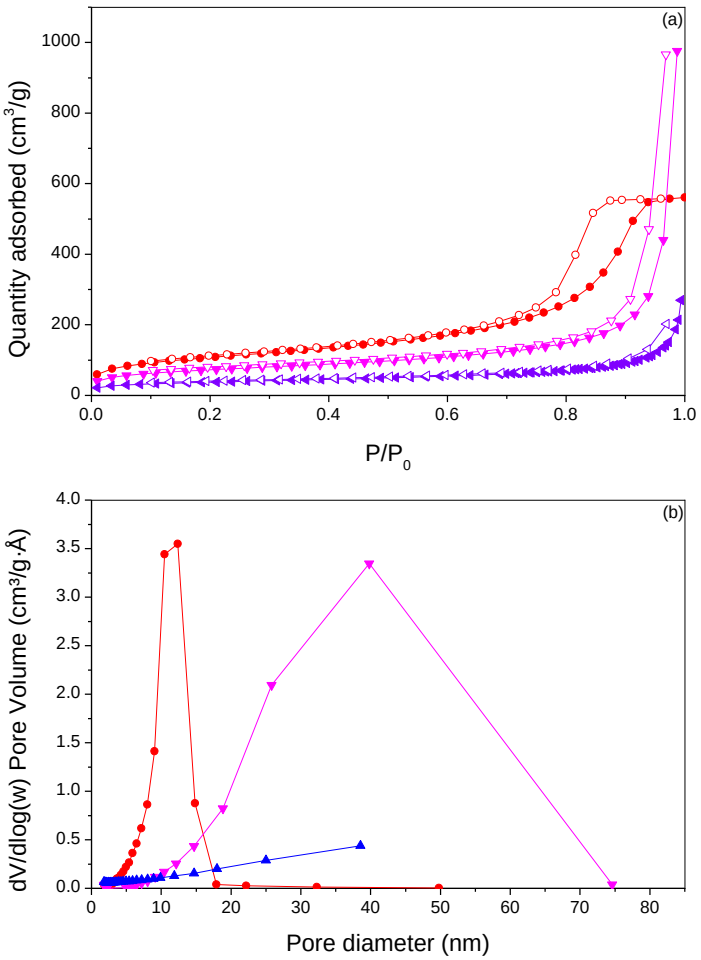

Figure 16-11: (a) N_2 adsorption (closed symbols) and desorption isotherms (open symbols) and (b) PSD for $BaCO_3$_100_D (,), $BaCO_3$_300_D (B) and $BaCO_3$_500_D (Ω).

(d) Mg(OH)$_2$ isotherms and PSD

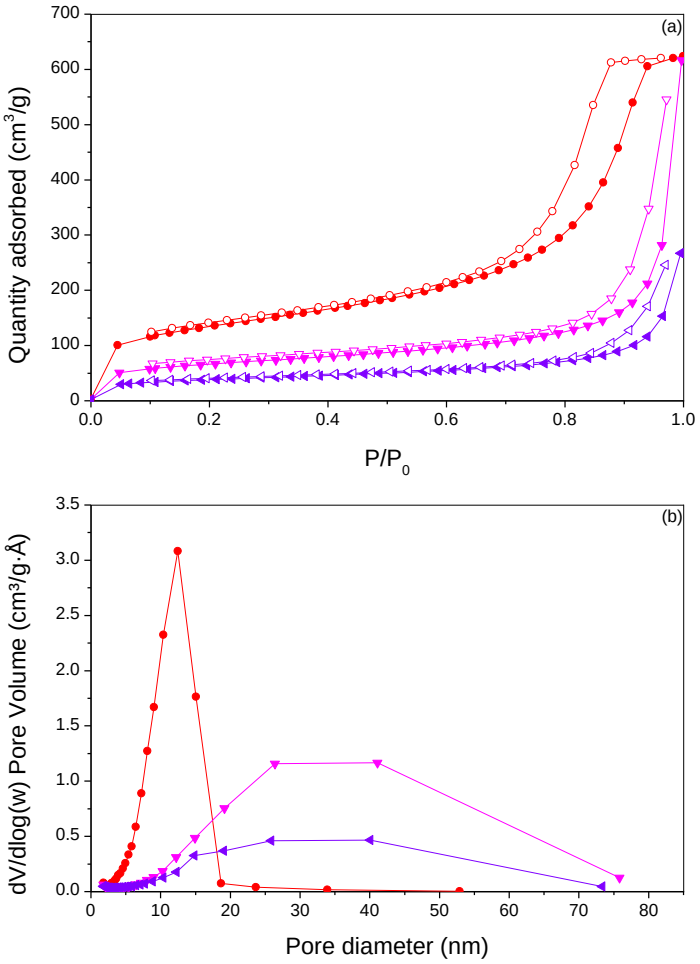

Figure 16-12: (a) N_2 adsorption (closed symbols) and desorption isotherms (open symbols) and (b) PSD for Mg(OH)$_2$_100_D (,),Mg(OH)$_2$_300_D (B) and Mg(OH)$_2$_500_D (Ω).

16.2.2 Carbonised gels

As expected, as the number of micropores within the structures increase, pyrolysis again increases adsorption at low P/P$_0$ and decreases the average pore diameter. These trends are demonstrated in the isotherms and PSD displayed in Figure 16-13.

(a) $CaCO_3$ isotherms and PSD

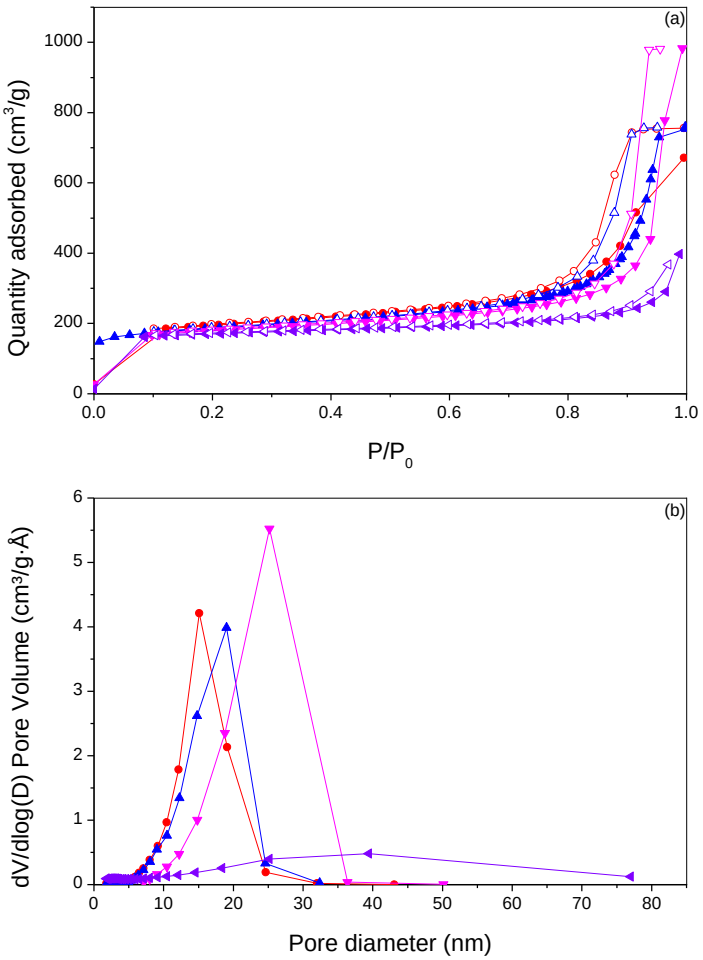

Figure 16-13: (a) N_2 adsorption (closed symbols) and desorption isotherms (open symbols) and (b) PSD for $CaCO_3$_100_DP (,), $CaCO_3$_200_DP (7), $CaCO_3$_300_DP (B) and $CaCO_3$_500_DP (Ω).

17 Appendix E – BATE pH calculations

This Appendix compares the BATE pH calculations for Na_2CO_3 and NaOH sols, prepared at equivalent concentrations, demonstrating that some Na_2CO_3 is capable of deprotonating R twice, resulting in a higher (more basic) initial sol pH that it's NaOH counterpart.

17.1 Na_2CO_3_100

1.1685×10^{-2} M Na_2CO_3 reacts with 1.17×10^{-2} M H_2A (R) therefore some Na_2CO_3 molecules are deprotonating 2 R molecules:

17.1.1 1st Dissociation

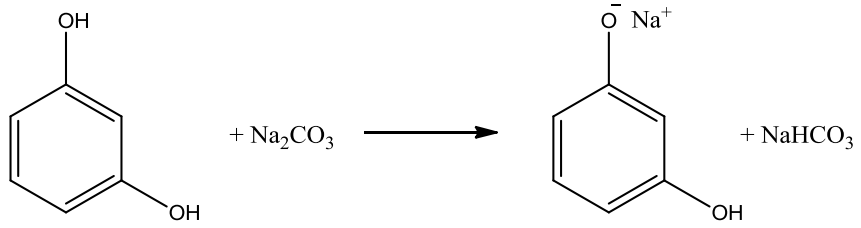

1.1685×10^{-2} M $H_2A(R)$ + 1.1685×10^{-2} M $Na_2CO_3 \rightarrow$ 1.1685×10^{-2} M $NaHCO_3$

1.1685×10^{-2} M HA^- (R^-)

1.1685×10^{-2} M Na^+

17.1.2 2nd Dissociation of H_2A

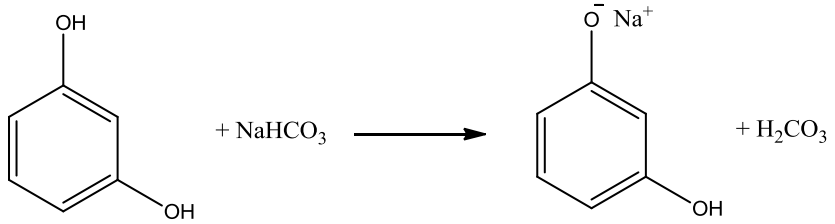

1.1984^{-3} H_2A + 1.01984×10^{-3} M $NaHCO_3 \rightarrow$ 1.01984×10^{-3} M HA^-

1.01984×10^{-3} M H_2CO_3

1.01984×10^{-3} M Na^+

17.1.3 2nd Dissociation of HA-

A small amount of HA^- is then dissociated to A^{2-}:

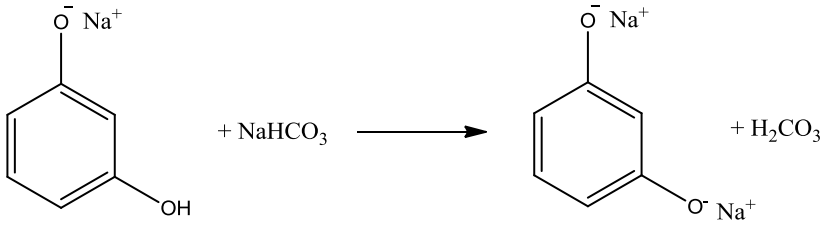

4.484×10^{-5} M HA^- + 4.484×10^{-5} M $NaHCO_3$ → 4.484×10^{-5} M A^{2-}

4.484×10^{-5} M H_2CO_3

17.1.4 Total concentrations

$[HA^-]$ = $1.1685 \times 10^{-2} + 1.01984 \times 10^{-3} - 4.484 \times 10^{-5}$ = 1.266×10^{-2} M

$[NaHCO_3]$ = $1.1685 \times 10^{-2} – 1.01984 \times 10^{-3} – 4.484 \times 10^{-5}$ = 1.062×10^{-2} M

$[H_2CO_3]$ = $1.01984 \times 10^{-3} + 4.484 \times 10^{-5}$ = 1.065×10^{-3} M

$[A^{2-}]$ = 4.484×10^{-5} M

17.1.5 Calculating pH:

1st Dissociation:

$$H_2A \overset{pK_{a1}}{\Longleftrightarrow} H^+ + HA^-$$

$$K_{a1} = \frac{[H^+][HA^-]}{[H_2A]}$$

2nd Dissociation:

$$HA^- \overset{pK_{a2}}{\Longleftrightarrow} H^+ + A^{2-}$$

$$K_{a2} = \frac{[H^+][A^{2-}]}{[HA^-]}$$

pH can then be calculated as follows:

$$pH = -log_{10}[H^+]_{TOTAL}$$

$$[H^+]_{TOTAL} = [H^+]_1 + [H^+]_2$$

Where:

$$[H^+]_1 = \frac{[H_2A]k_{a1}}{[HA^-]}$$

$$[H^+]_2 = \frac{[HA^-]k_{a2}}{[A^{2-}]}$$

$k_{a1} = 10^{-pk_{a1}} = 10^{-9.32} = 4.786 \times 10^{-10}$

$$[H^+]_1 = \frac{[1.1573] \times 4.786 \times 10^{-10}}{[1.270484 \times 10^{-2}]} = 4.3596 \times 10^{-8}$$

$k_{a2} = 10^{-pk_{a2}} = 10^{-9.81} = 1.549 \times 10^{-10}$

$$[H^+]_2 = \frac{[4.484 \times 10^{-5}] \times 1.549 \times 10^{-10}}{[4.484 \times 10^{-5}]} = 1.549 \times 10^{-10}$$

$$[H^+]_{TOTAL} = 4.3596 \times 10^{-8} + 1.549 \times 10^{-10} = 4.375 \times 10^{-8}$$

$$pH = -log_{10}[4.375 \times 10^{-8}] = 7.36$$

17.2 $NaHCO_3$_100

3.3 x 10^{-3} M $NaHCO_3$ reacts with 3.3 x 10^{-3} M H_2A (R):

17.2.1 1st Dissociation

$$R + NaHCO_3 \rightarrow H_2CO_3 + R^-Na^+$$

3.284 x 10^{-3} M H_2A (R) + 3.284 x 10^{-3} M Na_2CO_3→ 3.284 x 10^{-3} M H_2CO_3

3.284 x 10^{-3} M HA^- (R^-)

3.284 x 10^{-3} M Na^+ (B^+)

17.2.2 2nd Dissociation of H_2A

6 x 10^{-6} M R^- then dissociates further to R^{2-}.

17.2.3 Total concentrations

[HA^-]	= 3.284 x 10^{-3} - 6 x 10^{-6}	= 3.278 x 10^{-3} M
[$NaHCO_3$]	= 1.17 x 10^{-2} – 3.284 x 10^{-3}	= 8.416 x 10^{-3} M
[H_2CO_3]	= 3.284 x 10^{-3}	= 3.284 x 10^{-3} M
[A^{2-}]	= 6 x 10^{-6} M	= 6 x 10^{-6} M

17.2.4 Calculating pH

$$[H^+] = \frac{[1.1667] \times 4.786 \times 10^{-10}}{[3.278 \times 10^{-3}]} = 1.7034 \times 10^{-7}\ M$$

$$pH = -log_{10}[1.7034 \times 10^{-7}] = 6.77$$

17.3 NaOH_100

1.17 x 10^{-2} M NaOH reacts with 1.17 x 10^{-2} M H_2A (R).

17.3.1 1st Dissociation

$$R + NaOH \rightarrow H_2O + R^-Na^+$$

1.17 x 10^{-2} M H_2A (R) + 1.17 x 10^{-2} M NaOH →	1.17 x 10^{-2} M H_2O
	1.17 x 10^{-2} M HA^- (R^-)
	1.17 x 10^{-2} M Na^+

17.3.2 2nd Dissociation of H_2A

3.775 x 10^{-5} M R^- then dissociates further to R^{2-}.

17.3.3 Total concentrations

$[H_2A]$	= 1.17 M – 1.17 x 10^{-2}	= 1.1583 M
$[HA^-]$	= 1.17 x 10^{-2} - 3.775 x 10^{-5} M	= 1.167 x 10^{-2} M
$[NaHCO_3]$	= 1.17 x 10^{-2} – 3.284 x 10^{-3}	= 8.416 x 10^{-3} M
$[H_2CO_3]$	= 3.284 x 10^{-3}	= 3.284 x 10^{-3} M
$[A^{2-}]$	= 6 x 10^{-6} M	= 6 x 10^{-6} M

17.3.4 Calculating pH

$$[H^+] = \frac{[1.1583] \times 4.786 \times 10^{-10}}{[1.167 \times 10^{-2}]} = 4.7503 \times 10^{-8}\, M$$

$$pH = -log_{10}[4.7503 \times 10^{-8}] = 7.32$$

18 Appendix F – LCMS results

This Appendix illustrates the chromatogram and MS results obtained, for a sample of prepared RF gels during LCMS measurements, and assigns the main chromatography peaks. These results indicate that similar products are formed during the reaction for the difference catalysts studied. The LCMS results for a sol prepared with no catalyst are given in Section 9.3.

18.1 Na_2CO_3_100_T_{15}

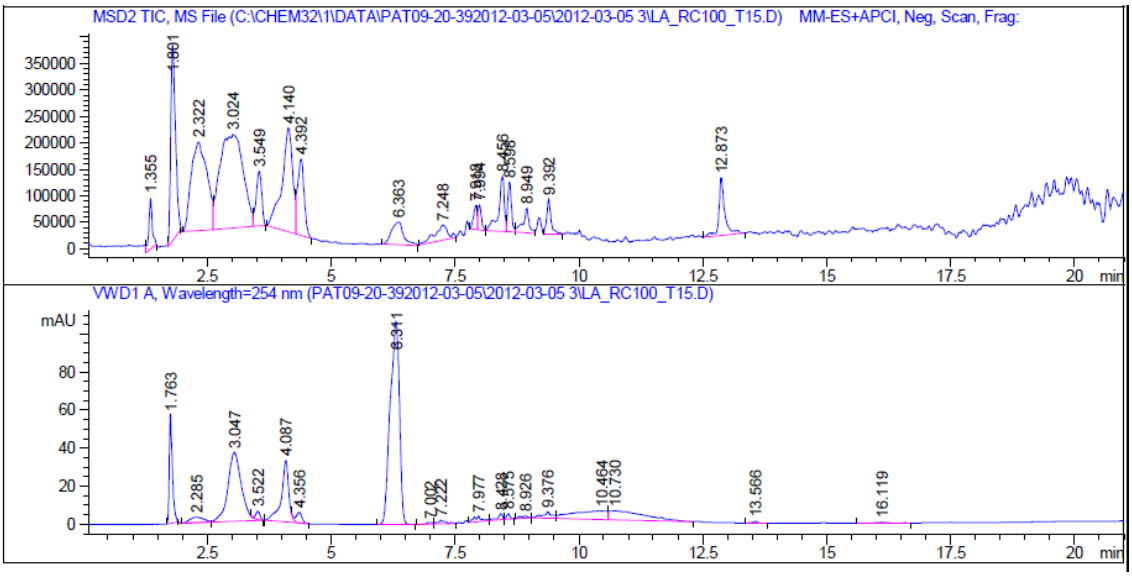

Figure 18-1: Negative mass spec profile and liquid chromatogram for Na_2CO_3_100_T_{15}.

Table 18-1: LC-MS assignment for Na_2CO_3_100_T_{15}

Retention time(minns)	Identified Mass (g)	Assignment
1.801	169.1	Monomer (n = 1 or 2)
2.322	199.1	Monomer (n = 3)
3.024	169.1	Monomer (n = 1 or 2)
3.549	169.0	
4.140	169.1/139.1	Monomer (n = 2)/(n = 1)
4.392	199.1	Monomer (n = 3)
6.363	109.1	Resorcinol
7.248	320.1/290.1	Dimer (n = 2 or 3)
7.918	321.0	
7.994	321.1	
8.456	261.1	Dimer (n = 0 or 1)
8.598	291.1	Dimer (n = 1 or 2)
8.949	261.1	Dimer (n = 1)
9.392	231.1	Dimer (n = 0)

18.2 $CaCO_3$_300_T_{40}

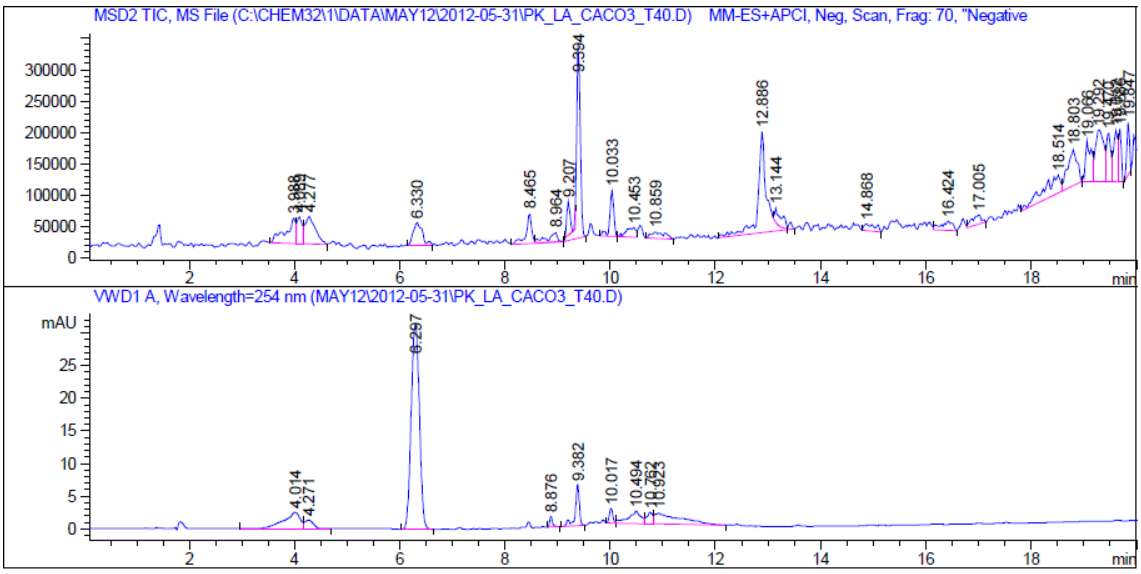

Figure 18-2: Negative mass spec profile and liquid chromatogram for $CaCO_3$_300_T_{40}.

Table 18-2: LC-MS peak assignment for $CaCO_3$_300_T_{40}

Retention time (min)	Identified mass (g)	Assignment
4.089	139.1	Monomer
3.988	139.1	
4.277	139.1	
6.330	109.1	Resorcinol
8.465	261.2	Dimer (n = 0 or 1)
8.864	261.0	
9.207	261.1	
9.394	231.1	Dimer (n = 0)
10.033	353.1	Dimer (n = 3 or 4)
10.453	475.0	Tetramer (n = 0)
10.859	475.1	Tetramer (n = 0)
12.886	531.2/265.3	Trimers (n = 4 or 6)

18.3 $(NH_4)_2CO_3$_300_T_{25}

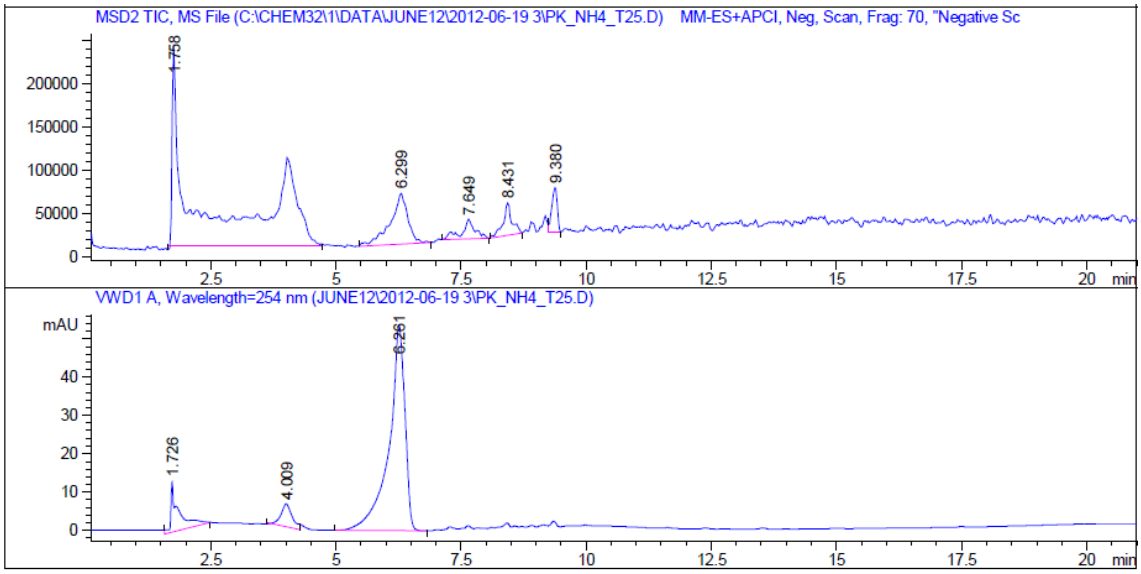

Figure 18-3: Negative mass spec profile and liquid chromatogram for $(NH_4)_2CO_3$_300_T_{15}.

Table 18-3: LC-MS peak assignment $(NH_4)_2CO_3$_300_T_{15}

Retention time (min)	Identified mass (g)	Assignment
1.758	169.1	Monomer
6.299	109.1	Resorcinol
7.649	260.1	Dimer (n = 0 or 1)
8.431	261.1	
9.380	231.1	Dimer (n = 0)

19 Appendix G – LCMS products

This section illustrates possible polymerisation products that may be observed during LCMS during the reaction. The substituted (CH_2OH) groups can be positioned on the 2, 4 or 6 position of any of the resorcinol rings displayed.

19.1 Monomers

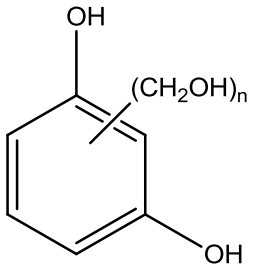

Figure 19-1: Hydroxy-methyl derivative, MW when n=1=140 g, n=2=170 g, n=3=200 g.

19.2 Dimers

19.2.1 Methylene bridged

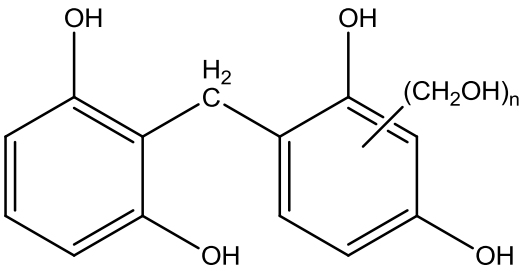

Figure 19-2: Methylene bridged dimer, MW n=0 =232 g, n=1=262 g, n=2=292 g, n=3=322 g.

19.2.2 Methylene ether bridged

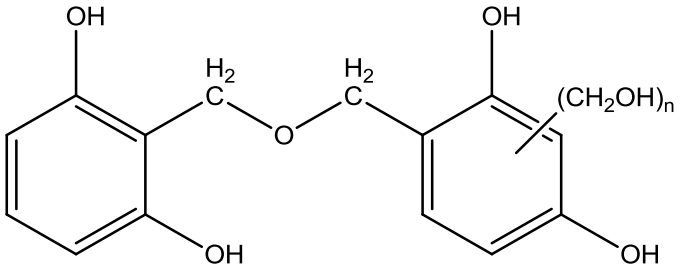

Figure 19-3: Methylene ether bridged dimer, MW n=0=262 g, n=1=292 g, n=2=322 g, n=3=352 g.

19.3 Trimers

19.3.1 Methylene bridged

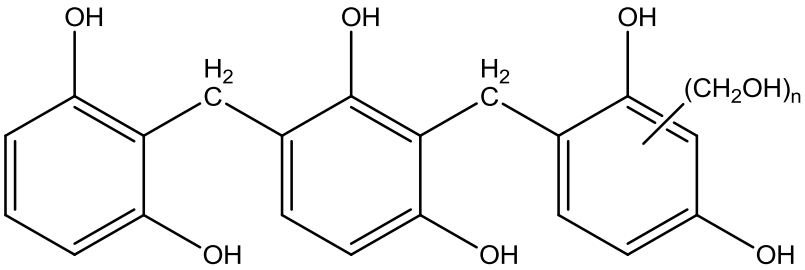

Figure 19-4: Methylene bridged trimer, MW n=0=354 g, n=1=384 g, n=2=414 g, n=3=444 g.

19.3.2 Methylene ether bridged

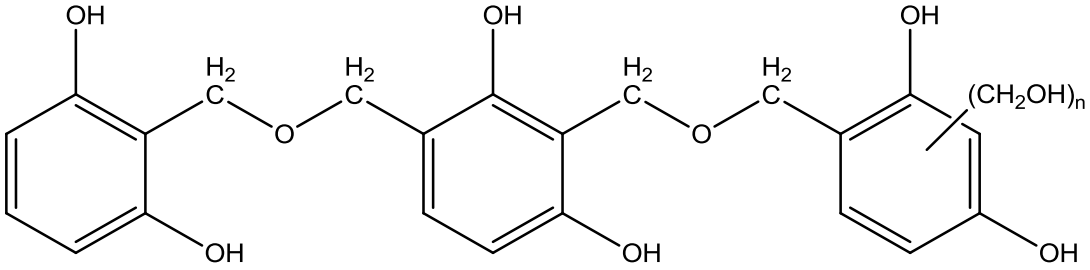

Figure 19-5: Methylene ether bridged trimer, MW n=0=414 g, n=1=444 g, n=2=474 g, n=3=504 g.

19.4 Tetramers

19.4.1 Methylene bridged

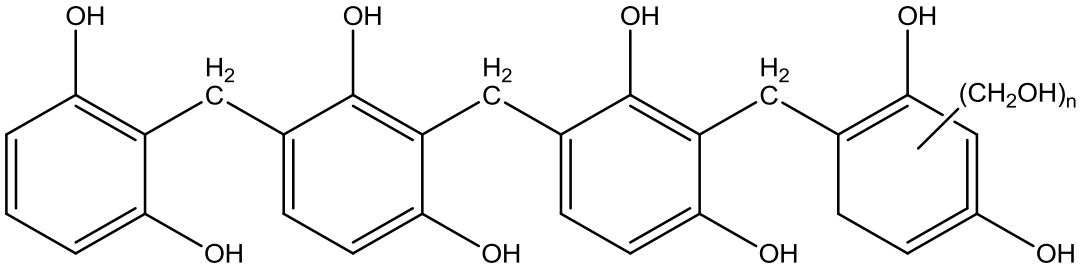

Figure 19-6: Methylene bridged tetramer, n=0=476 g, n=1=506 g, n=2=536 g, n=3=566 g.

19.4.2 Methylene ether bridged

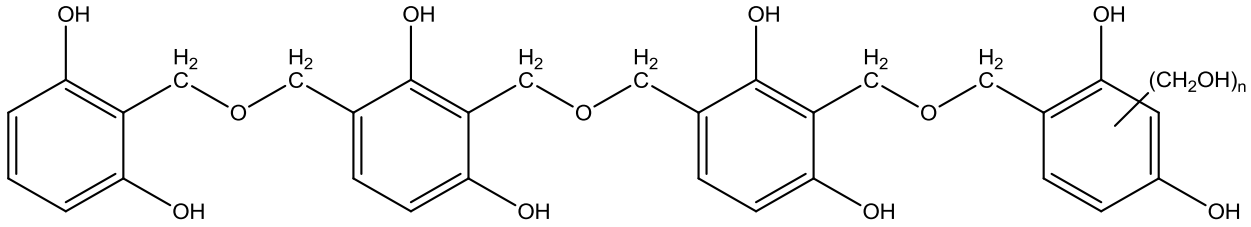

Figure 19-7: Methylene ether bridged tetramer, n=0=566 g, n=1=596 g, n=2=626 g, n=3=656 g.

Table 19-1: Methylene bridged products

No.of repeating units	No. of CH_2OH groups, n						
	0	**1**	**2**	**3**	**4**	**5**	**6**
				Mass			
1	110	140	170	200	-	-	-
2	232	262	292	322	352	382	412
3	354	384	414	444	474	504	534
4	476	506	536	566	596	626	656
5	598	628	658	688	718	748	778
6	720	750	780	810	840	870	900
7	842	872	902	932	962	992	1022

Table 19-2: Methylene ether bridged products

No.of repeating units	No. of CH_2OH groups, n						
	0	**1**	**2**	**3**	**4**	**5**	**6**
				Mass			
1	110	140	170	200	-	-	-
2	262	292	322	352	382	412	442
3	414	444	474	504	534	564	594
4	566	596	626	656	686	716	746
5	718	748	778	808	838	868	898
6	870	900	930	960	990	1020	1050

20 Appendix H – LC linear regression

This appendix details the LC peak areas obtained for all sol samples studied on column 1, 2 and 3. Utilising the calibration results, linear regression analysis was then used to calculate the molar [R] concentration.

Table 20-1 (a): LC results obtained on column 3

Time (min)	R peak area (x 10^6)	[R]/M	Time (min)	R peak area (x 10^6)	[R]/M	Time (min)	R peak area (x 10^6)	[R]/M
Na_2CO_3_600			**$KHCO_3$_50**			**KOH_50**		
0	2.61	0.95	0	2.23	0.799	0	2.41	0.868
10	2.88	1.05	10	2.06	0.731	10	2.01	0.712
20	2.51	0.91	20	1.76	0.618	20	1.70	0.592
30	2.36	0.85	30	1.17	0.389	30	0.11	0.365
40	2.04	0.73	40	6.53	0.189	40	0.639	0.183
60	1.68	0.58	45	4.49	0.109			
70	1.35	0.46						
80	1.14	0.38						
90	0.893	0.28						
100	0.631	0.18						

Table 20-2 (b): LC results obtained on column 2

Time (min)	R peak area (x 10^6)	[R]/M	Time (min)	R peak area (x 10^6)	[R]/M	Time (min)	R peak area (x 10^6)	[R]/M
Na_2CO_3_100			**$NaHCO_3$_100**			**Cs_2CO_3_400**		
0	4.25	0.790	0	4.61	0.864	0	5.70	1.08
10	3.83	0.705	10	4.11	0.764	10	5.87	1.12
20	2.95	0529	20	3.44	0.627	20	5.07	0.956
30	1.99	0.336	30	2.79	0.498	30	4.55	0.852
40	1.15	0.167	40	2.10	0.358	40	3.68	0.675
45	0.421	0.020	50	1.30	0.197	50	2.72	0.483
Na_2CO_3_200			**$NaHCO_3$_200**			60	1.42	0.220
0	5.06	0.954	0	6.86	1.28	70	1.52	0.240
10	4.44	0.829	10	6.04	1.15	**$CaCO_3$_200**		
20	3.52	0.635	20	4.67	0.875	0	5.01	0.943
30	2.93	0.525	30	3.91	0.723	10	4.50	0.841
40	2.13	0.364	40	3.58	0.655	20	3.65	0.669
50	1.36	0.208	50	2.56	0.451	30	3.21	0.582
Na_2CO_3_400			60	1.37	0.211	40	2.37	0.413
0	5.88	1.12	70	1.42	0.221	**$CaCO_3$_400**		
10	5.50	1.04	**Cs_2CO_3_200**			0	5.73	1.09
20	4.71	0.884	0	5.05	0.952	10	5.28	0.999
30	3.89	0.717	10	4.47	0.835	20	4.64	0.870
40	3.61	0.662	20	3.68	0.676	30	3.98	0.736
50	2.72	0.482	30	3.00	0.539	40	3.47	0.633
60	1.96	0.329	40	2.29	0.396	50	2.82	0.502
70	1.23	0.182	**NO_C**			**$(NH_4)_2CO_3$_200**		
NaOH_200			0	5.98	1.14	0	4.91	0.925
0	7.16	1.38	15	7.07	1.36	10	4.87	0.916
10	6.60	1.26	30	6.51	1.25	20	4.15	0.771
20	4.83	0.909	45	6.75	1.29	30	3.79	0.698
30	4.41	0.823	60	6.29	1.20	40	2.99	0.537
40	3.95	0.730	75	4.85	0.911	50	2.52	0.443
50	2.93	0.524	90	4.41	0.822	60	1.89	0.316
60	2.61	0.461	105	3.93	0.726			
			120	3.28	0.596			
			135	2.44	0.426			
			150	1.75	0.288			

Table 20-3 (a): LC results obtained on column 1

Time (min)	R peak area (x 10^6)	[R]/M	Time (min)	R peak area (x 10^6)	[R]/M	Time (min)	R peak area (x 10^6)	[R]/M

Na_2CO_3_100		
0	10.1	1.12
10	8.22	0.911
20	5.27	0.590
30	3.33	0.378
40	22.5	0.260
45	1.66	0.196

Na_2CO_3_200		
0	12.7	1.17
10	10.7	0.926
20	7.17	0.602
30	5.78	0.474
40	4.13	0.321
45	3.34	0.248
50	2.11	0.134

Na_2CO_3_300		
0	12.3	1.07
10	11.4	0.998
20	9.07	0.779
30	8.62	0.737
40	6.30	0.521
50	4.23	0.330
60	3.38	0.251

Na_2CO_3_600		
0	11.7	1.02
10	11.5	1.00
20	10.3	0.888
30	7.63	0.645
40	7.33	0.617
50	5.68	0.465
60	4.13	0.321
70	3.48	0.261
80	2.74	0.192
85	2.36	0.157

Na_2CO_3_500		
0	13.2	1.16
10	12.6	1.11
20	11.0	0.956
30	10.2	0.885
40	7.97	0.676
50	6.50	0.540
60	5.22	0.421
70	3.59	0.270
80	2.47	0.166
90	2.89	0.206

$NaHCO_3$_100		
0	12.7	1.11
10	11.5	1.01
20	7.77	0.658
30	6.92	0.579
40	5.55	0.453
50	3.83	0.293

$NaHCO_3$_200		
0	11.8	1.03
10	11.2	0.972
20	8.14	0.692
30	8.03	0.682
40	7.50	0.633
50	6.00	0.494
60	4.99	0.401
70	1.96	0.120
80	2.97	0.213

$CaCO_3$_100		
0	10.8	0.943
10	9.86	0.852
20	7.83	0.664
30	5.83	0.479
40	4.26	0.333

NaOH_100		
0	12.1	1.06
10	10.8	0.941
20	8.35	0.712
30	6.66	0.555
40	5.04	0.405
50	3.57	0.269

NaOH_200		
0	14.4	1.27
10	11.5	1.00
20	10.1	0.874
30	8.60	0.735
40	6.85	0.573
60	3.84	0.294
70	2.68	0.186

NaOH_250		
0	12.8	1.12
10	12.7	1.12
20	12.3	1.08
30	10.2	0.885
40	9.43	0.811
50	7.33	0.617
60	6.01	0.495
70	4.82	0.385
80	3.26	0.240
90	2.37	0.157

21 Appendix I - F titration results

This Appendix details the F titration results obtained for all sol samples studied, where the required volume of NaOH was multiplied by 0.03003 to give the weight of F present in 10 ml sample. The moles of F (per 10 ml) were then calculated by dividing the weight by the molar mass of F (30.0262 g/mol), which was multiplied by 100 to give the molar concentration of F.

Table 21-1 (a): F titration results

Time (min)	ml NaOH	g F/10 ml	mols F x 10^{-2}/10 ml	F Molar remaining
$NaHCO_3$_100				
0	18.20	0.547	1.82	1.82
15	14.50	0.435	1.45	1.44
30	12.15	0.365	1.22	1.22
45	7.05	0.212	0.705	0.705
$NaHCO_3$_200				
0	17.00	0.511	1.70	1.70
15	15.50	0.465	1.55	1.55
30	14.15	0.425	1.42	1.42
45	12.00	0.360	1.20	1.20
60	9.65	0.290	0.965	0.965
Cs_2CO_3_200				
0	15.75	0.473	1.58	1.58
15	14.20	0.426	1.42	1.42
30	11.55	0.347	1.16	1.16
45	9.40	0.282	0.940	0.940
Cs_2CO_3_400				
0	16.05	0.482	1.61	1.61
15	16.35	0.491	1.64	1.64
30	12.65	0.380	1.27	1.27
45	11.55	0.347	1.16	1.16
60	10.70	0.321	1.07	1.07
NaOH_100				
0	17.90	0.548	1.79	1.79
15	15.10	0.453	1.51	1.51
30	12.25	0.368	1.23	1.23
45	7.15	0.215	7.15	7.15

Table 21-2 (b): F titration results (continued)

Time (min)	ml NaOH	g F/10 ml	mols F x 10^{-2}/10 ml	F Molar remaining
NaOH_200				
0	17.60	0.529	1.76	1.76
15	15.90	0.477	1.59	1.59
30	14.65	0.440	1.47	1.47
45	12.95	0.389	1.30	1.30
60	11.05	0.332	1.11	1.11
$CaCO_3$_200				
0	15.85	0.476	1.59	1.59
15	16.70	0.502	1.67	1.67
30	15.35	0.461	1.54	1.54
30	12.65	0.380	1.27	1.27
45	11.25	0.338	1.13	1.13
$CaCO_3$_400				
0	18.00	0.541	1.80	1.80
15	15.50	0.465	1.55	1.55
30	14.25	0.428	1.43	1.43
45	13.80	0.414	1.38	1.38
60	6.00	0.180	0.600	0.600
$(NH_4)_2CO_3$_200				
0	16.05	0.482	1.61	1.61
15	16.35	0.491	1.64	1.64
30	12.65	0.380	1.27	1.27
45	11.55	0.347	1.60	1.60
60	10.70	0.321	1.07	1.07
No_C				
0	18.10	0.544	1.81	1.81
15	17.40	0.523	1.74	1.74
30	16.80	0.505	1.68	1.68
60	15.10	0.453	1.51	1.51
75	13.25	0.398	1.33	1.33
90	13.10	0.393	1.31	1.31
105	10.05	0.302	1.01	1.01
120	10.40	0.312	1.04	1.04
135	8.05	0.242	0.805	0.805
Na_2CO_3_100				
0	16.80	0.505	1.68	1.68
15	12.00	0.360	1.20	1.20
30	8.20	0.246	0.820	0.820
40	8.90	0.177	0.590	0.590

Table 21-3 (c): F titration results (continued)

Time (min)	ml NaOH	g F/10 ml	[F] (x 10^{-2}/10 ml)	[F]/M
Na_2CO_3_200 repeats				
0	17.46	0.524	1.75	1.75

15	14.33	0.430	1.43	1.43
30	11.45	0.344	1.15	1.15
45	7.42	0.223	0.742	0.742
0	17.35	0.521	1.74	1.74
15	14.23	0.427	1.42	1.42
30	11.0	0.333	1.11	1.11
45	6.81	0.205	0.681	0.681
0	17.30	0.524	1.75	1.75
15	14.02	0.421	1.40	1.40
30	12.21	0.367	1.22	1.22
45	6.71	0.201	0.671	0.671
0	17.96	0.539	1.80	1.80
15	14.63	0.439	1.46	1.46
30	11.75	0.353	1.18	1.18
45	6.96	0.209	0.696	0.696
0	17.46	0.524	1.75	1.75
15	14.13	0.424	1.41	1.41
30	11.40	0.342	1.14	1.14
45	6.76	0.203	0.676	0.676
0	17.46	0.524	1.75	1.75
15	14.93	0.448	1.49	1.49
30	12.11	0.364	1.21	1.21
45	7.21	0.217	0.722	0.722
Na_2CO_3_400				
0	18.00	0.541	1.80	1.80
15	15.65	0.470	1.57	1.57
30	13.30	0.399	1.33	1.33
40	12.00	0.360	1.20	1.20
60	9.15	0.275	0.915	0.915
80	7.90	0.237	0.790	0.790
Na_2CO_3_600				
0	18.00	0.541	1.80	1.80
15	16.50	0.495	1.65	1.65
30	15.05	0.452	1.51	1.51
45	14.20	0.426	1.42	1.42
60	13.55	0.407	1.36	1.36
70	12.15	0.365	1.22	1.22
90	10.90	0.327	1.09	1.09

22 Appendix J - DoE Regression model

22.1 Statistical analysis for a 2 factor factorial design

The total sum of squares is calculated using Equation 165 and is essentially the sum of all response values squared, minus the sum of the total response squared divided by 2^k (n):

$$SS_T = \sum_{i=1}^{a}\sum_{j=1}^{b}\sum_{k=1}^{n} y_{ijk}^2 - \frac{y_{...}^2}{ab\ldots n}$$

Equation 165

Where *n = number of replicates*

The sum of squares for the main effects can be calculated as follows:

$$SS_A = \frac{1}{b\ldots n}\sum_{i=1}^{a} y_{i..}^2 - \frac{y_{...}^2}{ab\ldots n}$$

Equation 166

$$SS_B = \frac{1}{a\ldots n}\sum_{j=1}^{b} y_{.j.}^2 - \frac{y_{...}^2}{ab\ldots n}$$

Equation 167

And the sum of squares for the interaction effect can be calculated in two stages. Firstly the sum of squares between the ab cell totals (sum of squares due to subtotals):

$$SS_{subtotals} = \frac{1}{n}\sum_{i=1}^{a}\sum_{j=1}^{b} y_{ij}^2 - \frac{y_{...}^2}{abn}$$

Equation 168

Then the interaction sum of squares can be calculated as:

$$SS_{AB} = SS_{subtotals} - SS_A - SS_B$$

Equation 169

The sum of squares for the error can be calculated by subtraction:

$$SS_E = SS_T - SS_{AB} - SS_A - SS_B$$

Equation 170

$$SS_E = SS_T - SS_{subtotals}$$

Equation 171

The associated degrees of freedom for each sum of squares are as follows:

Table 22-1: Degrees of freedom for a 2^2 factorial design

Effect	Degrees of Freedom
A	a-1
B	b-1
AB	(a-1)(b-1)
Error	ab(n-1)
Total	abn - 1

Each sum of squares divided by its associated degrees of freedom gives rise to the mean square value, $\boldsymbol{MS_x}$ where x = A, B, AB, E, and to test the significance of the effects and interactions the MS values can be divided by the MS_E value and an ***F test*** can be performed (i.e. if ***Fcalc > Fcrit*** the F test fails and the effects are significant) [198].

The above equations can be extended for designs that include more factors.

23 Appendix K – Papers

23.1 Draft paper

Monitoring particle size changes during sol-gel transitions of RF xerogels using UV-Vis spectrometry

Lynsey Anderson[a,b1], Stewart Taylor[a,b], Alison Nordon[b] and Ashleigh Jane Fletcher[a]

a. Department of Chemical and Process Engineering, University of Strathclyde Glasgow, G1 1XJ
b. WestCHEM, Department of Pure and Applied Chemistry & Centre for Process Analytics and Control Technology (CPACT), University of Strathclyde, Glasgow, G1 1XL

1 Abstract

UV-Vis spectrometry was used to monitor the gelation of Resorcinol-Formaldehyde (RF) derived xerogels and the results obtained show that this technique can be used as a quick analytical tool to determine changes in RF particle size during sol-gel transformation. This method can be used to monitor samples during the sol-gel transition and, requiring no further sample manipulation, means results can be obtained within a few minutes, allowing particle formation for different sol compositions to be rapidly compared. Results presented demonstrate application of the technique to sol samples prepared with Group I and Group II metal carbonate catalysts, where UV-Vis absorbance at 500, 600 and 750 nm increases linearly with particle sizes above 20 nm. These preliminary results suggest that, with the aid of a reference library, UV-Vis spectrometry could be used as an alternative technique for the determination of RF particle size, offering quicker and simpler analysis compared to traditional techniques.

2 Introduction

Since their first synthesis by Pekala *et al*. [1] Resorcinol-Formaldehyde (RF) gels have been widely studied. Interest in these organic materials stems from their highly tuneable porous properties, by altering synthesis variables, throughout the multi-step sol gel process, RF gels with pores ranging from microporous (< 2 nm) to macroporous (> 50 nm) can be prepared, making them useful for a wide range of applications; possible monolithic structures, high surface areas, small pores and high electrical conductivity of RF carbon gels make them suitable for many electrochemical applications, for example as electrodes in Electrochemical Double Layer Capacitors (EDLCs) [2] and LiO_2 batteries [3], the ability to prepare different forms of carbon gels and tunable properties also make them attractive materials for applications in adsorption and catalysis [4].

Pore sizes of the RF gels can be manipulated by controlled aggregation of primary particles within the sol [5, 6] and as described by Pekala *et al*. [1, 7, 8] this is mainly achieved via selection of catalyst

[1] Corresponding author
lynsey.anderson@strath.ac.uk
Tel –
Fax –

concentration or the molar ratio of R to catalyst (R/C). When high catalyst concentrations (or low R/C) are present, many small clusters are initially formed resulting in materials with small particles and pores, whereas small catalyst concentrations (high R/C) promote preferential growth of polymer clusters, resulting in gels with larger particles and pores. The catalyst is not the only factor affecting particle size of RF gels and many other variables have been shown to have an effect. Lee *et al*. [9] prepared gels using an emulsion technique and demonstrated that particle size could be controlled by altering stirring rate, with increased agitation resulting in smaller RF particles. Similar results were reported by Sharma *et al*. [10] who established that stirring time also influenced particle aggregation, with longer stirring times resulting in larger particles. Additionally solid content may be varied, i.e. the percentage of reactants to sol volume, which affects the rate of reaction and, as a result, can be used to control particle size. High solid content cause the reaction between R and F to occur rapidly, causing a similar effect to that observed for high catalyst concentrations leading to small mass fragments and small pores, the inverse is observed for low solid content [11]. Scherdel *et al*. [12] reported that particles as large as a few micrometers (> 1000 nm) could be prepared by using low percentage solids (R + F) and very low catalyst concentrations.

As a number of parameters influence RF particle size, in turn impacting on final porosity of the organic gels, it is of significance that the process of aggregation can be easily monitored. Traditional monitoring methods include Dynamic Light Scattering (DLS), Small Angle X-Ray Scattering (SAXS) and microscopic techniques such as Scanning Electron Microscopy (SEM) or Transmission Electron Microscopy (TEM). DLS is a spectroscopic technique that involves the determination of a time autocorrelation function for scattered light. Interaction of light with the sample is dependent upon the size of suspended particles [13, 14]; consequently interpretation of the autocorrelation function allows average particle sizes to be determined. This technique typically involves minimal sample preparation; however work within this group has shown that sample filtration prior to DLS analysis reduces the noise component, therefore, increasing the sensitivity of the results obtained [15]. Obtaining the auto correlation function for a sample takes only a few minutes, however, subsequent analysis to can be complex and time consuming. SAXS is a similar technique to DLS but involves measurement of X-ray scattering, like DLS, SAXS requires intricate data analysis [16]. Microscopic techniques, SEM and TEM, are typically used for examining the external and internal structure of solid RF gels and are, therefore, not suitable for monitoring particle size growth within solutions [17-19].

As stated above, although DLS and SAXS allow the particle sizes of RF sols to be monitored as the reaction progresses [20-22], the complex data analysis required makes it difficult to compare different sols as they are prepared. Consequently this study investigates the use of UV-Vis spectrometry as a means of rapidly monitoring RF particles, eliminating the need for further sample preparation and complex data manipulation. Various RF sols were prepared with a number of different Group I and

Group II metal carbonate catalysts and their UV-Vis absorbance monitored over the range of 200-800 nm, throughout the sol-gel transition. DLS was used to measure changes in RF particle size and the relationship between absorbance and particle size was investigated.

3 Experimental

3.1 RF xerogel preparation

RF xerogels were synthesised by the polycondensation of R and F in aqueous medium, using either sodium carbonate Na_2CO_3, caesium carbonate Cs_2CO_3 or calcium carbonate $CaCO_3$ as catalyst, with molar R/C ratios of both 200 and 400 for all three catalsysts. An appropriate amount of R was dissolved in deionised water, the catalyst was added, before the addition of F and the sol was stirred at room temperature for 30 minutes. After this time the sol was placed in an oven at 85 ± 5 °C to allow the gelation and curing processes to proceed.

3.2 DLS

Particle growth in the initial stages of the RF reaction was monitored using an ALV/CGS 3 Compact Goniometer System in conjunction with an ALV/LSE 5004 Multiple Tau Digital Correlator. This system used a He:Ne laser at 632.8 nm, and measured the scattered intensity at an angle of 90° to the beam path. After the 30 minute stir the sol was passed through a 0.2 µm PTFE filter (Whatman™ Puradisc™), which removed any undesired particulates. Small sample cells were then filled with equal volumes of the filtered sol. One of the cells was placed directly in the cell holder of the DLS equipment, allowing a measurement at time zero to be obtained. The other cells were placed in an oven at 85 ± 5 °C to begin gelation and were removed sequentially at the required time intervals and quenched to room temperature before the scattered intensity was measured.

The scattered intensities obtained were used to generate autocorrelation functions. In order to obtain diffusion coefficients these functions were fitted with a third order cumulant and the calculated coefficients were substituted into the Stokes Einstein Equation (Equation 1) to give hydrodynamic radii of the particles at each stage of the gelation process.

$$d(H) = \frac{kT}{3\pi\eta D}$$

Equation 1

Where $d(H) = Hydrodynamic\ diameter\ (m)$

$D = translational\ diffusion\ coefficient\ (m^2 s^{-1})$

$k = Boltzmann's\ coefficient\ (m^2 K g s^{-2} K^{-1})$

$T = Absolute\ temperature\ (K)$

η = Viscosity (Pa s)

3.3 UV-Vis absorbance measurements

UV-Vis absorbance measurements were carried out using a Varian Cary 5000 UV-Vis-NIR spectrometer over a range of 200 nm to 800 nm. For each of the prepared sols a small sub sample (~ 0.8 ml) was immediately removed after the 30 minute stir. This sample was extracted into a 2mm wide quartz cuvette and an absorbance spectrum was measured. This sample was classified as T_0. The remaining sol was placed in the oven and small samples were extracted at sequential time intervals and absorbance measured, allowing time resolved spectra to be obtained. Samples were measured, for each prepared sol, until the viscosity was such that the sample could not be extracted into the quartz cell, at this stage the sols were close to the gelation point.

4 Results and discussion

4.1 Relationship between absorbance and RF particle size

Figure 4-1 shows an example UV-Vis spectrum for an RF sol (Na_2CO_3_200 at 12 minutes), clearly illustrating three main absorbance peaks which can be assigned using adsorption bands given in literature. The peak at approximately 280 nm is ascribed to phenol and aldehyde groups within the forming gel, and the peaks at approximately 220 nm and 350 nm result from conjugated benzene rings [23]. Similar scattering as a result of conjugation was demonstrated for the UV-Vis absorbance of fullerene (C_{60}) solutions by Mzerl *et al*. [24] and Kato *et al*. [25].

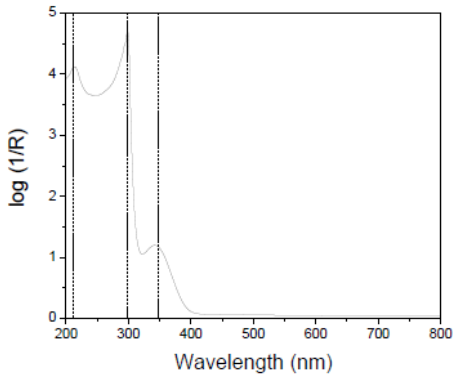

Figure 4-1: UV-Vis absorbance spectrum for Na_2CO_3_200 at T_{12}

Time resolved spectra for all RF sols studied are shown in Figure 4-2, demonstrating that absorbance at 350 nm intensifies with increasing reaction time. Similar to results reported by Kato *et al*. [25], for fullerene solutions, this increased absorbance can be explained by a change in the sol colour (colourless to

red) indicative of increasing particle size, growing conjugation [26] and dense packing of RF particles, as the polymerisation reaction proceeds.

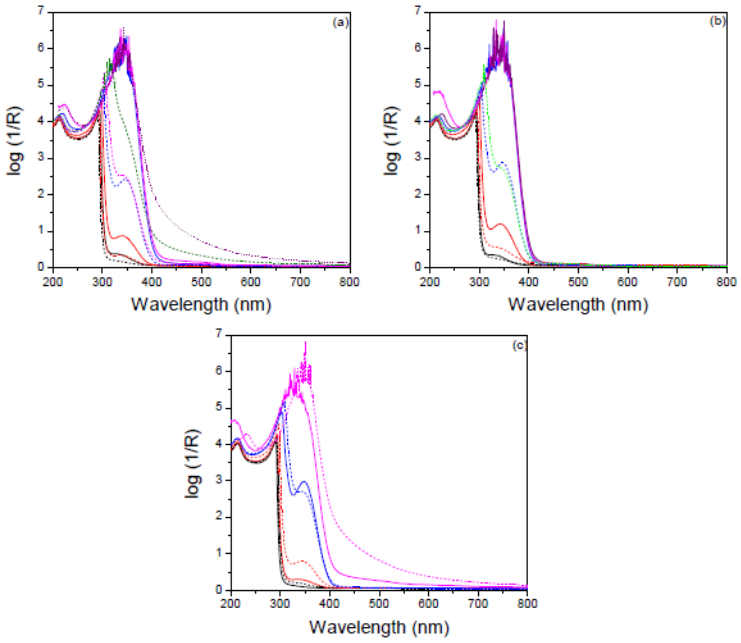

Figure 4-2: UV-Vis spectra for (a) Na_2CO_3_200 (solid lines), at T_0 (black), T_{12} (red), T_{25} (blue), T_{30} (pink) and T_{37} (purple), and Na_2CO_3_400 (dotted lines) at T_0 (black), T_{12} (red), T_{25} (blue), and T_{40} (green); (b) Cs_2CO_3_200 (solid lines) at T_0 (black), T_{12} (red), T_{30} (blue), and T_{40} (pink), and Cs_2CO_3_400 (dotted lines) T_0 (black), T_{12} (red), T_{25} (blue), T_{30} (pink), T_{40} (green), and T_{45} (purple); (c) $CaCO_3$_200 (solid lines) T_0 (black), T_{12} (red), T_{25} (blue), and T_{40} (pink), and $CaCO_3$_400 (dotted lines) at T_0 (black), T_{12} (red), T_{30} (blue), and T_{40} (pink)

For particle sizes in the region of 100 - 250 nm, Kato *et al*. [25] reported an almost linear relationship at an absorbance of 340 nm. To investigate whether a similar relationship between RF particle size and absorbance exists, the DLS particle size (Figure 4-3) at various reaction times was plotted against UV-Vis absorbance at 350 nm (350 nm was chosen as this is the wavelength where peak maximum is observed), as illustrated in Figure 4-4.

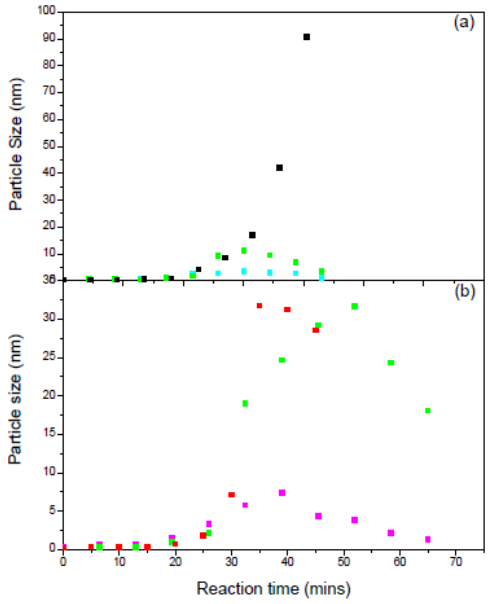

Figure 4-3: DLS particle size as a function of reaction time for (a) Na_2CO_3_200 (■), Cs_2CO_3_200 (■), $CaCO_3$_200 (■) and (b) Na_2CO_3_400 (■), Cs_2CO_3_400 (■) and $CaCO_3$_400 (■).

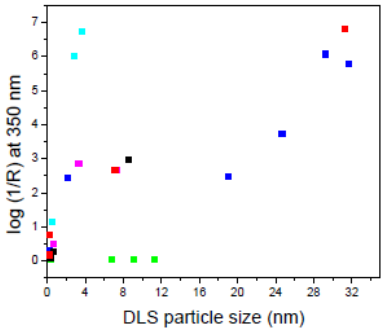

Figure 4-4: UV-Vis absorbance at 350 nm for Na_2CO_3_200 (■), Na_2CO_3_400 (■), Cs_2CO_3_200 (■), Cs_2CO_3_400 (■), $CaCO_3$_200 (■) and $CaCO_3$_400 (■)

Figure 4-4 shows that no correlation exists between RF particle size and UV-Vis scattering at 350 nm, one explanation for this is that the surface area of the RF particles also has an effect on the amount of light absorbed by the sol. This effect was demonstrated by Fu *et al*. [27] who reported that as the particle size of a pigment dispersion decreased, the surface area increased and the absorption increased.

In order to test this theory absorbance spectra for Na, Cs and Ca catalysed gels were directly compared (Figure 4-5). The spectra for R/C 200 sols at T_{12} indicate that, absorbance at 350 nm is in the order Na > Cs < Ca. This order of absorption is not as expected, as the Cs and Ca sols exhibit favoured particle aggregation and as a result increased colloidal particle size (as demonstrated by Figure 4-3), however, the smaller Na particles will have a larger surface area, which will scatter incident light in all directions, limiting the amount of light passing through and increasing sample absorbance. However, the spectra for sols prepared with R/C 400 at T_{40}, display the opposite trend, with Na_2CO_3_400 displaying lower absorbance than Cs_2CO_3_400 and $CaCO_3$_400. This order is as expected, with absorption increasing in the order of increasing particle size. At this lower concentration the density of particles is reduced, thus the effect of particle surface area is less significant and UV absorption is based on particle size, with absorbance in the order of increasing pore diameter (Na_2CO_3_400_T_{40} = 7.37 nm, Cs_2CO_3_400_T_{40} = 24.67 nm, $CaCO_3$_400_T_{40} = 31.78 nm). From these results it appears that there are two opposing factors contributing to the UV-Vis scattering of RF sols (i.e. decreasing particle size increases surface area, which increases absorbance, but in general absorbance increases with increasing particle size) and as a result the absorbance at approximately 350 nm cannot be used to determine particle size within the sol.

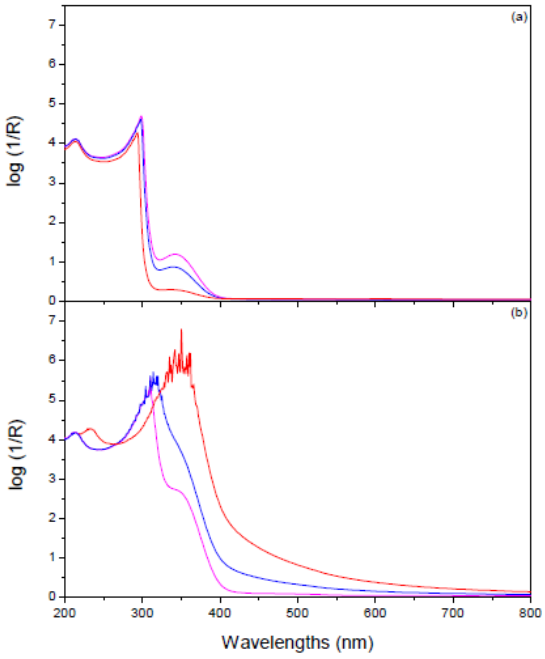

Figure 4-5: UV-Vis spectra for (a) Na_2CO_3_ 200 (pink), Cs_2CO_3_200 (blue) and $CaCO_3$_200 (red) sols at T_{12}, and (b) Na_2CO_3_ 400 (pink), Cs_2CO_3_400 (blue) and $CaCO_3$_400 (red)

7

K. Goodner [28, 29] demonstrated that change in adsorption in the red region was dependent only on th turbidity of the sample and not on the sample chemistry. Goodner established that samples with the san chemical structure but different turbidities showed varying absorbance at 750 nm, demonstrating a linea relationship between absorbance at 750 nm and sample turbidity. Inspection of RF absorbance spectra (Figure 4-2) shows that, as reaction proceeds, absorbance in the green to red region (500 to 800 nm) increases. If the first region of decay in DLS is considered (i.e. the initial reaction, where particles grow gradually, before clusters aggregate quickly causing a significant increase in particle size) and the avera particle size is plotted against the UV-Vis absorbance (log 1/R), at 500, 600 and 750 nm, it is evident th there is a relationship between particle size and absorbance. Figure 4-6 (a) to (c) illustrate that there is little change in the absorbance as the particles grow to approximately 20 nm, as the reaction proceeds further, particles grow and aggregate, resulting in a significant increase in turbidity (cloudiness) of the sample and a change in colour from pale yellow to deep red, at this stage there is a linear relationship between particle size and absorbance at 500, 600 and 750 nm as shown in Figure 4-6.

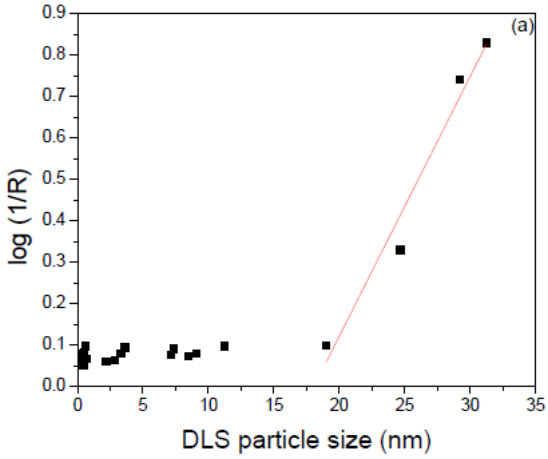

8

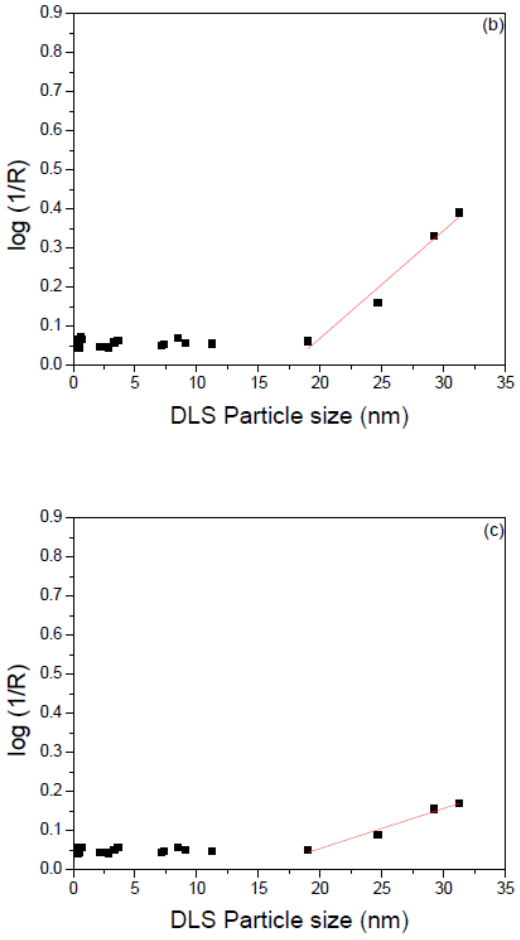

Figure 4-6: Plot of log (1/R) as a function of DLS particle size at (a) 500 nm, (b) 600 nm and (c) 750 nm, for $CaCO_3$, Cs_2CO_3 and Na_2CO_3 at R/C ratios of 200 and 400

5 Conclusion

The method presented in this study demonstrates that UV-Vis spectrometry can be used to monitor particle formation, during the sol-gel transition of RF xerogels. The UV-Vis absorbance measurements can be applied directly to RF sols, requiring no further sample preparation or dilution. Subsequently, as demonstrated by Figure 4-6, UV-Vis spectrometry can be used as a quick analysis tool to determine whether there are significant changes in particle size during gelation, and could be applied to different RF sol compositions or used to compare varying synthesis processes.

The linear relationships shown for these preliminary results also suggest that, with the collation of a reference library of particle sizes, it may possible to use UV-Vis spectrometry to determine RF particle sizes above 20 nm. This study demonstrates that wavelengths of 500, 600 and 750 nm can be used for particle size determination; however, as displayed in Figure 4-6, measurements at 500 nm provide absorbance values 2 x and 4 x as high as measurements at 600 and 750 nm respectively. For this reason 500 nm would be optimum wavelength for monitoring RF sol – gel transitions. In comparison to other methods used for particle size determination, i.e. DLS, SAXS and microscopic techniques, this method is simple and rapid allowing sol samples to be analysed straight from the oven and for results to be obtained in a matter of minutes.

6 References

[1] Pekala RW, Kong FM. A SYNTHETIC ROUTE TO ORGANIC AEROGELS - MECHANISM, STRUCTURE, AND PROPERTIES. Journal De Physique. 1989 Apr 1989;50(C4):33-40.

[2] Pekala RW, Farmer JC, Alviso CT, Tran TD, Mayer ST, Miller JM, et al., editors. Carbon aerogels for electrochemical applications. 5th International Symposium on Aerogels; 1997 Sep 08-10 Apr; Montpellier, France1998.

[3] Fricke J, Tillotson T. Aerogels: production, characterization, and applications. Thin Solid Films. 1997 1997;297:212-23.

[4] Moreno-Castilla C, Maldonado-Hodar FJ. Carbon aerogels for catalysis applications: An overview. Carbon. 2005;43(3):455-65.

[5] D. W Schaefer, R. Pekala, Beaucage G. Origin of porosity in resorcinol-formaldehyde aerogels. Journal of Non-Crystalline Solids. 1995;186:159-67.

[6] Horikawa T, Hayashi J, Muroyama K. Controllability of pore characteristics of resorcinol-formaldehyde carbon aerogel. Carbon. 2004 2004;42(8-9):1625-33.

[7] Pekala RW, Kong FM. Resorcinol-formaldehyde aerogels and their carbonized derivatives. National meeting of the American Chemical Society. Dallas, Texas, USA1988. p. 15.

[8] Pekala RW, Schaefer DW. STRUCTURE OF ORGANIC AEROGELS .1. MORPHOLOGY AND SCALING. Macromolecules. 1993 Sep;26(20):5487-93.

[9] lee H-J, Song J-H, Kim J-H. Synthesis of resorcinol/formaldhyde gel particles by the sol-gel emulsion gel technique. Materials Letters. 1998;37:1998.

[10] Sharma CS, Kulkarni MM, Sharma A, Madou M. Synthesis of carbon xerogel particles and fractal-like structures. Chemical Engineering Science. 2009 Apr;64(7):1536-43.

[11] Bock V, Emmerling A, Fricke J. Influence of monomer and catalyst concentration on RF and carbon aerogel structure. Journal of Non-Crystalline Solids. 1998;225:69-73.

[12] Scherdel C, Scherb T, Reichenauer G. Spherical porous carbon particles derived from suspensions and sediments of resorcinol-formaldehyde particles. Carbon. 2009 Aug;47(9):2244-52.

[13] Bruce J, Berne J, Pecora R. Dynamic Light Scattering: With Applications to Chemistry, Biology and Physics. New York: Dover Publications; 2000.

[14] Brown W, editor. Dynamic Light Scattering The method and some applications. Oxford: Clarendon Press; 1993.

[15] Taylor S. DLS study of the formation of RF xerogels. 2012.

[16] Yamamoto T, Mukai SR, Endo A, Nakaiwa M, Tamon H. Interpretation of structure formation during the sol-gel transition of a resorcinol-formaldehyde solution by population balance. Journal of Colloid and Interface Science. 2003 Aug 15;264(2):532-7.

[17] Wang JB, Yang XQ, Wu DC, Fu RW, Dresselhaus MS, Dresselhaus G. The porous structures of activated carbon aerogels and their effects on electrochemical performance. Journal of Power Sources. 2008 Oct;185(1):589-94.

[18] Sepehri S, Garcia BB, Zhang QF, Cao GZ. Enhanced electrochemical and structural properties of carbon cryogels by surface chemistry alteration with boron and nitrogen. Carbon. 2009 May;47(6):1436-43.

[19] El Mir L, Kraiem S, Bengagi M, Elaloui E, Ouederni A, Alaya S. Synthesis and characterization of electrical conducting nanoporous carbon structures. Physica B-Condensed Matter. 2007 May;395(1-2):104-10.

[20] Berthon S, Barbieri O, Ehrburger-Dolle F, Geissler E, Achard P, Bley F, et al. DLS and SAXS investigations of organic gels and aerogels. Journal of Non-Crystalline Solids. 2001 Jun 1;285(1-3):154-61.

[21] Huber MM, Klein H, Ratke L. DLS-based fractal analysis in early stage gelation. Particle & Particle Systems Characterization. 2004 Feb;20(6):379-81.

[22] Yamamoto T, Yoshida T, Suzuki T, Mukai SR, Tamon H. Dynamic and static light scattering study on the sol-gel transition of resorcinol-formaldehyde aqueous solution. Journal of Colloid and Interface Science. 2002 Jan 15;245(2):391-6.

[23] Laboratory NP. http://www.kayelaby.npl.co.uk/chemistry/3_8/3_8_7.html. 2012 [September 2012].

[24] A.Mrzel, A.Mertelj, A. Omerzu, M. Cŷ opic, Mihailovic D. Investigation of Encapsulation and Solvatochromism of Fullerenes in Binary Solvent
Mixtures. J Phys Chem. 1999;B(103):11256-60.

[25] Haruhisa Kato, Ayako Nakamura, Kayori Takahashi, Kinugasa S. Size effect on UV-Vis absorption properties of colloidal C60 particles in water. Physical Chemistry Chemical Physics. 2009(11):4946–8.

[26] Harold Hart, Craine LE, David J. Hart, editors. Organic Chemistry - a short course. 11 ed. Boston, NY: Houghton Mifflin Company; 2003.

[27] J. M. Fu, Y. Li, J. L. Guo. Optical behavior of organic pigments in aqueous dispersions and its application. J Colloid Interface Sci. 1998;202(2):450 - 5.

[28] Goodner KL. www.sensusflavors.com, Turbidity, Tea, And UV-VIS. Ohio: Sensus Technical Note (SEN-TN-0008); 2008 [cited 2012 Sep].

[29] Goodner KL. www.sensusflavors.com, Estimating Turbidity (NTU) From Absorption Data. Sensus Technical Note (SEN-TN-0010); 2008 [cited 2012 Sep].

23.2 Published paper

Chemical Engineering Science 92 (2013) 13–20

Contents lists available at SciVerse ScienceDirect

Chemical Engineering Science

journal homepage: www.elsevier.com/locate/ces

Polysulfone mixed matrix gas separation hollow fibre membranes filled with polymer and carbon xerogels

V.M. Magueijo, L.G. Anderson, A.J. Fletcher, S.J. Shilton*

Department of Chemical and Process Engineering, University of Strathclyde, James Weir Building, 75 Montrose Street, Glasgow G1 1XJ, Scotland, United Kingdom

HIGHLIGHTS

- A novel range of porous xerogel nanoparticles has been synthesised.
- Mixed matrix hollow fibres for gas separation have been spun with xerogel fillers.
- Filler presence can improve membrane mechanical strength.
- Filler presence can improve gas transmission and separation properties.

GRAPHICAL ABSTRACT

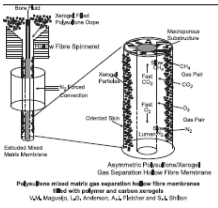

ARTICLE INFO

Article history:
Received 10 September 2012
Received in revised form
14 January 2013
Accepted 18 January 2013
Available online 29 January 2013

Keywords:
Mixed matrix membranes
Hollow fibres
Fibre spinning
Xerogels
Porosity
Gas separation

ABSTRACT

This work involves the preparation, tensile testing and gas separation characterization of polysulfone mixed matrix hollow fibres filled with polymeric sol based, and subsequently carbonised, xerogels. The pore characteristics of the xerogels were determined using a surface area and porosity analyser. The xerogel materials were reduced to submicron particles by grinding and wet milling, and the resultant particle size was determined using dynamic light scattering. Using dry/wet forced convection spinning, mixed matrix hollow fibre membranes (MMMs) were spun from solutions of polysulfone loaded with the submicron xerogel particles. At 5% loading, all MMMs exhibited higher strain at break and higher strength than unfilled membranes. Compared to unfilled fibres, MMMs were stiffer when filled with hard xerogel inclusions but became more pliable when filled with soft xerogel particles. Knudsen diffusion becomes an important gas transport mechanism in the membranes filled with mesoporous xerogels. When compared to the unfilled hollow fibres, these membranes showed a strong increase in the permeation of low molecular weight, high kinetic diameter gases, leading to a decline in fast/slow gas selectivities. All types of MMM gave higher CO_2/O_2 (fast/fast) and CH_4/N_2 (slow/slow) selectivities than unfilled hollow fibres. The MMMs filled with a microporous xerogel gave a higher CO_2 pressure normalized flux when compared to the unfilled fibres without sacrificing the CO_2/CH_4 selectivity. Future work should focus on the tailoring of the pore size of the xerogels and on the wet milling procedure to obtain smaller filler particles.

1. Introduction

Robeson (1991) showed the existence of a trade-off between gas permeability coefficient and selectivity for polymeric membranes. He obtained, for a range of gas pairs, an 'upper bound' plot which showed the highest selectivity that could be expected for a polymer with a particular permeability coefficient. A recent revision has concluded that, for many gas pairs, the position of the 'upper bound' has experienced only minor shifts (Robeson, 2008).

Mixed matrix membranes represent an advance in membrane technology capable of improving the gas separation performance of polymeric membranes and surpassing the Robeson 'upper bound'. Since the early work by Paul and Kemp (1973), a vast amount of

* Corresponding author. Tel.: +44 141 548 2380; fax: +44 141 552 2302.
E-mail address: simon.shilton@strath.ac.uk (S.J. Shilton).

0009-2509/$ - see front matter © 2013 Elsevier Ltd. All rights reserved.
http://dx.doi.org/10.1016/j.ces.2013.01.043

literature on mixed matrix membranes has been published and the recent review papers by Aroon et al. (2010) and Chung et al. (2007) both present an excellent outline of important developments in this research field.

A mixed matrix membrane (MMM) consists of a continuous polymeric matrix filled with dispersed particulate inclusions (also known as *fillers*), such as zeolites, silica, carbon nanotubes (Aroon et al., 2010), and metal organic frameworks (MOFs) (Zornoza et al., 2013; Jeazet et al., 2012). Although the particulate inclusions can be porous or non-porous, the majority of MMMs contains porous particles. The effect of porous particles on the mechanical and gas separation characteristics of the MMM will depend on such properties as the size, composition, porous structure and surface chemistry of the particles. Regarding gas separation, while in dense polymeric membranes it is determined by the solution–diffusion transport mechanism, in MMMs filled with porous particles, other transport mechanisms are present and these contribute to the gas separation performance. The transport mechanism is strongly dependent on the pore size of the particles. In general, molecular sieving and/or surface diffusion are the dominating mechanisms when pore sizes are smaller than 2 nm (micropores), Knudsen diffusion dominates when pore sizes are between 2 nm and 50 nm (mesopores), and above 50 nm (macropores), viscous flow is the controlling mechanism (Yoshimune and Haraya, 2011).

Despite polymer-filler adhesion challenges, glassy polymers tend to be more suitable for the preparation of MMMs than more permeable but less selective rubbery polymers (Aroon et al., 2010). Polysulfone is a spinnable glassy polymer and a long-standing material of choice for the preparation of mixed matrix hollow fibre membranes (Zimmerman et al., 1997). The group at Strathclyde has studied forced convection spinning of gas separation hollow fibre membranes for various polymer systems (Jones et al., 2011), including polysulfone (Gordeyev and Shilton, 2004; Ismail et al., 1999, 1997; Sharpe et al., 1999), and has extended this work into the development of MMMs (Bhardwaj et al., 2003; Gordeyev et al., 2001).

Resorcinol-formaldehyde (RF) xerogels/aerogels and their carbon derived gels were first synthesized by Pekala and Alviso (1992). In the past two decades, these materials have received considerable attention due to their tuneable properties, with particular focus on the control of the surface area, pore volume and pore size distribution via the careful manipulation of the synthesis and processing conditions (Al-Muhtaseb and Ritter, 2003; Job et al., 2004; Tao et al., 2008). Their flexible production and functionalization renders these nanoporous materials not only suitable for applications such as adsorption (Yamamoto et al., 2004) and catalysis (Job et al., 2006), but also for membrane gas separation (Yoshimune et al., 2008; Qin et al., 2010; Zhang et al., 2008).

In the work reported here, asymmetric polysulfone hollow fibre membranes were filled with submicron particles of xerogels derived from the polycondensation of resorcinol (R) and formaldehyde (F) in aqueous media. Three different xerogels with distinct pore properties were used and their effect on the gas permeation performance of the membranes was analysed. Zhang et al. (2008) prepared mixed matrix flat sheet membranes containing an RF carbon xerogel and used them for gas separation; however, to the knowledge of the authors, the present work represents the first journal paper to report the preparation and gas separation performance of mixed matrix hollow fibres filled with this type of material.

2. Experimental

The experimental work involved the following steps: (a) synthesis and characterization of RF xerogels with tailored pore properties; (b) wet milling of the xerogels and particle size characterization of the resulting dispersions; (c) preparation of polymeric spinning dopes with and without xerogel particles; (d) dry/wet spinning of the polymeric dopes to obtain filled and unfilled hollow fibre membranes; and (e) tensile characterization and gas permeation testing of the produced membranes.

2.1. Synthesis and characterization of the polymer and carbon xerogels

Three xerogel types with different target pore characteristics were prepared (Pekala and Alviso, 1992). The corresponding synthesis conditions are presented in Table 1. The xerogels were prepared from the sol–gel polymerisation of resorcinol (R) and formaldehyde (F) in an aqueous solution using either sodium carbonate (Na_2CO_3) or ammonium carbonate ($(NH_4)_2CO_3$) as a catalyst (C). A stoichiometric *R*/*F* ratio of 0.5 was utilised with the molar ratio of *R*/*C* fixed at 300 for Na_2CO_3 and 75 for $(NH_4)_2CO_3$. Twenty percent w/v sols were prepared by mixing the required amounts of R (Sigma Aldrich reagent plus 99%), F (Sigma Aldrich 37 wt% formaldehyde solution in H_2O with 10–15% methanol as stabiliser), C (Sigma Aldrich ACS anhydrous) and distilled H_2O whilst stirring for approximately 45 min. The solutions were gelled and cured for three days at 85 ± 5 °C. The water within the gels was then removed by solvent exchange by submerging the gels in an agitated acetone solution for three to four days. Following the solvent exchange, the gels were dried in a vacuum oven at 70 ± 5 °C for two days to form the dried xerogels. Carbon xerogels were prepared by pyrolysing subsamples of the dried xerogels in a 200 $cm^3\,min^{-1}$ flow of argon at 900 °C with a hold time of 2 h and a heating rate of 20 °C min^{-1}.

Representative samples were outgassed at 110 °C for 16 h at vacuum and nitrogen isotherms of the three xerogel types were measured at −196 °C with an ASAP 24:20 surface area and porosity analyser (Micromeritics). The BET equation was used to calculate the specific surface area, and BJH and t-plot methods were used for mesopore and micropore analysis. Using the desorption isotherm, the BJH method was applied to obtain the pore size distributions, while the total pore volume was determined as the volume of N_2 adsorbed at saturation point.

2.2. Preparation of the mixed matrix hollow fibre membranes

2.2.1. Preparation of the spinning dopes

The unfilled dope was prepared according to the procedure described in Fig. 1(A) while the filled dopes were prepared by incorporating the xerogel particles into the standard unfilled dope composition according to the procedure described in Fig. 1(B). Four different filled dopes were prepared to produce membranes with a RFX loading of 5% w/w, CX loadings of 5% w/w and 10% w/w, and

Table 1
Conditions employed in the synthesis of the xerogels.

Xerogel	Catalyst	*R*/*F* ratio	*R*/*C* ratio	Drying	Pyrolysis	Target pore characteristics
Resorcinol-formaldehyde Xerogel (**RFX**)	Na_2CO_3	0.5	300	Yes	No	Mesoporous
Carbon xerogel (**CX**)	Na_2CO_3	0.5	300	Yes	Yes	Meso and microporous
Microporous carbon xerogel (**μCX**)	$(NH_4)_2CO_3$	0.5	75	Yes	Yes	Microporous

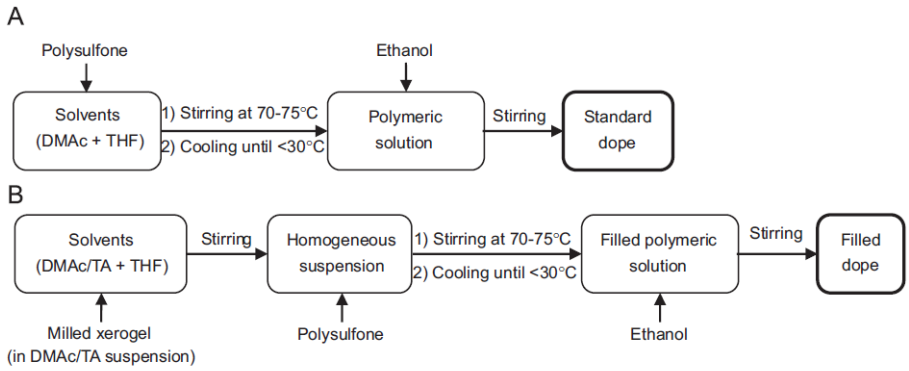

Fig. 1. Experimental procedure for the preparation of unfilled (A) and filled (B) dopes.

Table 2
Composition of the prepared dopes.

	Prepared dope				
	Unfilled	RFX_5	CX_5	CX_{10}	μCX_5
Polysulfone (g)	22	22	22	22	22
N,N-dimethylacetamide (g)	32	32	32	32	32
Tetrahydrofuran (g)	32	32	32	32	32
Ethanol (g)	14	14	14	14	14
Xerogel (g)	0	1.16	1.16	2.44	1.16
Filler loading (% w/w)	0	5	5	10	5

a μCX loading of 5% w/w. The filler loading in the membranes is defined as follows:filler loading (% w/w)=(weight of xerogel/(weight of polysulfone+xerogel)) × 100

The filled dopes and the resultant mixed matrix membranes will henceforth be designated by abbreviations containing the acronym of the xerogel used and a numeric subscript at the end that specifies the filler loading. For example, RFX_5 designates a dope or membrane filled with RF xerogel at a filler loading of 5% w/w. Table 2 follows this nomenclature and presents the mass composition of all prepared dopes.

2.2.1.1. Unfilled dope. The unfilled dope was prepared by dissolving polysulfone (Udel P1700 from Amoco, M_w=35,400) in a solvent/non-solvent mixture according to the following composition: 22% w/w polysulfone, 32% w/w *N,N*-dimethylacetamide (DMAc, ≥99.9% w/w), 32% w/w tetrahydrofuran (THF, ≥99.9% w/w) and 14% w/w ethanol (≥99.5% w/w). All chemicals were supplied by Sigma Aldrich unless otherwise stated. Polysulfone was first dissolved in DMAc+THF by stirring under total reflux at 70–75 °C until a clear solution was obtained. Under constant stirring, the mixture was then cooled to a temperature below 30 °C followed by the addition of the non-solvent (ethanol).

2.2.1.2. Filled dopes. Prior to the preparation of each filled dope, the corresponding xerogel was reduced to submicron particles through a two stage comminution procedure involving pre-grinding and wet milling. The xerogel was first ground with a mortar and a pestle until a particle size smaller than 1 mm was obtained. The resultant powder was dried at 120 °C for 12 h. The necessary weight of pre-ground xerogel was then added to a solution of 0.1% w/w tannic acid (TA) (dispersant, Acros Organics) in DMAc. The resulting dispersion was sonicated for 10 min and transferred to a Fritsch Pulverisette 6 planetary ball mill where the pre-ground xerogel was wet milled for 12 h at 400 rpm using zirconium dioxide spheres with nominal diameter of 5 mm. After milling, the finely ground xerogel dispersion was sonicated for 10 min, diluted in 0.1% w/w tannic acid in DMAc, analysed by dynamic light scattering (DLS) and then immediately used to prepare the corresponding filled dope.

2.2.2. Spinning of the filled and unfilled dopes

The unfilled and filled polymeric dopes were spun to produce asymmetric hollow fibre membranes for gas separation. The membranes were produced via a dry/wet spinning process with forced convection in the dry gap, using the spinning apparatus schematically illustrated in Fig. 2. During spinning, the dope reservoir was kept at ambient temperature and, in the case of filled dopes, under constant magnetic stirring. The dopes were filtered through a 150 μm inline filter (Nupro) and extruded at a constant dope extrusion rate of 2.5 $cm^3\ min^{-1}$ through a spinneret with *OD*=635 μm and *ID*=229 μm. A 20% w/w aqueous solution of potassium acetate was used as the bore coagulant liquid and, using an HPLC pump, fed to the spinneret at a constant flow rate of 0.8 $cm^3\ min^{-1}$.

After extrusion from the spinneret, the fibre passed through a cylindrical forced convection chamber (diameter=5 cm, height=4.5 cm) which was flushed with 4 L min^{-1} of nitrogen gas. The nitrogen was fed in a cross-flow mode (nitrogen flow normal to the membrane surface). Water at room temperature was used in all external coagulation baths and the jet stretch ratio of the fibres (wind up speed/extrusion speed) was kept constant at 1. After spinning, the hollow fibre membranes underwent a solvent exchange drying process: first they were immersed in deionised water for 2 days, then kept in a methanol bath for 1 day, and finally, left to dry at ambient conditions.

2.3. Tensile characterization of the spun fibres

The tensile properties of the hollow fibres were measured on an Instron 1122 Materials Testing Instrument operating at a full scale load of 5 N. For each type of fibre, 10 to 15 samples with 30 mm gauge length were drawn at room temperature until fibre breakage. The drawing speed was constant and equal to 20 mm min^{-1}.

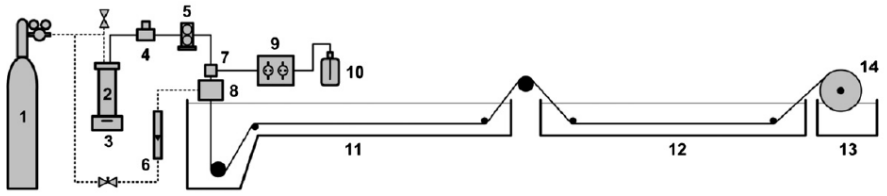

Fig. 2. Spinning apparatus used to prepare the asymmetric hollow fibre membranes for gas separation.

2.4. Electron microscopy

The hollow fibres were cut and mounted on sample stubs. They were then sputter-coated with gold before being viewed with the electron microscope (HITACHI SU-6600 field emission scanning electron microscope).

2.5. Gas permeation measurements

The hollow fibre membranes were potted into single fibre modules and tested with pure gases before and after coating with a 3% w/w silicone (PDMS) (Sylgard 184, Dow Corning) solution in hexane (*n*-hexane, ≥96.5% w/w, Sigma-Aldrich). Coating with silicone is a standard procedure used to repair small defects or pores that exist in the membrane active layer (Henis and Tripodi, 1980; Ward et al., 1980). The pressure normalized flux of each fibre was measured for oxygen, nitrogen, methane and carbon dioxide at ambient temperature and at a transmembrane pressure (ΔP) of 5 bar. For each fibre, the pair gas selectivities were determined by taking the ratio of the pressure-normalized fluxes.

3. Results and discussion

3.1. Morphology and pore characteristics of the polymer and carbon xerogels

The morphological properties and bulk densities of the synthesized xerogels are presented in Table 3. Both RFX and the subsequent pyrolysed CX were obtained in the form of hard particles. Due to their hardness, these large chunks were difficult to grind with a mortar and pestle. On the other hand, the preparation of μCX yielded a soft material, a friable powder. The difference in the form and hardness of the xerogels seems to be related to the type or amount of catalyst used (see Table 1). Note that while RFX and CX where both prepared with Na_2CO_3 as catalyst and an *R*/*C* ratio of 300, μCX was prepared with a different catalyst and *R*/*C* ratio ($(NH_4)_2CO_3$ and 75, respectively). In terms of the measured bulk densities, the three xerogels exhibited very different values. The pyrolysis of RFX to give CX increases considerably the bulk density of the xerogel, while the route involving ammonium carbonate as catalyst produced μCX, a much lighter material.

The pore characteristics of the xerogels were determined using a surface area and porosity analyser. Results are given in Table 4, where S_{BET} is the surface area, Dp_{av} is the average pore size, and V_{mic}, V_{mes} and V_{tot} are the microporous (<2 nm), mesoporous (2–50 nm) and total specific volumes, respectively. According to Table 1, each xerogel was intended to have different pore characteristics, and

Table 3
Morphology and bulk density of the prepared xerogels.

Xerogel	Form	Hardness	Measured bulk density (g/cm^3)
RFX	Dark brown monoliths	Hard	1.083
CX	Black monoliths	Hard	1.769
μCX	Black powder	Soft	0.805

Table 4
Pore characteristics of the xerogels.

Xerogel	S_{BET} (m^2/g)	V_{tot} (cm^3/g)	V_{mic} (cm^3/g)	V_{mes} (cm^3/g)	Ratio V_{mic}/V_{tot}	Dp_{av} (nm)
RFX	388.5 ± 2.8	0.6154	0.0196	0.5958	0.032	6.42
CX	566.1 ± 9.0	0.5500	0.1574	0.3926	0.286	5.17
μCX	463.1 ± 12.6	0.2485	0.2258	0.0227	0.909	0.66

± Values in table are standard deviations.

Table 4 shows that this was obtained. RFX exhibited almost complete mesoporosity, with only 3.2% v/v of its total specific volume within the microporous range, and had a measured average pore diameter of 6.42 nm. As expected, pyrolysis increases the surface area and microporosity of the xerogel thus reducing the average pore size. Indeed, when compared with the non-pyrolysed RFX, the pyrolysed CX exhibited a larger surface area and a marked increase in the microporous volume (V_{mic} 8 times higher). Despite this sharp increase in microporosity, only 28.6% v/v of the total specific volume of CX corresponds to micropores. Hence, although CX exhibited a mix of meso- and microporosity, the measured average pore diameter was 5.17 nm, still well within the mesoporous range. In opposition to RFX, μCX displayed almost complete microporosity with 90.9% v/v of its total specific volume within the microporous range. Perhaps because the preparation of μCX followed a different synthesis route, this xerogel yielded a much lower value of V_{tot} when compared with both RFX and CX. Therefore, although μCX was essentially microporous, which is always advantageous for gas separation purposes, it was not as porous as the other xerogels (disadvantage). Lack of porosity represents fewer potential pathways for gas transmission.

3.2. Particle size of the xerogels after wet milling

The preparation of the filled dopes involved the preliminary wet milling of the xerogels to obtain dispersions of submicron particles. The wet milling step is of crucial importance because the presence of large particles or aggregates of particles in the

spinning dopes will produce membranes with defective active layers. Immediately after wet milling, the dispersions of fine xerogel particles were diluted and analysed by dynamic light scattering. The DLS results are shown in Fig. 3, in the form of the measured normalized intensity autocorrelation functions of the scattered light. After wet milling, the dispersions of particles were immediately used to prepare the filled dopes, hence, in Fig. 3, each autocorrelation curves is labelled according to the ensuing filled dope.

The steady monotonic decay of the autocorrelation functions from 1 to values close to 0 indicates that the xerogel dispersions had insignificant levels of aggregates and were essentially monodisperse. On close inspection, only the autocorrelation function for CX_5 displays a very small second decay for lag times above 2×10^{-3} s which is indicative of a minute population of aggregates. Therefore, it is reasonable to conclude that the comminution procedure was effective in reducing the large xerogel particles to discrete submicron particles. The average hydrodynamic radii of the obtained xerogel dispersions were measured by the DLS software via cumulant analysis and varied between 134.6 nm and 211.8 nm (Fig. 3, inset). Differences in hydrodynamic radii between the inclusion types may be due to final particle shape (isotropic/plate-like), or efficacy of milling due to differences in particle brittleness (hardness).

3.3. Tensile properties of the membranes

Fibre behaviour under tensile stress has been standardised with respect to fibre linear density or weight per unit length (units: g/km or tex), as opposed to cross sectional area. In this way performance relates to the properties of the solid matrix within the fibre regardless of porosity (Shilton et al., 1994). The tensile curves obtained for the fabricated membranes are presented in Fig. 4. From their analysis, the following tensile properties were quantified and are shown in Table 5: (a) strain at break; (b) fibre strength (*i.e.* tenacity)=specific stress at break; and (c) elastic modulus (*i.e.* Young's modulus)=slope of stress-strain curve before yield point.

All membranes with 5% w/w filler loading (RFX_5, CX_5 and μCX_5) showed higher values of strain at break and tenacity than

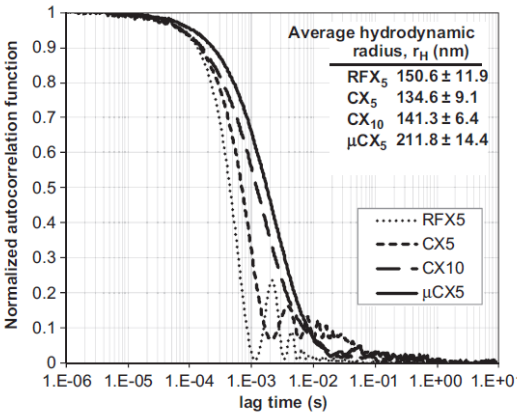

Fig. 3. DLS results for the dispersions of fine xerogel particles used to prepare filled dopes: curves represent the normalized autocorrelation functions for diluted xerogel dispersions in DMAc+0.1% tannic acid. Inset: average hydrodynamic radius of the particles calculated using cumulant analysis (±values are standard deviations).

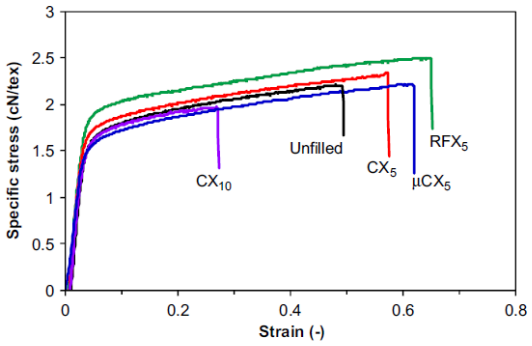

Fig. 4. Tensile curves obtained for the fabricated hollow fibre membranes.

Table 5
Tensile properties of the hollow fibre membranes.

Membrane type	Linear density (tex)	Strain at break (%)	Tenacity (cN/tex)	Young's modulus (cN/tex)
Unfilled	59.5 ± 0.7	47.3 ± 2.8	2.21 ± 0.03	70.7 ± 1.4
RFX_5	60.5 ± 0.8	66.3 ± 4.3	2.50 ± 0.05	74.9 ± 1.5
CX_5	55.7 ± 0.9	58.3 ± 4.5	2.33 ± 0.05	76.7 ± 1.5
CX_{10}	60.7 ± 1.8	28.3 ± 2.3	1.98 ± 0.07	73.1 ± 1.4
μCX_5	54.1 ± 0.6	62.3 ± 4.9	2.26 ± 0.08	62.3 ± 1.6

±Values in table are standard deviations.

the unfilled membranes. The experimental data indicates that, independently of the xerogel used, the filled membranes become tougher than the unfilled ones when a 5% w/w filler loading is used. Having in mind that the toughness of a fibre is defined as the area below the stress–strain curve, the toughening effect can be easily seen in sure 4. Similarly, Fig. 4 clearly illustrates a sharp decline in toughness when a filler loading of 10% w/w was used. Indeed, the values of strain at break and tenacity obtained for CX_{10} were well below the ones obtained for the unfilled membranes (Table 5). A possible explanation for CX_{10} being less tough/more brittle is that a higher filler loading might lead to the formation of more (or larger) defects in the membrane structure.

Regarding the Young's modulus, which is a measure of the stiffness of a fibre in the elastic region, the results can be interpreted in terms of the type of filler used. Table 5 shows that, in comparison with the unfilled fibres, the Young's modulus increases when the RFX and CX xerogels are used as fillers, while the opposite occurs when μCX is used. According to Table 3, both RFX and CX are hard fillers while μCX is soft; hence, there is a connection between the stiffness of the membrane with the morphology of the filler used. This relationship suggests that the inclusions themselves play an important role in determining stiffness and hence there is a good interfacial adhesion between the xerogel particles and the polymeric matrix in the MMMs.

3.4. Electron microscopy

Images of the cross sections of the MMMs are provided in Fig. 5 to give a visual impression of the morphologies of the composite materials. Further outer wall shots are given for the best performing MMM type (μCX_5) in Fig. 6. The high magnification ($\times$10,000) outer wall image is suggestive of a membrane surface free from filler protrusions. The μCX_5 particle diameter is around 400 nm and hence any eruption points would be seen if they were present.

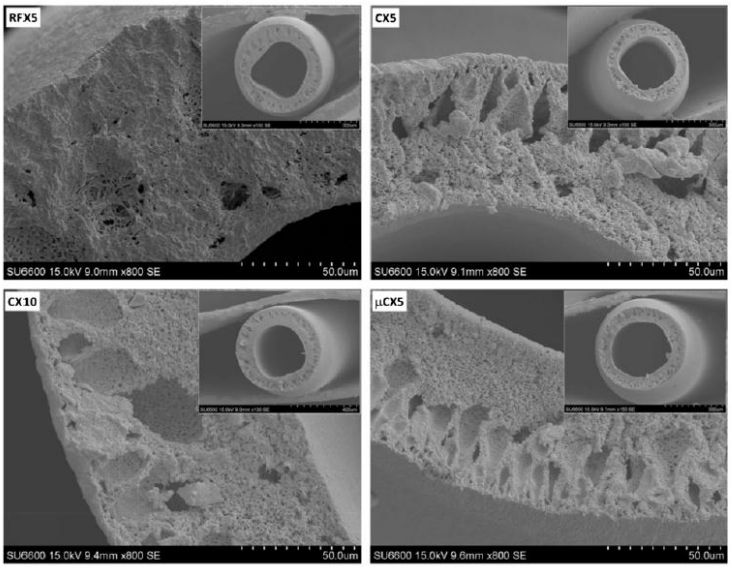

Fig. 5. Cross-section SEM images of the filled hollow fibre membranes. Larger image: detail; inset: full cross section.

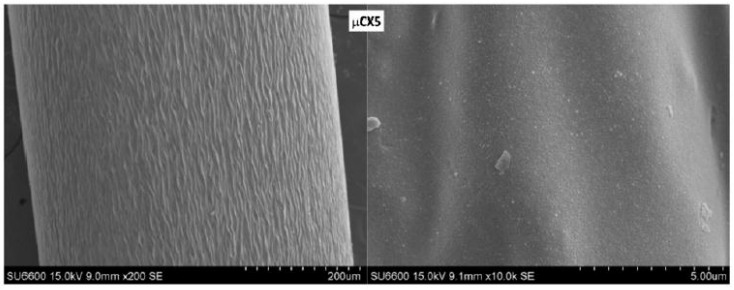

Fig. 6. Outer surface SEM images of membrane μCX5 at low (× 200) and high (× 10 k) magnifications.

3.5. Gas permeation results for mixed matrix hollow fibre membranes filled with submicron xerogel particles

The filled and unfilled hollow fibre membranes were tested with pure gases before and after coating. The pressure normalized fluxes and selectivities of the uncoated membranes are presented in Table 6. As would be expected, fluxes are high and selectivities low, indicative of defective active layers and Knudsen diffusion as the mechanism of gas transmission. The RFX_5 filled fibres exhibit the greatest fluxes and lowest selectivities suggesting the highest levels of defects in these uncoated membranes.

The pressure normalized fluxes and selectivities of the coated membranes are presented in Table 7. Coating repairs the active layer defects and markedly reduces fluxes and increases selectivity to solution diffusion levels. As seen from the pressure normalised fluxes, carbon dioxide and oxygen are now favoured compared to the 'slower' and larger kinetic diameter gases, namely methane and nitrogen.

The presence of fillers does not have a strong effect on the transmission of the fast, low kinetic diameter, solution diffusion dependent gases, namely carbon dioxide and oxygen. Pressure normalised fluxes for these gases are consistent across all membrane types, including unfilled. This suggests that defects are not playing a significant role in the behaviour of the mixed matrix membranes. On the other hand, the larger kinetic diameter, but lower molecular weight, penetrants such as methane and nitrogen are strongly affected by inclusions, as these gases take greater advantage of Knudsen diffusion opportunities, either through the pores within the xerogel particles, or through any fissures between the particles and the surrounding polymer material. Fast/fast selectivities *i.e.*, CO_2/O_2 and slow/slow selectivities *i.e.*, CH_4/N_2, are consistent across all membrane types—the transmission of fast gases does not rely on the pores offered by the filler particles, and the slow gases take equal opportunity of those pores. In contrast, the fast/slow selectivities *i.e.*, CO_2/CH_4 and O_2/N_2, vary significantly with filler presence, the greater the Knudsen diffusion opportunity for the slow low molecular weight gases, the greater the depression of selectivity.

In Table 7, the membranes CX_5 and CX_{10} exhibit similar pressure normalised fluxes for any particular gas. If filler induced defects

Table 6
Gas permeation results for uncoated hollow fibre membranes.

Membrane	Pressure normalized fluxes (GPU)				Selectivities			
	P_{CH_4}	P_{N_2}	P_{O_2}	P_{CO_2}	P_{O_2}/P_{N_2} (fast/slow)	P_{CO_2}/P_{CH_4} (fast/slow)	P_{CO_2}/P_{O_2} (fast/fast)	P_{CH_4}/P_{N_2} (slow/slow)
Unfilled	185 ± 37	134 ± 29	135 ± 28	187 ± 27	1.00 ± 0.03	1.02 ± 0.07	1.40 ± 0.09	1.38 ± 0.04
RFX_5	450 ± 203	322 ± 149	309 ± 132	353 ± 123	0.98 ± 0.07	0.83 ± 0.13	1.18 ± 0.12	1.41 ± 0.04
CX_5	219 ± 27	156 ± 21	175 ± 20	262 ± 16	1.13 ± 0.02	1.20 ± 0.08	1.50 ± 0.09	1.41 ± 0.02
CX_{10}	255 ± 20	180 ± 14	184 ± 12	263 ± 11	1.02 ± 0.02	1.03 ± 0.06	1.43 ± 0.06	1.41 ± 0.03
μCX_5	405 ± 68	293 ± 49	280 ± 35	365 ± 31	0.96 ± 0.05	0.91 ± 0.08	1.31 ± 0.06	1.38 ± 0.004

1 GPU = 10^{-6} [cm^3(STP) s^{-1} cm^{-2} $cmHg^{-1}$]; ± values in table are standard deviations.
The pressure-normalized flux and selectivity values are the average of several modules tested. The selectivities do not equate to the ratio of the pressure-normalized fluxes in the table because of a mathematical quirk: the average of the selectivities of the modules tested in each membrane category does not equal the ratio of the average pressure-normalized fluxes.

Table 7
Gas permeation results for coated hollow fibre membranes.

Membrane	Pressure normalized fluxes (GPU)				Selectivities			
	P_{CH_4}	P_{N_2}	P_{O_2}	P_{CO_2}	P_{O_2}/P_{N_2} (fast/slow)	P_{CO_2}/P_{CH_4} (fast/slow)	P_{CO_2}/P_{O_2} (fast/fast)	P_{CH_4}/P_{N_2} (slow/slow)
Unfilled	2.11 ± 0.13	1.95 ± 0.22	15.0 ± 0.7	84.9 ± 5.3	8.35 ± 0.29	40.3 ± 3.4	5.49 ± 0.47	1.09 ± 0.10
RFX_5	5.05 ± 2.20	4.33 ± 1.79	14.5 ± 2.8	80.4 ± 10.2	3.89 ± 1.01	18.6 ± 8.0	5.69 ± 0.52	1.30 ± 0.06
CX_5	3.88 ± 1.06	3.31 ± 0.52	17.8 ± 1.3	103.3 ± 7.5	5.95 ± 0.46	32.7 ± 3.8	6.06 ± 0.33	1.18 ± 0.12
CX_{10}	3.78 ± 0.58	3.28 ± 0.43	16.5 ± 0.8	93.5 ± 6.6	5.08 ± 0.58	25.2 ± 4.7	5.67 ± 0.29	1.15 ± 0.03
μCX_5	2.45 ± 0.31	2.19 ± 0.25	15.3 ± 1.1	95.4 ± 5.1	7.03 ± 0.71	39.1 ± 2.0	6.20 ± 0.11	1.16 ± 0.05

1 GPU = 10^{-6} [cm^3(STP) s^{-1} cm^{-2} $cmHg^{-1}$]; ± values in table are standard deviations.
The pressure-normalized flux and selectivity values are the average of several modules tested. The selectivities do not equate to the ratio of the pressure-normalized fluxes in the table because of a mathematical quirk: the average of the selectivities of the modules tested in each membrane category does not equal the ratio of the average pressure-normalized fluxes.

Table 8
Filler inter-particle spacing and size of a polymer molecule.

Membrane Type	Filler particle diameter (nm)	Number of particles per m^3	Inter-particle spacing (nm)	Size of a polysulfone molecule (nm)
RFX_5	301.2	4.03×10^{18}	628	71.6*
CX_5	269.2	3.38×10^{18}	666	
CX_{10}	282.6	6.10×10^{18}	547	
μCX_5	423.6	1.83×10^{18}	817	

* Knowing the molecular weight of the membrane polymer (M_w = 35,400) and the weight (M_{ws} = 442) and approximate length (X_s = 80 Å) of each repeating unit in the macromolecular chain, the size of the polysulfone molecules can be estimated (Strobl, 1997): $X_{polymer} = X_s(M_w/M_{ws})^{1/2}$.

were at play, then higher fluxes would be expected from the CX_{10} membranes due to the greater number of filler particles, but this is not the case. The 'fast/slow' selectivities of the CX_5 membranes are somewhat higher than those for CX_{10}. The lower prevalence of inclusions in the CX_5 membranes, as reflected in the inter-particle spacings (Table 8) calculated from a method described by Bhardwaj et al. (2003), would allow a greater proportion of the gas transmission to be solution diffusion through the polymer rather than flow through the pore network of the filler. The procedure to calculate inter-particle spacing can be found in Appendix A.

The lowest coated selectivities are found in the RFX_5 filled fibres. This is not surprising given the lack of microporosity, prevalence of mesopores, and hence large pore sizes in the RFX inclusions (Table 4). This would increase the flow of the low molecular weight Knudsen dependent, *i.e.* 'slow' (with respect to solution diffusion) penetrants through these samples. The fact that 'fast/slow' gas selectivities are higher for the CX_{10} filled fibres than for the lower loaded RFX_5 fibres, demonstrates an interesting interplay between alternative routes for gas transmission through MMMs. A greater presence of inclusions containing more micropores is more favourable in a gas separation MMM than a lower presence of inclusions containing more mesopores. This confirms the favourability of sub-Knudsen micropores over larger mesopores (which would be true even if loading levels were the same) but also indicates good filler/polymer adhesion. If filler induced imperfections were significant here, increased Knudsen flow, and hence lower 'fast/slow' selectivities, would prevail in the higher loaded CX samples.

In general, the coated pressure normalised fluxes for the μCX_5 MMMs are similar to those of unfilled hollow fibres. This would be expected as the μCX inclusions are highly microporous and hence suppress Knudsen diffusion compared to their mesoporous counterparts (Table 4). It is interesting that the μCX_5 membranes give a high carbon dioxide pressure normalised flux compared to unfilled fibres with almost the same CO_2/CH_4 selectivity. Strikingly, all four MMM types give higher CO_2/O_2 (fast/fast) and CH_4/N_2 (slow/slow) selectivities than unfilled hollow fibres. The μCX_5 hollow fibres give the highest CO_2/O_2 (fast/fast) selectivity.

4. Conclusions and recommendations

With regard to mechanical properties, at 5% w/w loading, all MMMs have higher strain at break and higher strength (tenacity) than unfilled membranes. Compared to unfilled fibres, MMMs are stiffer when filled with hard xerogel inclusions but become more pliable when filled with soft xerogel particles.

As expected, Knudsen diffusion becomes an important gas transport mechanism in the membranes filled with mesoporous xerogels (xerogels where mesoporosity dominates). When compared to the unfilled membranes, these membranes showed a strong increase in the permeation of gases with high kinetic diameter and low

molecular weight ("slow gases" in the unfilled membrane), leading to a decline in the "fast/slow" gas selectivities.

A very interesting result was that all four types of MMM gave higher CO_2/O_2 (fast/fast) and CH_4/N_2 (slow/slow) selectivities than unfilled hollow fibres. Most importantly, the mixed matrix membranes filled with a microporous xerogel gave a higher CO_2 pressure normalized flux when compared to the unfilled fibres without sacrificing the CO_2/CH_4 selectivity.

To improve further the gas separation performance of MMMs membranes filled with RF based xerogels, future work must focus on the tailoring of the pore size of the xerogels and on the wet milling procedure to obtain smaller filler particles.

Acknowledgements

The authors wish to thank Dr Nadeem Javid (Department of Pure and Applied Chemistry, University of Strathclyde) for the DLS analysis of the xerogel suspensions, and Mr Christophe Petit and Professor Shanwen Tao (Department of Chemical and Process Engineering, University of Strathclyde) for the use of the planetary ball mill. The authors also wish to thank Dr Nicholas Hudson and Mr James Morrow (Department of Pure and Applied Chemistry, University of Strathclyde) for the use of the Instron machine.

Appendix A. Filler inter-particle spacing

Given the weight fraction of filler in the membrane, C_{filler}, the filler particle weight, $M_{particle}$, and the densities of both the polymer, $\rho_{polymer}$, and filler, ρ_{filler}, the number of filler particles per unit volume of polymer matrix and, hence, an inter-particle spacing, assuming uniform dispersion, can be calculated using geometry.

Density of polymer/filler composite:

$$\rho_{comp} = \rho_{filler}\rho_{polymer}/[\rho_{polymer}C_{filler} + \rho_{filler}(1 - C_{filler})]$$

Number of particles per unit volume of composite material:

$$n_{particle} = \rho_{comp}C_{filler}/M_{particle}$$

Inter-particle spacing for isotropic fillers:

$$X_{p-p,i} = (n_{particle})^{-1/3}$$

The inter-particle spacing can then be compared to the diameter of the filler particle in order to gauge the proximity of the inclusions in the polymer.

References

Al-Muhtaseb, S.A., Ritter, J.A., 2003. Preparation and properties of resorcinol formaldehyde organic and carbon gels. Adv. Mater. 15, 101–114.
Aroon, M.A., Ismail, A.F., Matsuura, T., Montazer-Rahmati, M.M., 2010. Performance studies of mixed matrix membranes for gas separation: a review. Sep. Purif. Technol. 75, 229–242.
Bhardwaj, V., Macintosh, A., Sharpe, I.D., Gordeyev, S.A., Shilton, S.J., 2003. Polysulfone hollow fibre gas separation membranes filled with sub-micron particles. Ann. N.Y. Acad. Sci. 984, 318–328.
Chung, T.-S., Jiang, L.Y., Lia, Y., Kulprathipanja, S., 2007. Mixed matrix membranes (MMMs) comprising organic polymers with dispersed inorganic fillers for gas separation. Prog. Polym. Sci. 32, 483–507.
Gordeyev, S.A., Shilton, S.J., 2004. Forced convection spinning of gas separation hollow fibre membranes: some underlying factors, mechanisms and effects. J. Membr. Sci. 229, 225–233.
Gordeyev, S.A., Sharpe, I.D., Shilton, S.J., 2001. Processing and properties of polysulfone hollow fibre membranes for gas separation filled with sub-micron carbon fibres. Macromol. Symp. 170, 273–281.
Henis, J.M.S., Tripodi, M.K., 1980. A novel-approach to gas separations using composite hollow fibre membranes. Sep. Sci. Technol 15, 1059–1068.
Ismail, A.F., Dunkin, I.R., Gallivan, S.L., Shilton, S.J., 1999. Production of super selective polysulfone hollow fiber membranes for gas separation. Polymer 40, 6499–6506.
Ismail, A.F., Shilton, S.J., Dunkin, I.R., Gallivan, S.L., 1997. Direct measurement of rheologically induced molecular orientation in gas separation hollow fibre membranes and effects on selectivity. J. Membr. Sci. 126, 133–137.
Jeazet, H.B.T., Staudt, C., Janiak, C., 2012. Metal-organic frameworks in mixed-matrix membranes for gas separation. Dalton Trans. 41, 14003–14027.
Job, N., Heinrichs, B., Lambert, S., Pirard, J-P., Colomer, J-F., Vertruyen, B., Marien, J., 2006. Carbon xerogels as catalyst supports: study of mass transfer. AIChE J. 52, 2663–2676.
Job, N., Pirard, R., Marien, J., Pirard, J-P., 2004. Porous carbon xerogels with texture tailored by pH control during sol–gel process. Carbon 42, 619–628.
Jones, C.A., Gordeyev, S.A., Shilton, S.J., 2011. Poly(vinyl chloride) (PVC) hollow fibre membranes for gas separation. Polymer 52, 901–903.
Paul, D.R., Kemp, D.R., 1973. The diffusion time lag in polymer membranes containing adsorptive fillers. J. Polym. Sci. Polym. Symp 41, 79–93.
Pekala, R.W., Alviso, C.T., 1992. Carbon aerogel and xerogels. In: C.L. Renschler et al. (Eds.), Novel Forms of Carbon: Materials Research Society Symposium Proceedings. 270, 3–14.
Qin, G., Wang, C., Wei, W., 2010. Preparation of a mesoporous carbon membrane from resorcinol and formaldehyde. Carbon 48, 4197–4214.
Robeson, L.M., 2008. The upper bound revisited. J. Membr. Sci 320, 390–400.
Robeson, L.M., 1991. Correlation of separation factor versus permeability for polymeric membranes. J. Membr. Sci 62, 165–185.
Sharpe, I.D., Ismail, A.F., Shilton, S.J., 1999. A study of extrusion shear and forced convection residence time in the spinning of polysulfone hollow fiber membranes for gas separation. Sep. Purif. Technol 17, 101–109.
Shilton, S.J., Bell, G., Ferguson, J., 1994. The rheology of fibre spinning and the properties of hollow-fibre membranes for gas separation. Polymer 35, 5327–5336.
Strobl, G., 1997. The Physics of Polymers. Springer, Berlin.
Tao, Y., Endo, M., Kaneko, K., 2008. A review of synthesis and nanopore structures of organic polymer aerogels and carbon aerogels. Recent Patents on Chemical Engineering 1, 192–200.
Ward, R.R., Chang, R.C., Danos, J.C., Carden, J.A.jnr, 1980. Monsanto Co., Process for Coating Bundles of Hollow Fiber Membranes, US Pat., 4214020.
Yamamoto, T., Endo, A., Ohmori, T., Nakaiwa, M., 2004. Porous properties of carbon gel microspheres as adsorbents for gas separation. Carbon 42, 1671–1676.
Yoshimune, M., Haraya, K., 2011. Microporous carbon membranes. In: Basile, A., Gallucci, F. (Eds.), Membranes for Membrane Reactors: Preparation, Optimization and Selection. John Wiley & Sons Ltd, Chichester, UK.
Yoshimune, M., Yamamoto, T., Nakaiwa, M., Haraya, K., 2008. Preparation of highly mesoporous carbon membranes via a sol–gel process using resorcinol and formaldehyde. Carbon 46, 1031–1036.
Zhang, Y.F., Musselman, I.H., Ferraris, J.P., Balkus jnr, K.J., 2008. Gas permeability properties of mixed-matrix matrimid membranes containing a carbon aerogel: a material with both micropores and mesopores. Ind. Eng. Chem. Res. 47, 2794–2802.
Zimmerman, C.M., Singh, A., Koros, W.J., 1997. Tailoring mixed matrix composite membranes for gas separations. J. Membr. Sci. 137, 145–154.
Zornoza, B., Tellez, C., Coronas, J., Gascon, J., Kapteijn, F., 2013. Metal organic framework based mixed matrix membranes: an increasingly important field of research with a large application potential. Microporous Mesoporous Mater. 166, 67–78.

References

[1] Job N, Pirard R, Marien J, Pirard JP. Porous carbon xerogels with texture tailored by pH control during sol-gel process. Carbon. 2004;42(3):619-28.

[2] Sharma CS, Kulkarni MM, Sharma A, Madou M. Synthesis of carbon xerogel particles and fractal-like structures. Chemical Engineering Science. 2009 Apr;64(7):1536-43.

[3] Lin C, Ritter JA. Effect of synthesis pH on the structure of carbon xerogels. Carbon. 1997;35(9):1271-8.

[4] Pierre AC, Pajonk GM. Chemistry of Aerogels and Their Application. Chem Rev. 2002;102:4243-65.

[5] Kistler S. Coherent Expanded Aerogels. J Phys Chem. 1932 1932;36(1):52-64.

[6] Lide DR. CRC Handbook of Chemistry and Physics, Internet Version 2006, . Boca, Raton, FL: CRC Handbook of Chemistry and Physics, Internet Version 2006, Taylor and Francis; 2006.

[7] Barbieri O, Ehrburger-Dolle F, Rieker TP, Pajonk GM, Pinto N, Rao AV, editors. Small-angle X-ray scattering of a new series of organic aerogels. 6th International Symposium on Aerogels (ISA-6); 2000 Oct 08-11
Jun 1; Albuquerque, New Mexico2001.

[8] Fricke J, Tillotson T. Aerogels: Production, characterization, and applications. Thin Solid Films. 1997 1997;297:212-23.

[9] NIST. http://webbook.nist.gov/cgi/cbook.cgi?ID=C124389&Mask=4. NIST; 2011 [cited 2013 August].

[10] http://www.methanol.org/Technical-Information/Resources/Technical-Information/Physical-Properties-of-Pure-Methanol.aspx. [cited 2013 August].

[11] Pekala RW, Kong FM. A synthetic route to organic aerogels - mechanism, structure, and properties. Journal De Physique. 1989 Apr 1989;50(C4):33-40.

[12] Pekala RW. Organic aerogels from the polycondensation of resorcinol with formaldehye. Journal of Materials Science. 1989 Sep;24(9):3221-7.

[13] Ingram AR. Electronic interpretation of the uncatalyzed reaction between resorcinol and formldehyde in alcohols and dioxane. Canadian Journal of Chemistry. 1951 1951;29:863-70.

[14] Raff RAV, Silverman BH. Kinetics of the uncatalyzed reactions between resorcinol and formaldehyde. Industrial and Engineering Chemistry. 1951;43(6):1423-7.

[15] Al-Muhtaseb SA, Ritter JA. Preparation and properties of resorcinol-formaldehyde organic and carbon gels. Advanced Materials. 2003 Jan;15(2):101-14.

[16] Zubizarreta L, Arenillas A, Dominguez A, Menendez JA, Pis JJ. Development of microporous carbon xerogels by controlling synthesis conditions. Journal of Non-Crystalline Solids. 2008 Feb;354(10-11):817-25.

[17] Jabeen N, Mardan A. Effect of water removal on the textural properties of resorcinol/formaldehyde gels by azeotropic distillation. Journal of Materials Science. 1998 Nov 15;33(22):5451-3.

[18] ElKhatat AM, Al-Muhtaseb SA. Advances in Tailoring Resorcinol-Formaldehyde Organic and Carbon Gels. Advanced Materials. 2011 Jul;23(26):2887-903.

[19] Harold Hart, Craine LE, David J. Hart, editors. Organic Chemistry - a short course. 11 ed. Boston, NY: Houghton Mifflin Company; 2003.

[20] A. Pizzi, Mittal KL, editors. Handbook of Adhesive Technology, Second Edition, Revised and Expanded. New York: Marcel Dekker; 2003.

[21] Reuß M, Ratke L. Subcritically dried RF-aerogels catalysed by hydrochloric acid. Journal of Sol-Gel Science and Technology. 2008 Jul;47(1):74-80.

[22] D. Walton, Lorrimer P. Polymers (Oxford Chemistry Primers). Oxford: Oxford University Press; 2000.
[23] Okada K. Preparation and Characterisation of Xerogels. In: Hubbard AT, editor. Enclyopedia of Surface and Colloid Science
New York: Marcel Dekker; 2002. p. 4292-305.
[24] Brinker CJ, Scherer GW. Sol-Gel Science. San Diego: Academic Press, INC.; 1990.
[25] Horikawa T, Hayashi J, Muroyama K. Controllability of pore characteristics of resorcinol-formaldehyde carbon aerogel. Carbon. 2004 2004;42(8-9):1625-33.
[26] D. Wu, R. Fu, Z. Sun, Yu Z. Low-density organic and carbon aerogels from the sol-gel polymerization of phenol with formaldehyde Journal of Non-Crystalline Solids. 2005;351:915.
[27] Tamon H, Ishizaka E. SAXS study on gelation process in preparation of resorcinol-formaldehyde aerogel. Journal of Colloid and Interface Science. 1998 Oct;206(2):577-82.
[28] Berthon S, Barbieri O, Ehrburger-Dolle F, Geissler E, Achard P, Bley F, et al. DLS and SAXS investigations of organic gels and aerogels. Journal of Non-Crystalline Solids. 2001 Jun 1;285(1-3):154-61.
[29] Petricevic R, Reichenauer G, Bock V, Emmerling A, Fricke J, editors. Structure of carbon aerogels near the gelation limit of the resorcinol-formaldehyde precursor. 5th International Symposium on Aerogels; 1997 Sep 08-10
Apr; Montpellier, France1998.
[30] Pekala RW, Schaefer DW. Structure of organic aerogels. 1. Morphology and scaling. Macromolecules. 1993 Sep;26(20):5487-93.
[31] Yamamoto T, Nishimura T, Suzuki T, Tamon H. Control of mesoporosity of carbon gels prepared by sol-gel polycondensation and freeze drying. Journal of Non-Crystalline Solids. 2001 Aug;288(1-3):46-55.
[32] D. W Schaefer, R. Pekala, Beaucage G. Origin of porosity in resorcinol-formaldehyde aerogels. Journal of Non-Crystalline Solids. 1995;186:159-67.
[33] Bernards TNM. Silicate Sol-gel Chemistry as studied by Hydroylsis-Gelation Time Curves. Eindhoven: Philips Electronics; 1997.
[34] Keefer KD, Schaefer DW. Growth of fractally rough colloids Physical Review Letters. 1987 Mar 16;58(11):1155-.
[35] Gommes CJ, Roberts AP. Structure development of resorcinol-formaldehyde gels: Microphase separation or colloid aggregation. Physical Review E. 2008 Apr;77(4).
[36] W.B. Russel, D.A. Saville, Schowalter WR. Colloidal Dispersions. Cambridge: Cambridge University Press; 1989.
[37] Parfitt GD. Dispersion of Powders in Liquid 3rd Edition. London: Applied Science; 1981.
[38] JP. Hsu, Lui B. Effect of Particle Size on Critical Coagulation Concentration. Journl of Colloid and Interface Science. 1998(198):186-9.
[39] Kunz W, Henle J, Ninham BW. 'Zur Lehre von der Wirkung der Salze' (about the science of the effect of salts): Franz Hofmeister's historical papers. Current Opinion in Colloid & Interface Science. 2004 Aug;9(1-2):19-37.
[40] Chaplin M. http://www.lsbu.ac.uk/water/hofmeist.html. 2012 [cited 2013 February].
[41] Kunz W. Specific Ion Effects. Toh Tuck Link: World Scientific Publishing Co. Pte. Ltd.; 2010.
[42] Omta AW, Kropman MF, Woutersen S, Bakker HJ. Negligible effect of ions on the hydrogen-bond structure in liquid water. Science. 2003 Jul 18;301(5631):347-9.
[43] Batchelor JD, Olteanu A, Tripathy A, Pielak GJ. Impact of protein denaturants and stabilizers on water structure. Journal of the American Chemical Society. 2004 Feb 25;126(7):1958-61.

[44] Gurau MC, Lim SM, Castellana ET, Albertorio F, Kataoka S, Cremer PS. On the mechanism of the Hofmeister effect. Journal of the American Chemical Society. 2004 Sep 1;126(34):10522-3.
[45] Zhang Y, Cremer PS. Interactions between macromolecules and ions: the Hofmeister series. Current Opinion in Chemical Biology. 2006 Dec;10(6):658-63.
[46] Tamon H, Ishizaka H, Yamamoto T, Suzuki T. Preparation of mesoporous carbon by freeze drying. Carbon. 1999;37(12):2049-55.
[47] Czakkel O, Marthi K, Geissler E, Laszlo K. Influence of drying on the morphology of resorcinol-formaldehyde-based carbon gels. Microporous and Mesoporous Materials. 2005 Nov;86(1-3):124-33.
[48] Job N, Thery A, Pirard R, Marien J, Kocon L, Rouzaud JN, et al. Carbon aerogels, cryogels and xerogels: Influence of the drying method on the textural properties of porous carbon materials. Carbon. 2005 Oct;43(12):2481-94.
[49] http://wwwaerogelorg/?p=891&px=%2FAerogels+of+Different+Compositions%2Flifeo facarbonaerogelwithlabels-aerogeldotorgjpg. [cited 2013 August].
[50] J. Aleman, A. V. Chadwick, J. He, M. Hess, K. Horie, R.G. Jones, et al. Definitions of terms relating to the structure and processing of sols, gels, networks, and inorganic-organic hybrid materials (IUPAC Recommendations 2007). Pure Appl Chem. 2007;70(10):1801-29.
[51] Marsh H, editor. Introduction to Carbon Science. London: Butterworth & Co.; 1989.
[52] Clark J. http://www.chemguide.co.uk/basicorg/bonding/methane.html. 2000 [cited 2013 July].
[53] Dutch S. http://www.uwgb.edu/dutchs/Petrology/Diamond%20Structure.HTM. 2001` [cited 2013 July].
[54] Ltd NGI. http://www.n-kokuen.com/e/whatis/index.htm. 2000 [cited 2013 July].
[55] Zubizarreta L, Arenillas A, Pirard JP, Pis JJ, Job N. Tailoring the textural properties of activated carbon xerogels by chemical activation with KOH. Microporous and Mesoporous Materials. 2008 Nov;115(3):480-90.
[56] Samant PV, Goncalves F, Freitas MMA, Pereira MFR, Figueiredo JL. Surface activation of a polymer based carbon. Carbon. 2004 2004;42(7):1321-5.
[57] Mirzaeian M, Hall PJ. Preparation of controlled porosity carbon aerogels for energy storage in rechargeable lithium oxygen batteries. Electrochimica Acta. 2009;54(
):7444-51.
[58] Kuhn J, Brandt R, Mehling H, Petricevic R, Fricke J, editors. In situ infrared observation of the pyrolysis process of carbon aerogels. 5th International Symposium on Aerogels; 1997 Sep 08-10
Apr; Montpellier, France1998.
[59] Poljansek I, Krajnc M. Characterization of Phenol-Formaldehyde Prepolymer Resins by In Line FT-IR Spectroscopy. Acta Chim Slov. 2005;52:238-44.
[60] Hwang SW, Hyun SH. Capacitance control of carbon aerogel electrodes. Journal of Non-Crystalline Solids. 2004 Nov;347(1-3):238-45.
[61] Durairaj RB, editor. Resorcinol: Chemistry, Technology and Applications. Berlin: Springer; 2005.
[62] Morales-Torres S, Jose Maldonado-Hodar F, Francisco Perez-Cadenas A, Carrasco-Marin F. Textural and mechanical characteristics of carbon aerogels synthesized by polymerization of resorcinol and formaldehyde using alkali carbonates as basification agents. Physical Chemistry Chemical Physics. 2010 2010;12(35):10365-72.
[63] Job N, Gommes CJ, Pirard R, Pirard J-P. Effect of the counter-ion of the basification agent on the pore texture of organic and carbon xerogels. Journal of Non-Crystalline Solids. 2008 Oct 15;354(40-41):4698-701.
[64] Cohaut N, Thery A, Guet JM, Rouzaud JN, Kocon L. The porous network in carbon aerogels investigated by small angle neutron scattering. Carbon. 2007 May;45(6):1185-92.

[65] Awadallah-F A, Elkhatat AM, Al-Muhtaseb SA. Impact of synthesis conditions on meso- and macropore structures of resorcinol-formaldehyde xerogels. Journal of Materials Science. 2011 Dec;46(24):7760-9.
[66] Zanto EJ, Al-Muhtaseb SA, Ritter JA. Sol-gel-derived carbon aerogels and xerogels: Design of experiments approach to materials synthesis. Industrial & Engineering Chemistry Research. 2002 Jun;41(13):3151-62.
[67] Bock V, Emmerling A, Fricke J. Influence of monomer and catalyst concentration on RF and carbon aerogel structure. Journal of Non-Crystalline Solids. 1998;225:69-73.
[68] Tamon H, Ishizaka H, Mikami M, Okazaki M. Porous structure of organic and carbon aerogels synthesized by sol-gel polycondensation of resorcinol with formaldehyde. Carbon. 1997;35(6):791-6.
[69] Jena A, Gupta K. Advances in Pore Structure Evaluation by Porometry. Chemical Engineering & Technology. 2010 Aug;33(8):1241-50.
[70] Kraiwattanawong K, Tamon H, Praserthdam P. Influence of solvent species used in solvent exchange for preparation of mesoporous carbon xerogels from resorcinol and formaldehyde via subcritical drying. Microporous and Mesoporous Materials. 2011 Feb;138(1-3):8-16.
[71] Tamon H, Ishizaka H. Influence of gelation temperature and catalysts on the mesoporous structure of resorcinol-formaldehyde aerogels. Journal of Colloid and Interface Science. 2000 Mar;223(2):305-7.
[72] Hulsey SS, Alviso CT, Kong FM, Pekala RW, editors. The effect of pyrolysis temperature and formulation on pore-size distribution and surface-area of carbon aerogels. Symp on Novel Forms of Carbon; 1992 Apr 27-May 01; San Francisco, Ca1992.
[73] Lin C, Ritter JA. Carbonization and activation of sol-gel derived carbon xerogels. Carbon. 2000;38(6):849-61.
[74] Wiener M, Reichenauer G, Hemberger F, Ebert HP, editors. Thermal conductivity of carbon aerogels as a function of pyrolysis temperature. 17th European Conference on Thermophysical Properties; 2005 Sep 05-08
Nov; Bratislava, SLOVAKIA2006.
[75] Lu AH, Li WC, Salabas EL, Spliethoff B, Schuth F. Low temperature catalytic pyrolysis for the synthesis of high surface area, nanostructured graphitic carbon. Chemistry of Materials. 2006 Apr;18(8):2086-94.
[76] Conceicao FL, Carrott PJM, Carrott M. New carbon materials with high porosity in the 1-7 nm range obtained by chemical activation with phosphoric acid of resorcinol-formaldehyde aerogels. Carbon. 2009 Jun;47(7):1874-7.
[77] Pekala RW, Kong FM. Resorcinol-formaldehyde aerogels and their carbonized derivatives. National meeting of the American Chemical Society. Dallas, Texas, USA1988. p. 15.
[78] Bock V, Emmerling A, Saliger R, Fricke J. Structural Investigation of Resorcinol Formaldehyde and Carbon Aerogels Using SAXS and BET. Journal of Porous Materials. 1997 Oct;4(4):287-94.
[79] lee H-J, Song J-H, Kim J-H. Synthesis of resorcinol/formaldhyde gel particles by the sol-gel emulsion gel technique. Materials Letters. 1998;37:1998.
[80] Scherdel C, Scherb T, Reichenauer G. Spherical porous carbon particles derived from suspensions and sediments of resorcinol-formaldehyde particles. Carbon. 2009 Aug;47(9):2244-52.
[81] Pekala RW, Farmer JC, Alviso CT, Tran TD, Mayer ST, Miller JM, et al., editors. Carbon aerogels for electrochemical applications. 5th International Symposium on Aerogels; 1997 Sep 08-10
Apr; Montpellier, France1998.
[82] Murata Manufactoring Co. L.
http://www.murata.com/products/edlc/tech_guide/priciple_feature/images/ind_img02.gif.
[cited 2013 September].

[83] Conway BE, editor. Electrochemical Supercapacitors - Scientific Fundamentals and Technological Applications. New York: Kluwer Academic/Plenum; 1999.
[84] Frackowiak E. Carbon materials for supercapacitor application. Physical Chemistry Chemical Physics. 2007;9(15):1774-85.
[85] Chuan Lin JARaBNP. Correlation of Double-Layer Capacitance with the Pore Structure of Sol-Gel Derived Carbon Xerogels. Journal of the Electrochemical Society. 1999 1/6/99;146(20):3639-43.
[86] Nagy Z. http://electrochem.cwru.edu/encl/art-f04-fuel-cells-pem.htm. [cited 2013 September].
[87] Job N, Marie J, Lambert S, Berthon-Fabry S, Achard P. Carbon xerogels as catalyst supports for PEM fuel cell cathode. Energy Conversion and Management. 2008 Sep;49(9):2461-70.
[88] J. Marie, S. Fabry-Berthon, P. Achard, M. Chatenet, E. Chainet, R. Pirard, et al. Platinum Supported on resorcinol-formaldehyde based carbon aerogels for PEMFC electrodes: Influence of the carbon support in electrocatalytic properties. J Appl Electrochem. 2007 2007;37:147-53.
[89] Moreno-Castilla C, Maldonado-Hodar FJ. Carbon aerogels for catalysis applications: An overview. Carbon. 2005;43(3):455-65.
[90] Yamamoto T, Sugimoto T, Suzuki T, Mukai SR, Tamon H. Preparation and characterization of carbon cryogel microspheres. Carbon. 2002 2002;40(8):1345-51.
[91] Yamamoto T, Endo A, Ohmori T, Nakaiwa M. Porous properties of carbon gel microspheres as adsorbents for gas separation. Carbon. 2004;42(8-9):1671-6.
[92] Kabbour H, Baumann TF, Satcher JH, Saulnier A, Ahn CC. Toward new candidates for hydrogen storage: High-surface-area carbon aerogels. Chemistry of Materials. 2006 Dec;18(26):6085-7.
[93] Bruce J, Berne J, Pecora R. Dynamic Light Scattering: With Applications to Chemistry, Biology and Physics. New York: Dover Publications; 2000.
[94] Brown W, editor. Dynamic Light Scattering The method and some applications. Oxford: Clarendon Press; 1993.
[95] MalvernInstruments. http://www.malvern.com/labeng/technology/dynamic_light_scattering/classical_90_degree_scattering.htm. [cited 2012 August].
[96] MalvernInstruments. Dynamic Light Scattering: An Introduction in 30 Minutes. Worcestershire: Malvern Instruments Worldwide.
[97] A. Braithwaite, Smith FJ, editors. Chromatographic Methods - Fifth Edition. Dordrecht: Kluwer Academic Publishers; 1999.
[98] Lindsay S. High Performance Liquid Chromatography - Second Edition. Barnes J, editor. New York: John Wiley & Sons; 1992.
[99] McMaster MC. HPLC A Practical User's Guide. New York: VCH Publishers, Inc.; 1994.
[100] Hanai T. HPLC A Practical Guide. Cambridge: The Royal Society of Chemistry; 1999.
[101] Swadesh JK, editor. HPLC Practical and Industrial Applications - Second Edition. London: CRC Press; 2001.
[102] http://faculty.sdmiramar.edu/fgarces/LabMatters/Instruments/UV_Vis/Cary50_Pic/conv entional-spectrophotometer.png. [cited 2013 August].
[103] www.ionsource.com; Interpreting Electrospray Mass Spectra. 2012 [cited 2012 Sept].
[104] B. J. Clark, T. Frost, Russel MA, editors. UV-Spectroscopy - Techniques, instrumentation and data handling. New York: Chapman and Hall; 1993.

[105] Reusch W. http://www2.chemistry.msu.edu/faculty/reusch/VirtTxtJml/Spectrpy/UV-Vis/spectrum.htm. 2013 [cited 2013 August].
[106] Rao CNR, editor. Ultra-Violet and Visible Spectroscopy Chemical Applications. New York: Plenum Press; 1967.
[107] http://www.chemguide.co.uk/analysis/uvvisible/theory.html#top. [cited 2012 September].
[108] Fleming I, editor. Molecular Orbitals and Organic Chemical Reactions - Student Edition. New Jersey: John Wiley & Sons 2009.
[109] http://www.chemguide.co.uk/basicorg/bonding/benzene2.html. [cited 2012 September].
[110] Kilway KV. http://cas.umkc.edu/chemistry/Faculty/courses/Kilway/Ch13.pdf. [cited 2012 September].
[111] Varian. http://www.bu.edu/photonics/files/2011/02/Cary5000brochure.pdf. [cited 2012 September].
[112] http://spotlite.nih.gov/assay/images/a/a8/Manual_sect17_fig15.gif. [cited 2012 September].
[113] PerkinElmer. http://www.perkinelmer.com/CMSResources/Images/44-74556GDE_TGABeginnersGuide.pdf. 2011 [cited 2011 August]; Available from: http://www.perkinelmer.com/CMSResources/Images/44-74556GDE_TGABeginnersGuide.pdf.
[114] Datta SK, Higuchi M, Morita M. Analysis of phenol-resorcinol-formaldehyde resins. Journal of Wood Science. 1999 1999;45(5):411-6.
[115] Speyer R. Thermal Analysis of Materials. New York: Marcel Dekker Inc.; 1994.
[116] http://www.kentchemistry.com/links/Kinetics/BondEnergy.htm. [cited 2012 August].
[117] J. I. Goldstein, D. E. Newbury, P. Echlin, D. C. Joy, A. D. Romig J, C. E. Lyman, et al. Scanning Electron Microscopy and X-Ray Microanalysis - A Text for Biologists, Materials Scientists, and Geologists. New York: Plenum Press; 1992.
[118] C. E. Lyman, D. E. Newbury, J. I. Goldstein, D. B. Williams, A. D. Romig J, J. T. Armstrong, et al. Scanning Electron Microscopy, X-Ray Microanalysis, and Analytical Electron Microscopy-A Laboratory Workbook. New York: Plenum Press; 1990.
[119] http://www.microscopy.ethz.ch/sem.htm. 2012 [cited 2012 August].
[120] Jooshesh A. Factors affecting the depth of field for SEM: University of Victoria.
[121] http://www.uiowa.edu/~cmrf/methodology/sem/sem11.gif. 2012 [cited 2012 August].
[122] Rouquerol J, Avnir D, Fairbridge CW, Everett DH, Haynes JH, Pernicone N, et al. Recommendations for the characterization of porous solids Pure and Applied Chemistry. 1994;66(8):1739-58.
[123] Sing KSW, Everett DH, Haul RAW, Moscou L, Pierotti RA, Rouquerol J, et al. Reporting physisorption data for gas solid systems with special reference to the determination of surafec-area and porosity (Recommendations 1984). Pure and Applied Chemistry. 1985;57(4):603-19.
[124] Gregg SJ, Sing KSW. Adsorption, Surface Area and Porosity. New York: Academic Press Inc.; 1967.
[125] Fifth Edition ed. Oxford: Oxford University Press; 2004. Dictionary of Chemistry.
[126] Burgess CCV, Everett DH, Nuttall S. Adsorption hysteresis in porous materials. Pure & Appl, Chem. 1989;61(11):1845-52.
[127] Micromeritics. http://www.micromeritics.com/Repository/Files/Gas_Adsorption_Theory_poster.pdf. [cited 2010 August]; Available from: http://www.micromeritics.com/Repository/Files/Gas_Adsorption_Theory_poster.pdf.
[128] Langmuir I. The constitution and fundamental properties of solids and liquids. Part I. Solids. JACS. 1916;38:2221.

[129] Siminiceanu I, Lazau I, Ecsedi Z, Lupa L, Burciag C. Textural Characterization of a New Iron-Based Ammonia Synthesis Catalyst. Chem Bull "Politehnica" Univ (Timisoara). 2008 2008;53 (67):1-2.
[130] J. H. de Boer, B. C. Lippens, B. G. Linsen, J. C. Broekhoff, A. van den Heuval, Th. J. Osinga. The t-Curve of Multimolecular N2-Adsorption. Journal of Colloid and Interface Science. [Journal aricle]. 1966 1966;21:405-14.
[131] Kaneko K. Determination of pore-size and pore-size distribution. 1. Adsorbents and catalysts Journal of Membrane Science. 1994 Nov 28;96(1-2):59-89.
[132] Atkinson D, McLeod AI, Sing KSW. Adsorptive properties of microporous carbons - Primary and secondary micropore filling. Journal De Chimie Physique Et De Physico-Chimie Biologique. 1984 1984;81(11-1):791-4.
[133] Sing KSW. The use of physisorption for the characterization of microporous carbons. Carbon. 1989 1989;27(1):5-11.
[134] Kaneko K, Ishii C. Superhigh surface-area determination of microporous solids. Colloids and Surfaces. 1992 Nov 9;67:203-12.
[135] Setoyama N, Suzuki T, Kaneko K. Simulation study on the relationship between a high resolution alpha(s)-plot and the pore size distribution for activated carbon. Carbon. 1998 1998;36(10):1459-67.
[136] Sayari A, Liu P, Kruk M, Jaroniec M. Characterization of large-pore MCM-41 molecular sieves obtained via hydrothermal restructuring. Chemistry of Materials. 1997 Nov;9(11):2499-506.
[137] Micromeritics Instrument Inc. ASAP 2420 Operators Manual. ASAP 2420 Operators Manual. Norcorss GA2007.
[138] Rege SU, Yang RT. Corrected Horvath-Kawazoe equations for pore-size distribution. Aiche Journal. 2000 Apr;46(4):734-50.
[139] D. H. Williams, I. Fleming. Spectroscopic Methods in Organic Chemistry 5th Edition. UK: The McGraw Hill Companies; 1995.
[140] A.D. Cross, R. A. Jones. An Introduction to Practical Infra-red Spectroscopy. UK: Butterworths; 1969.
[141] D. A. Burns, E. W. Ciurczak. Handbook of Near Infrared Analysis. New York: Marcel Dekker Inc.; 1992.
[142] http://cqd.eecs.northwestern.edu/research/qcl/absorption(1).jpg. 2009 [cited 2009 January].
[143] PerkinElmer. http://www.utsc.utoronto.ca/~traceslab/ATR_FTIR.pdf. Shelton: Perkin Elmer; 2005 [cited 2013 September].
[144] Brereton RG. Chemometrics – Data Analsysis for the Laboratory and Chemical Plant
England: John Wiley & Sons Ltd.; 2003.
[145] http://www.chembuddy.com/?left=BATE&right=pH_calculation. Poland: BPP Marcin Borkowski; [cited 2011 April].
[146] http://www.hannainst.co.uk/product_info.php?cPath=6567_7043&products_id=2754. HANNA Instruments; [cited 2012 March].
[147] Peat S. Understanding and Controlling the Development of Gas-Storage Materials. [Undergraduate Research Project]. In press 2011.
[148] Razouk H. pH-Control Effect on the Characterisation of RF-Gels, Utilising NaHCO3 as a Catalyst, and Using the Addition of HNO3. Glasgow: The University of Strathclyde; 2012.
[149] Darwent Bd. http://www.nist.gov/data/nsrds/NSRDS-NBS31.pdf. Washington DC1970 [cited 2013 March].
[150] Yamamoto T, Mukai SR, Endo A, Nakaiwa M, Tamon H. Interpretation of structure formation during the sol-gel transition of a resorcinol-formaldehyde solution by population balance. Journal of Colloid and Interface Science. 2003 Aug 15;264(2):532-7.

[151] GrenierLoustalot MF, Larroque S, Grande D, Grenier P, Bedel D. Phenolic resins .2. Influence of catalyst type on reaction mechanisms and kinetics. Polymer. 1996 Apr;37(8):1363-9.
[152] Astarloa-Aierbe G, Echeverria JM, Egiburu JL, Ormaetxea M, Mondragon I. Kinetics of phenolic resol resin formation by HPLC. Polymer. 1998 Jun;39(14):3147-53.
[153] Liu X, Zhang W, Sui G, Ning Q. Determination of phenol and formaldehyde in resol resins by high performance liquid chromatography. Se pu = Chinese journal of chromatography / Zhongguo hua xue hui. 2007 2007-Jul;25(4):562-4.
[154] Guzzetta A. Reverse Phase HPLC Basics for LC/MS; An IonSource Tutorial. IonSource; 2001 [cited 2012 March].
[155] Parriott D, editor. A Practical Guide to HPLC Detection. London: Academic Press Incorporated; 1993.
[156] M. Nic JJ, B. Kosata. IUPAC. Compendium of Chemical Terminology, 2nd ed. (the "Gold Book"). Compiled by A. D. McNaught and A. Wilkinson. Blackwell Scientific Publications, Oxford (1997). XML on-line corrected version: http://goldbook.iupac.org (2006-) IUPAC; 2006 [cited 2013 March].
[157] Singer DC, editor. A Laboratory Quality Handbook of Best Practices. Wisconsin: ASQ Quality Pres; 2001.
[158] Haslam J, Soppet WW. A note on the rapid determination of free formaldehyde in phenol-formaldehyde syrups. Journal of Applied Chemistry. 1953;3:328-29.
[159] Bennett CT, Salamon MS. A General Method for the Determination of Aldehydes in Essential Oils, with Particular Reference to the Determination of Citronella1 in Java Citronella Oil and Citral in Lemon Oil. Analyst. 1927:693-95.
[160] Gardziella A, Pilato L, Knop A, editors. Phenolic Resins; Chemistry, Applications, Standardization, Safety and Ecology. New York: Springer; 2000.
[161] Hebalkar N, Arabale G, Sainkar SR, Pradhan SD, Mulla IS, Vijayamohanan K, et al. Study of correlation of structural and surface properties with electrochemical behaviour in carbon aerogels. Journal of Materials Science. 2005 Jul;40(14):3777-82.
[162] Wang JB, Yang XQ, Wu DC, Fu RW, Dresselhaus MS, Dresselhaus G. The porous structures of activated carbon aerogels and their effects on electrochemical performance. Journal of Power Sources. 2008 Oct;185(1):589-94.
[163] Sepehri S, Garcia BB, Zhang QF, Cao GZ. Enhanced electrochemical and structural properties of carbon cryogels by surface chemistry alteration with boron and nitrogen. Carbon. 2009 May;47(6):1436-43.
[164] El Mir L, Kraiem S, Bengagi M, Elaloui E, Ouederni A, Alaya S. Synthesis and characterization of electrical conducting nanoporous carbon structures. Physica B-Condensed Matter. 2007 May;395(1-2):104-10.
[165] Jørgensen A. Clustering excipient near infrared spectra using different chemometric methods. 2000.
[166] C. Berho, M. F. Pouet, S. Bayle, N. Azema, O. Thomas. Study of UV-vis responses of mineral suspensions in water. Colloids and Surfaces A: Physicochemical and Engineering Aspects. 2004;243(1-3):9-16.
[167] ABB. http://www05.abb.com/global/scot/scot205.nsf/veritydisplay/dbe07c4cc884e19185257a2100461a9a/$file/FTIR%20Laboratory%20Analyzer%20Brochure%202012%20MB3000%20%28H%29%20.pdf. Canada 2012 [cited 2013 August].
[168] Aranovich G, Donohue M. Analysis of adsorption isotherms: Lattice theory predictions, classification of isotherms for gas-solid equilibria, and similarities in gas and liquid adsorption behavior. Journal of Colloid and Interface Science. 1998;200(2):273-90.
[169] Lu X, Caps R, Fricke J, Alviso CT, Pekala RW. Correlation between structure and thermal - conductivity of organic aerogels. Journal of Non-Crystalline Solids. 1995 Aug;188(3):226-34.

[170] Lee YJ, Jung JC, Yi J, Baeck SH, Yoon JR, Song IK. Preparation of carbon aerogel in ambient conditions for electrical double-layer capacitor. Current Applied Physics. 2010 Mar;10(2):682-6.
[171] Taylor S. DLS study of the formation of RF xerogels. 2012.
[172] Gaca KZ. Kinetics and mechanisms of early stages of resorcinol-formaldehyde polymerization. Glasgow: University of Strathclyde; 2012.
[173] Kendall EW, Frei J, Bruce R. Trethewey J, Benton LD, editors. Characterization of the polymerization of phenol formaldehyde resin using high pressure differential scanning calorimetry and liquid chromatography. Plastic Laminates Symposium; 1998.
[174] Pilato L, editor. Electonic Book; Phenolic resins: a century of progress. Heidelberg (Germany); London; New York: Springer; 2012.
[175] Peat S. Understanding and Controlling the Development of Gas-Storage Materials: pH study of Organic and Carbon Xerogels [Undergraduate thesis]. Glasgow: The University of Strathclyde; 2011.
[176] Bordwell FG. Equilibrium acidities in dimethyl sulfoxide solution. Acc Chem Res. 1988(21):456 - 63.
[177] Kielland J. Individual activity coefficients of ions in aqueous solutions. Journal of the American Chemical Society. 1937 Jul-Dec;59:1675-8.
[178] G. Astarloa-Aierbe, J.M. Echeverria, M.D. Martin, Mondragon I. Kinetics of phenolic resol resin formation by HPLC. 2. Barium hydroxide. Polymer 1998;39 (15):3467-72.
[179] Reuss M, Ratke L. RF-aerogels catalysed by ammonium carbonate. Journal of Sol-Gel Science and Technology. 2010 Jan;53(1):85-92.
[180] Saliger R, Reichenauer G, Fricke J. Evolution of microporosity upon CO_2-activation of carbon aerogels. In: Unger KK, Kreysa G, Baselt JP, editors. Characterisation of porous solids V: Elsevier; 2000. p. 381-90.
[181] Saliger R, Bock V, Petricevic R, Tillotson T, Geis S, Fricke J. Carbon aerogels from dilute catalysis of resorcinol with formaldehyde. Journal of Non-Crystalline Solids. 1997 Dec;221(2-3):144-50.
[182] Mirzaeian M, Hall PJ. The control of porosity at nano scale in resorcinol formaldehyde carbon aerogels. Journal of Materials Science. 2009 May;44(10):2705-13.
[183] Andrzej Szczurek, Gisele Amaral-Labat, Vanessa Fierro, Antonio Pizzi, Celzard A. Bimodal activated carbons derived from resorcinol-formaldehyde cryogels. Science and Technology of Advanced Materials. 2011 2011;12:1-12.
[184] Wen ZB, Qu QT, Gao Q, Zheng XW, Hu ZH, Wu YP, et al. An activated carbon with high capacitance from carbonization of a resorcinol-formaldehyde resin. Electrochemistry Communications. 2009 Mar;11(3):715-8.
[185] Mojtaba Mirzaeian, Hall PJ. High Capacity Carbon Based Electrodes for Lithium/Oxygen Batteries. Power System Technology. 2007;31(20):90-6.
[186] W. Schaerti, H. Sillescu. Brownian dynamics of polydisperse colloidal hard-spheres - equilibrium structures and random close packings. J Stat Phys. 1994;77:1007 - 25.
[187] Magueijo VM, Anderson LG, Fletcher AJ, Shilton SJ. Polysulfone mixed matrix gas separation hollow fibre membranes filled with polymer and carbon xerogels. Chemical Engineering Science. 2013 Apr;92:13-20.
[188] Yamamoto T, Yoshida T, Suzuki T, Mukai SR, Tamon H. Dynamic and static light scattering study on the sol-gel transition of resorcinol-formaldehyde aqueous solution. Journal of Colloid and Interface Science. 2002 Jan 15;245(2):391-6.
[189] Huber MM, Klein H, Ratke L. DLS-based fractal analysis in early stage gelation. Particle & Particle Systems Characterization. 2004 Feb;20(6):379-81.
[190] Keck CM, Mueller RH. Size analysis of submicron particles by laser diffractometry-90% of the published measurements are false. International Journal of Pharmaceutics. 2008 May 1;355(1-2):150-63.

[191] http://www.kayelaby.npl.co.uk/chemistry/3_8/3_8_7.html. National Physics Laboratory; 2012 [cited 2012 September].
[192] A.Mrzel, A.Mertelj, A. Omerzu, M. Cÿ opic, Mihailovic D. Investigation of Encapsulation and Solvatochromism of Fullerenes in Binary Solvent Mixtures. J Phys Chem. 1999;B(103):11256-60.
[193] Haruhisa Kato, Ayako Nakamura, Kayori Takahashi, Kinugasa S. Size effect on UV-Vis absorption properties of colloidal C60 particles in water. Physical Chemistry Chemical Physics. 2009(11):4946–8.
[194] J. M. Fu, Y. Li, J. L. Guo. Optical behavior of organic pigments in aqueous dispersions and its application. J Colloid Interface Sci. 1998;202(2):450 - 5.
[195] Goodner KL. www.sensusflavors.com, Turbidity, Tea, And UV-VIS. Ohio: Sensus Technical Note (SEN-TN-0008); 2008 [cited 2012 Sep].
[196] Goodner KL. www.sensusflavors.com, Estimating Turbidity (NTU) From Absorption Data. Sensus Technical Note (SEN-TN-0010); 2008 [cited 2012 Sep].
[197] McLean C. Characterisation and Particle Growth Monitoring of Resorcinol-Formaldehyde Xerogels. Glasgow: The University of Strathclyde; 2013.
[198] Montgomery DC. Design and Analysis of Experiments. 7th ed. Hoboken, New Jersey: John Wiley & Sons Inc.; 2008.
[199] StatSoft I. (Electronic Version): Electronic Statistics Textbook. WEB: http://www.statsoft.com/textbook/. Tulsa, OK: StatSoft; 2013.